

Retrieval of aerosol optical thickness
over snow and ice surfaces in the Arctic using
Advanced Along Track Scanning Radiometer

Larysa Istomina

Universität Bremen 2012

Retrieval of aerosol optical thickness over snow and ice surfaces in the Arctic using Advanced Along Track Scanning Radiometer

Vom Fachbereich Physik, Elektro- und Informationstechnik
der Universität Bremen
genehmigte
Dissertation
zur Erladung des akademischen Grades
Doktor rer. nat.

von: Dipl.-Phys. u. Astron.
Larysa Istomina
aus Bremen

eingereicht am: 07. September 2011
Tag des mündlichen Kolloquiums: 16. December 2011

1. Gutachter: Prof. Dr. John P. Burrows
2. Gutachter: Prof. Dr. Justus Notholt

Abstract

Atmospheric aerosols influence energy balance of the Arctic region via scattering solar radiation, influencing albedo and lifetime of clouds, and via deposition on snow and ice surfaces. To know about the impact of arctic aerosols is crucial, because the Arctic region is a very sensitive area and an important factor in global circulation and climate.

Due to severe conditions and remoteness of the area, there are few ground based or airborne data available on atmospheric aerosols in the Arctic. Remote sensing has therefore a strong potential to provide the necessary spatial and temporal observation coverage of the area. Passive remote sensing of aerosols in the Arctic region is a challenging task: the underlying snow and ice reflect much more than aerosol layer in the atmosphere, i.e. the underlying surfaces compose most of the top of atmosphere signal observed by the satellite. State-of-the art algorithms are not able to resolve this task, leading to gaps in aerosol data in the Polar regions.

This thesis describes an algorithm, which takes into account the bright reflecting underlying surface and establishes the retrieval of the atmospheric aerosol amount in the Arctic region using passive remote sensing. The goal of this work is to provide the maps of aerosol optical thickness over snow and help to better understand the global aerosol distribution.

The algorithm is a multi-angle approach, based on the dual-viewing Advanced Along-Track Scanning Radiometer (AATSR) onboard ENVISAT. A number of conducted simulation and modeling studies preceded the establishment of automatic snow/cloud discrimination algorithm and aerosol optical thickness retrievals in the visible and infrared spectral regions. Extensive validation and application studies, which have been chosen in order to cover possibly greater spatial and temporal range of data, show the ability of the developed methods to provide the maps of aerosol optical thickness over various snow types, for different aerosol types. The results of the aerosol retrieval for pollution events featuring mineral dust, volcanic aerosol, biomass burning and pollution associated with boreal forest fires are compared to independent space borne and ground based observations and showed coinciding temporal and spatial dynamics of the aerosol distribution. Additionally, a cloud screening routine, based on visible and infrared AATSR observations, was also successfully validated against independent space borne and ground based data and ensures the absence of cloud contamination in the resulting aerosol product. Applied together, these methods allow for the first time the retrieval of aerosol amount over snow and ice on local to global scales.

The developed methods and resulting aerosol product are of major importance for better understanding of aerosol distribution over snow and its effect on the local and global energy balance, which is necessary for the evaluation of the Arctic climate status. The resulting aerosol product can be also used as the atmospheric correction for the snow surface retrievals not only in the Arctic region, but also over any snow covered surface.

List of publications

1. Publications in peer-reviewed journals

As first author:

- **Istomina L.**, W. von Hoyningen-Huene, A. A. Kokhanovsky, and J. P. Burrows. The detection of cloud free snow covered areas using AATSR measurements, *Atmos. Meas. Tech.*, 3, 1-13, 2010.
- **Istomina L.**, von Hoyningen-Huene, W., Kokhanovsky, A. A., Schultz, E., and Burrows, J. P.: Remote sensing of aerosols over snow using infrared AATSR observations, *Atmos. Meas. Tech.*, 4, 1133-1145, 2011.
- **Istomina L.**, W. von Hoyningen-Huene, A. A. Kokhanovsky, and J. P. Burrows. Retrieval of aerosol optical thickness over snow and ice using dual-view AATSR observations in the visible spectral region, **in preparation**.

As coauthor:

- Stankevich D., **Istomina L.**, Shkuratov Yu., Videen G. Electromagnetic phase differences in the coherent backscattering enhancement mechanism for random media consisting of large non-transparent spheres, *Applied Optics*, Vol. 46, Issue 9, 1562-1567, 2007.
- Stankevich D., **Istomina L.**, Shkuratov Yu., Videen G. The coherent backscattering effects in a random medium as calculated using a ray tracing technique for large non-transparent spheres, *Journal of Quantitative Spectroscopy and Radiative Transfer*, 106, 1-3, 509-519, 2007.
- W. von Hoyningen-Huene, J.M. Yoon, M. Vountas, **L.G. Istomina**, G. Rohen, T. Dinter, A.A. Kokhanovsky, and J.P. Burrows. Retrieval of spectral aerosol optical thickness over land using ocean color sensors MERIS and SeaWiFS, *Atmos. Meas. Tech.*, 4, 151-171, 2011.
- C. Schlundt, A. A. Kokhanovsky, W. von Hoyningen-Huene, T. Dinter, **L. Istomina**, and J. P. Burrows. Synergetic cloud fraction determination for SCIAMACHY using MERIS, *Atmos. Meas. Tech.*, 4, 319-337, 2011.
- Krijger, J. M., Tol, P., **Istomina, L. G.**, Schlundt, C., Schrijver, H., and Aben, I.: Improved identification of clouds and ice/snow covered surfaces in SCIAMACHY observations, *Atmos. Meas. Tech. Discuss.*, 4, 1113-1138, 2011.

2. Conference and workshops contributions:

- **Istomina L.G.**, W. von Hoyningen-Huene, Kokhanovsky A. A., Rozanov V. V., Schreier M., Burrows J.P. The Algorithm of AOT retrieval over snow and ice: developing and testing on simulated radiative-transfer data // 2nd EUFAR Summer School on Airborne Cloud and Aerosol Science, 17-25 April, 2008, Utrecht, The Netherlands, 2008.
- **Istomina L.G.**, W. von Hoyningen-Huene, Kokhanovsky A. A., Rozanov V. V., Schreier M., Stock M., Treffeisen R., Herber A., Burrows J.P. Sensitivity study of the dual-view algorithm for aerosol optical thickness retrieval over snow and ice // Proceedings of 2nd MERIS/(A)ATSR user workshop, ESRIN, Frascati, Italy, 22-26 Sept. 2008, ESA SP-666, 2009.
- **Istomina L.**, W. Von Hoyningen-Huene, A. Kokhanovsky, M. Schreier, V. Rozanov, and J.P. Burrows. Retrieval of aerosol optical thickness over snow using dual-view satellite observations // Book of abstracts, General Assembly of European Geosciences Union, Vienna, Austria, 18-24 April 2009.
- **Istomina L.**, W. von Hoyningen-Huene, A. Kokhanovsky, J. P. Burrows. The retrieval of aerosol optical thickness in Arctic region using dual-view AATSR measurements // POLARCAT workshop, 2-5 June 2009, Durham, New Hampshire, 2009.
- **Istomina L.**, W. von Hoyningen-Huene, A. Kokhanovsky, J. P. Burrows. The determination of AOT over snow using AATSR observations // 439. WE-Heraeus Seminar on Determination of Atmospheric Aerosol Properties Using Satellite Measurements, 17-19 August 2009, Bad Honnef, Germany, 2009.
- **Istomina L.**, W. von Hoyningen-Huene, A. Kokhanovsky, J. P. Burrows. The retrieval of aerosol optical thickness over snow using AATSR observations // Abstracts of American Geophysical Union Fall Meeting, 14-18 December 2009, San Francisco, California, 2009.
- **Istomina L.G.**, W. von Hoyningen-Huene, A.A. Kokhanovsky, and J.P. Burrows. Retrieval of aerosol optical thickness in Arctic region using dual-view AATSR observations // Proceedings of ESA Atmospheric Science Conference, Barcelona, Spain, 7-11 Sept. 2009, ESA SP-676, 2010.
- **Istomina L.G.**, W. von Hoyningen-Huene, A.A. Kokhanovsky, and J.P. Burrows. Remote Sensing of Aerosols in Arctic Region // AWI-IUP Blockseminar "Polar Processes - II", 13 July 2010, Bremerhaven, Germany, 2010.
- **Istomina L.G.**, W. von Hoyningen-Huene, A.A. Kokhanovsky, and J.P. Burrows. Retrieval of aerosol optical thickness over snow using AATSR observations // 38th COSPAR Scientific Assembly, July 18-25 2010, Bremen, Germany, 2010.
- **Istomina L.G.**, W. von Hoyningen-Huene, A.A. Kokhanovsky, and J.P. Burrows. Aerosol remote sensing over snow using infrared AATSR observations // Book of abstracts, General Assembly of European Geosciences Union, Vienna, Austria, 03-08 April 2011.

Contents

Abstract	5
List of publications	7
Contents	9
1 Introduction and motivation	11
1.1. Aerosol satellite remote sensing	14
1.2 Aim of this work.....	18
1.3 Outline of this thesis	19
2 Scientific Background	21
2.1 Introduction to the Earth’s atmosphere.....	21
2.1.1 Radiative balance of the atmosphere.....	23
2.1.2 Aerosols and clouds	25
2.1.3 Aerosol radiative forcing.....	29
2.2 The Arctic, its climate system and role in global climate.....	32
2.2.1 Snow and ice coverage.....	34
2.2.2 Atmospheric aerosol in the climate of the Arctic region. Arctic Haze	40
2.3 Scattering in the atmosphere.....	44
2.3.1 Molecular Rayleigh scattering	45
2.3.2 Particle Mie scattering.....	46
2.3.3 Integrated optical properties of an aerosol medium	48
2.4 Radiative transfer in the atmosphere	49
2.4.1 Description of the radiative transfer.....	50
2.4.2 The forward radiative transfer model SCIATRAN	56
2.5 Description of the instruments.....	57
2.5.1 The satellite instrument AATSR.....	57
2.5.2 Ground-based AERONET measurements.....	59
3 Developing the retrieval of tropospheric aerosol from satellite	63
3.1 Satellite data selection	63
3.2 The snow flagging approach.....	64
3.2.1. Theoretical basis of spectral cloud screening over snow	65

3.2.2. Snow flagging in VIS and NIR: disturbance from aerosols, trace gases and physical parameters of snow	66
3.2.3. Cloud screening in TIR: snow emissivity and cloud reflectance.....	72
3.2.4. Sensitivity study	74
3.3 AOT retrieval in the visible range of spectrum.....	79
3.3.1 Optical properties of aerosol and snow in the visible.....	80
3.3.2 Theoretical basis.....	82
3.3.3 Sensitivity study	85
3.3.4 Choosing the aerosol type and LUT calculations.....	93
3.3.5 Application limits and sources of errors.....	94
3.4 AOT retrieval in the infrared range of spectrum.....	96
3.4.1 The main features of aerosol and snow in the infrared.....	97
3.4.2 Theoretical basis.....	102
3.4.3 Sensitivity study	104
3.4.4 Choosing the aerosol type and LUT calculation.....	104
3.4.5 Application limits and sources of errors.....	107
3.5 Summary	109
4 Validation	113
4.1 Comparison to MPL and MODIS data.....	113
4.2 Comparison with AERONET	118
4.3 Comparison with MERIS.....	124
5 Case studies.....	129
5.1 Case study: dust formation and transport on Greenland during July 04/05, 2008	129
5.2 Case study: biomass burning pollution transport to Ny Ålesund, spring 2006.....	133
5.3 Case study: boreal forest burning in Canada and transport to Alaska, summer 2004.	138
5.4 Case study: Kizimen volcano eruption at Kamchatka, spring 2011	141
5.5 Case study: Antarctic background aerosol, 6 th January 2011.....	143
6 Summary and outlook.....	145
Bibliography	149
List of abbreviations.....	165
List of used symbols	167
Acknowledgements.....	169

1 Introduction and motivation

The fundamental role of the Arctic in the global climate system is to be the Northern Hemisphere “heat sink”. One of the main ruling forces of the global atmospheric circulation is the poleward transport of energy by the atmosphere and oceans from the equatorial regions, which receive the largest amount of solar radiation on an annual average, but emit less than they receive. The remaining part is heat transfer into the Arctic. Therefore changes of the energy balance in the Arctic region may distort the atmospheric circulation of the whole planet, which in turn may result in a lot of climatic consequences, also on regional and global scale. Atmospheric aerosols¹ play a major role in the Arctic climate, both locally in terms of air pollution and visibility reduction and regionally with respect to their radiative forcing effects (scattering and absorbing solar radiation, deposition on the snow surface and thus changing its albedo, changing the lifetime and albedo of clouds). Aerosols in the Arctic are even more important than elsewhere because their scattering and absorption effects are enhanced by the high albedo of the underlying snow and ice surfaces, which enables multiple acts of light scattering between the surface and aerosol particles and might produce significant warming at the surface (Randles et al., 2004). Arctic atmosphere has been degrading in air quality since the industrial development in the 18th century, and especially in the 20th century, as the amount of aerosol pollution on Earth was strongly increasing. There are very few sources of pollution in the Arctic itself, but this region was found to be highly affected by the long range transport from midlatitudes. In 1957, the term “Arctic haze” has been introduced by Mitchell (1957) to describe the regular pollution events occurring in the Arctic during late winter and spring and associated with the long range transport of industrial and natural pollution. There are high uncertainties about the fact what fraction of pollution leaves the Arctic and what fraction is deposited within the Arctic region on land and sea surfaces. But it is clear that some of the aerosol contaminants end up in Arctic ecosystems (Meijer et al., 2003). At the same time, recent researches (e.g. D. Shindell, G. Faluvegi, 2009) indicate the alarming climate response to the regional radiative forcing in the Arctic associated with aerosol pollution (Fig. 1.1). Satellite records beginning in 1979 show a strong decline in the extent of floating sea-ice (Fig. 1.2), with extreme minima for every September since 2002 (Stroeve et al., 2005). The sea-ice cover appears to be thinning (Rothrock et al., 2003; Lindsay and Zhang, 2005). Paleoclimate research indicates that recent Arctic temperatures are the highest of the past 400 years (Overpeck et al., 1997). The Arctic climate system may be moving toward an entirely new energy balance (Overpeck et al., 2005.)

¹ The definition will be given in 2.1.2

1 Introduction and motivation

In order to realistically evaluate the reasons and perspectives of such changes in the Arctic climate, also more information about the distribution and amount of the polar aerosols is strongly necessary. This will help to assess and understand the status of the global climate as well, as atmospheric aerosols are the largest uncertainty in global climate models and the mechanisms of their effect on climate are not well understood even for midlatitude conditions, and even less in the Polar regions. Due to the hard weather conditions and remoteness of the area, there are only a few ground based stations which measure the aerosol amount and optical properties in the Arctic.

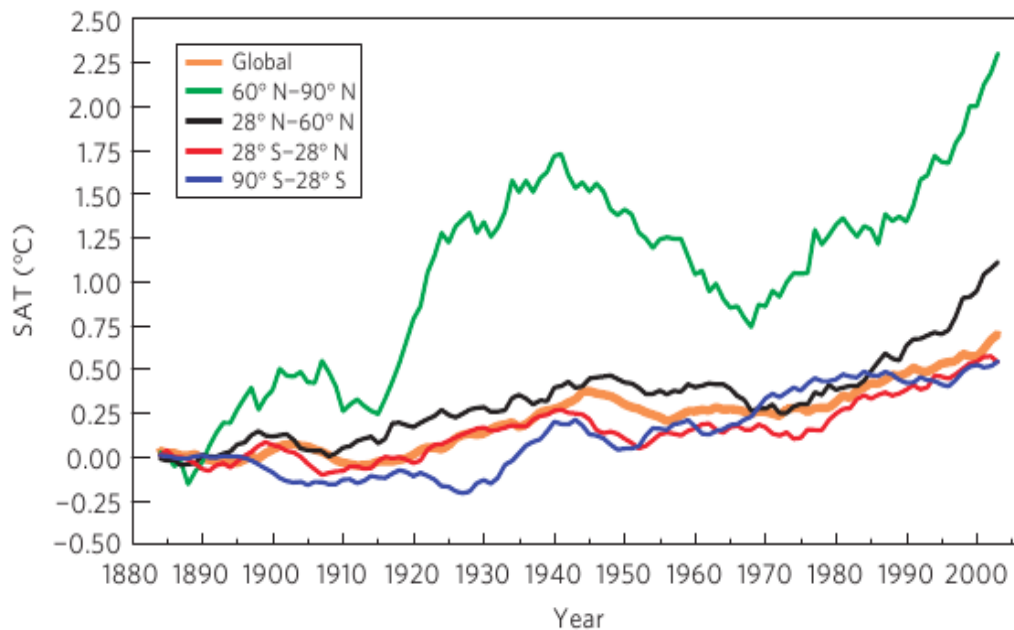


Fig. 1.1 Area-weighted change of mean observed surface air temperatures (SAT) over the indicated latitude bands. The values are nine-year running means relative to the 1880-1890 mean. Note the steep curve corresponding to the Arctic region as compared to the other latitude bands. From Shindell, Faluvegi, 2009.

Because of short lifetime of aerosols in the troposphere, the aerosol is highly variable in both space and time and ground based observations do not have the potential to satisfy the need for aerosol data on a global scale during long periods of time.

The currently available information on the atmospheric aerosols in the Arctic is listed below:

1. Aerosol product from a few ground based stations in the Arctic available on a constant basis (AERONET: <http://aeronet.gsfc.nasa.gov>, AEROCAN: <http://www.aerocanonline.com/templates/nature/index.html>);
2. Aerosol product available on episodic basis, like aerosol measurements from pollution episodes (Stohl et al., 2006; Stohl et al., 2007; Treffeisen et al., 2007), airborne campaigns (Dörnbrack et al., 2010; POLARCAT: <http://www.polarcat.no/>) or temporal effort of scientific community such as research within the International Polar Year (ICSU, 2004);

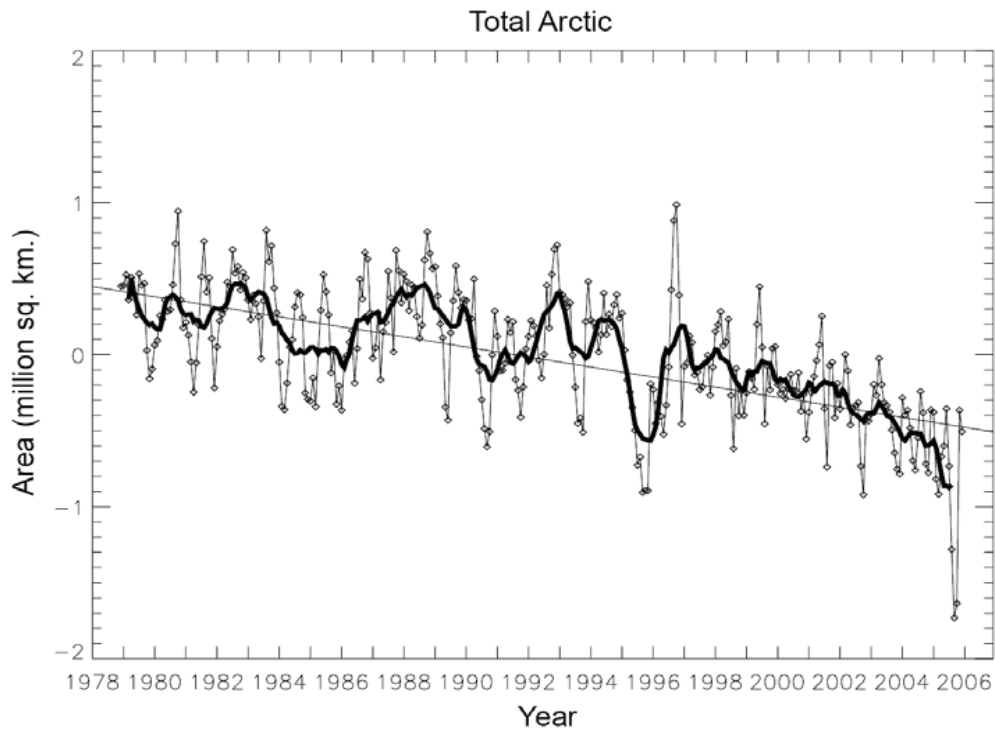


Fig. 1.2. Time series of monthly anomalies of the area of minimum extent of Arctic sea ice from 1979 to 2004. The thick solid line represents 12-month running means; the thin straight line is least-squares linear fit. From Serreze and Francis, 2006, courtesy of National Snow and Ice Data Center, Boulder, CO.

3. Modeling of chemical dynamics and particle dispersion in the atmosphere, like GEM-AQ (Global Environmental Multiscale Air Quality, O'Neil et al., 2006), or FLEXPART models (Stohl et al., 2005);
4. Active remote sensing, e.g. CALIPSO which acquires aerosol optical thickness² (AOT) from integrated backscatter profiles (<http://www-calipso.larc.nasa.gov/>). Among passive remote sensing only MISR (Multi-angle Imaging SpectroRadiometer, <http://www-misr.jpl.nasa.gov/>) provides aerosol product over snow; this product is, however, not quality assured (personal communication with Ralph Kahn, 2010).

Among all the listed data sources, only the first data source is providing data on a constant temporal basis, yet often interrupted in the difficult Arctic conditions. The spatial coverage of these data is poor. Satellite remote sensing has the potential to provide much better temporal and spatial coverage necessary to analyze highly variable aerosol spatial and temporal distribution on local to global scales. However, atmospheric remote sensing over bright reflecting snow and ice surfaces presents a problem, which has not been solved so far. Until now, there are no published researches on the retrieval of aerosol amount over snow and ice, which work on the global scale with no assistance from complementary field or airborne measurements of the surface optical properties. The current understanding of global aerosol distribution has therefore gaps in the Polar regions (see Fig. 1.3). The focal point of this thesis is to fill in these gaps and provide information on aerosol amount and distribution over

² The definition is given in Sect. 2.3

bright reflecting snow and ice surfaces, particularly in the Arctic region, using passive remote sensing means.

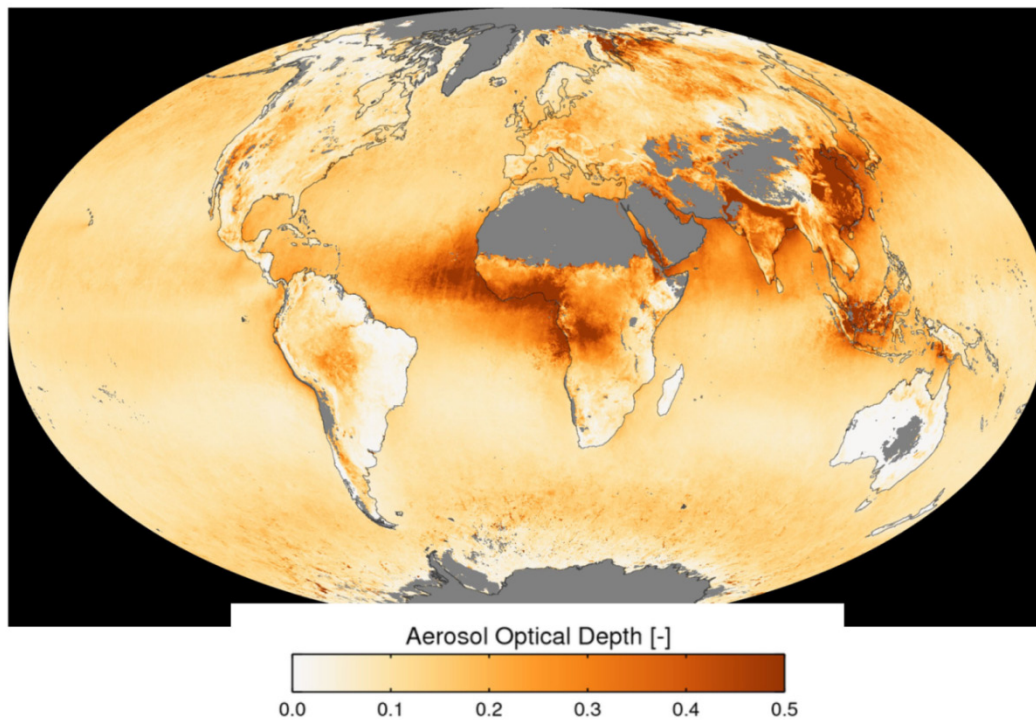


Fig. 1.3. The annual mean of aerosol optical depth at 550 nm from Moderate Resolution Imaging Spectroradiometer (MODIS) for 2006. Note the heavy aerosol load over the Eastern Russia and Siberia that appears to be intensified over the Arctic Ocean. This has been caused by biomass burning of agricultural lands and boreal forest in Russia during May and transported across Scandinavia into the Arctic.

1.1 Aerosol satellite remote sensing

To understand the effects of aerosols on climate, their spatial and temporal distribution needs to be known at a global scale; neither ground based nor airborne measurements are capable of providing the necessary coverage of the data. Since decades it was recognized that solar radiation scattered back to space is influenced by aerosols (as well as other atmospheric compounds and the surface properties), and analyzing the top of atmosphere (TOA) radiation observed by a satellite has the potential of bringing information about aerosol amount and optical properties.

The effect of atmospheric aerosols on the TOA radiance cannot be evaluated without the knowledge about the underlying surface. This is because an increasing aerosol load decreases the role of the surface in the TOA radiance (via decreasing the transmittance) and increases the atmospheric role in it (via increasing reflective properties of atmospheric layer). For the simplest case of black underlying surface (ocean of land with the spectral albedo less than 0.05 in the VIS), the main effect of the AOT increase is the increase of the TOA reflectance (see Fig.1.4). As the surface albedo increases, the decrease of the aerosol transmittance with

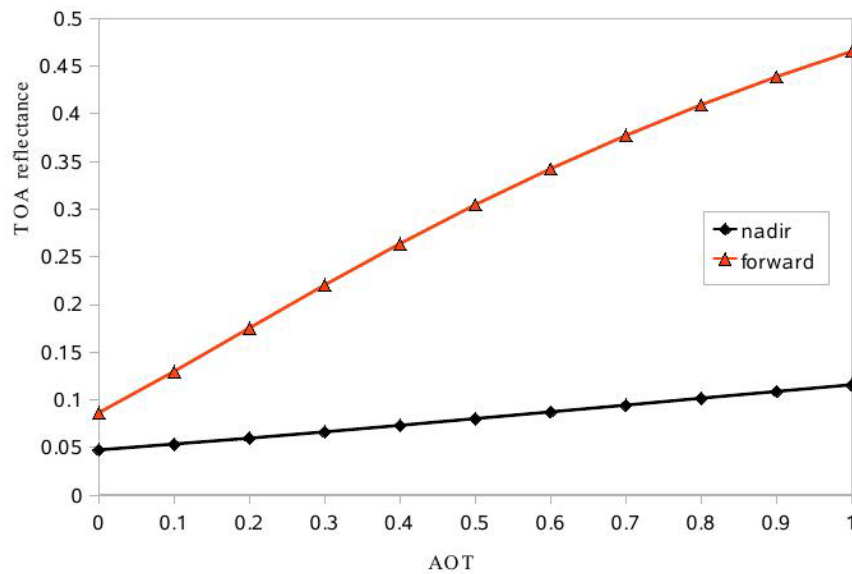


Fig. 1.4 The dependence of TOA reflectance on AOT(550nm) of 2km layer of maritime aerosol over a black Lambertian reflector for two observational geometries: nadir (satellite zenith angle = 0°) and forward (satellite zenith angle = 55°). Solar zenith angle = 65° , relative azimuth = 0° . Ozone absorption and Rayleigh scattering are taken into account. Calculated with forward RT model SCIATRAN (see Sect. 2.4.2).

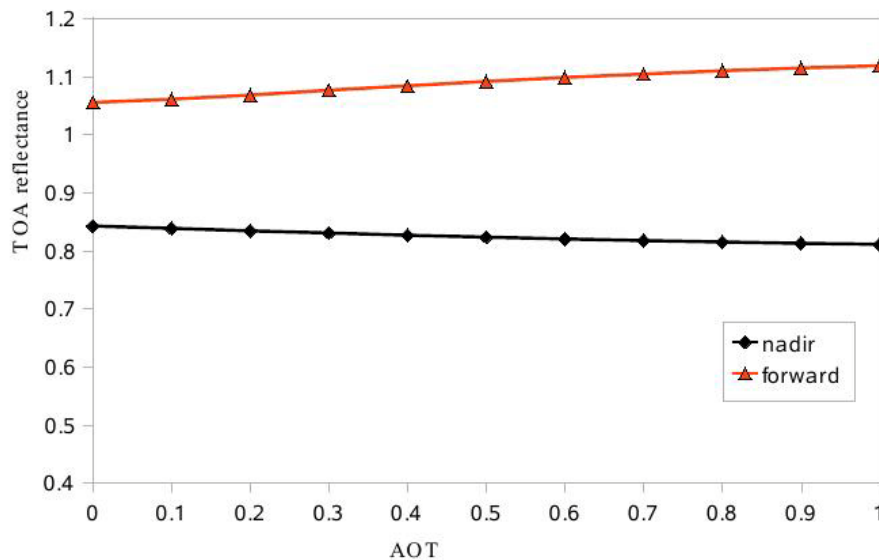


Fig. 1.5 The dependence of TOA reflectance on AOT(550nm) of 2km layer of maritime aerosol over a bright non-Lambertian snow surface for two observational geometries: nadir (satellite zenith angle = 0°) and forward (satellite zenith angle = 55°). Solar zenith angle = 65° , relative azimuth = 0° . Ozone absorption and Rayleigh scattering are taken into account. The bidirectional reflectance distribution function (BRDF) of snow is equal to 0.93 for the nadir geometry and 1.05 for the forward geometry. Calculated with forward RT model SCIATRAN.

increasing AOT plays greater role, being extremely important for the brightest surfaces. For the brightest surfaces the role of the reflectance of the aerosol layer on the TOA radiance will be very small, as the high surface reflectance dominates the aerosol reflectance in the visible

1 Introduction and motivation

spectral region (VIS) both via single scattering and multiple scattering (see Fig. 1.5). For low absorbing aerosols the dependence of the TOA reflectance on the AOT will therefore be much less pronounced over bright surfaces than over dark surfaces, as can be seen from Fig. 1.4 and 1.5.

Snow has the highest spectral albedo among all the surface types in the VIS (spherical albedo 0.8-0.9 for snow at 550nm). The effects discussed above are most significant for the case of snow surface, and also depend on the geometry of observations (Fig. 1.5) due to the directional behavior of snow optical properties (see Sect. 2.2.1). It is also visible from Fig. 1.4 and 1.5 that the TOA reflectance of the system “surface + atmosphere” is not a simple sum of the surface and atmospheric components. Multiple scattering between the surface and atmosphere increases as the surface reflectance grows. Along with the direct surface component in the TOA reflectance, the multiple scattered component also depends drastically on the surface optical properties. This makes it important for remote sensing applications to have a good understanding about the directional and spectral optical properties of underlying surfaces, especially for those with high spectral reflectance. The least “convenient” surface for the AOT retrieval is therefore snow: rapid temporal and significant spatial variability of both spectral and directional optical properties of snow, together with its high spectral albedo in the visible spectral region, make snow surface maybe the least “convenient” surface for the AOT retrieval. The drastic difference of snow optical properties as compared to the other surface types (water, vegetation, bare soil, etc.) makes it impossible to use conventional AOT retrieval algorithms developed for use over land or open water for the AOT retrieval over snow.

The level of difficulty of the AOT retrievals over various surface types is connected to the level of the surface contamination of the TOA radiance signal. For a given AOT of 0.1 at 550nm (see Fig. 1.4) the TOA atmospheric reflectance is about 0.05, which is of the same order of magnitude as the ocean and land spectral albedos, but only about 5%-10% of the snow spectral albedo at this wavelength (see Table 1.1).

Table 1.1. Evaluation of the AOT retrieval “convenience” for the four main surface types.

Surface type	Albedo (550nm)	Aerosol role in TOA signal	Surface	
			Temporal variability	Spatial variability
Ocean	<0.05	High	Low	Low
Vegetation	0.05-0.1	Moderate	Moderate	Moderate
Desert	0.2	Low	Low	Moderate
Snow and ice	0.3-0.95	Very low	High	High

As opposed to the case of bright snow surface, the case of e.g. open water has been elaborated since mid- 1970s (Griggs, 1975; Fraser, 1976, Durkee et al., 1991; Husar et al., 1997). Currently, there is a variety of AOT retrieval algorithms designed for various satellite sensors and capable of retrieving AOT over various ocean and land surface types. But given the high spatial, temporal and directional variability of snow optical properties, the subtraction of the surface signal from the TOA reflectance becomes an immensely challenging task over snow and ice surfaces.

The common AOT retrieval algorithms are very much sensor dependent, as each satellite instrument has unique spectral and spatial resolutions and observation geometries. But all of them solve the radiative transfer (RT) equation (see Sect. 2.4) in order to extract the aerosol role from the TOA radiance measured from space. For this the knowledge of the surface properties is needed; while some of the retrievals utilize ready surface reflectance databases, others retrieve surface and aerosol properties simultaneously. Some of the major sensors involved in aerosol remote sensing and the key publications describing their AOT retrieval are MODIS, Multi-angle Imaging SpectroRadiometer (MISR), Medium Resolution Imaging Spectrometer (MERIS), Sea-viewing Wide Field-of-view Sensor (SeaWiFS), Advanced Along-Track Scanning Radiometer (AATSR) and its precursors Along-Track Scanning Radiometer (ATSR) and ATSR2, POLarization and Directionality of the Earth Reflectance (POLDER), Second Global Imager (SGLI) and its precursor GLI, Spinning Enhanced Visible Infra-Red Imager (SEVIRI), Advanced Very High Resolution Radiometer (AVHRR), etc. All these satellite sensors can be roughly separated into two groups relevant for the current study: multi-view instruments (POLDER, MISR, AATSR) and single-view instruments (all others).

Among the single-view instruments, MODIS and its extensive algorithm of the AOT retrieval over land and ocean surfaces is probably the most developed by now. The collective effort of the scientific community resulted in many publications, some of which are listed further:

- AOT retrieval over ocean: e.g. Kaufman et al., 1997; Levy et al., 2003;
- AOT retrieval over land: e.g. Tanré et al., 1997; Vermote et al., 1997;
- AOT retrieval over land and ocean: e.g. Remer et al., 2005; Levy et al., 2010; Lyapustin et al., 2011).

The relatively high for a radiometer spectral resolution of this instrument and availability of complementary products such as global surface reflectance databases enables the coverage and quality of the MODIS AOT product over most of the surface types, with the latest inclusion of bright reflecting desert case (Lyapustin et al., 2011).

Both the land and ocean parts of the AOT retrieval are based on the correlation of surface spectral reflectances in the visible and shortwave infrared (SWIR) spectral regions, with the assumption of negligible aerosol influence in the SWIR. However, this approach cannot be used for snow surfaces due to strong variability of the snow directional reflectance properties along the spectrum.

Observations from different angles could improve such observations. The importance of multiangular observations for aerosol retrievals over land has been underlined by e.g. Leroy et al. (1997) and Herman et al. (1997). This observational scheme enables gathering additional information about the target via observing it from several different viewing angles.

1 Introduction and motivation

The AOT retrieval task usually includes more unknown than known values (i.e. aerosol remote sensing is an ill-conditioned problem with too little experimental parameters), with the two major unknowns being the AOT and the surface directional reflectance. So, one needs at least two different observations of the target in order to retrieve both parameters, in addition to assumptions and models to provide the other parameters. An additional observation angle is therefore of immense importance in cases when additional spectral channels are not available, or cannot be used due to high variability of the surface spectral behavior. Multiangular instruments POLDER (Deuze et al., 2001), MISR (Martonchik et al., 2004; Martonchik et al., 2002; Diner et al., 2005) and AATSR (Xue et al., 2009; Sayer et al., 2010; North, 2002; Grey et al., 2006a; Thomas et al., 2005; Veefkind et al., 1998) perform AOT retrievals over ocean and land, and have the potential to provide enough information for AOT retrievals also over bright reflecting surfaces. The aim of the current work is therefore to develop an algorithm for multi-angle observations over bright surfaces. For this purpose, the data from the dual viewing AATSR sensor onboard ENVISAT is utilized (see Sect. 2.5.1).

An overview and comparison of AOT retrievals over land using various satellite retrievals and instruments can be found in (Kokhanovsky et al., 2007; Grey et al., 2006b).

Currently there are no publications considering the passive remote sensing algorithms over snow and ice regions which can be used for aerosol observations in the Arctic. Therefore the task of this work is the investigation of the feasibility of an estimation of aerosol information over such bright surfaces and closing the existing gap in the satellite observations.

1.2 Aim of this work

The objective of this work is to develop an AOT retrieval method for snow covered regions using the dual view multispectral satellite sensor data. This task includes the following key points:

- Developing a method of considering the role of the high reflecting snow surface in the TOA radiance signal in the visible spectral regions and evaluating its accuracy;
- Evaluating the accuracy of existing approximate solutions of the radiative transfer equation for the case of very bright surface and utilizing one of them for the AOT retrieval;
- Developing a method to account for the surface contamination for the AOT retrieval in the IR spectral region, which stems from varying snow surface emittances;
- Setup the modeling techniques to associate the AOT with the aerosol TOA reflectance for various AOTs and observation-illumination geometries (LUT³ approach);
- Elaborating the assumptions on the aerosol optical properties in the visible and infrared (IR) spectral regions (phase function and single scattering albedo input parameters for the RT modeling of LUTs)

³ Look-up table, a precalculated table connecting the aerosol amount to the atmospheric TOA reflectance for a set of varying observation-illumination geometries, wavelengths, aerosol or surface types.

- Application and validation of the approach using available ground based and spaceborne data of the aerosol pollution events in the Arctic region.
- Developing an automatic cloud clearing and snow flagging routine which provides the mask of clear snow pixels for the AOT retrieval;

As the output of the developed approach we should get the AOT maps for snow covered regions. The resulting algorithms and methods can also be applied to another multiangle, multispectral satellite sensors, potentially to the data of the AATSR-like sensor SLST (Sea and Land Surface Temperature Instrument) onboard the future Sentinel3 mission (launch planned on 2013).

1.3 Outline of this thesis

Chapter 2 of this thesis explains the necessary scientific background. The role of the Arctic in global climate and the radiative forcing of aerosol in both global and regional Arctic climate systems are discussed for better understanding of the motivation behind this work. In the second half of Chapter 2 the theory of the radiative transfer and light scattering in the atmosphere is given. The forward RT model SCIATRAN, used satellite sensors and ground based measurements are described.

Chapter 3 is dedicated to the satellite data selection and three parts of the AOT retrieval over snow developed within this work, which are

- 1) the cloud clearing and snow flagging;
- 2) the AOT retrieval over snow in the visible spectral range, which utilizes the AATSR dual viewing observations in order to decrease the drastic influence of high snow spectral albedo on the TOA radiance signal;
- 3) the AOT retrieval over snow in the IR spectral region, which utilizes both AATSR observational angles for the surface correction as well. The details on the LUT calculations with the forward RT model, sensitivity study and expected sources of errors of these algorithm parts are also given in this chapter.

Chapter 4 is dedicated to the validation of all the three parts of the presented algorithm. The section 4.1 describes how our cloud screening approach was validated with the use of MODIS and Micro Pulse Lidar data, sections 4.2 and 4.3 give the validation of the AOT retrieval over snow in the visible and infrared spectral regions using ground based AOT measurements.

Chapter 5 presents the applications of both AOT retrieval parts to the following pollution events in the Arctic:

- formation and transport on Greenland during July 04/05, 2008;
- biomass burning pollution transport to Ny Ålesund, spring 2006;
- boreal forest burning in Canada and transport to Alaska, summer 2004;
- Kizimen volcano eruption at Kamchatka, spring 2011.

Within these case studies the AOT maps over snow are presented for the selected scenes at local and also global scales for the whole Arctic region, along with the comparisons to

1 Introduction and motivation

ground based and space-borne observations. The algorithm was also applied to a scene featuring background aerosol in the Antarctic region.

Chapter 6 contains final remarks and conclusions, and provides an outlook for the future research.

2 Scientific Background

2.1 Introduction to the Earth's atmosphere

The atmosphere can be defined as gas layers surrounding the Earth, mainly consisting of N₂, O₂, H₂O, CO₂ and other trace gases. Basic information about these can be found in standard textbooks, such as e.g. (Brasseur, Orlando, Tyndall, 1999). In this section, we will only cover some details about atmospheric vertical structure, circulation and chemical composition, necessary for understanding of the future sections on global heat budget, radiative forcing, and the role of the Arctic region in the global climate.

The atmosphere is characterized by specific vertical temperature gradients, changing its sign between the layers (see Fig. 2.1).

The *troposphere* is the lowest layer of atmospheric structure ranging from the surface to about 18 km in the tropics, 12 km at midlatitudes and 6-8 km at the poles. This layer contains about 85-90% of the atmospheric mass and can be characterized by high convective activity. The vertical transport of energy and mass exchanges happens at a temporal scale of several weeks. The *planetary boundary layer* is the lower region of the troposphere at the surface with the height about the order of 1 km. Above the troposphere (see Fig. 2.1) is the *stratosphere*, a very stable atmospheric layer ranging up to 50km containing 90% of the atmospheric ozone. The atmospheric layer between 50 and 90 km is called the *mesosphere* and the temperature gradient again reverses as compared to the stratosphere, causing instability and vertical mixing. The layer above 85-90 km is called the *thermosphere*, and the vertical temperature increases with height to the values that depend mostly on the solar activity. The upper atmospheric layer contacting with the interplanetary medium is called the *exosphere*.

Due to the Earth's axial tilt of 23.44°, the solar radiation is distributed unevenly along the latitude. This causes circulation of air masses in the north-south direction (see Fig. 2.2), with rising motion at low latitudes and sinking motion at mid- and high latitudes. This meridional circulation is modified by the Earth's rotation, and the residual meridional component transfers heat from equatorial to polar regions. Figure 2.2 shows a schematic representation of the atmospheric circulation patterns for Northern Hemisphere summer. The transport paths from the equatorial region to the Poles are visible.

The Earth's atmosphere is a mixture of many chemical constituents, among which are the nitrogen N₂ (78%) and oxygen O₂ (21%). These gases together with the noble gases (argon, neon, helium, krypton, xenon) can be characterized by long lifetimes and are therefore well

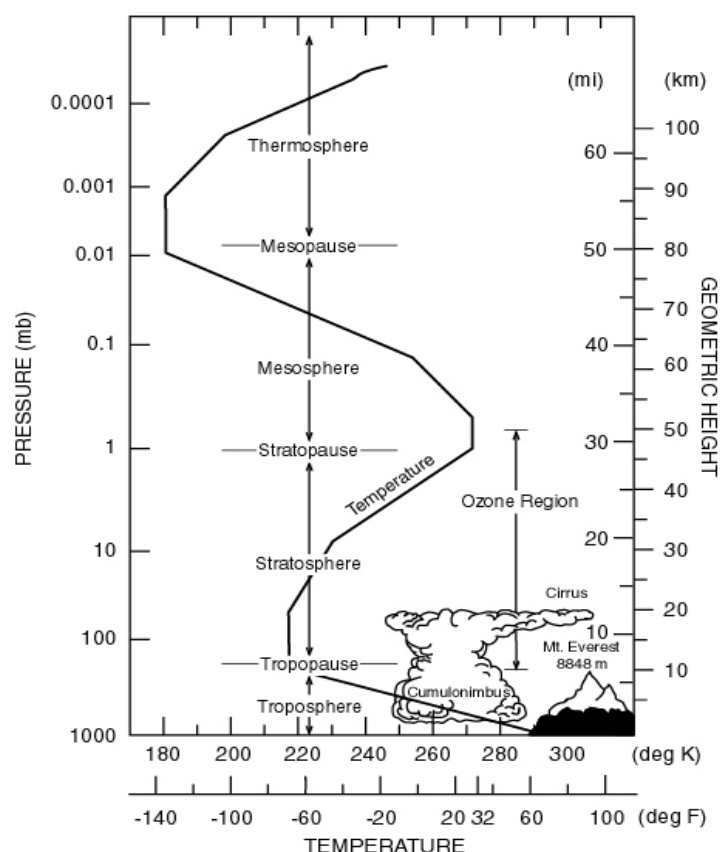


Figure 2.1. Atmospheric vertical structure. Note the behavior of the vertical temperature gradient at different heights. Figure adapted from (Brasseur, Orlando, Tyndall, 1999).

mixed up to the mesosphere. Water vapor, carbon dioxide, ozone, and many others are present at much lower concentrations in the atmosphere, but they influence the transmission of solar and terrestrial radiation in the atmosphere.

Except for the gaseous component of the atmosphere, there is also an aerosol component.

An *aerosol* is defined as a system of solid or liquid particles in gaseous suspension. In atmospheric physics the term “aerosol” is used in the meaning of “aerosol particle”. This defines atmospheric aerosols as *all the particles in the atmosphere larger than a few molecules and smaller than cloud droplets*.

Along with the effect of atmospheric aerosols on human environment and visibility, aerosols affect climate by scattering and absorbing solar radiation, by interacting with clouds and by providing surfaces for chemical reactions in the atmosphere. The mechanisms of these processes and the amount of aerosols on the global scale are not yet well known. Aerosols are considered to be one of the largest uncertainties in today’s climate modeling (IPCC, 2007).

This work is dedicated to aerosols, more detailed information on aerosols is necessary and will be provided in Sect 2.1.2 (aerosol types, chemical composition, size distribution, transport) and Sect. 2.1.3 (aerosol radiative forcing).

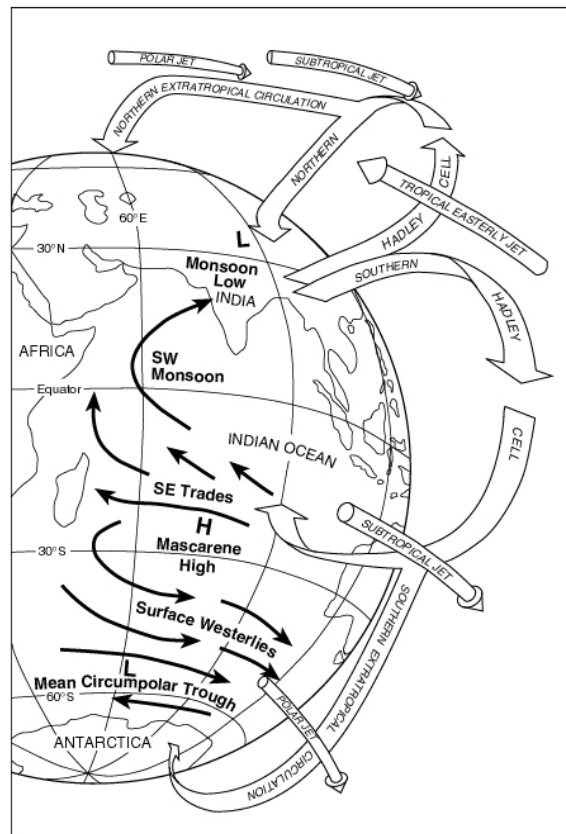


Figure 2.2. Circulation of the atmosphere during Northern Hemisphere summer. Figure adapted from (Brasseur, Orlando, Tyndall, 1999).

2.1.1 Radiative balance of the atmosphere

On the long term scale, the Earth can be considered to be in a state of radiative equilibrium, with the solar radiation serving as the only energy source. This source emits 99.9% of the radiation in the range of 0.15 to 4 μm (peak of intensity at 0.5 μm). The net incoming solar radiation to the Earth system at the top of atmosphere (TOA) can be written as:

$$\text{Net incoming solar} = (1 - A)S\pi R^2 \quad (2.1)$$

where S is the solar constant (1367 W m^{-2}), A is the planetary albedo (approximately 0.3), and R is the radius of the Earth (6371 km). *Albedo* is the ratio of radiation reflected from the surface to the incident radiation. The planetary albedo includes the effects of scattering and absorption by clouds, aerosols and atmospheric gases, as well as the surface albedo⁴. The

⁴ *Albedo* of the surface is defined as the ratio of solar radiation reflected by a surface (upward flux integrated over the hemisphere) to the incident direct beam illumination. This is also called the *directional-hemispheric reflectance*. The albedo measured near the Earth's surface usually contains a significant diffuse component and is termed the *bihemispherical reflectance factor* (Nolin and Liang, 2000). Albedo differs from *spectral reflectance*, which is the reflectance at a single wavelength or in a narrow spectral band. It is also sometimes called *spectral albedo*.

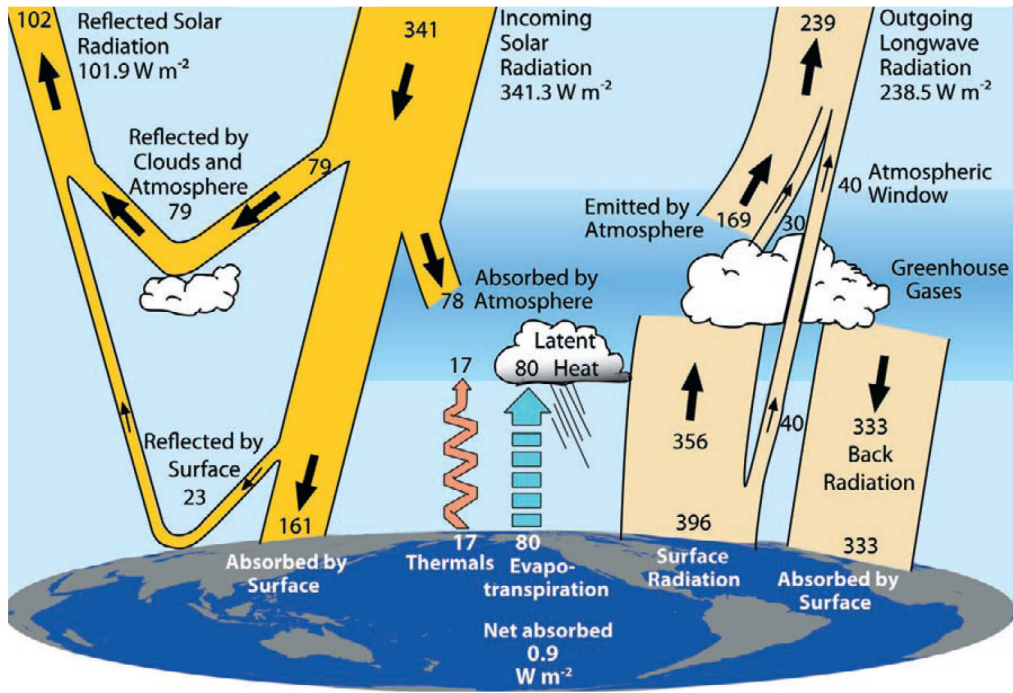


Fig. 2.3. Schematic diagram of the global energy budget. The values are expressed in $W m^{-2}$. The picture is adapted from Trenberth, Fasullo, Kiehl, 2009.

schematic representation of the Earth’s global energy budget and the role of the atmosphere in it are shown in Fig. 2.3.

In radiative equilibrium, the net TOA solar radiation flux is balanced by the radiation emitted to space by the Earth’s atmosphere and surface. This outgoing TOA longwave radiation can be written as:

$$\text{Outgoing longwave} = \sigma T_e^4 4\pi R^2 \tag{2.2}$$

where σ is the Stefan-Boltzmann constant ($5.7 \times 10^{-8} W m^{-2} K^{-4}$), and T_e is the effective radiation emission temperature of the Earth. It depends on both physical temperature and the longwave emissivity of the atmosphere and surface. This outgoing longwave radiation is in the wavelengths range of about 4-300 μm , peaking at about 10 μm . The atmosphere is semi-opaque to longwave radiation and the direct emission to space is only possible through the *atmospheric transparency windows*, e.g. 3-5 μm and 8-14 μm , where the role of the atmosphere can be neglected. One can use these spectral regions to obtain the information about the surface from the satellite, which is used in this work. The other longwave spectral regions are affected by gas absorption (Fig. 2.4).

In the visible region of spectrum, incoming solar radiation is attenuated when propagating through the Earth’s atmosphere due to absorption by gas constituents and by scattering

- 1) on molecular density fluctuations (molecular or Rayleigh scattering, independent of time and space and well known. It will be described in Sect. 2.4.1.);
- 2) on clouds and aerosol particles (aerosol scattering, highly variable in space and time, more details will be given in Sect. 2.4.2-2.4.3);

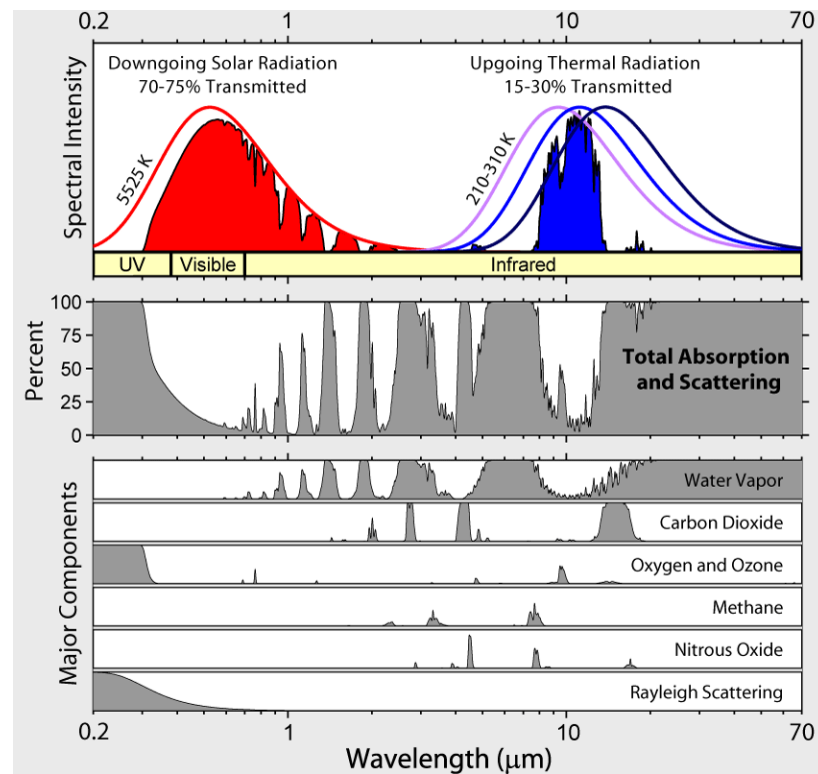


Figure 2.4. Patterns of absorption bands generated by various greenhouse gases and their impact on both solar radiation and upgoing thermal radiation from the Earth's surface (courtesy Robert A. Rohde).

3) on inhomogeneities, induced by turbulent motion of the atmosphere.

Attenuation on molecules and aerosols is much greater than that on turbulent cells, and while the Rayleigh scattering is relatively well known, the quantitative role of the aerosol in the energy budget of the planet is difficult to assess. The state of knowledge on the role of aerosol in the radiation budget will be covered in Sect. 2.1.3.

2.1.2 Aerosols and clouds

The main feature of atmospheric aerosols is their high spatial and temporal variability. Natural, anthropogenic, biogenic processes are responsible for production of particles from parts of nanometers to tens or even hundreds of micrometers, with their chemical composition varying widely not only from place to place but also from particle to particle.

Aerosols can be produced by ejection into the atmosphere (primary aerosol), or by physical and chemical processes inside the atmosphere (secondary aerosol). Examples of primary aerosol are sea spray and windblown dust. Secondary aerosols are produced by condensation of atmospheric gases or by cooling water vapor (gas to particle conversion). The size, shape and chemical composition of aerosols is determined by their production mechanisms. The variety of these natural (forest fires, windblown dust, organics, sea salt, volcanoes, gas to

2 Scientific Background

particle conversion of volcanic SO₂ and biogenic NO_x) and anthropogenic (biomass burning, industrial dust and soot, windblown dust, gas to particle conversion of power plants and traffic NO_x and SO₂) sources creates a great variety of aerosol types of different shape, size distribution, chemical composition and radiative properties. Particles produced with coagulation or condensation have almost correct shapes and are more or less close to spheres. Otherwise produced aerosol particles can only be thought of being spheres as a very rough approximation. Fig 2.5 illustrates the variety of particle shapes of several aerosol types such as fly ash, pollen, sea salt and soot.

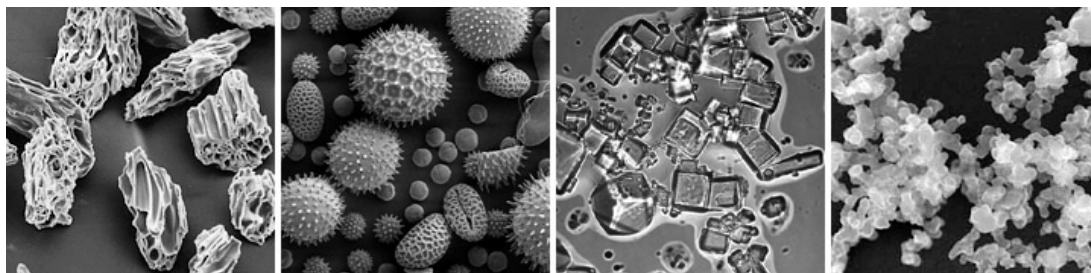


Figure 2.5. The wide variety of aerosol shapes. From left to right: volcanic ash, pollen, sea salt, and soot. Micrographs courtesy USGS, UMBC (Chere Petty), and Arizona State University (Peter Buseck).

Particles of incorrect shapes cannot be fully described in terms of just one dimension (diameter). When speaking of “particle size” of nonspherical particles, one can utilize the following possibilities to conveniently describe the size of the particle using just one dimension (Kokhanovsky, 2004):

- Volume diameter, which is the diameter of a sphere having the same volume as the particle;
- Surface diameter, which is the diameter of a sphere having the same surface area as the particle;
- Surface volume diameter, which is the diameter of a sphere having the same volume to the surface area ratio as the particle;
- Projected area diameter, which is the diameter of the circle having the same area as the projected area of the particle resting in a stable position or randomly oriented.

In the absence of possibility to describe each aerosol particle separately, we are forced to address much simpler descriptions in which the whole aerosol load is described by one parameter – particle size – and the total number of particles of a given size within the given air volume. For this purpose, one can use (with different level of accuracy) the common gamma and lognormal size distributions. E.g. water soluble, dust, soot and oceanic aerosols can be characterized by lognormal size distribution, whereas stratospheric aerosol – by gamma size distribution (Kokhanovsky, 2004).

The aerosol particles are often grouped around several size subranges, i.e. the aerosol size distribution exhibits “modes”. They are schematically showed in Fig. 2.6 together with the corresponding production and removal mechanisms. Whitby and Cantrell (1976) also proposed the commonly used descriptors for the subpopulations: nucleation or Aitken (diameter < 0.1 μm), accumulation (diameter between ~ 0.1 μm and 2.0 μm), and coarse (diameter > 2.0 μm) modes. Additionally, particles smaller than 2 μm are referred as the fine particles.

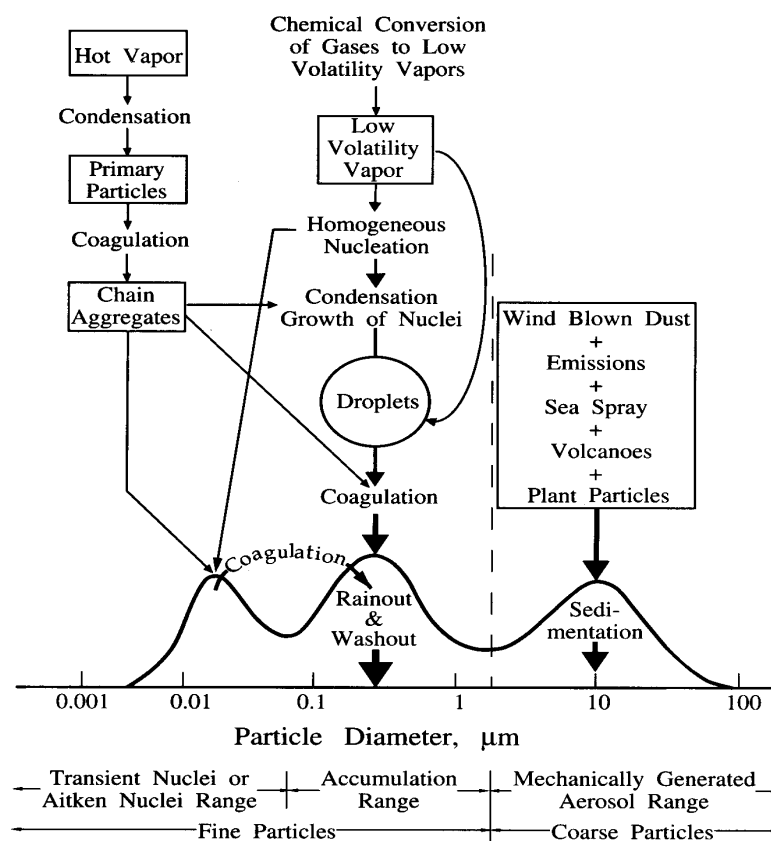


Figure 2.6. The distribution of particle surface area in the atmosphere. Modes, sources and removal mechanisms are indicated (Whitby and Cantrell, 1976).

The spatial and temporal variability of stratospheric and tropospheric aerosol is usually different. The hydrological cycle taking place in the troposphere is in part responsible for this variability. Physical and chemical sources of stratospheric aerosols are fewer in number (mainly volcano eruptions), and stratospheric particles have a relatively long lifetime, a consequence of the lack of wet removal processes and the stable thermal structure of the stratosphere, which inhibits dynamic mixing processes. Aerosol residence time determines the homogeneous or inhomogeneous nature of the global aerosol distribution.

The lifetime of aerosol particles depends on the efficiency of their removal mechanisms. The mean lifetime may generally be computed from:

$$\Sigma_{res} = \frac{1}{\beta_d + \beta_w + \beta_t} \quad (2.3)$$

where β_d is the first-order loss rate constant for dry deposition, β_w is that for wet deposition, and β_t is that for transport to the stratosphere.

Dry particle deposition is dominated by large particles with the diameter $> 1 \mu\text{m}$ and is gravitational settling (sedimentation) which takes place in the lower troposphere and happens within seconds (very large particles at the surface) up to tens of days (smaller particles in the tropopause). Coagulation affects wide range of particle sizes of the fine mode and takes place throughout the whole troposphere, taking for up to hundreds of days. Wet removal (precipitation) affects particles of accumulation mode and happens within several days in the

2 Scientific Background

middle and low troposphere depending on particle size and hygroscopicity. This is the primary mechanism of aerosol removal.

Therefore, the residence time of tropospheric aerosols can vary over several orders of magnitude, from a few minutes to a month, depending upon particle size and other properties, and enables tropospheric aerosol to be transported over relatively large distances, e.g. with Asian and Saharan dust reaching far into the Atlantic and even as far as Greenland or South America (Hobbs, 1993). Arctic Haze is the result of long-range transport from the continents. Aerosol sources, sinks and transport pathways are responsible for the existing geographical aerosol distribution shown in Fig. 1.3.

The residence time of stratospheric aerosols is much greater and can reach several years, creating a spatially uniform aerosol layer. The major source of stratospheric aerosols is the volcano eruptions. For stratospheric aerosols, the dry removal mechanisms are still valid, but no wet removal occurs (except for possible role as condensation nuclei for polar stratospheric clouds). Stratospheric aerosols can rarely be transported to the troposphere and affect radiative properties of cirrus clouds. An example of time needed for removal of stratospheric aerosols after a volcano eruption is shown in Fig. 2.7.

It is visible that it took 3 years at Mauna Loa and 5 years at Barrow for the stratospheric aerosols to be totally removed from the atmosphere. One disturbing point to note is that it appears to take much longer for aerosols to be removed from polar regions than from tropical regions. The reasons are in different atmospheric circulations and aerosol removal processes, which will be covered in Sect. 2.2.2.

Haze is a special result due to aerosols in the air. To define the haze particles, one has to refer to the classic experiments of Coulier (1875) and Aitken (1920) who demonstrated that water vapor condenses in particle free air only at the supersaturation of several hundred percent⁵, whereas in the presence of some condensation nuclei, water droplets form at supersaturations of about 2% or less. Atmospheric aerosol particles can serve as cloud condensation nuclei (CCN) and affect the cloud formation in case they are $>0.5 \mu\text{m}$ (for insoluble particles) or $>0.1 \mu\text{m}$ (for water soluble aerosol); the larger the particle, the lower the critical supersaturation at which it can become a CCN. In a slightly supersaturated condition, very small water soluble particles will only grow by condensation till the equilibrium with the water vapor pressure around them and then stop their growth. Such droplets are called *unactivated droplets* or *haze*. Haze can significantly decrease the intensity of solar radiation reaching the surface, it can also cause sharp decrease in visibility.

Aerosols can also affect clouds in the atmosphere and vice versa. The cloud droplets are tens to hundreds of micrometers in diameter. Clouds and aerosols are connected: aerosols act as cloud condensation nuclei and clouds depend on aerosols for their formation. If they evaporate, they can leave behind aerosol particles with changed chemical and optical properties. This source of aerosol mass is comparable in strength to other major sources like oceans and deserts (Hobbs, 1993). This changes radiative properties of clouds, which in turn

⁵Supersaturation in % = $(e/e_s - 1) \cdot 100$, where e is the vapor pressure of the air and e_s is the saturated vapor pressure over a plane surface of water.

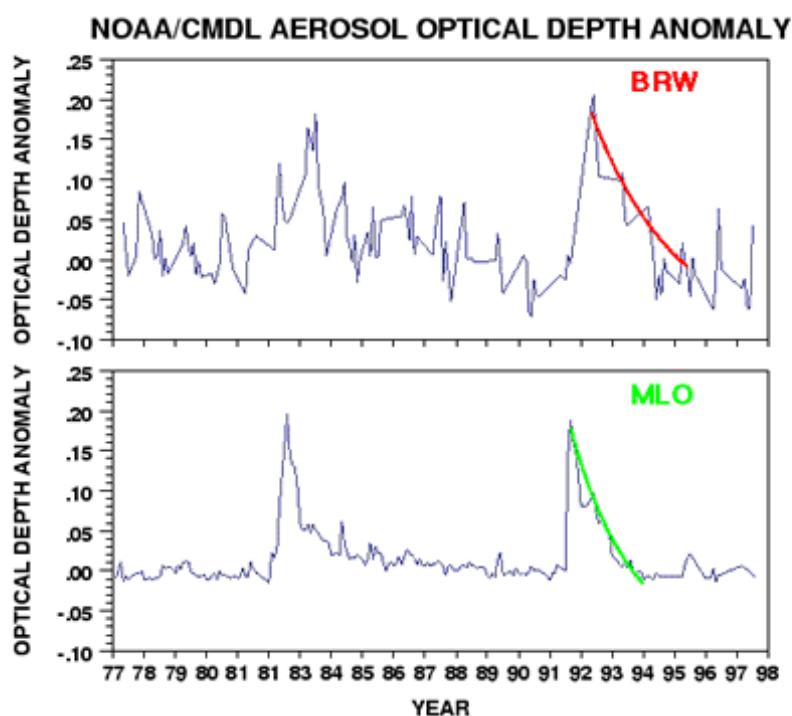


Figure 2.7. In 1991 Mt. Pinatubo injected into the stratosphere 30 million tons of aerosols. This caused aerosol optical depth anomaly of about 0.2. The top panel shows measurements at Barrow, Alaska; the lower panel shows measurements at Mauna Loa, Hawaii. Source: NOAA/CMDL:

is linked to energy balance of the atmosphere. The details of this climate forcing will be covered in Sect. 2.1.3.

Aerosols also affect the formation of ice clouds. Ice particles can be nucleated either directly from the water vapor, or from freezing of supercooled droplets, at temperatures around and below -40°C . Ice can also form at higher temperatures by nucleation in the presence of atmospheric aerosol called ice nuclei. Ice nuclei need to satisfy several requirements: they are insoluble in water; large particles are more effective than small; good ice nuclei generally have chemical bonding and crystallographic structures similar to that of ice; and certain topographic surface features can play an important role in ice nucleation.

Cloud influence the global energy budget by controlling the amount of solar radiation absorbed by the earth and by partitioning this energy between the atmosphere and the earth's surface. Both aerosols and clouds take part in aerosol-cloud-climate interactions. The details of these climate forcing mechanisms will be covered in Sect. 2.1.3, while the basic information about the radiative and microphysical properties of aerosols and clouds will be given in Sect. 2.1.2.

2.1.3 Aerosol radiative forcing

The brightest objects seen at the satellite photographs of the Earth are clouds and snow-covered surfaces. These reflect back to space most of the incoming solar radiation and affect the radiative balance of the planet. Atmospheric aerosols can alter radiative properties of both clouds and snow. This section will focus on aerosol radiative forcing over darker surfaces and

2 Scientific Background

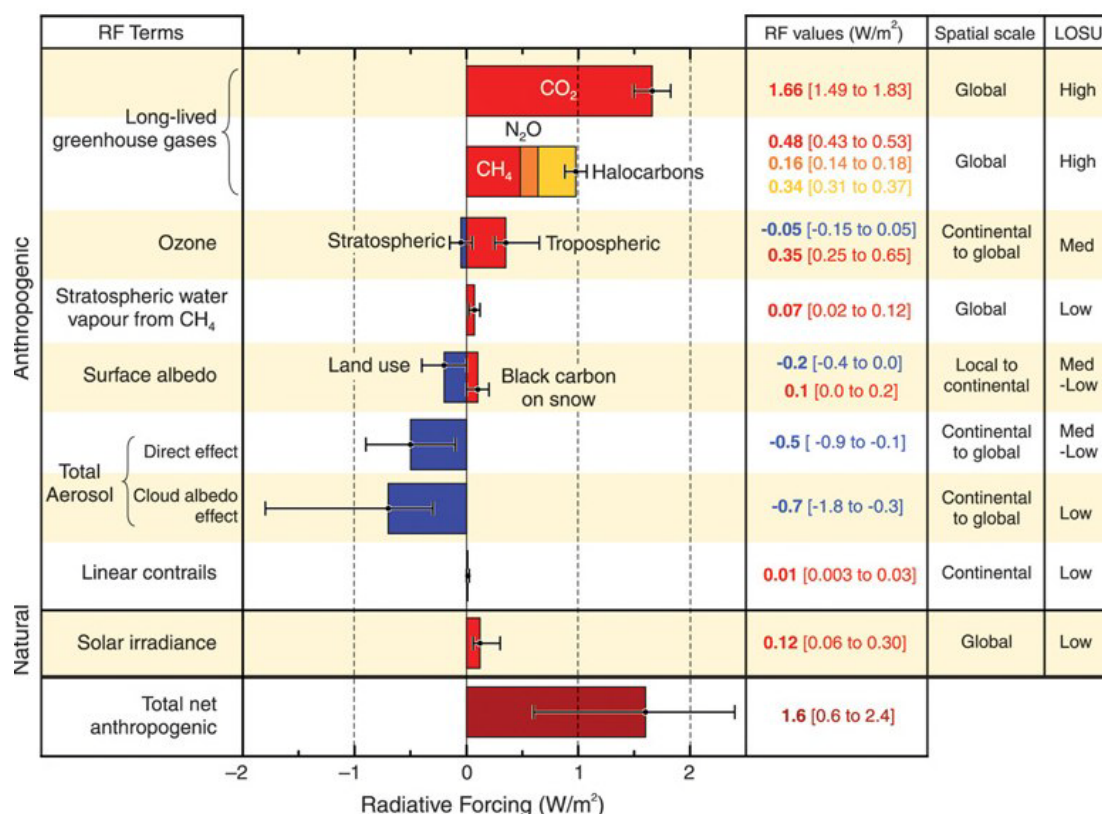


Figure 2.8. The global radiative forcings (RF) in 2005 relative to the beginning of industrial era (about 1750). Columns on the right show best estimates and confidence intervals (RF values); spatial scale of the forcing and the level of scientific understanding (LOSU). Volcanic aerosols are not included due to their episodic nature. Figure adapted from IPCC (2007).

aerosol effects on clouds, whereas the discussion of aerosol radiative forcing over snow and ice surfaces will be covered in Sect. 2.2.2.

According to Ramaswamy et al. (2001), radiative forcing can be defined as ‘the change in net (down minus up) irradiance (solar plus longwave) at the tropopause after allowing for stratospheric temperatures to readjust to radiative equilibrium, but with surface and tropospheric temperatures and state held fixed at the unperturbed values’. To assess and compare various mechanisms of climate change, it is convenient to use the radiative forcing value (expressed in Wm^{-2}). Aerosols cause also radiative forcing (RF) and in Fig. 2.8. it can be seen, that current understanding of this problem is low:

The *direct effect* is occurring when aerosols scatter and absorb shortwave and longwave radiation, both solar and reflected/emitted from the surface, which changes the radiative balance of the Earth-atmosphere system. The magnitude of direct RF is connected to aerosol single scattering albedo, extinction coefficient, scattering phase function (see definitions in Sect. 2.4). These optical properties vary both in space and time, therefore quantitative estimate of this RF is difficult, however, the tendency is that aerosols cause a net negative direct RF (cooling) over darker surfaces like oceans or dark forest areas, and a positive TOA RF (warming) over brighter surfaces such as desert, snow, ice or cloud cover (e.g. Chylek and Wong, 1995; Haywood and Shine, 1995).

The *indirect effect* is connected to the complex of aerosol-cloud interactions which result in the change of cloud microphysical, radiative properties, amount and lifetime (Figure 2.9). It is convenient to distinguish the effect of aerosol on the cloud droplet number concentration and size (the “first indirect effect” according to Ramaswamy et al., 2001, the “cloud albedo effect” Lohmann and Feichter, (2005), or the “Twomey effect” after the work by Twomey, 1977) from the aerosol effect on the liquid water content, cloud height, and lifetime (“second indirect effect” as in Ramaswamy et al. (2001), or the ‘cloud lifetime effect’(Lohmann and Feichter, 2005, or the “Albrecht effect” after the work by Albrecht, 1989).

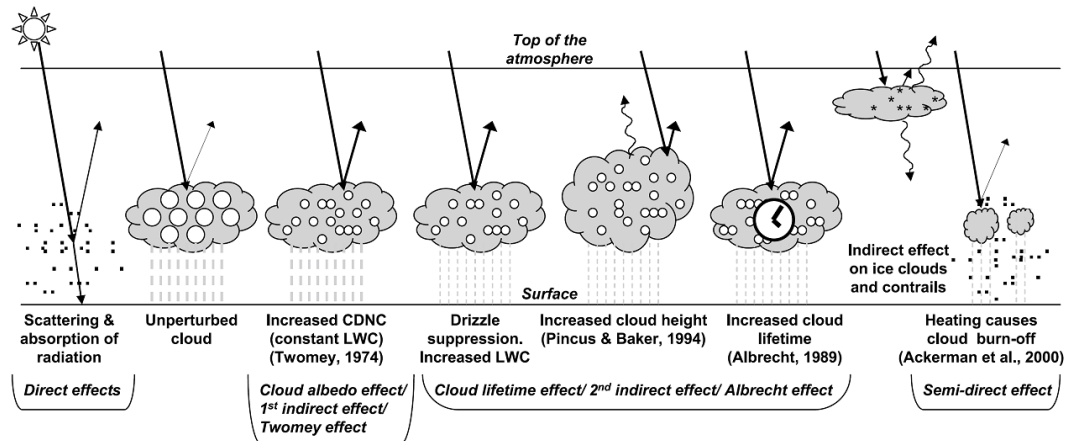


Figure 2.9. Schematic diagram showing the various radiative mechanisms associated with cloud effects that have been identified as significant in relation to aerosols according to IPCC, 2007. Source: IPCC 2007. The unperturbed cloud contains larger cloud drops as only natural aerosols are available as cloud condensation nuclei, while the perturbed cloud contains a greater number of smaller cloud drops as both natural and anthropogenic aerosols are available as CCN.

Clouds cover around 60% of the globe and have high variety in radiative forcing. The first indirect effect of the cloud albedo effect is therefore currently considered to be the main uncertainty in the radiative forcing of climate (IPCC, 2007). The magnitude of the indirect effects depends on the effectiveness of aerosol particles to serve as condensation nuclei. It depends on the aerosol size, chemical composition, mixing state, ambient environment. The reader is referred to the above mentioned sources for details on this subject as well as to the following works: Penner et al., (2001), Hansen et al., (1997), Ackerman et al. (2000), Jacobson (2002).

To assess total radiative forcing effects aerosols, information about aerosol optical thickness and its spatial distribution is needed. As shown in Fig 2.8, current progress in aerosol measurements and models only leads to low/medium level of scientific understanding. Large part of these uncertainties comes from lack of sufficient coverage of AOT data in Polar Regions.

2.2 The Arctic, its climate system and role in global climate

The Arctic can be defined as the region north to the Arctic Circle (66.5° N). According to broad climatic conditions, the Arctic can be separated into the High Arctic and Low Arctic. The High Arctic is considered to be a polar desert, whereas the tundra of the Low Arctic includes shrub vegetation. Surface air temperatures (approximately 2m above the surface) exhibit remarkable regional and seasonal variability (from -40 °C up to 10 °C or 20 °C) and also precipitation varies greatly. During the year, floating sea ice occupies most of the Arctic Ocean. Sea ice and snow cover are intimately coupled with the atmospheric energy budget and circulation. Among the permanent ice masses (which are glaciers, ice caps and ice sheets), the Greenland Ice Sheet is the largest in the Northern Hemisphere. This ice sheet covers the area of 1.71 million km² and occupies the volume of $2.93 \cdot 10^6$ km³ (Serreze, Barry, 2006), which, if completely melted, would cause a sea level rise of about 7.2m.

The Arctic cloud cover reaches 80% in summer and 60% in winter for the central Arctic Ocean. Over the Atlantic sector, there is about 80% cloud cover during the year. Much of the summer cloud cover consists of low level horizontally spread water clouds (stratus clouds).

The role of the Arctic in the global heat budget

The Arctic plays an important role in the global heat budget. Annual zonal averages of the net solar flux depend greatly on the latitude, with the equatorial region receiving more than the Polar Regions. Annual means of different latitudinal bands indicate that equatorial region emits to space less than it receives, and the polar regions emit more radiation than they receive from space (Serreze, Barry, 2006). The uneven solar heating results in the poleward transport of energy by the atmosphere and oceans that pumps the heat away from the equatorial region. At lower latitudes such a transport is mainly associated with the Hadley circulation cells. At the middle and high latitudes, where the Coriolis force becomes significant and the tropospheric flow is not strictly meridional, but from west to east, the poleward energy transport is carried out via surface cyclones and anticyclones. Similar poleward energy transport also occurs in the ocean, however, atmospheric transport plays greater role in pumping of the equatorial excess energy into the heat sinks in the Arctic and Antarctic.

The Arctic surface albedo is at its minimum in July and August, associated with the melting of the land and sea ice snow cover. This temporally coincides with the summer maximum of the Arctic cloud cover and is outweighed by it. Several weeks of midsummer is the only period when clouds in the Arctic produce a net cooling effect. Due to the high surface albedo of this region, clouds cause positive RF throughout most of the year. Variations in the Arctic cloud cover result in corresponding change in the date of snowmelt. Surface radiative fluxes are also connected to the cloud cover, but may vary nonlinearly according to varying surface conditions (Curry, 1995).

A prominent feature of the Arctic climate is the frequent occurrence of the low-level temperature inversions, when temperature increases with height for about 10-12K (as

compared to the temperature at the surface) above land or ice covered ocean. During winter, inversions occur very often, with frequency of occurrence decreasing toward spring and summer. In June or July inversions occur in approximately 50% of cases (Serreze, Barry, 2006). It is the Arctic inversions that are responsible for the strong stability of the Arctic atmosphere in winter. Temperature increase with height limits the depth of heat and moisture vertical mixing, thus trapping pollution gases and aerosols within the inversion layer till further heating up of the environment (Bridgman et al., 1989). Photochemical destruction of boundary-layer ozone at Arctic sunrise refers to the ozone-depleted air being trapped in the inversion layer (Barrie et al., 1988; Oltmans et al., 1989).

Climatic feedbacks

The Arctic can respond to the global warming in many ways different from the climatic feedbacks appropriate for other climatic zones. A comprehensive review of the Arctic climatic feedbacks is the work by Curry et al. (1996). Here we will highlight the most important of them:

a) *snow and ice albedo effect* (in case of climate warming, snow and ice cover will decrease, which increases the absorption of solar radiation and cause further warming);

b) *cloud-radiation feedbacks* (changes in cloud fraction may accompany warming and further modify surface temperature. Also, warming may increase CCN production, which increases cloud optical thickness and LWC. Warming may increase the global cloud cover via depleting ice clouds and substituting them with slower depleting water clouds.);

c) *water vapor feedbacks* (globally increased atmospheric humidity as a result of increased evaporation from warming oceans; in the Arctic, due to relative lack of convective coupling between the surface and the atmosphere, inversions, low temperature and humidity, the outcome of this feedback will be different. During the Arctic winter, temperature increase will increase the humidity in the lower troposphere, whereas during summertime the humidity in the upper troposphere will decrease due to advection from dry continental air rather than moist marine sources.);

d) *cloud-temperature feedbacks* (as the atmosphere warms, there will be a feedback associated with increased IR emission from clouds.);

e) *cloud phase and precipitation feedbacks* (increased amount of pollution aerosol in the Arctic would increase the amount of cloud water by decreasing the precipitation and thus extending the cloud lifetime, which in turn increases the CCN production via gas-to-particle conversion and aerosol production by clouds. Increased pollution may also result in deactivation of ice freezing nuclei and decreasing the aerosol scavenging by clouds. The result is a net increase of the aerosol amount. Blanchet and Girard (1995) suggested that an increase in the acid to insoluble mass ratio in the Arctic haze would increase the precipitation rate and the thus dehydrate the atmosphere, which in turn reduces the IR radiation at the surface. As cooling promotes condensation, more precipitation and further dehydration takes part.);

The magnitude and even the sign of some of the feedbacks are currently not well understood. The major uncertainty is associated with the cloud-radiation interactions and the behavior of

clouds in the changing climate. The best estimate of all the climate feedback in the Arctic is that they all are positive, except for aerosol-dehydration feedback proposed by Blanchet and Girard (1995) and for negative cloud-radiation feedback during the summertime in the Arctic.

2.2.1 Snow and ice coverage

The Earth snow and ice covered regions are known as the cryosphere. The cryosphere consists of the snow cover, sea ice, freshwater ice, ice sheets, glaciers, ice shelves, icebergs, and permafrost. On the global scale, the cryosphere represents an important part of the Earth's climate system.

In the polar regions, time from snow deposition onto the surface till it melts can be rather long, giving a lot of time for the aging processes which alter the shape of the ice crystals. As opposed to fresh snow, where the shape of the ice crystals is still recognizable, old snow consists of rounded or angular compressed grains. The difference between all types of snow on the one hand and ice on the other hand is that snow has a connected system of air pores and with time can undergo large changes in the internal structure towards porosity decrease and density increase. E.g. firn is snow, which has existed through at least one summer season and is carried over to the next winter. Alpine firn originates in conditions of repeated melting and refreezing whereas polar firn is created without appreciable melting. The aging processes, which affect the shape of the ice crystal in the snow medium are responsible for existence of many snow types with varying optical properties. Remote sensing over snow (as opposed to other surface types) is therefore not a trivial task.

Typical albedos for major surface types in the Arctic are summarized in Table 2.1. Geometry of illumination and heterogeneities in the physical properties of the surface cause a wide range of values within the general categories. Most surfaces are forward scattering and scattering differently in the different spectral regions. The provided range also includes variations in the spectral nature of the solar flux and the relative magnitude of direct versus diffuse components. Snow cover, both on land and sea ice, dominates the Arctic for much of the year. Warren (1982), Barry (1996), and Nolin and Liang (2000) provide comprehensive reviews on snow optical properties. Maykut (1986) discusses the spectral reflectance and albedo characteristics of the sea ice.

Table 2.1 Representative albedos for different Arctic surfaces (Arctic climate surface)

Fresh snow	0.70-0.90
Melting snow	0.50-0.60
Water	0.06-0.10
Dry tundra	0.23-0.26
Wet tundra	0.10-0.20
Multiyear sea ice	0.55-0.75
Thick firstyear sea ice	0.30-0.60
Meltponds on sea ice	0.15-0.40

Spectral reflectivity of snow is dependent on snow parameters such as: grain size and shape, impurity content, near-surface liquid water content, depth and surface roughness as well as solar elevation. Freshly fallen snow has small grains and a very high reflectance in the visible wavelength as seen in Fig. 2.10. As it ages, the reflectivity of snow decreases differently in the visible and IR regions, dropping much more at the longer wavelengths due to melting and refreezing within the surface layers and to the natural addition of impurities. Melting of snow increases the mean grain size and density by melting the smaller particles. Fig. 2.10 illustrates the changes in snow reflectance with different snow-crystal radii.

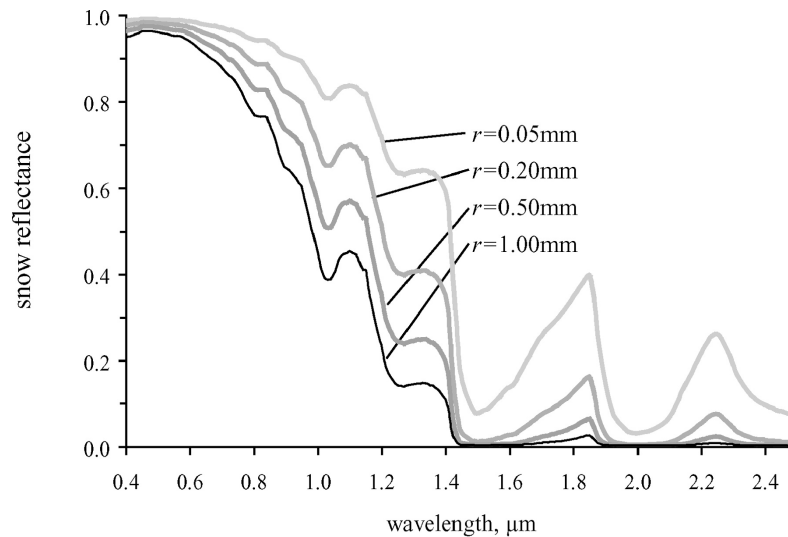


Figure 2.10 Spectral reflectance for a semi-infinite snowpack as a function of wavelength for grain radii for 0.05 to 1.00mm (from Dozier and Painter, 2004).

Reflectivity of ice in the visible and infrared from aircraft and satellites varies greatly, depending on the overlaying material, impurities and the presence of meltponds. Thus, a wide range of reflectivities is known to characterize ice features as seen from satellite. The comparison between the reflectance of fresh snow, firm and the glacier ice is shown in Fig. 2.11.

Snow BRDF angular dependence

For remote sensing applications over snow surfaces, it is important to have the information on snow optical properties in a variety of illumination-observation geometries. As reflection from a snow pack is anisotropic (as opposed to Lambertian⁶) due to reflection from ice crystals, albedo is no longer sufficient to describe the reflective properties of the surface. Therefore a directional value is introduced in many works, both dedicated to modeling and measuring snow reflective properties (e.g. Peltoniemi et al., 2005; Winther, 1994; Peltoniemi, 2007; Li and Zhou, 2004; Leroux et al., 1998b; Hudson et al., 2006; Winther et al., 1999; Kokhanovsky et al., 2005a; Negi et al., 2010; Aoki et al., 2000, etc.).

⁶A Lambertian surface is one that reflects radiation isotropically, i.e., with equal radiance in all directions, regardless of how it is illuminated. It is an “ideally rough” surface, reflective properties of which can be described by its albedo.

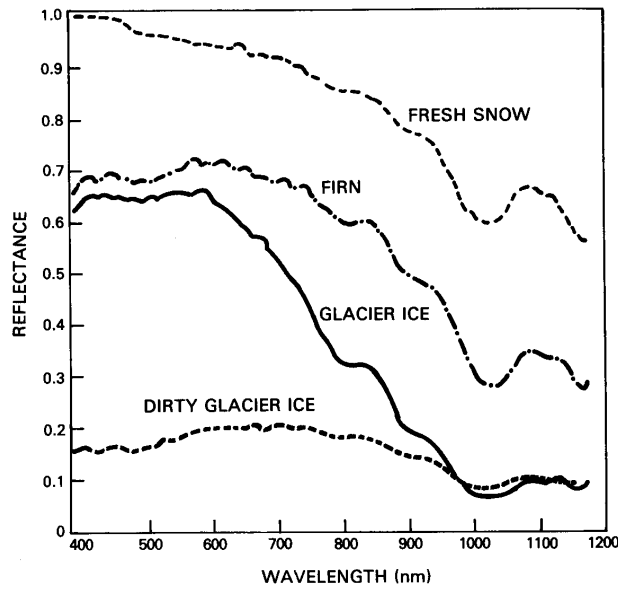


Fig. 2.11. Spectral reflectance curves for fresh snow, firn, glacier ice and dirty glacier ice. Note the extreme variability in the reflectance of ice and snow features. (adapted from Qunzhu et al., 1985).

In a theoretical case of isotropic parallel direct incident beam of light, the ratio of the radiance reflected into a particular direction to the incident irradiance can be used. This ratio is called the bidirectional reflectance-distribution function (BRDF, f):

$$f(\theta, \phi; \theta_0, \phi_0) = \frac{dI(\theta, \phi; \theta_0, \phi_0)}{\mu_0 dF(\theta_0, \phi_0)} \quad (2.4)$$

where θ and θ_0 are the viewing and solar zenith angles, respectively, $\mu_0 = \cos \theta_0$, ϕ and ϕ_0 are the azimuthal angles of the detector and the sun, respectively; $F(\theta_0, \phi_0)$ is the solar irradiance at the top of the atmosphere; and $I(\theta, \phi; \theta_0, \phi_0)$ is the radiance reflected into a particular direction. Unless the surface has azimuthally dependent surface features, such as sastrugi⁷, the dependence of f on both ϕ and ϕ_0 can be reduced to a dependence only on the relative azimuth $\phi_0 - \phi$.

The albedo is connected to the BRDF; it is the integral of f over all reflection angles:

$$a(\theta_0) = \int_0^1 \mu d\mu \int_0^{2\pi} f(\theta, \phi; \theta_0, \phi_0) d\phi' \quad (2.5)$$

where $\phi' = \phi_0 - \phi$ and $\mu = \cos \theta$. More simply, the albedo is the ratio of the upward flux (into the hemisphere) by downflux (directional) at a particular wavelength, usually measured above the surface. It is also sometimes called directional-hemispherical reflectance. For the nomenclature of reflectance values the reader is referred to the work by Nicodemus et al. (1977).

⁷Sastrugi are irregular ridges formed on an otherwise smooth snow surface by the prevailing winds. Sastrugi often occur in the polar regions; their direction corresponds to the forming wind direction. For more details on how sastrugi affect snow directional optical properties see Warren et al., 1998; Leroux and Fily, 1998.

Because of infinitesimal elements of solid angle used in the BRDF definition to indicate the angular dependencies of the radiance and irradiance, BRDF can never be measured directly. As actual measurements always involve non-zero intervals for the parameters to define position and direction, often deal with diffuse illumination or have other limitations, various reflectance factors can be used instead of the BRDF. They are bidirectional reflectance factor, hemispherical-directional reflectance factor (Li and Zhou, 2004) or anisotropic reflectance factor (Hudson and Warren, 2007).

Figure 2.12 illustrates a simulated bidirectional reflectance factor (BRF), $BRF = \pi BRDF$, for snow surface illuminated at a solar zenith angle of 65° , for the four VIS to IR wavelengths. It is visible that snow reflectance pattern is far from isotropic and exhibits a strong forward scattering peak, which gets even more prominent with the increase of the solar zenith angle (Li and Zhou, 2004). Snow shows a great spatial and temporal variety of types, associated with distinctively different directional reflectance patterns throughout the spectrum. Peltoniemi et al. (2005) measured directional and spectral reflectance characteristics of many snow types at various locations in Finland, from freshly fallen snow to wet, old, polluted snow at several visible and near infrared wavelengths, showing not only BRDF magnitude difference, but also difference of BRDF patterns depending on surface roughness, packing, wetness, grain size, pollution. Aoki et al. (2000) measured spectral albedo and bidirectional reflectance pattern at Hokkaido, Japan and studied the effects of snow impurities, density, layer structure, and grain size. They showed that the bidirectional reflectance patterns at visible wavelengths differ from that in the near-infrared region, with the anisotropy increasing with the increase of the wavelength. The effects of solar zenith angle, snow grain size, impurities, snowpack thickness, and incident conditions on the spectral albedo and BRDF were examined by Wiscombe and Warren (1980), Warren and Wiscombe (1980), Warren (1982).

The main effect of liquid water in snow is that it causes the grains to form clusters (Colbeck, 1979), which behave optically as large grains, so reflectance in the near-infrared decreases and does not grow back when the snow refreezes (O'Brien and Munis, 1975).

Absorbing impurities affect the reflectance in the visible wavelengths (Warren and Wiscombe, 1980), where there is a huge difference between the absorption coefficient of ice (10^{-8}) and soot or dust (0.001–1.0).

The variety of parameters determining optical properties of snow creates a large variety of snow types, which makes satellite retrievals of snow properties and remote sensing of aerosol and clouds over snow surfaces particularly challenging. While it is possible to parameterize or model measured BRDF of a given snow sample (Li, 1982; Han, 1996; Leroux et al., 1998b; Leroux and Fily, 1998; Xie et al., 2006; Li and Zhou, 2004; Hudson et al., 2006; Jin and Simpson, 2000; Kokhanovsky et al., 2005a; Mishchenko et al., 1999; Peltoniemi, 2007), the applicability of such a model or parameterization on global scale cannot be guaranteed. Strictly saying, a snow sample in the field measurement and snow-covered terrain have different reflective properties, which means that the reflective properties of the surface for remote sensing tasks should be determined by remote sensing means. At the same time, snow albedo is so high in the VIS and NIR regions of spectrum that the role of snow surface in the

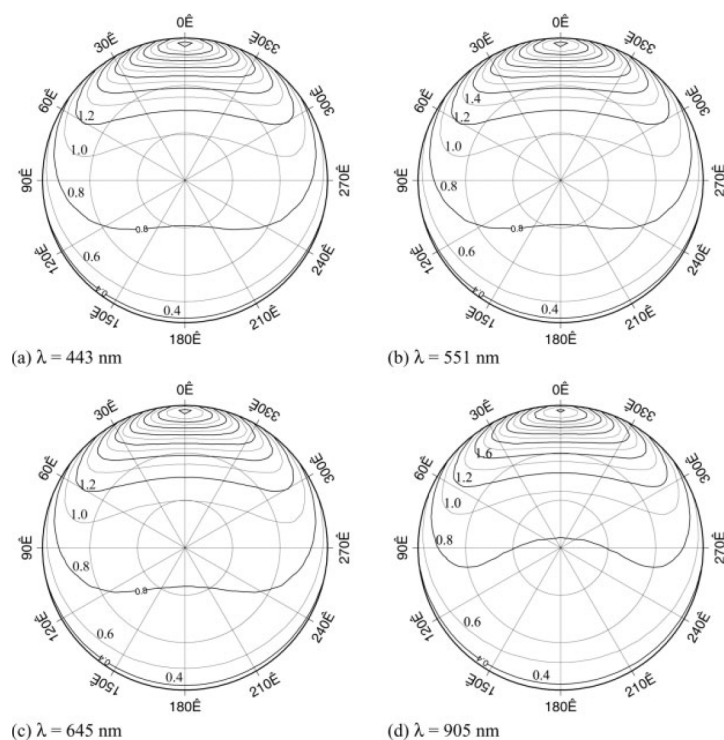


Figure 2.12. Polar plot of the simulated snow-surface bidirectional reflectance factor at wavelengths a) 443, b) 551, c) 645, d) 905 nm. The solar incidence angle is 65° . The contour interval is 0.2. The increment in zenith viewing angle between the circles is 30° . (Source: Li and Zhou, 2004)

TOA signal measured by a satellite sensor is dominating. This, combined with sometimes very rapid changes in the snowpack (reported by e.g. Peltoniemi et al., 2005), makes it apparent why a comprehensive description of reflective properties of snow-covered Arctic surfaces suitable for remote sensing tasks is currently not available.

Snow in the IR

Snow does not reflect much in the thermal infrared region. Figure 2.13 shows typical directional hemispherical reflectance spectra of fine, fresh snow, in the wavelength range from 2 to $14\ \mu\text{m}$. It is visible that for fresh snow IR reflectance does not exceed 1% throughout the thermal region. The emissivity⁸ of dry snow in the thermal IR region is about 0.965 to 0.995 (Rees, 2006). In this spectral region the absorption of ice is high (peak at $10\ \mu\text{m}$). The fine structure of snow increases its similarity to a black body. The snow and ice emissivity spectra are shown in Fig. 2.14 for comparison. The emissivity of water at these wavelengths is not much different from that of snow, so the effect of presence of liquid water can be neglected.

Snow density, grain shape, liquid water content, and grain size do not affect snow emissivity much and can be neglected; however, at off-nadir viewing angles, snow emissivity varies to

⁸*Emissivity* of a body describes its ability to radiate absorbed energy. It can be defined as the ratio of energy emitted by a given body to the energy emitted by a black body (a perfect emitter) with the same physical temperature.

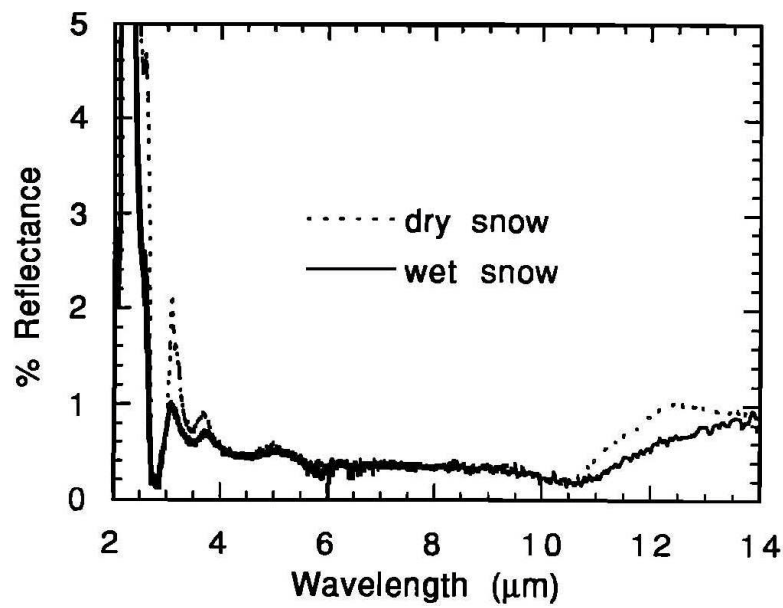


Figure 2.13. Directional hemispherical reflectance spectra of fine fresh snow, measured by Salisbury et al., 1994.

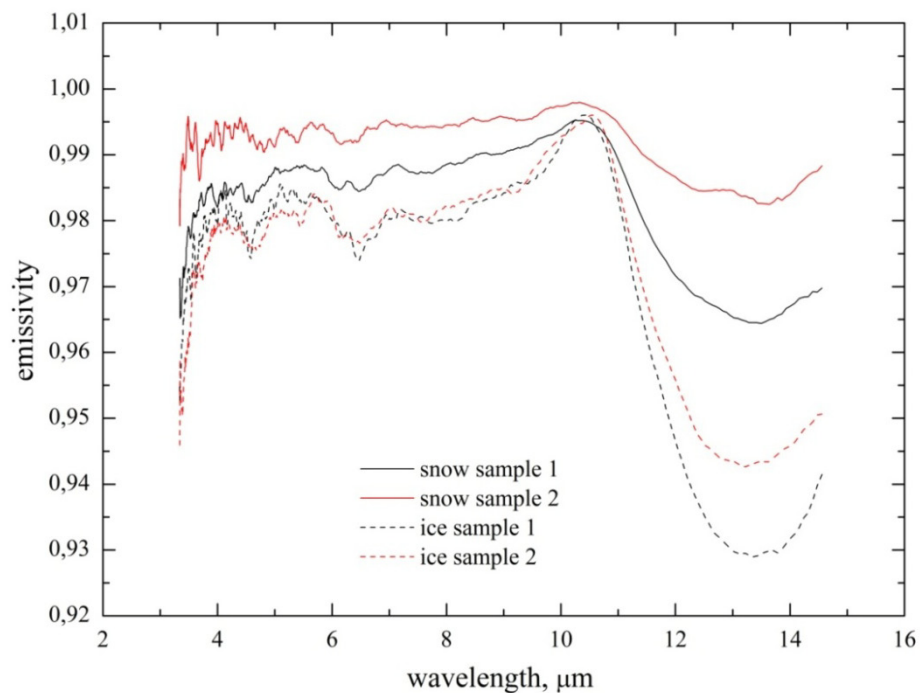


Figure 2.14. Thermal infrared emissivity spectra of two snow and two ice samples measured at Mammoth Lakes, USA, on 1.04.1996. Taken from UCSB Emissivity Library (Zhang, 1999)

produce differences between thermodynamic temperature and brightness temperature as large as 3 K at 12–14 μm (Dozier & Warren 1982).

More details on the snow IR behavior can be found in the above mentioned sources and in the review of Kuittinen (1997).

2.2.2 Atmospheric aerosol in the climate of the Arctic region. Arctic Haze

Unlike the common belief suggests Arctic environment is no longer pristine with exceptional atmospheric visibility and always clean snow cover. Industrial development affected the Arctic region, causing air quality degradation and the increase of the atmospheric pollution. The first evidence of reduced slant visibility was reported by aircraft pilots operating in the Arctic in late winter and early spring (Mitchell, 1957). The haze of unknown nature and source was named “Arctic Haze” and initiated subsequent studies of Arctic air and pollution sources (Barrie, 1986).

It was found that Arctic aerosol originates from maritime and terrestrial sources with the inclusions of anthropogenic component. The following characteristics of the Arctic aerosol were reported (Bigg, 1980):

- winter aerosol mainly consists of sulfuric acid droplets;
- spring aerosol consist of larger sulfuric acid particles with greater proportion of ammonium sulfate than in winter;
- large part of the acid droplets contained insoluble inclusions;
- seasalt component of the aerosol is present in summer aerosol for wind speeds of 5-12 m s⁻¹ (Leck et al., 2002);
- fragments of bacteria, microalgae, and organic compounds are present in the summer aerosols (from leads in the sea ice cover);
- mean optical depth⁹ is about 0.06 at Barrow, 0.08 at Alert (Bokoye et al., 2002), 0.053 at Koldewey (Herber et al., 2002) and doubling during the spring haze events.

Arctic haze exhibits highly pronounced seasonality with the late winter – early spring peak in the pollution level (Shaw and Wendler, 1972; Rahn et al., 1977). Springtime Arctic aerosol also exhibits large black carbon component (Rosen et al., 1981; Clarke and Noone 1985). The springtime Arctic aerosol (Arctic Haze) will be described in the next sub-section; for a review of Arctic air pollution, see Stonehouse (1986) and Barrie (1986). The other types of Arctic aerosol and their climatic effects are covered further in the current section.

Arctic Haze

As opposed to the background Arctic aerosol, which is present throughout the year, composed of sulfuric acid droplets and sea salt and originates from local natural sources (as few as there are), Arctic Haze is a seasonal pollution occurring in the late winter/early spring and originating from lower latitudes (often anthropogenic sources). Strong surface based inversions stabilize Arctic atmosphere in winter and prevent turbulent transfer, precipitation, and aerosol removal processes (Barrie et al., 1981; Shaw, 1981, 1995; Heintzerberg and Larssen, 1983). On the other hand, meridional transport of particulate matter from lower latitudes increases throughout the winter and spring (Iversen and Joranger, 1985). This results in transport of the pollution into the Arctic and trapping the particulates within the inversion

⁹*Aerosol optical depth* (AOD, τ) is a measure of the radiation attenuation in the atmosphere. For more detailed definition see Sect. 2.3.

layer until further atmosphere warming, which can take several weeks (Shaw, 1981, 1995). Various airborne and lidar studies showed that the trapped matter is located within the lowest 2 km above the surface (Leitch et al., 1984; Hoff, 1988; Pacyna and Ottar, 1988; Barrie, 1996), with the pollution layer having highly inhomogeneous structure (Radke et al., 1984; Brock et al., 1989).

Due to the specific origin of the Arctic haze phenomenon (being caused by atmospheric circulation peculiarities and not by pollution sources only emitting in late winter and spring), Arctic haze may originate from different sources (most times anthropogenic) and therefore have varying chemical composition. E.g., the chemically identifiable sources of pollution in the Arctic are industrial plants in northern and oil exploitation in the Tyumen area (Harris and Kahl, 1994).

The constituents of Arctic Haze were first measured at Barrow, Alaska (Rahn et al., 1977) and were then continued within many researches (Li and Barrie, 1993; Quinn et al., 2002; Shaw, 1983; Polissar et al., 1998, 2001; Heintzenberg, 1980; Hoff et al., 1983; Pacyna et al., 1984; Shaw, 1984; Clarke, 1989; Leitch et al., 1989; Trivett et al., 1989; Hillamo et al., 1993). These indicated that the haze is composed of a varying mixture of sulphate, particulate organic matter, ammonium, nitrate, dust and black carbon, with the inclusion of heavy metals coming from industrial sources. The particles of haze are well-aged, which proves the role of long-range transport in the formation of the haze.

The Arctic haze is an efficient scatterer of solar radiation (Waggoner and Weiss, 1980; Shaw, 1987); the presence of black carbon is responsible for the weak absorption (Hansen and Rosen, 1984; Noone and Clarke, 1988; Kahl and Hansen, 1989; Hopper et al., 1994). However, even the weakly absorbing aerosol may have large climatic effects in the Arctic. The highly reflective snow surface enhances interactions between the surface and the haze due to multiple scattering between the two (e.g., Shaw and Stamnes, 1980).

As outlined in the review by Tomasi et al. (2007), except for Arctic Haze there are other types of aerosol pollutions, which occur in the Arctic.

Diamond dust

Another phenomenon that affects the turbidity of the Arctic air and is often mixed up with Arctic haze is “diamond dust” or ice crystals precipitating out of clear sky at low temperatures (Ohtake et al., 1982). Diamond dust affects visibility (Leitch et al., 1989; Borys, 1989; Curry et al., 1990; Meyer et al., 1991), radiative balance of the Arctic (Curry 1983, 1987) and may play a role in the ozone destruction (Curry and Radke, 1993). Furthermore, the diamond dust may interact strongly with the Arctic haze (Bowling and Shaw, 1992; Borys, 1989; Curry and Radke, 1993). Both the submicron aerosol component of arctic haze and ice crystal precipitations influence radiation budget of the Arctic. These crystalline precipitations may also be connected with anthropogenic emissions. For example, enhancements in sublimation ice nuclei may occur as the Arctic becomes more contaminated.

Examples of Arctic pollution sources: Asian dust, smoke and biomass burning

Since the long range transport plays a great role in the formation of the Arctic aerosol, it is not surprising to discover that incursions of *Asian dust* occurred in the Arctic for many years (Shaw, 1983; Van Curen and Cahill, 2002; Bory et al., 2003). Rahn et al. (1977) describes a

2 Scientific Background

large episode of Asian dust transport (combined with haze) which he observed at Barrow in spring 1976. It was shown that the fraction of the particles larger than 0.4-0.8 μm was mainly crustal, originating from TaklaMakan and Gobi deserts in eastern Asia.

Stone et al., (2005) described the dust even on the Gobi desert in spring 2002, which caused an increase in AOD at visible and NIR wavelengths (up to 0.3 in mid-April at 500nm). As discussed by Tomasi et al. (2007), direct radiative forcing of this pollution event can be between -16 and -38 Wm^{-2} , providing negative climatic feedback.

Another high latitudes source of the Arctic haze is the *boreal forest fires* which occur across North America and Siberia each spring and summer. For example, during the summer 2004, boreal forests burned in Alaska and Canada and were the source of smoke at Barrow, Alert, Summit, and Zeppelin stations (Stohl et al., 2006). The estimates of direct aerosol radiative forcing given by Key et al. (2006) for an average case of boreal smoke event are between -45 and -18 Wm^{-2} for solar zenith angle equal to 65° and surface albedo equal to 0.47 and 0.80.

Stohl et al. (2007) described a record high air pollution event in the Scandinavian Arctic occurred in May 2006. This event has been associated with the transport of *biomass burning aerosols* from agricultural fires in Eastern Europe into the Arctic. The radiative effects of this event are described by Treffeisen et al. (2007). Depending on the underlying surface albedo, heating rates of about 0.43 – 0.64 K per day at the altitude of 0.5 km are reported for the surface albedo of 0.2 and 0.9 correspondingly.

Climatic effects of aerosols in the Arctic

It is known that haze contaminants end up in Arctic ecosystems (Meijer et al., 2003; Wania, 2003), and some of the pollution that has accumulated during the polar night is released to the mid-latitudes (Penkett et al., 1993; Heintzenberg et al., 2003). But the timing, mechanisms of removal and even the fraction of pollution that stays in the system are not well known (Quinn et al., 2007). It is therefore important to discuss the possible climatic effects of aerosol in the Arctic.

Direct effect

Aerosols scatter and absorb radiation, which affects the radiation balance of the Arctic (Shaw and Stamnes, 1980). This effect is called the *direct aerosol effect*. Due to the fact that small amount of radiation is normally absorbed in the polar regions, the Arctic may be particularly sensitive to radiative flux changes introduced by aerosols (Valero et al., 1989). Chylek and Coakely (1973) showed that absorbing aerosol over a bright snow surface produces warming effect. Porch and MacCracken, (1982), Leighton, (1983), Blanchet and List, (1987), Emery et al., (1992), Shaw et al., (1993) estimated the magnitude of this effect and gave the diurnal mean value between 2 and 20 Wm^{-2} . This agrees with the sun photometer measurements (Mendonca et al., 1981). The vertical distribution of the haze layers causes no effect on the radiation balance of the Arctic (Cess, 1983) but may impact atmospheric circulation. The attenuation of the solar radiation by aerosol layer which causes surface cooling would be compensated by the IR emission from the atmosphere (McCracken et al., 1986). The aerosol absorption and scattering will have a cooling effect on the surface, which will be partly compensated by the increased diffuse component of shortwave radiation and the decreased surface albedo. On balance, the net change of the surface radiation balance is likely to be a

small, positive warming, as opposed to the cooling effect expected globally as a result of aerosol direct climate forcing.

Indirect effects

Aerosol particles in the Arctic atmosphere affect microphysical properties of clouds. The complex of these effects, which include the increase of cloud droplet concentration, cloud droplets size decrease, drizzle suppression (Albrecht, 1989; Twomey, 1991), cloud lifetime and coverage increase (Hobbs and Rangno, 1998) is called the *indirect aerosol effect*.

Remarkable stability of the Arctic atmosphere, persistence of low-level stratus clouds and relatively long lifetime of aerosols during haze events, the impact of aerosols on cloud microphysics and optical properties may be larger in the Arctic than elsewhere on earth (Curry, 1995; Garrett et al., 2004).

Probably the most significant effect of the Arctic pollution is the decrease of the cloud droplet effective radius, which increases cloud IR emissivity and optical thickness (Curry and Herman, 1985; Garrett et al., 2002; Garrett and Zhao, 2006). The result of this increased downwelling IR irradiance is an increase of the snow pack melting rates in spring (Zhang et al., 1996). This corresponds to positive feedback between 3.3 and 5.2 Wm^{-2} (Garrett and Zhao, 2006).

The sulfate component of the Arctic haze is a particularly good CCN (Garrett et al., 2004), but slows down ice nucleation (Borys, 1989) and produces fewer IN than nearly insoluble aerosols (Blanchet and Girard, 1995). The presence of ice crystals in the Arctic atmosphere invites to look for another ice nucleation mechanism. Ohtake (1993) hypothesized that the atmospheric ice particles including diamond dust occur from freezing of sulfate aerosols. As the crystals fall out, the dehydration of the Arctic air occurs, especially during the Arctic winter.

Clouds affect aerosols via particle scavenging and precipitation, which are important sinks of aerosol. Scavenging by snow crystals is twice as efficient as that by rain drops (Shaw, 1986).

Surface albedo

One more mechanism of aerosol climate forcing particularly important in the Arctic is the deposition of absorbing aerosols onto the highly reflective snow surface, which reduces the snow albedo and enhances absorption of solar radiation at the ground (Warren and Wiscombe, 1980). The magnitude of snow albedo reduction was found to be around 1-3% (Clarke and Noone, 1985), which would cause warming of $+0.3\text{Wm}^{-2}$ (Hansen and Nazarenko, 2004). The resulting warming may lead to the melting ice and snow cover on tundra in Siberia, Alaska, Canada and Scandinavia (Foster et al., 1992; Stone et al., 2002). Jacobson (2004) found that black carbon on snow and sea ice caused a decrease in the surface albedo of 0.4% globally and 1% in the Northern Hemisphere. According to (Forster et al., 2007), the best estimate for surface albedo aerosol radiative forcing is around $+0.10 \pm 0.10 \text{ W m}^{-2}$.

2.3 Scattering in the atmosphere

Air molecules, trace gases and aerosols attenuate the incoming solar electromagnetic radiation. The way these atmospheric constituents absorb, scatter, or emit the radiation is described by the radiative transfer equation (RTE). The RTE can be formulated differently depending on the varying representations of the RT problem. This topic is described extensively in the literature (Chandrasekhar, 1950; Sobolev, 1956, 1975; Lenoble et al., 1985; Goody & Yung, 1989; Liou, 2002).

The intensity of radiation characterized as radiance I with the unit watts per square meter per steradian. It depends on wavelength and illumination geometry.

A fraction of the incident radiation is removed (absorbed and scattered to other directions) from the path of propagation in the atmosphere. The Beer-Lambert-Bouguer law describes the reduction of the radiation intensity I at wavelength λ :

$$dI(z, \mu, \varphi) = -\frac{\sigma_e(z)}{\mu} I(z, \mu, \varphi) dz \quad (2.6)$$

The direction of the incident radiance (μ, φ) is definitely determined by the zenith angle θ (with $\mu = \cos\theta$) and the solar azimuth angle φ ; z is the altitude, $\sigma_e(z)$ is the volume extinction coefficient which determines how radiation is attenuated by absorption and scattering in the atmosphere. The volume extinction coefficient is defined by the sum of volume absorption σ_a and volume scattering coefficient σ_s :

$$\sigma_e(z) = \sigma_a(z) + \sigma_s(z) \quad (2.7)$$

In RT calculations an integrated value is often used as a vertical component (as a measure of the altitude z). This value is optical thickness and can be written as follows:

$$\tau(\lambda, z) = \int_{z_0}^{TOA} \sigma_e(z) dz \quad (2.8)$$

The optical thickness (OT) is a measure of the penetrability or opacity of atmospheric constituents like aerosols, air, and gas molecules for a given wavelength. The total optical thickness of the atmosphere is the sum of the individual optical thicknesses:

$$\tau(\lambda, z) = \tau_R(\lambda, z) + \tau_G(\lambda, z) + \tau_A(\lambda, z) \quad (2.9)$$

with $\tau_R(\lambda, z)$, $\tau_G(\lambda, z)$ and $\tau_A(\lambda, z)$ being Rayleigh, gaseous and aerosols component optical thicknesses.

Considering the above definition of OT, the Beer-Lambert-Bouguer law can be rewritten:

$$I(\tau, \mu, \varphi) = I_0(\tau, \mu, \varphi) e^{-\frac{\tau(\lambda, z)}{\mu}} \quad (2.10)$$

As the radiation propagates in the atmosphere, it experiences not only energy removal from the light beam (due to extinction), but also an increase of energy (due to scattering from other directions). This increase can be written as follows:

$$dI(z, \mu, \varphi) = -\frac{\sigma_s(z)}{\mu} dz \int_{4\pi} I(z, \mu, \varphi, \Omega) p(z, \mu, \varphi, \Omega) d\Omega \quad (2.11)$$

where Ω is the unit solid angle and $p(z, \mu, \varphi, \Omega)$ is the phase function or scattering indicatrix, which determines how much radiation is scattered into a given direction, in this case into the light path (μ, φ) .

The losses and gains due to extinction and scattering result in the following change of radiation along the light path through the atmosphere:

$$\mu \frac{dI(\tau, \mu, \varphi)}{d\tau} = -I(\tau, \mu, \varphi) + \frac{\omega_0}{4\pi} \int_0^{2\pi} d\varphi' \int_{-1}^1 I(\mu', \varphi') p(\cos \vartheta) d\mu' \quad (2.12)$$

where ω_0 is the single scattering albedo, which is defined as the ratio of the total scattering to the total extinction, so that $\omega_0 = 1$ describes fully scattering medium and $\omega_0 = 0$ - fully absorbing medium; ϑ is the scattering angle defined as

$$\cos \vartheta = \mu\mu_0 + \sqrt{(1 - \mu^2)(1 - \mu_0^2)} \cos(\varphi - \varphi_0) \quad (2.13)$$

The equation 2.12 can be applied to radiative transfer problems in plane parallel media with discrete scatterers. To account for polarization, it must be rewritten in vector form, substituting the extinction and scattering coefficients with extinction and scattering matrices, and radiance intensity I with Stokes vector $\mathbf{I} = \{I, Q, U, V\}$ with I being radiance intensity and Q, U and V describing linear and circular polarization.

A lot of numerical and approximate solutions have been developed in order to solve the equation (2.12) (Lenoble, 1985). The radiative transfer programming code used within this work is SCIATRAN forward model (Rozanov et al., 1997, 2005).

Maxwell's electromagnetic theory describes single light scattering and absorption characteristics of an elementary volume light-scattering media. The scattering of the incident electromagnetic wave mainly depends on the relation between the wavelength and the characteristic particle size. Depending on this relation, three scattering regimes are usually distinguished and described with the solution of Maxwell's equations for spherical particles of different sizes: Rayleigh scattering, (for particles with the characteristic size much smaller than the wavelength), Mie or particle scattering (for particles with the characteristic size comparable to the wavelength), and ray or linear optics (for particles much larger than the wavelength). Within this work, the first two scattering regimes are necessary (for gaseous and aerosol scattering). They will be described in the next two subsections.

2.3.1 Molecular Rayleigh scattering

Molecules and very small particles in the air scatter incoming light in a similar way. If $d \ll \lambda$ (the case for gases), the electromagnetic field can be assumed homogeneous at the scattering body. The interaction of the particle with the electromagnetic wave results in the induction of a dipole moment inside of the particle. This is proportional to the power of the incident electrical field and oscillates according to the frequency of the incident electromagnetic wave, in turn resulting in re-emission of the electromagnetic wave. This scattering process is called the Rayleigh scattering (molecular scattering).

The scattered intensity in a direction with an angle θ to the incident radiation, at a distance r from the scattering body, for a media of mass concentration C , composed of spheres of diameter d and of density ρ , is then given by (Liou, 1992):

2 Scientific Background

$$I(\theta, r) = I_0 \frac{8\pi^4}{r^2\lambda^4} \frac{\rho^2 d^6}{c^2} \left(\frac{m^2-1}{m^2+2} \right)^2 (1 + \cos^2 \theta) \quad (2.14)$$

where I_0 is the incident intensity, m is the complex refractive index. Equation 2.14 is inversely proportional to λ^4 , which means that the scattering is much stronger for the shortwave radiation. As a result, the terrestrial longwave radiation is weakly scattered.

Rayleigh scattering is symmetric in the backward and forward directions: $I(\theta, r) = I(\pi - \theta, r)$. Also, Rayleigh scattering is an increasing function of particle size d and is a decreasing function of the distance r .

In RT studies the normalized phase function $p(\theta)$ is often used. It describes what fraction of the scattered radiation appears per unit solid angle in the direction θ . For Rayleigh scattering one can get:

$$p(\theta) = \frac{3}{16\pi} (1 + \cos^2 \theta) \quad (2.15)$$

The $\frac{3}{16\pi}$ is the normalization factor which appears from integrating the $(1 + \cos^2 \theta)$ over all solid angles. Some researchers prefer to use a different unit solid angle $\frac{\Delta\Omega}{4\pi}$ with makes the normalization factor being equal to $\frac{3}{4}$.

For Rayleigh particles of any shape, the asymmetry parameter

$$g = \frac{1}{2} \int_0^\pi p(\theta) \sin \theta \cos \theta d\theta \quad (2.16)$$

is always zero.

2.3.2 Particle Mie scattering

When the particle dimensions are comparable to the wavelength λ , a three-dimensional charge distribution is set up within the scatterer and it is no longer sufficient to just consider an induced dipole. The exact solution of the Maxwell equations for the scattering on a sphere with a given radius, a complex refractive index m at a wavelength λ was calculated by Gustav Mie in 1908. It was elaborated by Debye in 1909 and is described by e.g. van de Hulst (1981).

Following extinction, scattering and absorption efficiencies, single scattering albedo and the asymmetry factor can be derived from Mie theory. To define the efficiency factors, the following quantities need to be introduced:

- the extinction efficiency Q_e (energy removed from an incident wave with energy flux density I_0 , equals $\pi r^2 Q_e I_0$);
- the scattering efficiency Q_s (energy which reappears as scattered energy, $\pi r^2 Q_s I_0$);
- the absorption efficiency Q_a (the absorbed energy $\pi r^2 Q_a I_0$);
- The single scattering albedo ω_0 (the fraction of the energy removed from the incident wave which reappears as scattered radiation);
- The asymmetry factor g (the average or statistically expected value of the cosine of the scattering angle for the scattered radiation);

These values can be written in terms of the complex-valued Mie coefficients a_n and b_n , which provide the full solution to the scattering problem in the Mie theory.

$$\text{Extinction efficiency: } Q_e = \frac{2}{\alpha^2} \sum_1^{\infty} (2n+1) \text{Re}(a_n + b_n) \quad (2.18)$$

$$\text{Scattering efficiency: } Q_s = \frac{2}{\alpha^2} \sum_1^{\infty} (2n+1) \{|a_n|^2 + |b_n|^2\} \quad (2.19)$$

$$\text{Absorption efficiency: } Q_a = Q_e - Q_s \quad (2.20)$$

$$\text{Single scattering albedo: } \omega_0 = \frac{Q_s}{Q_e} \quad (2.21)$$

$$\text{Asymmetry factor: } g = \frac{4}{\alpha^2 Q_s} \sum_1^{\infty} \left\{ \frac{n(n+2)}{n+1} \text{Re}(a_n a_{n+1}^* + b_n b_{n+1}^*) + \frac{2n+1}{n(n+1)} \text{Re}(a_n b_n^*) \right\} \quad (2.22)$$

The extinction efficiency Q_e is an oscillating function of the size parameter α (see Fig. 2.15). It is visible that for a very large particle, the extinction efficiency converges at 2. This can be interpreted as a particle that removes twice the energy from the direct beam as compared to the energy fallen onto its cross-sectional area. This effect is called the “extinction paradox”.

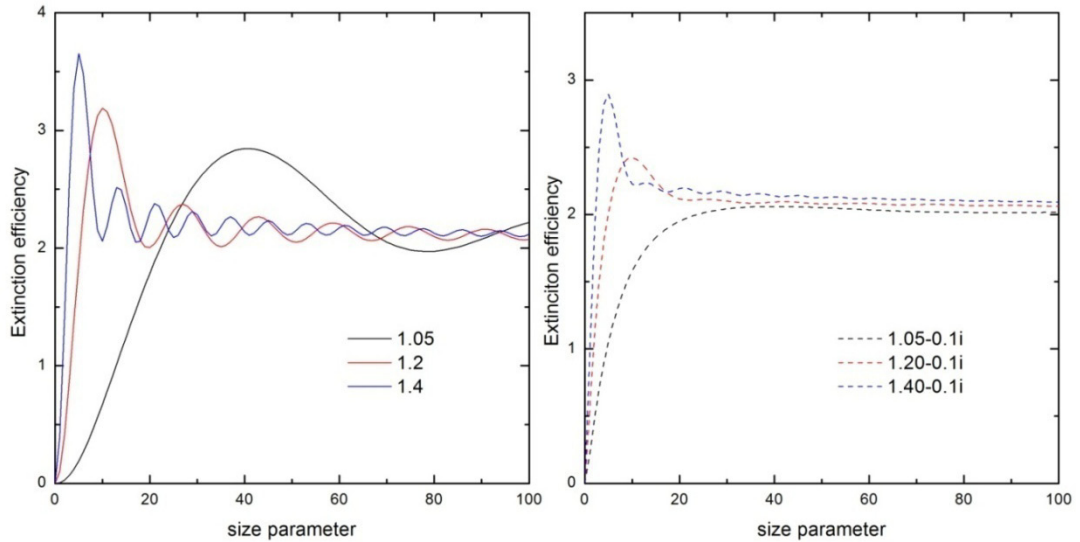


Figure 2.15. Extinction efficiency Q_e depending on the refractive index $m = n - \chi i$ and size parameter $\alpha = \frac{2\pi R}{\lambda}$.

It can be explained from the point of view of two different phenomena: diffraction and the geometrical optics effects of reflection, refraction and absorption are all occurring, with the efficiency of each equal to unity. This gives the convergence at 2.

Unlike the symmetric Rayleigh scattering, Mie scattering has a strong forward scattering peak, which is partly due to diffraction of photons on the sphere. The asymmetry toward the forward scattering increases with the increase of the particle size. When the particle size parameter exceeds unity the scattering diagram, in addition to more pronounced forward scattering, would start developing peaks ending up with a finer highly oscillatory structure for size parameters of about 10. The backward hemisphere of scattering is not so much affected by the particle size, but connected to particle absorption and refractive index. Increasing the absorption coefficient causes a decrease in the backward scattering and in the asymmetry

parameter. For a large reflecting sphere the reflected and diffracted component are in balance, creating an asymmetry factor of about $\frac{1}{2}$. The reflected component is isotropic, and the diffracted component is responsible for the forward scattering peak which becomes narrower with increasing radius.

2.3.3 Integrated optical properties of an aerosol medium

In order to describe an elementary volume of an aerosol medium consisting of large amount of randomly oriented aerosol particles, one needs to integrate the contributions of single particles over the particle number size distribution.

Then the definition of extinction coefficient for aerosol medium $\sigma_{e,\lambda}$ will look like:

$$\sigma_{e,\lambda} = \int_0^{\infty} \pi r^2 Q_e \left(\frac{r}{\lambda} \right) n(r) dr \quad (2.23)$$

where $n(r) = \frac{dN}{dr}$ is the number size distribution of N particles of aerosol. As can be seen, the wavelength dependence of the extinction coefficient is determined by the wavelength dependence of the extinction efficiencies only.

In Equation (2.23) the extinction coefficient is determined by the scattering efficiency weighted by its geometrical cross-section πr^2 . The number size distribution $n(r)$ that is used to describe the size distribution in aerosol is not able to indicate which particle size range contributes most to the scattering coefficient. For this purpose, Hansen and Hovenier (1974) suggested to use the effective radius r_e :

$$r_e = \frac{\int_0^{\infty} r^3 n(r) dr}{\int_0^{\infty} r^2 n(r) dr} \quad (2.24)$$

The bulk single scattering albedo represents the single scattering albedo of a population of particles. It can be written as the following ratio:

$$\bar{\omega}_0 = \frac{\int_0^{\infty} r^2 Q_s \left(\frac{r}{\lambda} \right) n(r) dr}{\int_0^{\infty} r^2 Q_e \left(\frac{r}{\lambda} \right) n(r) dr} \quad (2.25)$$

This ratio is unity for conservative scattering and zero for pure absorption.

For an aerosol media, the asymmetry factor g still can be used. It describes an average or statistically expected value of the cosine of scattering angle for the radiation scattered on a population of spherical particles:

$$g = \frac{\int_0^{\infty} r^2 Q_s \left(\frac{r}{\lambda} \right) g \left(\frac{r}{\lambda} \right) n(r) dr}{\int_0^{\infty} r^2 Q_s \left(\frac{r}{\lambda} \right) n(r) dr} \quad (2.26)$$

Here the individual asymmetry factors must be weighted in proportion to the energy, which the individual particles scatter, hence the appearance of the scattering efficiency Q_s .

Atmospheric scattering phase function $p(\vartheta)$ describes the probability of photon scattered in the direction of scattering angle ϑ . Generally it is composed of scattering on Rayleigh particles and aerosol particles, but unlike Rayleigh scattering phase function, the aerosol

contribution is strongly asymmetric and varies greatly. The aerosol phase function depends on aerosol type (size distribution, particle shape, chemical composition). For an example of an aerosol phase function, see e.g. Fig. 3.3.

Mie theory is only suitable to calculate the optical properties of spherical particles. The effect of non-spherical particles on the aerosol optical properties was studied rather recently by Mishchenko (1993) and it was shown that the phase function is very sensitive to the particle shape, with the deviation from the reference phase function of a spherical particle by up to 3 times in the middle scattering angles. It is therefore important to take the non-sphericity into account for satellite applications. For some of the aerosol particles the assumptions of spherical particles is realistic, due to hygroscopicity or origin of the aerosol particles (e.g. gas-to-particle conversion). To avoid possible inaccuracies connected with the particle shape, within this work we use calculated phase functions for theoretical studies, but measured phase functions for satellite retrievals.

Another important integrated aerosol property is already defined aerosol optical thickness τ_λ :

$$\tau_\lambda(z_0, z_1) = \int_{z_0}^{z_1} \sigma_{e,\lambda}(z) dz \quad (2.27)$$

The spectral behavior of the τ_λ can be represented by a power law function (Ångström, 1961):

$$\tau_\lambda \sim \lambda^{-\alpha} \quad (2.28)$$

where λ is the wavelength and α is the Ångström wavelength exponent. The latter is related to the slope of the aerosol size distribution: the smaller the particles dominating in the scattering, the greater is the Ångström α . As the TOA reflectance is directly proportional to τ_λ , the spectral behavior of the τ_λ will also have large effects on the spectral behavior of the TOA reflectance, introducing the same spectral behavior. This can be used in retrieval algorithms to extract information on the size distribution of the aerosol particles dominating the scattering.

2.4 Radiative transfer in the atmosphere

Radiative transfer equations (RTE) describe how light travels through the atmosphere, considering all processes of absorption, scattering, reflection, refraction and emission. All radiation input and losses at a certain altitude and direction need to be considered accounting for both direct and diffuse radiation. Losses are caused by absorption and scattering of the direct and diffuse radiation, the source of radiation is the scattering into the respective altitude and angle as well as the reflection at the Earth's surface. For our cases of cloud free relatively clean atmosphere, emission processes are negligible and therefore are not relevant for this study. The next section is dedicated to RTE solutions for plane parallel and spherical atmosphere with Lambertian and non-Lambertian underlying surface. These are useful for all applications of radiative transfer, which are radiative transfer modeling, remote sensing and ground based measurements. In the current work, we utilize all three, exploiting RT modeling for our theoretical studies and calculations of the look-up tables, ground based measurements serve as reference points for validation, and finally the remote sensing algorithms of aerosol retrieval developed within this work are based on the RTE solution.

2.4.1 Description of the radiative transfer

Let us consider a volume ΔV of infinitesimal length ds and area ΔA containing radiating matter. Then one can write the change (loss plus gain) of radiance I_λ along the path ds while propagating in the medium:

$$dI_\lambda = -\sigma_{e,\lambda}I_\lambda ds + \sigma_{e,\lambda}J_\lambda ds \quad (2.29)$$

Dividing this equation by $\sigma_{e,\lambda}ds$, we can write the RTE in its basic form (Schwartzschild equation):

$$\frac{dI_\lambda}{\sigma_{e,\lambda}ds} = -I_\lambda + J_\lambda \quad (2.30)$$

where I_λ is the radiance before entering the medium and J_λ are the source terms within the medium.

The energy losses occur due to scattering in the atmosphere (see Sect. 2.4). The energy gain is due to emission. Terrestrial temperature emission occurs at wavelengths above $3 \mu\text{m}$ with the source term described by the Planck law and depending on the physical temperature of the emitter. Spectral features based on discrete energy states of the molecules in the medium (rotation and vibration states) lead to emission lines or bands.

Plane-parallel atmosphere

To handle the vertical stratification of the atmosphere, the atmosphere has to be approximated by a set of layer having specific geometry. For cases of solar zenith angles below 60° , the atmosphere can be approximated by a plane parallel model. The layers in the plane-parallel atmosphere are characterized by homogeneous properties each. Such an atmosphere is bordered by the bottom and the top horizontal boundary layers.

Let us be given a light beam with the spectral radiance I_λ entering the atmospheric layer with the geometrical thickness dz at an incident angle θ and an azimuth angle φ . On its path $ds = \cos\theta dz = \mu dz$ the light beam experiences gains and losses of its energy according to the medium it is traveling through, and the RTE then is:

$$\mu \frac{dI_\lambda(\tau, \mu, \varphi)}{d\tau} = -I_\lambda(\tau, \mu, \varphi) + J_\lambda(\tau, \mu, \varphi) \quad (2.31)$$

This equation may be solved to yield the upwelling or downwelling intensity for a finite atmosphere bounded at the top and bottom.

After multiplication with $\exp(-\frac{\tau}{\mu})$ and integration from $\tau' = \tau$ to τ_1 , we can write for $\mu \geq 0$ (upward directed radiation) and an altitude τ :

$$I_\lambda^\uparrow(\tau, \mu, \varphi) = I_\lambda^\uparrow(\tau_1, \mu, \varphi) \exp\left(-\frac{\tau_1 - \tau}{\mu}\right) + \frac{1}{\mu} \int_\tau^{\tau_1} \exp\left(-\frac{\tau' - \tau}{\mu}\right) J_\lambda^\uparrow(\tau', \mu, \varphi) d\tau' \quad (2.32)$$

Correspondingly, for the downwelling radiation with $\mu < 0$ and at an altitude of τ :

$$I_\lambda^\downarrow(\tau, \mu, \varphi) = I_\lambda^\downarrow(0, \mu, \varphi) \exp\left(-\frac{\tau}{|\mu|}\right) + \frac{1}{|\mu|} \int_\tau^{\tau_1} \exp\left(-\frac{\tau - \tau'}{|\mu|}\right) J_\lambda^\downarrow(\tau', \mu, \varphi) d\tau' \quad (2.33)$$

$I_{\lambda}^{\downarrow}(0, \mu, \varphi)$ and $I_{\lambda}^{\uparrow}(\tau, \mu, \varphi)$ describe the inwards directed radiances into the atmosphere at the TOA $\tau = 0$ and at the ground $\tau = \tau_1$ (see Figure 2.16).

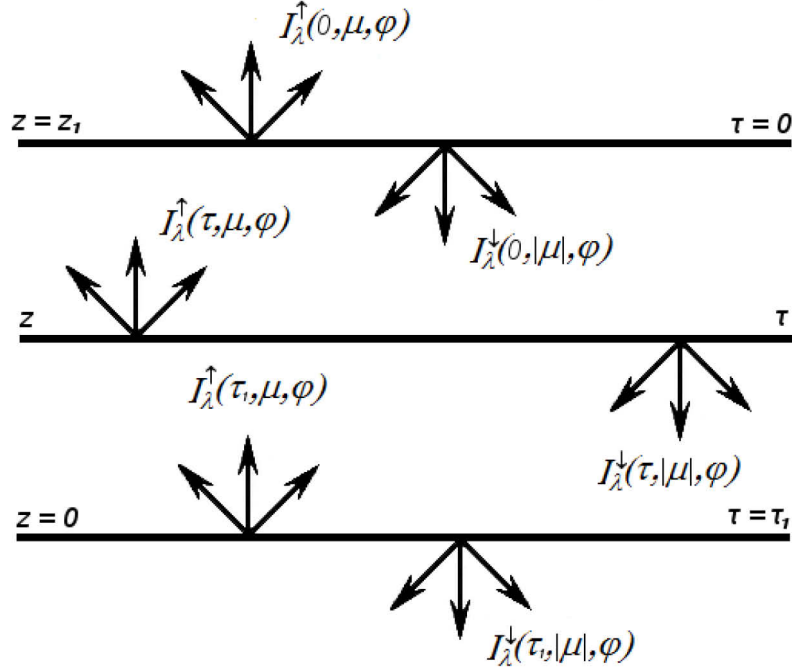


Figure 2.16. Schematic representation of the plane-parallel atmosphere.

For applications in RT modeling and remote sensing, it is useful to determine the radiant fluxes coming out at the TOA and at the surface. After applying these boundary conditions to Equations (2.32) and (2.33) for the upward directed radiation at TOA ($\tau = 0$):

$$I_{\lambda}^{\uparrow}(0, \mu, \varphi) = I_{\lambda}^{\uparrow}(\tau_1, \mu, \varphi) \exp\left(-\frac{\tau_1}{\mu}\right) + \frac{1}{\mu} \int_0^{\tau_1} \exp\left(-\frac{\tau}{\mu}\right) J_{\lambda}^{\uparrow}(\tau', \mu, \varphi) d\tau' \quad (2.34)$$

The first term on the right hand side is the altitude attenuated radiation from the surface. The second term describes the atmospheric part of the upward directed radiation.

The same for the downward directed radiation at the surface:

$$I_{\lambda}^{\downarrow}(\tau_1, \mu, \varphi) = I_{\lambda}^{\downarrow}(0, \mu, \varphi) \exp\left(-\frac{\tau_1}{|\mu|}\right) + \frac{1}{|\mu|} \int_0^{\tau_1} \exp\left(-\frac{\tau_1 - \tau'}{|\mu|}\right) J_{\lambda}^{\downarrow}(\tau', \mu, \varphi) d\tau' \quad (2.35)$$

As before, the first term on the right side is the downward radiation at the TOA which is attenuated by the optical thickness τ_1 . The second term is the downward directed radiation intensity scattered by the atmosphere.

Solving Equations (2.34) and (2.35) is needed to obtain the radiant flux densities at TOA and at the Earth's surface. This is in general a challenging task due to e.g. multiple integrations over the whole range of solid angles. Many numerical approaches deal with this problem (e.g., Stamnes et al., 1988; Siewert, 2000; Min and Duan, 2004). These attempts are mostly dedicated to homogeneous plane-parallel atmospheric layers which could lead to problems if horizontal structures dominate (e. g. convective clouds), but applicable for other cases.

Spherical atmosphere

For the cases of low sun (solar zenith angle is greater than 60°), the curvature of the atmosphere has to be considered.

The following sketch in Fig. 2.17 illustrates how the light beam path changes in the spherical atmosphere (path ds') relatively to the plane-parallel atmosphere without refraction (path ds) for a given solar elevation angle θ .

Atmospheric refraction also affects the path of the light beam and needs to be considered during the RT calculations. Its effect is shown in Fig. 2.18.

Considering the mentioned changes of the path length and corresponding changes of the air masses, one can write the Schwartzschild equation again:

$$\frac{dI_\lambda}{M(z)\sigma_{e,\lambda}ds'} = -I_\lambda + J_\lambda \tag{2.36}$$

For a pure molecular atmosphere, the relative optical air mass $M(z)$ is given by Kasten and Young (1989) or Bucholtz (1995):

$$M(z) = \frac{1}{\cos(z) + a \cdot (b - c)^{-c}} \tag{2.37}$$

The coefficients a , b , and c are according to Kasten& Young (1989):

$$a = 0.50572, b = 6.07995 \text{ and } c = 1.6364$$

In some case of strong vertical stratification (e.g. thin aerosol layer) the integration of the vertical profiles is needed. The use of incorrect air mass functions and vertical stratification can drastically affect the accuracy of e.g. RT modeling. For the path length element ds' and the extinction $\sigma_{e,\lambda}$, we can use the relative optical mass:

$$ds' = M(z)ds\sigma'_{e,\lambda} = M(z)\sigma_{e,\lambda} \tag{2.38}$$

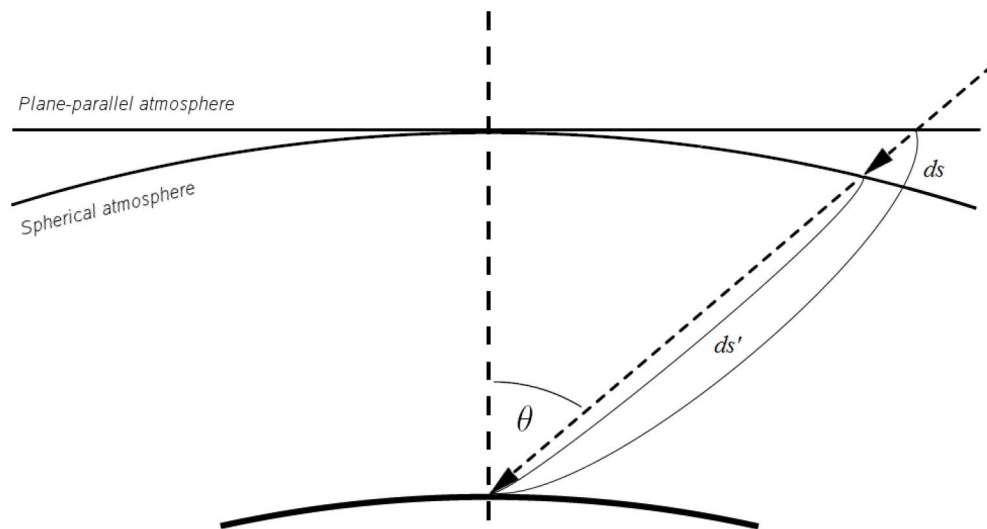


Figure 2.17. The shortening of the light beam path in the spherical atmosphere relatively to the plane-parallel atmosphere.

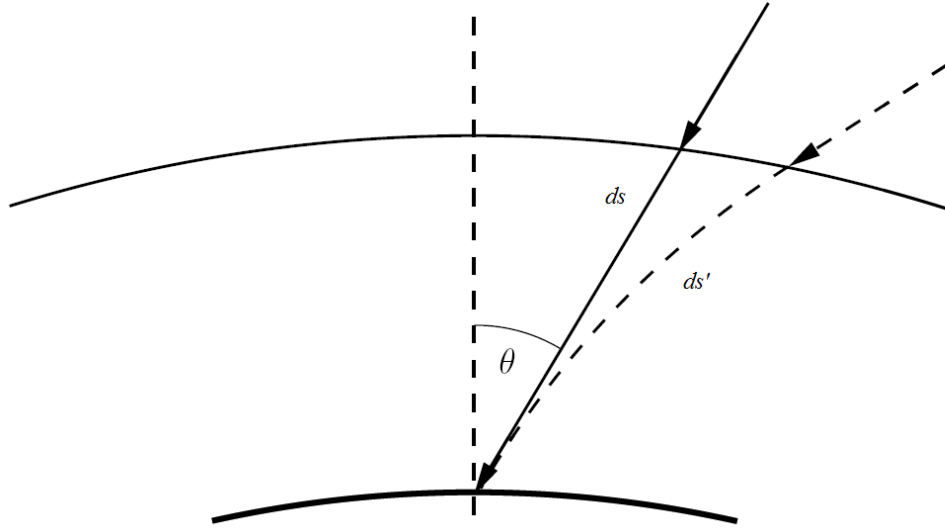


Figure 2.18. The lengthening of the light beam path in the spherical atmosphere due to refraction.

RTE solutions for the system “ground + atmosphere”

Let it be given that the ground is a uniform Lambertian reflector. The atmosphere and particularly the atmospheric aerosol concentration are assumed to be horizontally uniform.

It is convenient to express the signal received by the satellite using successive orders of scattering in the system ground+atmosphere (see e.g. Tanre et al., 1979). Let us use reflectances ρ rather than radiances I :

$$\rho = \frac{\pi I}{\mu_0 f} \quad (2.39)$$

where f is the solar flux at the TOA, and $\theta_0 = \arccos \mu_0$ is the solar zenith angle.

The apparent reflectance is then:

$$\rho(M, \mu_0, \mu, \varphi) = \rho_a(\mu_0, \mu, \varphi) + \exp\left(-\frac{\tau}{\mu_0}\right) \rho \exp\left(-\frac{\tau}{\mu}\right) + \quad (2.40)$$

$$E(\mu_0) \rho \exp\left(-\frac{\tau}{\mu}\right) + \left[\exp\left(-\frac{\tau}{\mu_0}\right) + E(\mu_0)\right] \rho E'(\mu) + \left\{ \sum_{n=1}^{\infty} \left[\exp\left(-\frac{\tau}{\mu_0}\right) + E(\mu_0)\right] (\rho r)^n \right\}$$

where τ is the optical thickness of the atmosphere, $\theta = \arccos \mu$ is the zenith viewing angle, φ is the relative azimuth angle. $\rho_a(\mu_0, \mu, \varphi)$ is the intrinsic atmospheric contribution in terms of reflectance (Figure 2.19, a), $\exp\left(-\frac{\tau}{\mu_0}\right) \rho \exp\left(-\frac{\tau}{\mu}\right)$ is the term that contains the information resulting from direct solar radiation reflected by the target (Figure 2.19, b), $E(\mu_0) \rho \exp\left(-\frac{\tau}{\mu}\right)$ is the contribution resulting from diffuse downward solar radiation attaining the ground at point M (Figure 2.19, c), $\left[\exp\left(-\frac{\tau}{\mu_0}\right) + E(\mu_0)\right] \rho E'(\mu)$ represents the first order contribution of the target background (Figure 2.19, d). The geometric series in Eq. (2.40) corresponds to

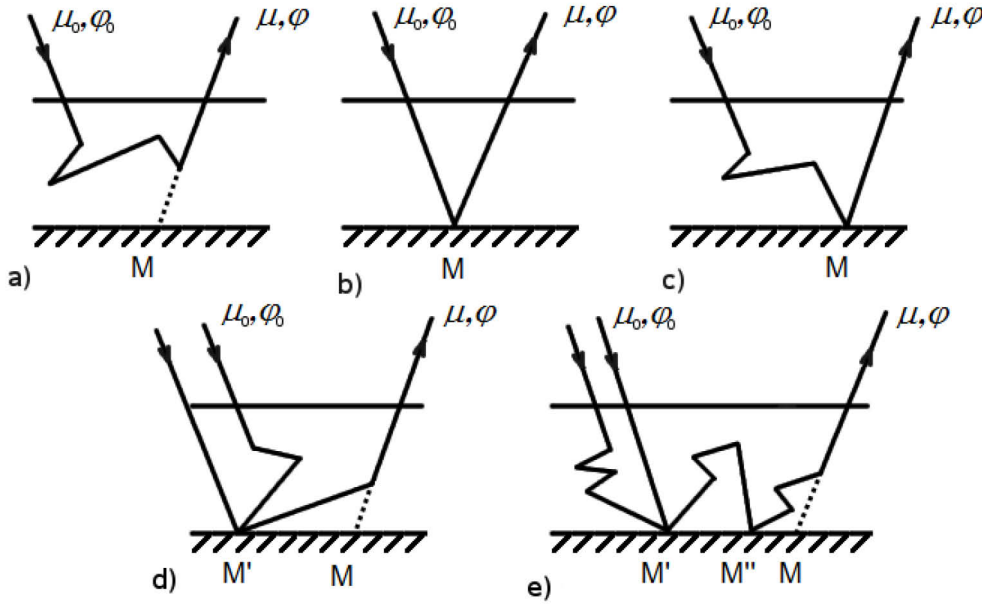


Figure 2.19. Successive orders of scattering in the ground+atmosphere system

higher orders of interaction with the ground, the term $[\exp(-\frac{\tau}{\mu_0}) + E(\mu_0)](\rho r)^n$ corresponds to radiation having interacted n times with the ground (Fig. 2.19, e).

Equation (2.40) can be also written in the following way:

$$\rho_{TOA}(\lambda, \mu_0, \mu, \varphi) = \rho_{atm}(\lambda, \mu_0, \mu, \varphi) + \frac{\rho_{sfc}(\lambda)T_1(\lambda, \mu_0)T_2(\lambda, \mu)}{1 - \rho_{sfc}(\lambda)r(\lambda)} \quad (2.41)$$

where $\theta = \arccos \mu$ is the observation zenith angle, φ is the relative azimuth angle, $\rho_{TOA}(\lambda, \mu_0, \mu, \varphi)$ is the total reflectance of the system “surface + atmosphere”, $\rho_{atm}(\lambda, \mu_0, \mu, \varphi)$ is the atmospheric reflectance (the reflectance of the aerosol, Rayleigh scattering, ozone absorption), $r(\lambda)$ is the atmospheric hemispherical albedo, $T_1(\lambda, \mu_0) = E(\mu_0) + \exp(-\tau/\mu_0)$ is the atmospheric transmittance from the top-of-atmosphere to the surface, $T_2(\lambda, \mu) = E(\mu) + \exp(-\tau/\mu)$ is the total atmospheric transmittance from the surface to a receiver (e.g., placed on a satellite), $E(\mu_0)$ and $E(\mu)$ are diffuse transmittances from top-of-atmosphere to the surface and from the surface to the receiver respectively, $\exp(-\tau/\mu_0)$ and $\exp(-\tau/\mu)$ are the direct transmittances from top-of-atmosphere to the surface and from the surface to the receiver respectively, $\rho_{sfc}(\lambda)$ is the Lambertian reflectance of the surface.

The normalized quantities $E(\mu_0)$ and r are given by:

$$E(\mu_0) = \frac{1}{\mu_0 f} \int_0^{2\pi} \int_0^{-1} I_d^\downarrow(\tau, \mu_0, \mu, \varphi) \mu d\mu d\varphi \quad (2.42)$$

where $I_d^\downarrow(\tau, \mu_0, \mu, \varphi)$ is the downward diffuse radiance at the bottom of the atmosphere for $\rho = 0$ (subscript λ is omitted for the sake of simplicity), and

$$r = \frac{1}{\pi} \int_0^{2\pi} \int_0^{-1} I^\downarrow(\tau, \mu) \mu d\mu d\varphi \quad (2.43)$$

where $I^\downarrow(\tau, \mu)$ is the downward radiance at the surface for the case of an incident upward isotropic radiation at the bottom of the atmosphere $I^\uparrow(\tau, \mu) = 1$.

Expression (2.41) appears in numerous researches dedicated to retrievals of aerosol and surface properties (serving as a key to determine atmospheric correction in the latter case) (Vermote et al., 1997; Veefkind et al., 1998; Curier et al., 2009; von Hoyningen-Huene et al., 2006; von Hoyningen-Huene et al., 2010; Dinter et al., 2009). Technically it can also be applied to non-Lambertian surfaces, by introducing BRDF effects in the numerator of the surface term of Eq. (2.41). However, its accuracy in this case is questionable due to the fact that directional properties of surface reflection function can have a significant effect on the redistribution of the incoming light, both direct and diffuse, and need to be taken into account more accurately. Ray tracing studies show that total intensity reflected from a dark particulate matter consists mainly of first orders of scattering, and the role of higher orders of scattering increases with the increase of single scattering albedo of the particles (e.g. Stankevich et al., 2007). Therefore for darker surfaces the effect of surface directional properties on coupling tends to be rather small. However, in case of very bright surfaces it becomes significant and needs to be accounted for.

Tanre et al. (1979) suggested an approximate analytical expression for top of atmosphere reflectance in case of non-Lambertian non-homogeneous surface, which accounts for light scattering between the observed point M, its neighbour surface areas, and the atmosphere of optical thickness τ :

$$\begin{aligned} \rho_{TOA}(M, \lambda) = & \rho_{atm}(\lambda, \mu_0, \mu, \varphi) + \rho_{sfc}(M, \lambda, \mu_0, \mu, \varphi) \exp\left(-\frac{\tau}{\mu_0}\right) \exp\left(-\frac{\tau}{\mu}\right) + \\ & \bar{\rho}_{sfc}(M, \lambda, \mu_0, \mu, \varphi) \exp\left(-\frac{\tau}{\mu}\right) E(\mu_0) + \langle \rho_{sfc}(M, \lambda, \mu_0, \mu, \varphi) \rangle T_1(\lambda, \mu_0) E(\mu) + \\ & \langle \rho_{sfc}(M, \lambda, \mu_0, \mu, \varphi) \rangle r(\lambda) \times \left[\frac{\bar{\rho}_{sfc}(M, \lambda, \mu_0, \mu, \varphi) \exp\left(-\frac{\tau}{\mu}\right) + \langle \rho_{sfc}(M, \lambda, \mu_0, \mu, \varphi) \rangle E(\mu)}{1 - \langle \rho_{sfc}(M, \lambda, \mu_0, \mu, \varphi) \rangle r(\lambda)} \right] T_1(\lambda, \mu_0) \end{aligned} \quad (2.44)$$

where $\rho_{TOA}(M, \lambda)$ is the total reflectance of the system “surface + atmosphere” with respect to the target point M, $\rho_{atm}(\lambda, \mu_0, \mu, \varphi)$ is the atmospheric reflectance (the reflectance of the aerosol, Rayleigh scattering, ozone absorption), $E(\mu_0)$ and $E(\mu)$ are diffuse transmittances from top-of-atmosphere to the surface and from the surface to the receiver respectively, $\exp(-\tau/\mu_0)$ and $\exp(-\tau/\mu)$ are the direct transmittances from top-of-atmosphere to the surface and from the surface to the receiver respectively, $T_1(\lambda, \mu_0) = E(\mu_0) + \exp(-\tau/\mu_0)$ is the total atmospheric transmittance from the top-of-atmosphere to the surface, $r(\lambda)$ is the atmospheric hemispherical albedo, $\rho_{sfc}(M, \lambda, \mu_0, \mu, \varphi)$ is the BRDF of the target M for a given observation-illumination geometry. The term $\bar{\rho}_{sfc}(M, \lambda, \mu_0, \mu, \varphi)$ is the average angular reflectance of the target illuminated with the diffuse light only; $\langle \rho_{sfc}(M, \lambda, \mu_0, \mu, \varphi) \rangle$ accounts for the effect of multiple light scattering from the environment of the target M in the observation direction. The last term is only different from $\bar{\rho}_{sfc}(M, \lambda, \mu_0, \mu, \varphi)$ in case of inhomogeneous spatial distribution of $\rho_{sfc}(M, \lambda, \mu_0, \mu, \varphi)$. In this study we assume the surface to have a homogeneous $\rho_{sfc}(M, \lambda, \mu_0, \mu, \varphi)$, therefore the dependence on the target M can be waived and the Eq. (2.44) can be written in a simplified form as:

$$\begin{aligned} \rho_{TOA}(M, \lambda) = & \\ & \rho_{atm}(\lambda, \mu_0, \mu, \varphi) + \rho_{sfc}(M, \lambda, \mu_0, \mu, \varphi) \exp\left(-\frac{\tau}{\mu_0}\right) \exp\left(-\frac{\tau}{\mu}\right) + \bar{\rho}_{sfc}(M, \lambda, \mu_0, \mu, \varphi) \times \\ & \left\{ \exp\left(-\frac{\tau}{\mu}\right) E(\mu_0) + T_1(\lambda, \mu_0) E(\mu) + r(\lambda) \frac{\bar{\rho}_{sfc}(M, \lambda, \mu_0, \mu, \varphi) T_1(\lambda, \mu_0) T_2(\lambda, \mu)}{1 - \bar{\rho}_{sfc}(M, \lambda, \mu_0, \mu, \varphi) r(\lambda)} \right\} \end{aligned} \quad (2.45)$$

with all the terms defined as above.

2.4.2 The forward radiative transfer model SCIATRAN

In current work, we need to solve integro-differential RTE in order to obtain:

- The dependence of aerosol TOA reflectance on AOT, observation-illumination geometry and wavelength;
- The dependence of snow surface BRDF on observation-illumination geometry;
- The dependence of TOA reflectance of the whole system “surface+atmosphere” on AOT and observation-illumination geometry.

We do this numerically using forward radiative transfer code SCIATRAN (Rozanov et al., 2005).

The SCIATRAN RT model can be optionally operated in the plane-parallel mode or in the spherical/pseudospherical mode accounting for the spherical shape of the Earth’s atmosphere. In the spherical mode, the atmosphere is considered to be symmetrical with respect to the solar principal plane. There are also a options to describe surface reflective properties: constant or wavelength dependent Lambertian albedo as well as by the BRDF for various surface. In the pseudospherical mode, the program is calculating the light paths for the direct solar beam in a spherical atmosphere and then solving the plane-parallel RTE.

A standard method to solve the integro-differential radiative transfer equation in a plane-parallel atmosphere is the discrete-ordinates method (Stamnes et al., 1988 and Siewert, 2000). This scheme is employed in the model. Alternatively, to calculate the outgoing radiance at the TOA either the finite difference scheme (Rozanov et al., 1997) or the finite element approach (Samarskij, 2002) is used. At first, a variable separation is being performed for the azimuthal dependence of the radiances and phase functions. For this, the scattering phase functions need to be presented as sums of Legendre polynomials and the radiances are rewritten as Fourier series. To transform the integrals into sums, the finite difference approach is applied, so that gradients between the two altitude levels of the altitude grid will be presented as finite differences. In addition to the altitude, also all the angles are discretised. The step must be small enough to assume the depending functions to be constant within it.

For the model run, the atmospheric state, surface reflective properties and the geometry of interest need to be defined. As our satellite retrievals are look-up table (LUT) based, a full set of illumination-observation geometries is usually calculated.

Within this work, we do not use plane parallel mode of calculations as Arctic illumination conditions very often feature low solar zenith angles and the sphericity of the atmosphere needs to be considered.

Specific aerosol and surface properties used for our RT calculations vary for different LUTs will be described in further sections dedicated to the satellite AOT retrievals and LUT calculations.

2.5 Description of the instruments

2.5.1 The satellite instrument AATSR

Within the current work, the AATSR (Advanced Along Track Scanning Radiometer) instrument has been used as a satellite sensor. The information given in this subsection as well as a lot of additional information about this instrument can be found in the official AATSR handbook by ESA, which is available at <http://envisat.esa.int/handbooks/aatsr/>.

AATSR located onboard the ENVISAT (ENVironmental SATellite, nominal orbit repeat cycle of 35 days, orbital period 100.6 minutes, inclination 98.54 degrees and descending node 10:00 a.m. local time) is a low-resolution conical imaging spectrometer operating in the visible, near-infrared, mid-infrared and thermal spectrum ranges. The spectral channels available in the AATSR data are summarized in Table 2.2.

Table 2.2 AATSR spectral channels

Channel	Centre Wavelength	Bandwidth	Primary Application
0.55 μm	0.555 μm	20 nm	Chlorophyll
0.66 μm	0.659 μm	20 nm	Vegetation Index
0.87 μm	0.865 μm	20 nm	Vegetation Index
1.6 μm	1.61 μm	0.3 μm	Cloud Clearing
3.7 μm	3.70 μm	0.3 μm	SeaSurfaceTemperature
11 μm	10.85 μm	1.0 μm	SeaSurfaceTemperature
12 μm	12.00 μm	1.0 μm	SeaSurfaceTemperature

The main feature of the AATSR instrument is its use of along-track scanning to offer dual view of the Earth's surface. The AATSR viewing geometry is shown in Figure 2.20.

The dual view is achieved by rotating an inclined-plane scan mirror in front of a reflecting telescope, thus performing a conical scan. The resulting conical scan is arranged to view downwards and ahead in the along-track direction, allowing each point on the Earth's surface to be viewed in turn, first at an angle of 55° (the forward view) and then at an angle close to

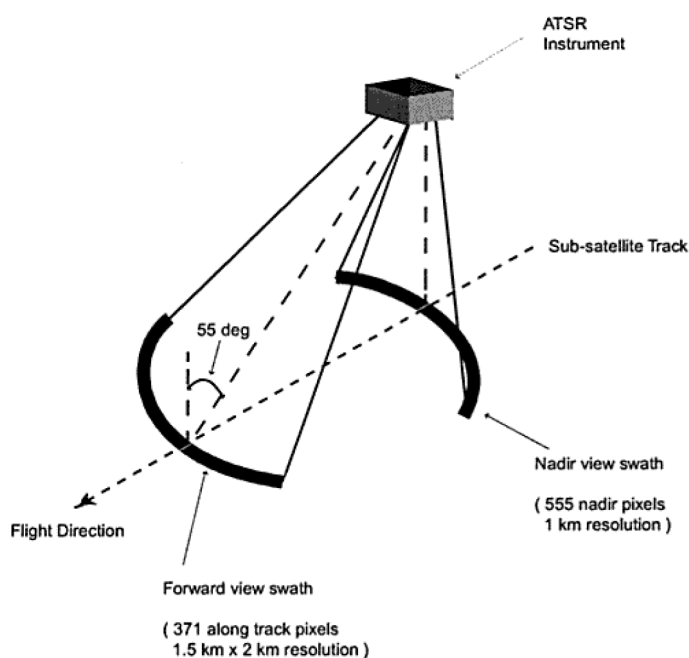


Figure 2.20. The AATSR viewing geometry.

vertical (the nadir view) as the satellite moves forward. These observations are separated in time by 150 sec, or approximately 1000 km on the ground, at the sub-satellite point. This unique feature of the instrument is particularly helpful in the task of remote sensing over snow and ice, as the two simultaneous views provide additional information about surface angular reflective properties and can be used to subtract the surface signal from the TOA signal.

The field of view comprises two 500 km-wide curved swaths, with 555 pixels across the nadir swath and 371 pixels across the forward swath. The nominal pixel size is 1 km^2 at the center of the nadir swath and 1.5 km^2 at the center of the forward swath. The scan cycle is repeated 6.6 times per second, and the sub-satellite point on the Earth's surface moves forward by one pixel (1km) during each scan cycle.

The AATSR scan cycle allows the detectors to view a sequence of five elements which are

- The along-track Earth view,
- A hot black-body target,
- The visible calibration unit,
- The nadir Earth view, and
- A cold blackbody target.

The two blackbody calibration targets observed between the Earth-views are critical to the radiometric quality of the AATSR thermal data; one of them is heated up to 305K, the other is unheated and is close to the ambient temperature ($\sim 256 \text{ K}$). This covers the full range of expected marine scene temperatures.

As a result, AATSR can be regarded as a near-ideal radiometer. The infrared calibration is applied automatically during the ground processing.

The visible and near-infrared channels are calibrated once per orbit via viewing the Sun at sunrise. Also, calibration of the visible channels will be performed automatically during ground processing.

During the pre-launch calibration, the 12, 11 and 3.7 μm channels were verified using high-accuracy external black bodies. Overall, the AATSR BTs were found to be within 30 mK of the target temperatures (210 to 315 K). The AATSR visible channels have also undergone a detailed laboratory calibration, to ensure that all instrument performance requirements are met.

Within this work, the Level-1b Gridded Brightness Temperature/ Reflectance (GBTR) are used. This product comprises calibrated and geolocated images of brightness temperature (BT) for the three infrared channels, or reflectance for the near-infrared and visible channels, together with cloud and land identification.

The forward and nadir views of AATSR are collocated during the geolocation procedure, when the position of each pixel on the Earth's surface of is determined and then regridded onto a rectangular grid. As the pixel density is lower in the forward view image, cosmetic fill is applied as needed. Land-flagging and cloud-clearing algorithms are applied at this stage.

Though AATSR level 1b products includes cloud clearing, in some cases of snow and ice surfaces it is not sufficient. Relatively comprehensive set of spectral channels of the instrument, especially the inclusion of NIR and TIR channels, made it possible to develop an improved version of cloud screening over these surfaces within this study (see Sect. 3.2).

2.5.2 Ground-based AERONET measurements

The AOT retrieval algorithms developed within this work have been validated against ground-based measurements available in scope of the AERONET (AERosolROboticNETwork) program.

The AERONET program is a federation of ground-based remote sensing aerosol networks, which provides a long-term, continuous and freely accessible database of aerosol optical, microphysical and radiative properties. The network imposes standardization of instruments, calibration, processing and distribution. The details on AERONET data and operation can be found at <http://aeronet.gsfc.nasa.gov>.

AERONET collaboration provides globally distributed observations of spectral aerosol optical Depth (AOD) which is available as three data quality levels: Level 1.0 (unscreened), Level 1.5 (cloud-screened), and Level 2.0 (cloud screened and quality-assured). Within this work only Level 2.0 data are used.

The CIMEL spectral radiometer used within the AERONET network is a solar-powered, robust, robotically-pointed sun and sky spectral sun photometer. The direct sun measurements are made in eight spectral bands (340, 380, 440, 500, 670, 870, 940 and 1020 nm) requiring approximately 10 seconds. The field of view of these measurements is 1.2 degrees.

2 Scientific Background

OD is calculated from spectral extinction of direct beam radiation at each wavelength based on the Lambert-Beer-Bouguer law. The Rayleigh and gaseous components are removed to isolate the AOD. For the Arctic stations, the AOD is most times available at a limited set of wavelengths (most frequent is 500nm).

In addition to the direct solar irradiance measurements, these instruments measure the sky radiance in four spectral bands (440, 670, 870 and 1020 nm) along the solar principal plane (i.e., at constant azimuth angle, with varied scattering angles) up to nine times a day and along the solar almucantar (i.e., at constant elevation angle, with varied azimuth angles) up to six times a day. These measurements are used to retrieve size distribution, phase function and aerosol optical depth. Sky radiance measurements are inverted with the Dubovik and Nakajima inversions (Holben et al., 2006) to provide aerosol properties of size distribution and phase function over the particle size range of 0.1 to 5 μm .

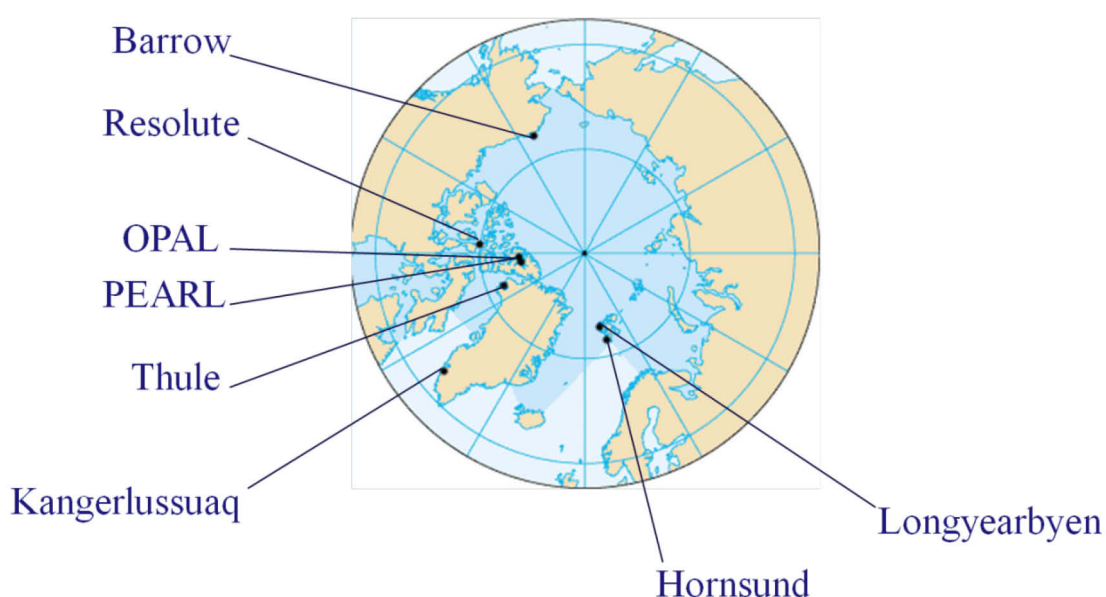


Figure 2.21 Eight High Arctic AERONET stations used for validation of satellite retrievals within this work.

An intercomparison with the reference instruments is used for calibration of the AERONET instruments. Such intercomparison is performed before and after field measurements in order to correct for possible calibration trends. For easily accessible stations re-calibration is performed 1-2 times per year. The reference CIMELs are calibrated using the Langley plots¹⁰ technique at Mauna Loa Observatory in Hawaii on a frequent basis. The observatory's location (isolated from most local and regional sources of aerosols) provides a very stable irradiance regime and fits well to this purpose.

¹⁰ The *Langley Plot* is a logarithm of the output digital number (DN) plotted against the optical air mass between a range of 5 and 2 (between 3.5 and 2 for 340 nm), where the intercept is the calibration coefficient (zero air mass DN) and the slope is the OD.

The calibration uncertainty of such calibration is approximately 0.01 - 0.02 in AOD (wavelength dependent). The Version 2 Level 2 AERONET algorithm gives an uncertainty of 5% for AOD less than 0.2 (Holben et al., 2006).

Data from the eight Arctic AERONET stations have been used within this work. They are shown in Fig. 2.21.

In addition to the AERONET data, a time sequence of sun photometer AOT measurements performed at Ny Ålesund, Svalbard, 78.923° N, 11.923° E by the Alfred Wegener Institute for Polar and Marine Research in spring 2006 was utilized for the comparison of the dynamic behavior of the aerosol pollution event seen from ground and from satellite (see Sect. 5.2).

3 Developing the retrieval of tropospheric aerosol from satellite

The work described within this thesis is dedicated to the development of the AOT retrieval over snow surfaces using passive remote sensing means. This task can be subdivided into several consequent steps to be solved in order to establish a comprehensive retrieving routine which has satellite scene as input and provides the AOT values for each pixel of this scene as output. These steps are:

- satellite data reading and checking whether it corresponds to certain quality conditions;
- picking out snow covered areas suitable for the AOT retrieval and checking whether they are cloud free;
- performing the AOT retrieval (was carried out for 550nm and 3.7 μ m in this work) and providing the output AOT maps.

The theoretical basis behind these steps, details on implementation as well as sensitivity analysis are presented further in this section. The validation and application of cloud screening, snow flagging and AOT retrievals described in the current section can be found in the next sections.

3.1 Satellite data selection

As was already mentioned in Sect. 2.5.1, spectral radiances and brightness temperatures from AATSR product of level 1b are used within this work. For the AOT retrieval, we use cloud free, snow covered scenes with valid radiance and brightness temperature values in the both views at all of the used spectral channels. That implies elimination of night time data and occasional pixel exception values in the day time data. A restriction for the solar zenith angle (SZA) was applied to SZA less than 85°, in order to exclude observations with a very low position of the sun and therefore exclude observations with low signal to noise ratio. Then, once it is known that a pixel belongs to the clear-sky category, it can be used for further retrievals, in our case for the AOT retrieval over snow. The reason for this is the fact that in the visible and infrared spectral regions, clouds between the surface and the satellite sensor may affect the results of the AOT retrievals drastically, especially when a thin cloud is not distinguished from an aerosol layer or a thick bright cloud is mistaken for the snow surface due to their similar optical properties in the visible spectral range (see Fig 3.1). Therefore cloud screening over snow is a very important, yet challenging task. While single case studies and retrievals of AOT for small amounts of data allows manual cloud detection (Istomina et al., 2009), for an extensive processing amounts an automatic, yet reliable cloud screening routine is of great importance.

As was already mentioned in Sect. 2.5.1 and as was underlined in the AATSR FAQ (<http://envisat.esa.int/instruments/aatsr/faq>), existing AATSR operational cloud mask included in the level-1b product is optimized for use over ocean (Birks, 2007; Simpson et al., 2005; Závody et al., 2000) and its performance is often questionable over land and brighter surfaces. It therefore does not always provide necessary quality sufficient for AOT retrieval over snow and cannot be used in this work.

Another limitation on the incoming satellite data is the underlying surface of the scene. In our particular case, each pixel of the scene should feature sufficient ice and snow fraction as the AOT retrieval developed within this work was designed especially for these kinds of surfaces. Therefore, two major tasks have to be solved before any AOT retrievals are possible. These are the snow

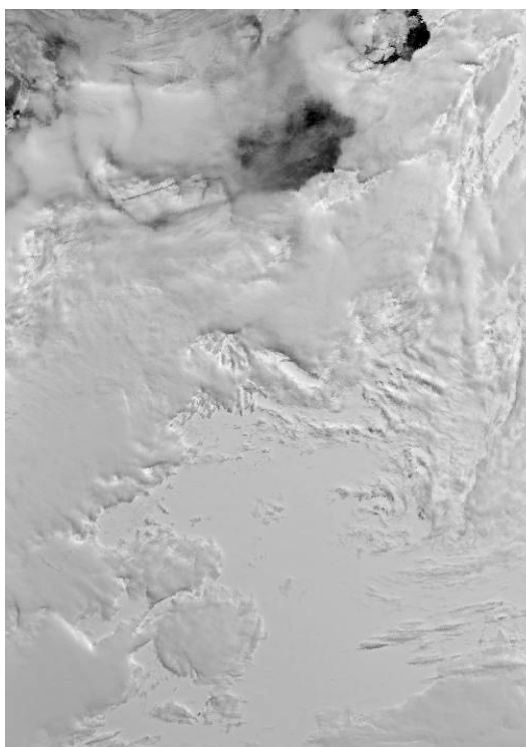


Figure 3.1 Clouds over snow at 550nm

/ice surface detection and cloud clearing of the scene. Within the current work, these tasks were united within one approach which utilizes a unique spectral signature of snow surfaces. In the next section, we present this so called snow flagging technique which was created especially for aerosol optical thickness retrieval in Arctic regions using the AATSR satellite sensor.

3.2 The snow flagging approach

Three basic approaches applicable to a radiometer data can be distinguished among the available cloud-screening algorithms:

1. Analysis of time-sequences of data, under the assumption that the short-term changes of the scene can be only introduced by clouds (e.g. Key and Barry, 1989; Diner et al., 1999; Lyapustin et al., 2008; Lyapustin and Wang, 2009; Gafurov and Bárdossy, 2009). Such an approach needs surfaces with a constant and pronounced structure (Lyapustin et al., 2008; Lyapustin and Wang, 2009). Their applications are limited over rapidly aging, changing surfaces or surfaces with poorly known BRDF (due to often varying observation-illumination geometries). The necessary time sequence of the data may not always be available (e.g. due to a narrow swath of the sensor).
2. Applying a reflectance or brightness temperature absolute threshold or their combination, e.g. ratio of reflectances in the form of NDVI. In this case only a few channels are used (e.g. Minnis et al., 2001; Bréon and Colzy, 1999; Lotz et al., 2009; Allen et al., 1990; Spangenberg et al., 2001; Trepte et al., 2001). The quality of the approach on the

global scale might vary due to the thresholds derived manually for a small set of testing scenes.

3. Spatial variability analysis (e.g. Martins et al, 2002). A great variety of available surface and cloud types allows the use of this approach only in the combination with the others.

Most of the cloud screening approaches are not focused on the case of the snow surface; however, several specific methods exist and utilize e.g. absolute (experimentally derived) thresholds in VIS, NIR and IR channels (Allen et al., 1990). This approach has problems with ice clouds over snow, especially thin ones (which is often the case in Arctic region). Sometimes a snow BRDF model is used to derive the threshold value for NIR spectral channel (Spangenberg et al., 2001; Trepte et al., 2001). This approach might have difficulties distinguishing cloudy condition from clean but polluted scene and therefore cannot be used within this work.

At the time of writing, the MODIS cloud detection scheme (Ackerman et al., 1998; Liu et al., 2004) is probably the most comprehensive among the cloud detection schemes available. This algorithm uses 19 out of 36 MODIS channels along with additional inputs, e.g. topography and illumination observation geometry for each 1-km pixel, land /water mask, ecosystem maps, and daily operational snow/ice products (taken from the NOAA and National snow and Ice Data Center). The resulting MODIS cloud mask contains 4 confidence levels (confident cloudy, uncertain, probably clear, confident clear). This algorithm has been validated against micropulse lidar and millimeter-wavelength cloud radar, and proved to be reliable. Therefore, the MODIS cloud mask product is used for validation of the developed AATSR snow flagging approach.

Our simple snow flagging approach is based on the analysis of the spectral shape of the TOA reflectance of a scene and does not require time sequences of data or absolute thresholds for reflectances or brightness temperatures. This approach has been designed to pick out cloud free snow covered regions, which serve as an input for AOT retrieval over snow. We did not pursue the task of recognizing different types of surface and clouds. The product of presented cloud screening method consists of two values: „applicable for AOT retrieval over snow or determination of snow reflection (clear snow flag = true)“ and „not applicable for AOT retrieval or determination of snow reflection (clear snow flag = false, i.e. clouds, land, ocean, etc.)“.

3.2.1 Theoretical basis of spectral cloud screening over snow

No other surface type presented in the satellite imagery has the unique features of bright reflecting, white snow surface. The task of snow detection therefore would be an easy one in the absence of clouds. However, optical properties of snow and clouds in the VIS are alike. The unique snow spectral signature (e.g. Warren, 1982) is to some extent also a feature of water and especially ice clouds (Kokhanovsky, 2006). The AATSR spectral coverage from VIS to NIR (AATSR channels 550nm, 660nm, 870nm, 1.6 μ m) enables detailed analysis of

the spectral behavior of the scene. For instance, the slightly different behavior of snow and clouds can already be seen in the TOA reflectance maps of an AATSR scene (Fig. 3.2). A combination of information from these channels may be utilized to discriminate snow and clouds despite of their similarities; these VIS-NIR channels can also be successfully used for “whiteness” test to discriminate snow and clouds from other surface types. Further discrimination can be done with the TIR channels (3.7 μ m, 10.8 μ m, 12 μ m), as the spectral shapes of snow and clouds differ there and present a good possibility for snow/cloud discrimination.

Possible snow impurities, snow grain size differences, and liquid water content create a variety of snow types that have different spectral behaviors (Warren, 1982). Some of these snow types under various atmospheric conditions are of frequent occurrence in the Arctic and should be taken into account while developing the cloud screening routine.

The following two subsections are dedicated to the description of our spectral snow flagging (VIS-NIR) and cloud screening criteria (TIR) along with the possible disturbance factors which had been taken into account.

3.2.2 Snow flagging in VIS and NIR: disturbance from aerosols, trace gases and physical parameters of snow

The VIS and NIR channels of the AATSR can be used to perform the “whiteness” tests at the 550nm, 660nm and 870nm wavelengths, and the “ice crystal NIR drop” test at the 1.6 μ m. Aerosol load of the scene will of course affect its spectral behavior; a forward RT modeling for the four mentioned VIS and NIR AATSR channels was performed to study the possible scatter introduced by aerosols. The forward RT model SCIATRAN developed at the University of Bremen (Roazanov et al., 2005) has been used for this purpose. The AOT range for the modeling was chosen to be from 0.0 to 3.0 at 550nm (the typical background AOT in the Arctic is as small as 0.05 (Tomasi et al., 2007) and can reach 0.5 during the Arctic haze events). We took the aerosol phase function measured for 550nm during the Arctic haze event on 23.03.2000, at Spitsbergen, Ny Ålesund, Svalbard, 78.923° N 11.923° E, by the Alfred Wegener Institute for Polar and Marine Research (see Fig. 3.3). Its smooth shape without significant forward backscattering (compare to the phase function of maritime aerosol in Fig. 3.3) is the characteristic of randomly shaped small absorbing particles.

The simulations have been performed for a lambertian snow surface with a spectral dependent albedo (data by R. Guzzi, IMG, CNR, Italy, Bologna, albedo equals 0.943 at 550nm). The following illumination-observation geometries have been used: the viewing zenith angle equal to 0°, solar zenith angle equal to 60°, and the relative azimuth angle equal to 0°, which represents realistic conditions of the AATSR overflight in the Arctic region. According to Mendonca et al. (1981), the single scattering albedo of Arctic haze appears to be rather high, larger than 0.9. Delene and Ogren (2002) reported the SSA of haze at Barrow, Alaska, to be 0.94. In the simulation, we assume the SSA of the aerosol equal to 1.0. The

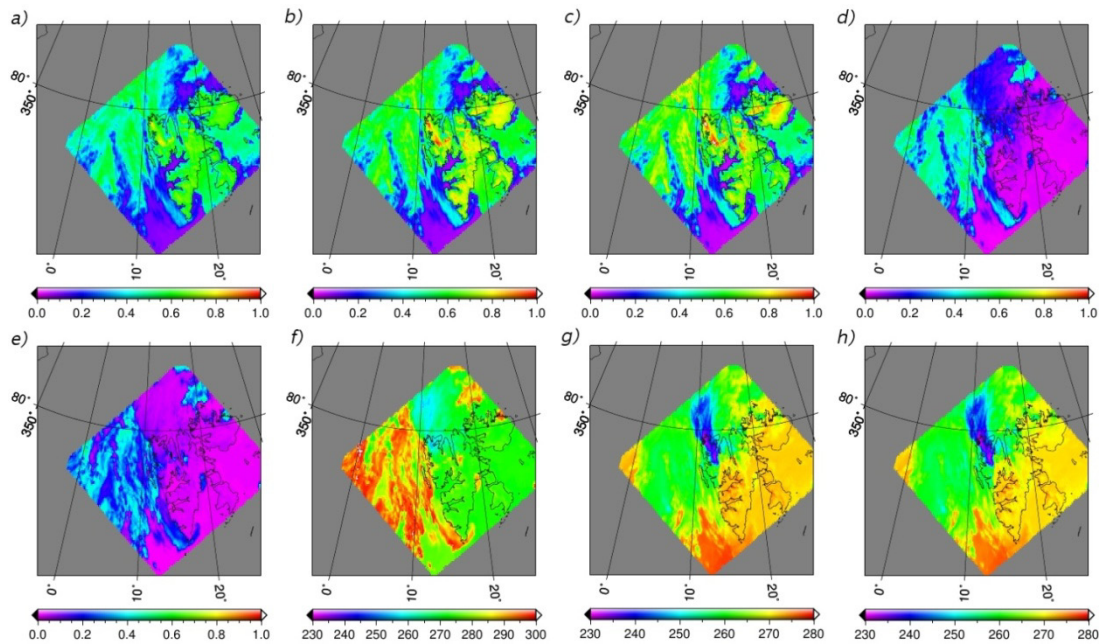


Figure 3.2. AATSR scene for 3rd of May 2006, Spitsbergen, reflectance at 550nm (a), 660nm (b), 865nm (c), 1600nm (d), 3700nm (e). Brightness temperature for 3.7 (f), 10.8 (g) and 12 μm (h).

aerosol is confined to the troposphere and assumed to be uniformly distributed in a 3km layer above the surface.

Fig. 3.4a shows the result of our simulation for the discussed surface and an aerosol load from 0 to 3.0 (step 0.2). Fig. 3.4b is the same as Fig. 3.4a, but with included Rayleigh scattering and O_3 absorption.

It can be seen that the shape of the spectral curve does not depend on AOT for channels 550nm, 660nm, 870nm in the “ideal” case (Fig. 3.4a) as well as in the “real” case with Rayleigh scattering and ozone absorption included. The inclusion of the ozone absorption and Rayleigh scattering results in a slight decrease of TOA reflectance at the 550nm channel.

As can be seen from Fig. 3.4, over such a bright surface increasing aerosol load would cause darkening of the scene at 550nm, 660nm and 870nm for the given geometry, due to aerosol layer redirecting the light scattered from the surface and decreasing upward flux at the TOA. This, however, does not affect the relation between the discussed channels. Channel 1.6 μm reacts to an increase of AOT with an increase of the TOA reflectance due to low snow albedo at this channel. It is important to note that these effects are only valid for the discussed geometry and a very bright surface (Kokhanovsky et al., 2010).

Rayleigh scattering and ozone absorption affect the shape of the spectrum, bringing the TOA reflectance in 550nm channel down by about 10% in comparison to the “ideal” case. The shape of the spectral curve is also affected in the 1.6 μm channel, where the TOA reflectance grows by more than 50% with the increase of the aerosol load until AOT equals 3. Therefore the spectral shape criterion used for the snow flagging should allow some scatter to account for the atmospheric effect.

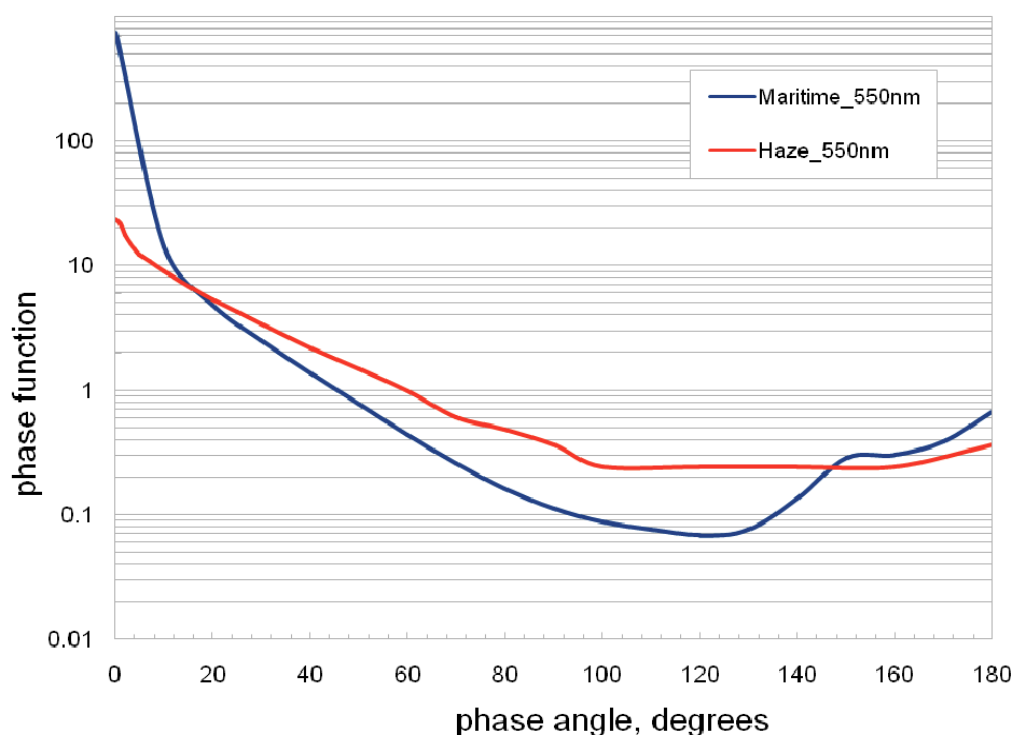


Figure 3.3. Phase function of Arctic haze aerosol used in the simulation of aerosol effect on the spectral shape of snow surface. See text for details.

The other factors which can disturb the shape of the spectral curve stem from the physical parameters of snow and not from the atmosphere above it. They are snow grain size, liquid water content and possible impurities of the snowpack, which can be soot, dust, or atmospheric aerosols fallen out on the snow surface. All these factors have been studied and are presented in literature aimed at both modeling and measurements of snow optical properties.

The effect of dust and soot impurities in snow has been studied by Warren and Wiscombe (1980). It is shown that the VIS spectral region is particularly sensitive to these impurities, whereas NIR and longwave emissivity of snow are not affected. The distortion of snow spectral albedo depends on dust and soot concentration. For example, 10ppmw of soot can decrease the albedo of snow by more than 50% in VIS for an extremely large snow grain size of 1000 μm (Warren and Wiscombe, 1980).

However, this effect is smaller for smaller grains and Arctic snow is believed to have a soot concentration of around 0.2ppmw, which reduces the snow albedo by approximately 20% in the 550nm and 660nm channels. For 870nm, this effect is already less than 10%. Similar effects take place in case of dust impurities: depending on snow grain size, extremely high dust concentrations can reduce the VIS albedo of snow drastically, but dust concentrations of 10 ppmw decrease snow albedo by less than 10% in VIS, for both small and large grain sizes. Aoki et al. (2000) modeled snow spectral albedo for several combinations of physical parameters such as snow density, impurities concentration, snow grain size and snow depth. These spectra differ from the pure snow spectrum only in the shortwave region, and by no

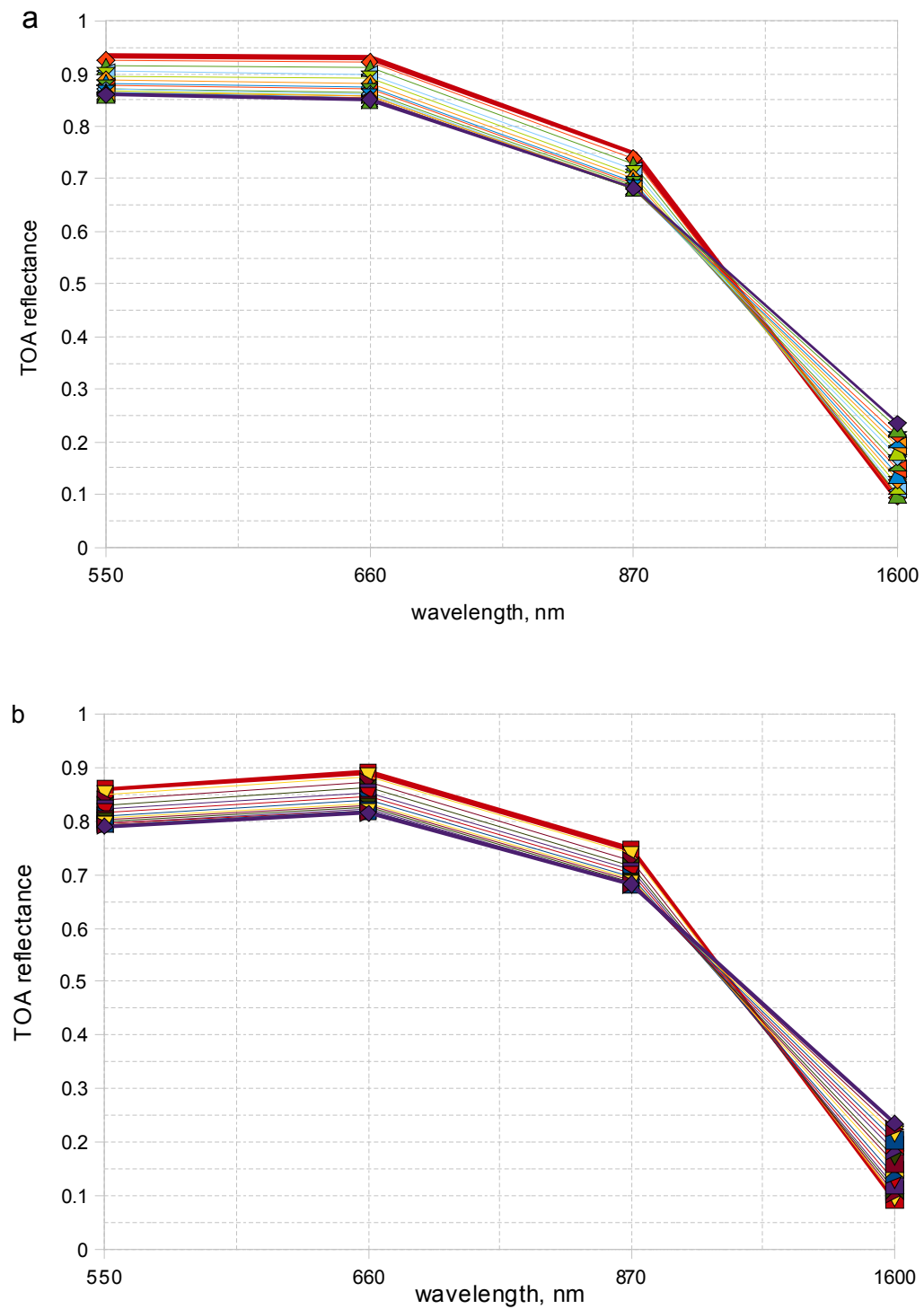


Figure 3.4. The sensitivity of TOA reflectance over snow surface to aerosol load, simulated with RT calculations, for Lambertian snow and aerosol only (a) and for snow, aerosol and O₃ absorption (b). AOT changes from 0 to 3, with the step 0.2. AOT = 0 is shown with the thick red line. AOT = 3.0 is shown with the thick violet line.

more than 10%, which proves that earlier discussed scatter values caused by soot and dust are sufficient for our task. The effect of snow age on the snow spectrum was studied by Domine et al. (2006). The comparison of wind crust, fresh snow and depth hoar spectra show that these spectra are quite similar to each other in the visible, but differ more in the IR. The 1.6 μm channel reacts on the snow aging with the albedo decrease, sometimes almost to zero. However, this effect does not destroy the main feature of snow spectral signature – the spectacular drop of albedo from 0.87 μm to 1.6 μm . Liquid water content, however, decreases the snow albedo also in the VIS and NIR (Gerland et al., 1999), but it does not change the spectral shape in the channels of AATSR and the relation between all the discussed VIS and NIR channels remains the same (Warren, 1982).

The effect of snow grain size on the snow spectrum is studied by e.g. Domine et al. (2008), Wiscombe and Warren (1980), and Tedesco and Kokhanovsky (2007). The snow spectrum is affected by the grain size mostly in NIR and only a bit in VIS. Snow albedo in the 550nm and 660nm channels is affected only by a few percent, at 870nm it goes up by around 10% for smaller grains and 10% down for larger grains. The snow albedo in the 1.6 μm channel increases for smaller grains up to 0.2 and drops down to almost zero for large grains, which is similar to the behavior of the albedo in the 870nm channel. This means that the relation between these two channels remains the same and the shape of the snow spectrum is not affected. All the above discussed effects are well presented in the literature and need not be illustrated separately here. To get the visual impression on the discussed effects, the reader is referred to the mentioned literature sources. As a comprehensive review of the various disturbance factors which affect snow spectral shape, the set of field measurements carried out by Negi et al. (2010) is recommended. This work presents measured snow spectral reflectance depending on various pollutants, liquid water content, grain size, observation-illumination geometry, age, depth and is of immense importance for getting an impression on the snow spectral behavior in different conditions.

All the discussed disturbance factors (aerosol load, Rayleigh scattering, ozone, soot and dust impurities, age and liquid water content, and snow grain size) affect the spectrum of the cloud free snow covered scene in different wavelength regions. The performed literature study and RT simulations made it possible to develop dynamic thresholds to evaluate the spectral shape of a pixel for snow signature in the VIS and NIR channels of AATSR. It is schematically shown in Fig. 3.5 for two the example spectra. They are the fresh snow spectrum (from the ASTER spectral library, CalTech, 2008), represented with the blue curve and the dry long grass spectrum (from the USGC Spectroscopy Lab library), represented with the black curve. Filled areas (violet for fresh snow and turquoise for dry long grass) show allowed freedom in the shape of each spectrum. As the criterion is relative, the allowed scatter will change from spectrum to spectrum. For our snow flagging routine, we only need to analyze the shape of a spectrum in four VIS and NIR AATSR channels. These channels are shown in Fig. 3.5 by vertical lines. However, for the sake of clarity we extended the graphic representation of the shape criteria outside of the four discussed channels. The numerical criteria only exist for the four discussed channels and should connect the TOA reflectances $\rho_{TOA}(\lambda)$ of those channels in the following way:

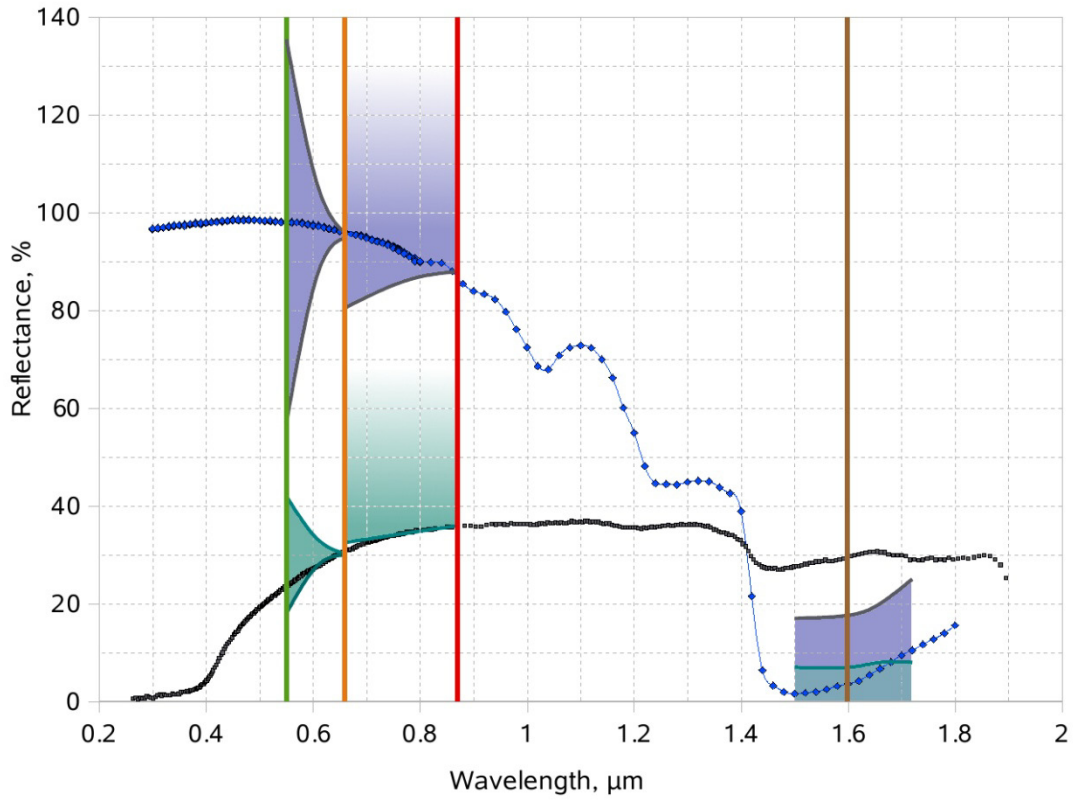


Figure 3.5. The allowed amount of TOA reflectance scatter is shown for fresh dry snow (blue curve) and dry long grass (black curve). Violet and turquoise areas are the schematic view of the spectral shape criterion. They show where the corresponding spectral curve should go to be still recognized as snow. It is visible that dry long grass spectrum does not satisfy the spectral shape criterion, e.g. at channel $1.6\mu\text{m}$.

$$\frac{\rho_{TOA}(0.87\mu\text{m}) - \rho_{TOA}(1.6\mu\text{m})}{\rho_{TOA}(0.87\mu\text{m})} > 80\% \quad (3.1)$$

$$\frac{\rho_{TOA}(0.87\mu\text{m}) - \rho_{TOA}(0.66\mu\text{m})}{\rho_{TOA}(0.87\mu\text{m})} < 10\% \quad (3.2)$$

$$\left| \frac{\rho_{TOA}(0.66\mu\text{m}) - \rho_{TOA}(0.55\mu\text{m})}{\rho_{TOA}(0.66\mu\text{m})} \right| < 40\% \quad (3.3)$$

Here the percentage is given for relative reflectance difference with the relation to $\rho_{TOA}(870\text{nm})$ for the first two criteria and to $\rho_{TOA}(660\text{nm})$ for the third one. From Fig. 3.5 it is visible that the fresh snow spectrum (blue curve) fits into our snow spectral shape criteria, whereas the spectrum of dry long grass does not. The $\rho_{TOA}(1.6\mu\text{m})$ of dry grass is too high and does not represent the main feature of a snow spectrum – the reflectance drop from 870nm to $1.6\mu\text{m}$. Also, the feature of vegetation spectra, the so called “red edge” (fast increase of reflectance at $0.4\text{-}0.7\mu\text{m}$), is visible in the figure and makes the $\rho_{TOA}(660\text{nm})$ be at the edge of the snow spectral shape criteria.

The discussed criteria are already enough to screen out optically thick warm clouds, but will have difficulties with cirrus and any optically thin clouds, especially ice clouds, because these do not significantly disturb the spectral signature of snow in these spectral regions. To screen out such clouds, we need to use TIR channels of AATSR. This problem is discussed in the next subsection.

3.2.3 Cloud screening in TIR: snow emissivity and cloud reflectance

In the previous subsection the three dynamic thresholds are used to pick out white (Eq. 3.2, 3.3) pixels featuring the “ice crystal IR drop” (Eq. 3.1). These thresholds perform surface discrimination in the VIS and IR, screening out all the various surface types except for snow. The information in the four VIS and NIR channels is not enough for a comprehensive cloud screening, because ice clouds, e.g. cirrus, have exactly the same spectral signature as snow in these channels. To classify the atmospheric state (clear/cloudy) of the scene, TIR channels of the AATSR can be used.

The 3.7, 10.8 and 12 μm channels provide additional information to distinguish surface and clouds. As was mentioned by Spangenberg et al. (2001), BT of the 3.7 μm channel contains not only emitted radiation, but also radiation scattered by the object, in our case by a cloud or snow.

IR properties of snow have been briefly discussed in Section 2.2.1. Snow thermal properties have been measured (Hori et al., 2006; English et al., 1995) and show that snow is very close to a black body and emits according its physical temperature. The reflection of snow is very low in the 3.7, 10.8 and 12 μm channels (Wald, 1994). This is not the case for clouds, because $\rho_{TOA}(3.7\mu\text{m})$ of cloud droplets is much higher depending on the effective radii of the particles and on the optical thickness of the cloud. Therefore the spectral shape of a cloud scene in the three TIR channels will differ from that of snow due to the different physical nature of these two objects.

To estimate the amplitude of reflectance contamination of BT(3.7 μm), we calculate the $\rho_{TOA}(3.7\mu\text{m})$ according to Spangenberg et al. (2001):

$$\rho_{TOA}(3.7\mu\text{m}) = \frac{[\varepsilon_{3.7\mu\text{m}} \cdot B_{3.7\mu\text{m}}(T_3) - \varepsilon_{3.7\mu\text{m}} \cdot B_{3.7\mu\text{m}}(T_4)]}{[(\mu_0 \cdot S_{3.7\mu\text{m}}) - \varepsilon_{3.7\mu\text{m}} \cdot B_{3.7\mu\text{m}}(T_4)]} \quad (3.4)$$

where T_3 is the measured 3.7 μm brightness temperature, T_4 is the measured 11 μm brightness temperature, μ_0 is the cosine of solar zenith angle, $S_{3.7\mu\text{m}}$ is the solar constant at 3.7 μm ($3.47 \text{ Wm}^{-2}\mu\text{m}^{-1}$), $\varepsilon_{3.7\mu\text{m}}$ is the clear snow emittance, $B_{3.7\mu\text{m}}(\text{BT})$ is the Planck function at 3.7 μm for some temperature BT.

An example of calculated $\rho_{TOA}(3.7\mu\text{m})$ is presented in Fig. 3.2e. Clouds apparently reflect more than snow and ocean (see ocean-land mask contours). This reflectance pattern is present in the reflectance part of AATSR BT(3.7 μm) (Fig. 3.2f) and this is the reason for the differences in the shapes of the spectral curves of snow and clouds at 3.7, 10.8 and 12 μm . It

is visible that snow BT does not change much throughout the three TIR channels, which corresponds to, e.g. measurements of snow emissivity in MODIS USCB Emissivity Library (Zhang, 1999). Measured emissivity is quite stable throughout the thermal region of the spectrum (variation around 2%). Hori et al. (2006) show that emissivity of snow for a given temperature depends on its physical parameters such as grain size and liquid water content. However, these dependencies cause a variation of snow emissivity of less than 5%. This scatter of the spectral shape can be taken into account and is still much smaller than that caused by the high reflectance of clouds in the 3.7 μm channel.

Independently of the physical temperature of snow, the relative BT differences of the 3.7, 10.8 and 12 μm channels are not to be larger than 3% (see Eq. 3.5. and 3.6). These criteria will screen out water, ice or mixed phase clouds, no matter warm or cold. Both warm and cold clouds are present in the discussed scene; in Fig. 3.2f, the blue color corresponds to cold, and orange to warm clouds. BT of snow and ocean is similar in all three discussed channels within the allowed scatter.

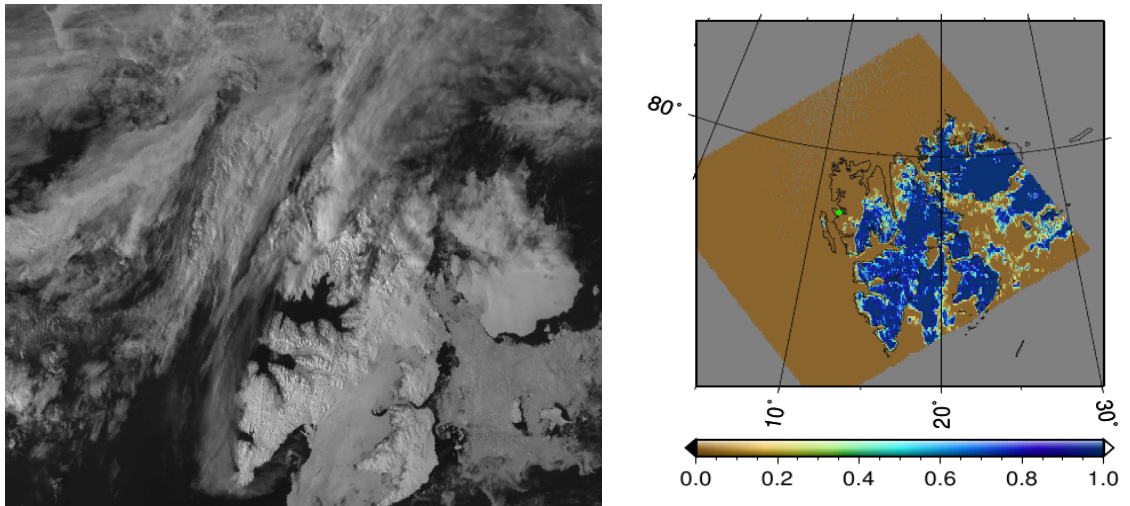


Fig. 3.6 The example of discussed cloud screening method: a) the initial AATSR scene, 3rd of May 2006, Spitsbergen, 550nm; b) the probability of clear atmosphere over snow – the result of the cloud screening over snow routine.

$$\left| \frac{BT(3.7\mu\text{m}) - BT(10.8\mu\text{m})}{BT(3.7\mu\text{m})} \right| < 3\% \quad (3.5)$$

$$\left| \frac{BT(3.7\mu\text{m}) - BT(12\mu\text{m})}{BT(3.7\mu\text{m})} \right| < 3\% \quad (3.6)$$

Combining all five dynamic thresholds connects reflectances and brightness temperatures in seven AATSR channels into a flexible, physically meaningful criterion to recognize the spectral signature of snow if it is present in the scene. The result of the developed snow detection method with all the suggested thresholds applied is shown in Fig. 3.6 (unscreened scene in all the 7 AATSR channels is shown in Fig. 3.2).

3.2.4 Sensitivity study

In order to study the role of various thresholds in the resulting performance of the method, we picked out two scenes over Alaska and Greenland featuring complicated cloud fields over snow surfaces and considered several combinations of the thresholds to be checked out. The false color composites of these scenes and the final snow flag product are shown in Fig. 3.7 and 3.8. The MODIS cloud product and the operational AATSR L1b cloud mask are also shown for comparison.

The amplitude of the “ice crystal IR drop” (Eq. 3.1) varies in different conditions; the current threshold value is set to be wide enough to allow most of the snow types be recognized as snow at the global scale. This relative threshold therefore has physical meaning, as opposed to manually set thresholds often appearing in cloud screening approaches.

In order to study the distribution of this dynamic threshold for cloudy fields and assess the possibility of confusing snow and thin cloud over snow using only NIR and VIS tests, we have set the shape criteria in a way to get the “white” (true values of Eq. 3.2 and 3.3), but “not cloud free” (false values of Eq. 3.5 and 3.6) scenes. The resulting distribution of the value at the right hand side of Eq. 3.1 would be able to show where the VIS and NIR thresholds together (the “snow flagging” criterion) are able to screen out clouds over snow and where not. Such distributions are plotted in Fig. 3.9 for the two cloudy fields over snow at Alaska (left panel, corresponds to Fig. 3.7) and Greenland (right panel, corresponds to Fig. 3.8). Here zero values mean “cloud free” as achieved with the TIR criteria only; all the other values of the relative difference in Eq. 3.1 indicate how spectacular the “ice crystal IR drop”

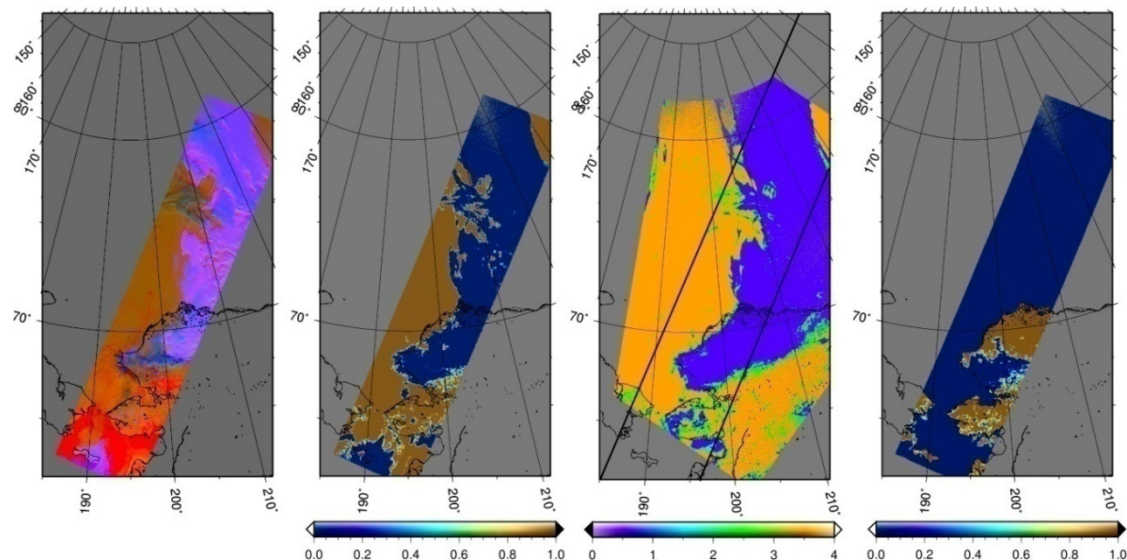


Figure 3.7. Alaska, AATSR: 30 April 2006, 22h17'44", orbit number 21783. MODIS: 30 April 2006, 22h05'. Left panel is the false color composite (red is $11\mu\text{m}$ BT, green is 550nm reflectance, blue is $1.6\mu\text{m}$ reflectance) of initial AATSR scene; second left panel is the clear snow mask of AATSR scene (0 – not snow, 1 – clear snow) achieved with presented method; third left panel is MODIS cloud mask: 1 – cloudy, 2 – probably cloudy, 3 – probably clear, 4 – clear; right panel is operational AATSR cloud mask from level-1b product: 0 – cloudy, 1- clear.

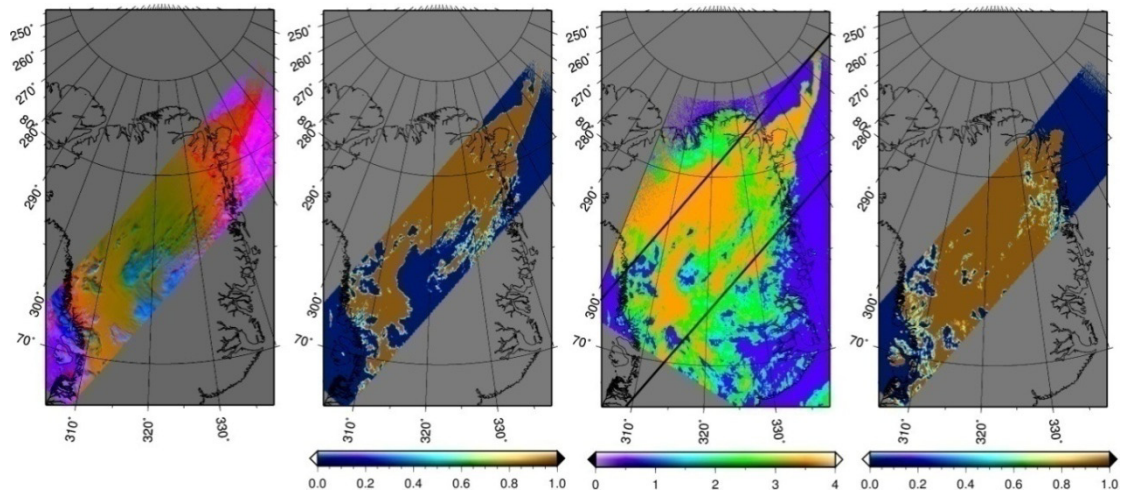


Figure 3.8. Greenland. AATSR: 4 May 2005, 15h07'47", orbit number 21836, MODIS: 4 May 2005, 15h00'. Left panel is the false color composite (red is $11\mu\text{m}$ BT, green is 550nm reflectance, blue is $1.6\mu\text{m}$ reflectance) of initial AATSR scene; second left panel is the clear snow mask of AATSR scene (0 – not snow, 1 – clear snow) achieved with presented method; third left panel is MODIS cloud mask: 1 – cloudy, 2 – probably cloudy, 3 – probably clear, 4 – clear; right panel is operational AATSR cloud mask from level-1b product: 0 – cloudy, 1- clear.

between the 870nm and $1.6\mu\text{m}$ is. According to our literature study and RT modeling, to accommodate most of the possible snow types including some reasonable atmospheric pollution, the relative difference between the two channels has to be not less than 80%.

Fig. 3.9 shows thick clouds with the values of this relative difference of less than 0.8. Such clouds would already be screened out without the TIR check. However, thinner clouds over snow that are semitransparent or ice clouds feature values of the drop between the 870nm and $1.6\mu\text{m}$ greater than 0.8 (which is snow-like). These clouds are shown with arrows in Fig. 3.9. They would not be screened out by the NIR and VIS check, but they are detected by the TIR check.

To see which clouds are screened out with the TIR black body check in more detail, we have set the following dynamic threshold combinations for the two studied scenes: for “white” surface (true values of Eq. 3.2 and 3.3) featuring snow-like values of the “ice crystal IR drop” (true value of Eq. 3.1) we plot the distribution of the right hand side value of the TIR relative difference (Eq. 3.5). The result is shown in Fig.3.10. Zero values in the figure indicate false values of the “whiteness” check or the “ice crystal IR drop” check. Positive values in the plots indicate how large the relative difference between $3.7\mu\text{m}$ and $11\mu\text{m}$ is. The threshold value derived from the study of snow IR properties is 0.03 (Eq. 3.5), with all greater values indicating a non black body (a cloud, or e.g. some certain surface types like bare soil or desert; they are not represented in this case). The poor suitability of the NIR and VIS checks for cloud screening (as opposed to surface classification, snow flagging in this case) is apparent; most of the cold clouds present in the both scenes are only detected with the TIR check. This simple yet effective cloud screening approach highlights one of many benefits of the TIR channels which should be considered when building satellite sensors.

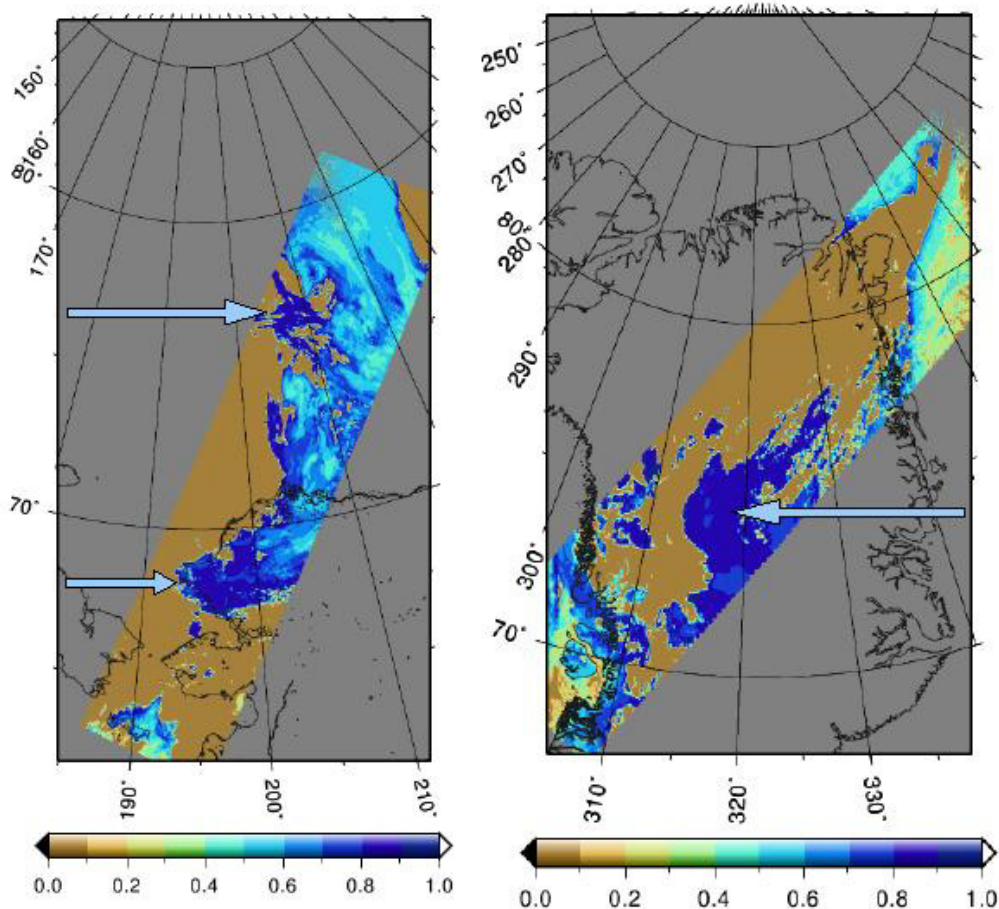


Figure 3.9. Distribution of the “ice crystal IR drop” (Eq. 3.1) between the 870nm and 1.6 μ m for Alaska (left panel, see also Fig. 3.7) and Canada (right panel, see also Fig. 3.8). Zero value is “cloud free black body” according to the TIR check. Positive values show how large the IR drop is (the threshold value is 0.8). Arrows show thin cold clouds featuring snow-like behavior at the 870nm and 1.6 μ m (relative difference greater than 0.8). They would not be recognized by the NIR and VIS check alone without the TIR check.

In case of absence of the TIR channels, cloud screening over snow becomes a tremendous task. The ice crystal IR drop (Eq. 3.1) should then be exploited as the main and the only criterion used for cloud detection, with all the other VIS wavelengths serving for the surface discrimination. In this case, the amplitude of the snow reflectance drop between the 870nm and 1.6 μ m designed to accommodate most of the snow types on the global scale will be too wide to screen out semi-transparent or ice clouds, which are of frequent occurrence in the Arctic. This is the reason why thresholds manually derived with the help of only a few scenes tend to be too strict with the risk of discarding many cloud free snow pixels (Krijger et al, 2005). To illustrate the idea about the influence of the Eq. 3.1 on the performance of the VIS-NIR checks, we plotted a ratio of cloud free pixels amounts achieved with TIR check only (Eq. 3.5, 3.6) to the amount of cloud free pixels achieved with the VIS/NIR check (Eq. 3.1, 3.2, 3.3) for the Alaska overflight (Fig. 3.7). The result is shown in Fig. 3.11. It is visible that for the given scene the amount of the „cloud free“ pixels according to these two different tests is equal when the threshold value is around 0.88. Fig. 3.12 illustrates the cloud mask patterns achieved with the restricted VIS/NIR check (left panel) and the initial TIR check

only in the right panel (compare to the TIR and VIS/NIR checks applied together in Fig. 3.7). Though the patterns are fairly similar, the performance of the TIR test is evidently better in the regions of thin clouds. Arrows show the open ocean area, which is screened out by the VIS/NIR test, but not screened out by the TIR check. This is due to the open ocean being a black body as well as snow, which means that the TIR checks can also be used for cloud detection over ocean.

As Negi et al. (2010) showed, snow spectral reflectance among other factors depends on the illumination-observation geometry. It is therefore important to understand that all the discussed snow spectral effects have been studied with respect to snow spherical albedo or snow nadir reflectance. We assume these effects to produce comparable changes to the snow spectral behavior for all the illumination-observation geometries in the VIS and NIR wavelengths and widen the VIS and NIR relative thresholds respectively. This approach is justified within suggested separation of the AATSR wavelengths, when VIS/NIR channels are used for surface discrimination and TIR channels are used for cloud detection. As the sensitivity study above illustrates, such separation gives good results for the case when the TIR channels are available. However, cloud detection algorithms which are lacking of the TIR channels and tend to restrict the NIR threshold, are at risk of incorrect screening out of cloud free snow pixels due to illumination-observation geometry changes combined with the snow grain size changes or snow contamination effects.

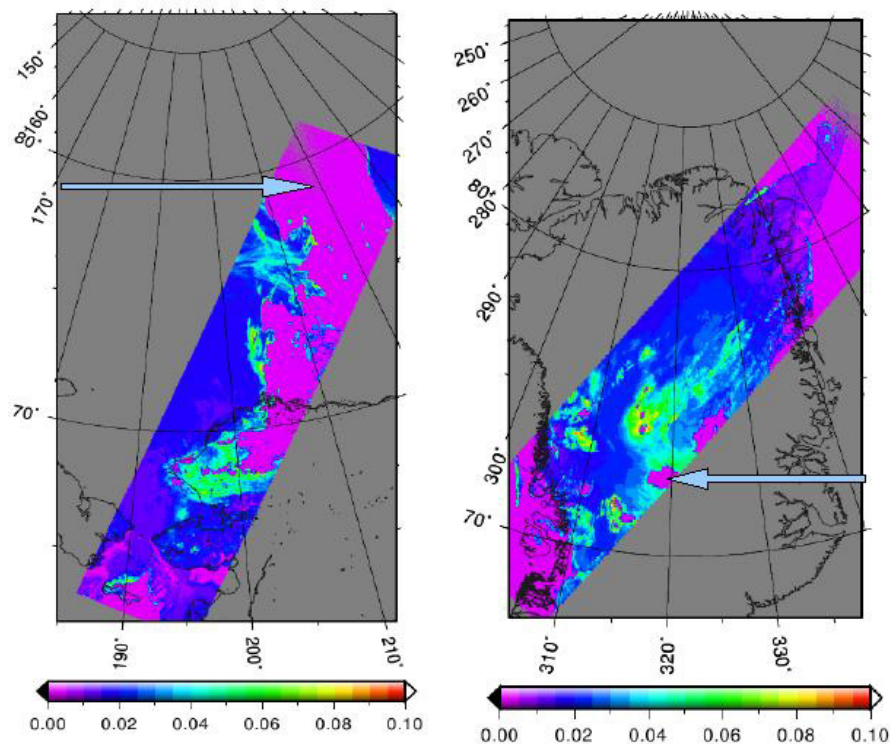


Figure 3.10. Distribution of the $3.7\mu\text{m} - 11\mu\text{m}$ relative difference for true values of VIS and NIR checks (Eq. 3.1, 3.2, 3.3). Zero values indicate false values of the NIR or VIS tests, i.e. the scene is not “white” or not featuring snow-like reflectance drop between the 870nm and 1.6μm. Thick clouds (shown by arrows) are screened out by Eq. 3.1. Zero values indicate the possible performance of the algorithm in the presence of VIS and NIR tests only. As all the cold thin clouds are screened out with the TIR check, such a performance would be insufficient for AOT retrievals over snow.

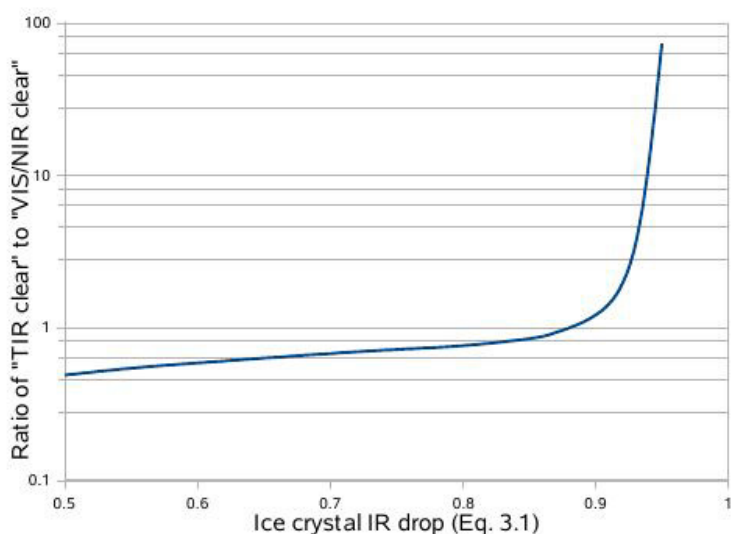


Fig. 3.11. The ratio of cloud free pixel number achieved with the TIR check only (Eq. 3.5, 3.6) to the amount of cloud free pixels achieved with the VIS/NIR check (Eq. 3.1, 3.2, 3.3) for the Alaska overflight (Fig. 3.7). The amount of cloud free pixels detected with each of the tests is equal for the magnitude of the ice crystal IR drop = 0.88. Though this magnitude of the threshold will be effective for the given scene (and for similar scenes featuring rather clean fresh snow), it will be less effective on the global scale, where more various snow types are present.

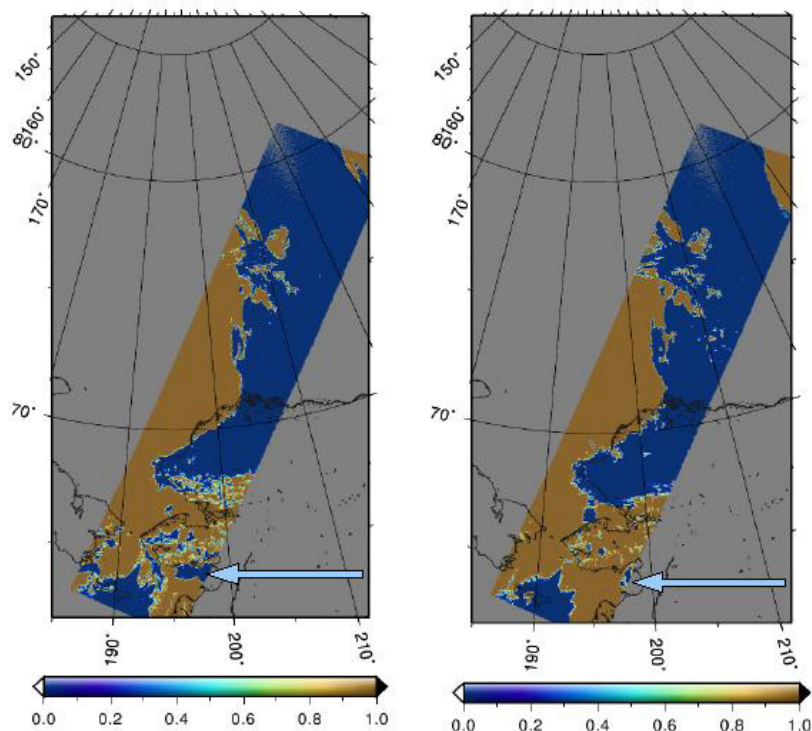


Fig. 3.12 Comparison of the TIR and VIS/NIR parts of the algorithm applied separately to the scene over Alaska. Left panel: only VIS/NIR check with manually derived magnitude of the NIR threshold (Eq. 3.1) equal to 0.88 and initial values of VIS thresholds (Eq. 3.2, 3.3). Right panel: only TIR check. Arrows show cloud free ocean, which is screened out by VIS/NIR snow flag and not screened out by TIR cloud flag, as expected.

The above discussed dynamic thresholds sensitivity studies do not substitute the validation of the algorithm; a comprehensive validation of our snow flagging algorithm in its final form (Eq. 3.1 – 3.3, 3.5, 3.6) against Micro Pulse Lidar data and further comparison to the MODIS cloud product are presented in Section 4.1.

3.3 AOT retrieval in the visible range of spectrum

Among aerosol retrievals over different surfaces in the visible spectral range, the ratio “aerosol to surface signal” at the TOA is the smallest for snow covered scenes (as compared to open water, vegetation, bare soil, desert, and other surface types). This is due to very high snow spectral albedo in the visible spectral region and usually low aerosol load in the Arctic. From ground-based observations of AOT in the Arctic we know that a typical value of AOT is below 0.1 in clear conditions. So, the measured TOA signal consists mostly of the surface reflectance. In these conditions, even minor error in assumed snow BRDF will cause a great error in the retrieved amount of aerosol. However, the amount of information available about the underlying surface is usually very low due to great spatial and temporal variability of snow reflective properties. Therefore the AOT retrieval over snow from satellite is an difficult task, with an unknown amount of aerosol present in the scene combined to the unknown reflectance of the underlying surface. Conventional single-view aerosol retrieval algorithms (e.g. Dinter et al., 2009; Remer et al., 2005; Levy et al., 2003; Levy et al., 2010; Kaufman et al., 1997) need to retrieve both quantities simultaneously or assume the surface optical properties in order to retrieve the AOT, creating therefore an unknown inaccuracy in the retrieved product. Such an approach would probably work for surfaces with stable temporal and spatial properties (e.g. for the clear ocean surface), which is not the case of snow surface.

The mentioned above spatial and temporal variability of snow directional reflectance comes from many physical factors that affect snow optical properties. The BRDF structure of snow is much too far from Lambertian surface, with the assumption of snow to be a Lambertian surface is only reasonable in case of fresh fallen snow (Winther, 1994). There are a lot of attempts to measure or model snow BRDF, see e.g. (Peltoniemi et al., 2005; Winther, 1994; Peltoniemi, 2007; Li and Zhou, 2004; Leroux et al., 1998b; Hudson et al., 2006; Winther et al., 1999; Kokhanovsky et al., 2005a; Negi et al., 2010; Aoki et al., 2000), and it is clear that the reflective properties of snow are very sensitive and react rapidly on many parameters of the environment. In other words, there are a lot of types of snow possible.

In order to get more information about the angular properties of the underlying surface, it is possible to utilize the TOA reflectance measured over the same scene but in two different directions. The AATSR sensor was chosen for this work for to this very reason – it performs dual-view observations. Within this scheme, the scene is observed twice – first time in the so-called forward view with the observation zenith angle around 55°, and then, after approximately 150 seconds, comes the nadir view with the observation zenith angle around 0°. This observational scheme gives the possibility to retrieve AOT with minor assumptions about the surface BRDF.

The aerosol retrievals developed for this sensor and its precursors (North, 2002; Veefkind et al., 1998; Curier et al., 2009; Sogacheva et al., 2009) cannot be used for the case of snow surfaces for a number of reasons, mostly due to poor applicability of used assumptions to the case of snow surface. For example, the assumption about surface directional reflectance having the same shape at 1.6 μ m and 550nm used by (Curier et al., 2009) is not valid for snow surface (Peltoniemi et al., 2005, Kokhanovsky et al., 2005a; Negi et al., 2010). Therefore a new AOT retrieval algorithm had to be developed for snow and ice surfaces. The algorithm utilizes the solution of the RTE for the system “surface and atmosphere” written in an approximated form for the forward and nadir views and then divided one by another in order to only account for the asymmetry of the TOA reflectance and not for its magnitude; this approach reduces the role of unknown snow spectral albedo in the retrieval. The surface BRDF shape is also used as a ratio of forward and nadir surface reflectances; this ratio is approximated with the corresponding ratio of the TOA forward and nadir reflectances under the assumption that the atmosphere is causing only minor asymmetry between the forward and nadir views as compared to the surface BRDF shape. The atmospheric role was evaluated using the look-up table approach for a single aerosol type “Arctic haze”, which represents aerosol appearing during regular spring haze events in the Arctic. The following subsections describe the basic surface and aerosol properties to be considered while AOT retrieval over snow in the visible spectral range, theoretical basis of the retrieval, sensitivity study of the retrieval to various assumptions, calculation of the look-up tables, and limitations. The validation and application studies will be given in the next sections. The AOT retrieval over snow and ice in the visible is designed for any wavelength where snow spectral reflectance is large enough (e.g. 550nm, 660nm, 870nm of AATSR). Its performance is demonstrated for 550nm in the current work.

3.3.1 Optical properties of aerosol and snow in the visible

Section 2.2.1 gives an overview of general snow optical properties; here we will only present snow and aerosol optical properties relevant for the AOT retrieval at 550nm.

Snow can be described as highly reflective non-Lambertian surface; in the current study, we use two ways to represent this kind of surface:

- 1) a parameterization of field snow BRDF measurements (Degünther and Meerkötter, 2000). The BRDF of this surface for the two solar zenith angles (45° and 65°) is shown in Fig. 1. A slight backscattering peak and a stronger forward scattering peak are visible, making the asymmetry of this function largest in the principal plane. However, the asymmetry in the direction perpendicular to the principal plane is not so high. This feature of snow BRDF tends to be rather common for most types of snow.
- 2) a semianalytical model of a medium consisting of fractal grains (Kokhanovsky et al., 2005a). The snow reflectance resulting modeled in this way was compared to the results of field measurements of snow surface BRDF and showed good comparison to each other.

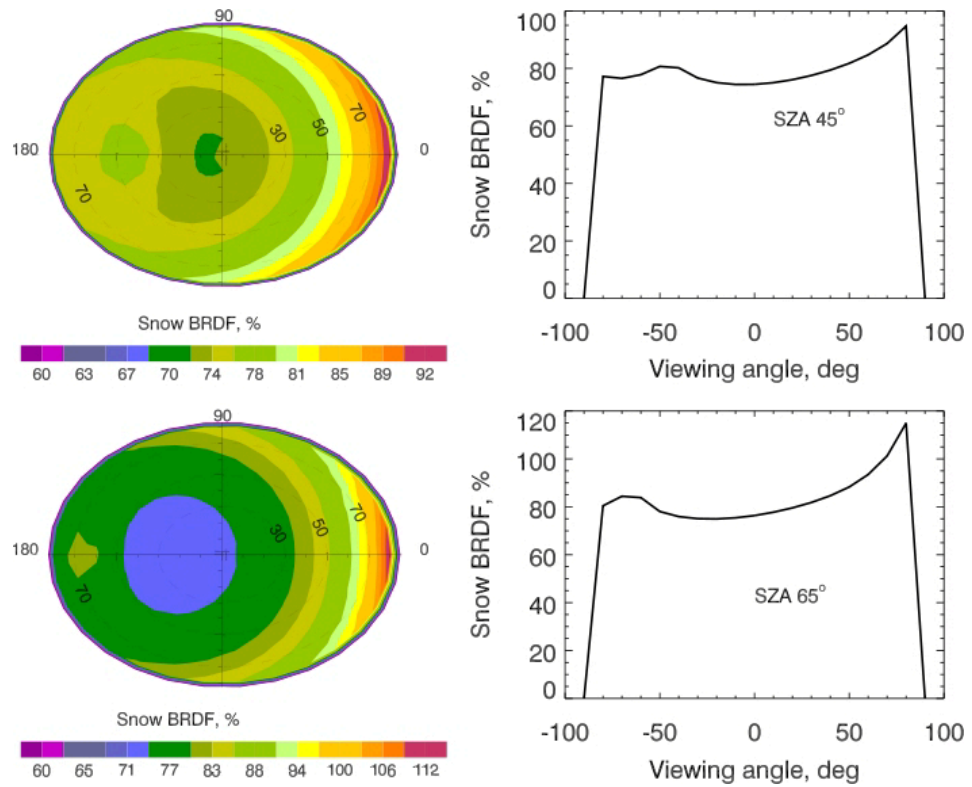


Fig. 3.13. Modeled snow BRDF from (Degünther and Meerkötter, 2000) for two sun zenith angles, 45° (upper left figure, principal plane cut in the upper right figure) and 65° (lower left figure, principal plane cut in the lower right figure). Note the strong forward scattering peak and rather Lambertian behavior around nadir observation geometries across the principal plane.

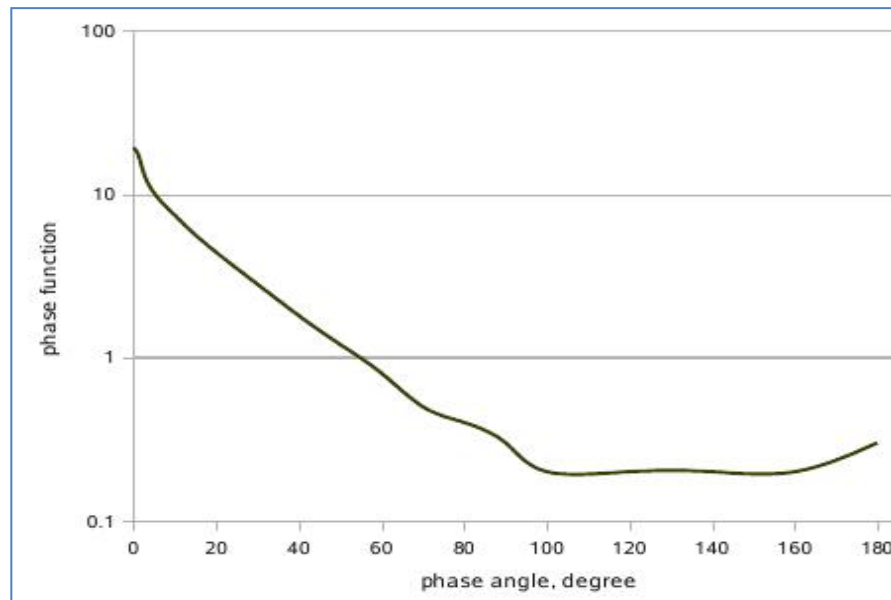


Fig. 3.14. Measured aerosol phase function of Arctic haze which was used for the accuracy study of Eq. 3.8 and 3.12, see text for details.

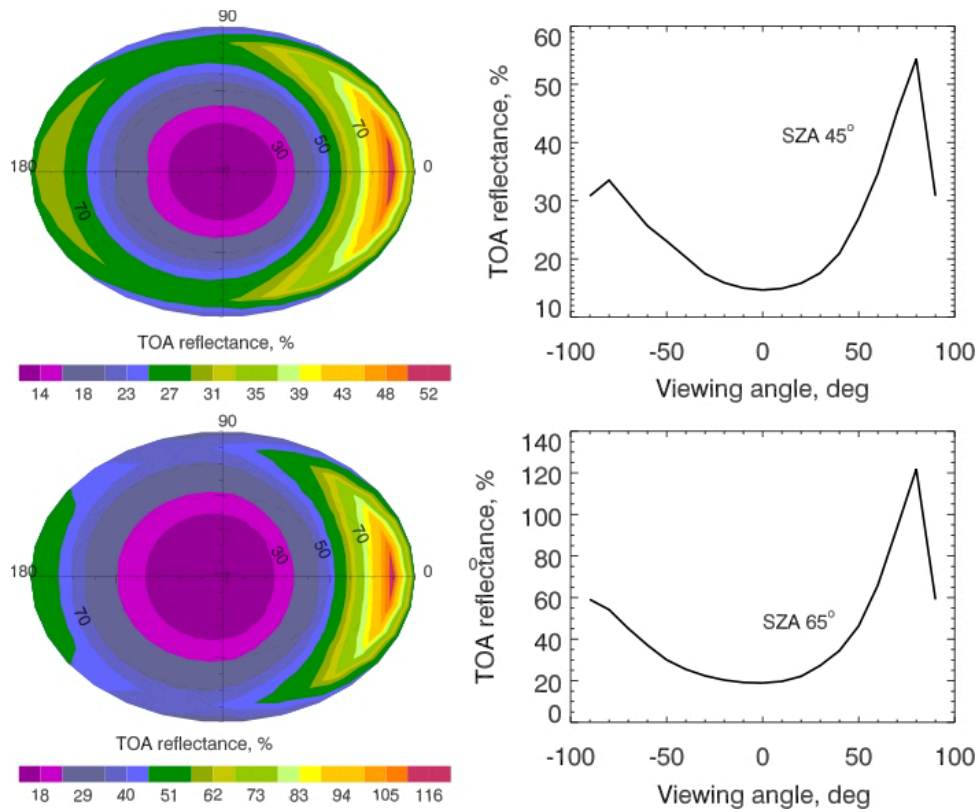


Fig. 3.15. Calculated top of atmosphere reflectance of an aerosol layer with the AOT=1.0, shown for solar zenith angles equal to 45° (upper row) and 65° (lower row). The phase function used in the RT simulation is shown in Fig. 3.14. Note the absence of backscattering effects and a much deeper reflectance drop around the nadir observation geometries.

The aerosol phase function, which has been used for the calculation of $\rho_{atm}(\lambda, \mu_0, \mu, \varphi)$, was measured for 550nm during Arctic haze event on 23rd of March 2000, and Spitsbergen, Ny Ålesund, Svalbard, 78°55'00" N, 11°56'00"E, by the Alfred Wegener Institute of Polar and Marine Research. It is shown in Fig. 3.14.

The top of atmosphere reflectance of such an aerosol load confined to the troposphere within 3 km above the surface is shown in Fig. 3.15.

3.3.2 Theoretical basis

The AOT retrieval in the visible part of spectrum is based on extracting the aerosol effect from the measured TOA reflectance and comparing it to one of the separately computed lookup tables (LUT). In order to utilize LUT approach to make the inversion and retrieve AOT, we need to express the measured top of atmosphere radiances analytically. As before, let us use reflectances ρ rather than radiances I:

$$\rho = \frac{\pi I}{\mu_0 f} \tag{3.7}$$

where f is the solar flux at the top of the atmosphere, and $\theta_0 = \arccos \mu_0$ is the solar zenith angle.

Assuming that the atmosphere and aerosol load are horizontally uniform and have a total optical thickness τ , and underlying surface is Lambertian, one can write the well-known RTE solution for the system “surface + atmosphere”:

$$\rho_{TOA}(\lambda, \mu_0, \mu, \varphi) = \rho_{atm}(\lambda, \mu_0, \mu, \varphi) + \frac{\rho_{sfc}(\lambda) \cdot T_1(\lambda, \mu_0) T_1(\lambda, \mu)}{1 - \rho_{sfc}(\lambda) \cdot s(\lambda)} \quad (3.8)$$

where $\theta = \arccos \mu$ is the observation zenith angle, φ is the relative azimuth angle, $\rho_{TOA}(\lambda, \mu_0, \mu, \varphi)$ is the total reflectance of the system “surface + atmosphere”, $\rho_{atm}(\lambda, \mu_0, \mu, \varphi)$ is the atmospheric reflectance (the reflectance of the aerosol, Rayleigh scattering, ozone absorption), $s(\lambda)$ is the atmospheric hemispherical albedo, $T_1(\lambda, \mu_0) = E(\mu_0) + \exp(-\tau/\mu_0)$ is the atmospheric transmittance from the top-of-atmosphere to the surface, $T_2(\lambda, \mu) = E(\mu) + \exp(-\tau/\mu)$ is the total atmospheric transmittance from the surface to a receiver (e.g., placed on a satellite), $E(\mu_0)$ and $E(\mu)$ are diffuse transmittances from top-of-atmosphere to the surface and from the surface to the receiver respectively, $\exp(-\tau/\mu_0)$ and $\exp(-\tau/\mu)$ are the direct transmittances from top-of-atmosphere to the surface and from the surface to the receiver respectively, $\rho_{sfc}(\lambda)$ is the Lambertian reflectance of the surface.

This equation can also be used for the case of non-Lambertian surface (see Sect. 3.3.3).

With the use of AATSR dual-view observations we can somewhat reduce the role of the underlying surface by writing Eq. 3.8 for both views and then dividing them by each other to get the ratio of surface BRDF:

$$\frac{\rho_{sfc}^f(\lambda, \mu_0, \mu, \varphi)}{\rho_{sfc}^n(\lambda, \mu_0, \mu, \varphi)} = \frac{\rho_{TOA}^f(\lambda, \mu_0, \mu, \varphi) - \rho_{atm}^f(\lambda, \mu_0, \mu, \varphi)}{\rho_{TOA}^n(\lambda, \mu_0, \mu, \varphi) - \rho_{atm}^n(\lambda, \mu_0, \mu, \varphi)} \cdot \frac{T_2^n(\lambda, \mu)}{T_2^f(\lambda, \mu)} \quad (3.9)$$

where all the terms are defined as in Eq. 3.8 and superscripts f and n stand for *forward* and *nadir* respectively.

The retrieval based on this equation is not sensitive to the snow albedo; it is sensitive only to the BRDF shape. This is an advantage of such a retrieval as compared to the use of a single view only (Eq. 3.8), because snow albedo changes due to temperature, humidity, age, pollution present on the snow surface and is hard to take into account. The shape of snow BRDF, though also varying, shows common features like strong forward scattering peak around principal plane for observing zenith angles more than -60° and a depression in the principal plane for observer zenith angles around $+10^\circ - 0^\circ$ (Winther, 1994), for other angles

the BRDF is most times quite smooth. So, the ratio $\frac{\rho_{sfc}^f(\lambda, \mu_0, \mu, \varphi)}{\rho_{sfc}^n(\lambda, \mu_0, \mu, \varphi)}$ should depend on azimuth with low asymmetry (close to Lambertian) in the direction perpendicular to the principal plane, and higher asymmetry in the principal plane.

3 Developing the satellite aerosol retrieval

The way to define the ratio $\frac{\rho_{sfc}^f(\lambda, \mu_0, \mu, \varphi)}{\rho_{sfc}^n(\lambda, \mu_0, \mu, \varphi)}$ depends on the channel, for which the retrieval is being performed, and still on the snow type of the observed scene. Various models and observations show that the shape of snow BRDF is not constant throughout the snow spectrum, and becomes more highlighted with the wavelength increasing (Peltoniemi et al., 2005). The same effect takes place when snow changes from fresh snow (high albedo, Lambertian reflector) to aged, impure snow (lower albedos, more pronounced BRDF shape) (Peltoniemi et al., 2005). In the infrared region of spectrum, e.g. 1.6 μm , the BRDF of snow may show significant variation of shape in the direction of increasing forward scattering and corresponding decreasing of scattering in the other directions (Peltoniemi et al., 2005). For our particular case of low sun this means that the forward to nadir ratio of surface reflectances in 1.6 μm may differ from that of 550nm significantly, achieving much larger values (2-10 at 1.6 μm to 1.1-1.3 at 550nm).

Therefore the dual-view AOT retrieval for channels 550nm and 1.6 μm applied over land (Curier et al., 2009) is not applicable here.

Experiments show that the ratio $\frac{\rho_{sfc}^f(550, \mu_0, \mu, \varphi)}{\rho_{sfc}^n(550, \mu_0, \mu, \varphi)}$ cannot be defined in a universal way (say, taking preassumed snow model) as a single value for the whole set of global data. Attempts to do so (Istomina et al., 2009) showed strong relief/shadows contamination of the result. To avoid this, it is possible to weight the preassumed snow model by the measured $\rho_{TOA}(\lambda, \mu_0, \mu, \varphi)$, defining the forward to nadir reflectance ratio as:

$$\frac{\rho_{sfc}^f(550, \mu_0, \mu, \varphi)}{\rho_{sfc}^n(550, \mu_0, \mu, \varphi)} = \frac{\rho_{sfc, sim}^f(550, \mu_0, \mu, \varphi)}{\rho_{sfc, sim}^n(550, \mu_0, \mu, \varphi)} \cdot \frac{\rho_{TOA, sim}^n(550, \mu_0, \mu, \varphi, \tau)}{\rho_{TOA, sim}^f(550, \mu_0, \mu, \varphi, \tau)} \cdot \frac{\rho_{TOA}^n(550, \mu_0, \mu, \varphi)}{\rho_{TOA}^f(550, \mu_0, \mu, \varphi)} \quad (3.10)$$

where $\rho_{sfc, sim}(550, \mu_0, \mu, \varphi)$ is the simulated snow surface reflectance, $\rho_{TOA, sim}(550, \mu_0, \mu, \varphi, \tau)$ is the simulated top-of-atmosphere reflectance for a given AOT, and $\rho_{TOA}(550, \mu_0, \mu, \varphi)$ is the observed top-of-atmosphere reflectance. It is obvious that if we guessed the aerosol type correctly and found the true AOT while solving Eq. 3.9, atmospheric effect of two last terms in Eq. 3.10 cancel each other out, and all what is left on the right side of Eq. 3.10 is the true surface reflectance ratio. In other words, we use modeled $\rho_{sfc, sim}(550, \mu_0, \mu, \varphi)$ and $\rho_{TOA, sim}(550, \mu_0, \mu, \varphi, \tau)$ ratios to remove the atmospheric effect of $\rho_{TOA}(550, \mu_0, \mu, \varphi)$ ratio in order to obtain the forward to nadir ratio of the surface reflectances. Similar approach have been used in e.g. (Vermote et al., 1997) and tested in (Istomina et al., 2010a). For snow model we used a semianalytical model of a medium consisting of fractal grains (Kokhanovsky et al., 2005a). The snow reflectance resulting modeled in this way was compared to the results of field measurements of snow surface BRDF and showed good comparison to each other.

3.3.3 Sensitivity study

Though expression 3.8 was initially written for the case of Lambertian surface, it can also be applied to non-Lambertian surfaces as an approximate solution. This can be done via introducing BRDF effects in the numerator of the surface term of Eq. 3.8. Of course, the accuracy of such an approximation needs to be studied, because directional properties of surface reflection function can have a significant effect on the redistribution of the incoming light, both direct and diffuse, and need to be taken into account more accurately. This becomes even more important for the case of bright non-Lambertian surface, i.e. snow.

Tanre et al. (1979) suggested an approximate analytical expression for top of atmosphere reflectance in case of non-Lambertian non-homogeneous surface, which accounts for light scattering between the observed point M, its neighbor surface areas, and the atmosphere of optical thickness τ :

$$\begin{aligned} \rho_{TOA}(M, \lambda) &= \rho_{atm}(\lambda, \mu_0, \mu, \varphi) + \rho_{sfc}(M, \lambda, \mu_0, \mu, \varphi) \exp(-\tau / \mu_0) \exp(-\tau / \mu) \\ &+ \bar{\rho}_{sfc}(M, \lambda, \mu_0, \mu, \varphi) \exp(-\tau / \mu) E(\mu_0) + \langle \rho_{sfc}(M, \lambda, \mu_0, \mu, \varphi) \rangle T_1(\lambda, \mu_0) E(\mu) \\ &+ \langle \rho_{sfc}(M, \lambda, \mu_0, \mu, \varphi) \rangle s(\lambda) \\ &\times \left[\frac{\bar{\rho}_{sfc}(M, \lambda, \mu_0, \mu, \varphi) \exp(-\tau / \mu) + \langle \rho_{sfc}(M, \lambda, \mu_0, \mu, \varphi) \rangle E(\mu)}{1 - \langle \rho_{sfc}(M, \lambda, \mu_0, \mu, \varphi) \rangle \cdot s(\lambda)} \right] T_1(\lambda, \mu_0) \end{aligned} \quad (3.11)$$

where $\rho_{TOA}(M, \lambda)$ is the total reflectance of the system “surface + atmosphere” with respect to the target point M, $\rho_{atm}(\lambda)$ is the atmospheric reflectance (the reflectance of the aerosol, Rayleigh scattering, ozone absorption), $E(\mu_0)$ and $E(\mu)$ are diffuse transmittances from top-of-atmosphere to the surface and from the surface to the receiver respectively, $\exp(-\tau/\mu_0)$ and $\exp(-\tau/\mu)$ are the direct transmittances from top-of-atmosphere to the surface and from the surface to the receiver respectively, $T_1(\lambda, \mu_0) = E(\mu_0) + \exp(-\tau/\mu_0)$ is the atmospheric transmittance from the top-of-atmosphere to the surface, $s(\lambda)$ is the atmospheric hemispherical albedo, $\rho_{sfc}(M, \lambda, \mu_0, \mu, \varphi)$ is the bidirectional reflection function (BRDF) of the target M for a given observation-illumination geometry. The term $\bar{\rho}_{sfc}(M, \lambda, \mu_0, \mu, \varphi)$ is the average angular reflectance of the target illuminated with the diffuse light only; $\langle \rho_{sfc}(M, \lambda, \mu_0, \mu, \varphi) \rangle$ accounts for the effect of multiple light scattering from the environment of the target M in the observation direction. The last term is only different from $\bar{\rho}_{sfc}(M, \lambda, \mu_0, \mu, \varphi)$ in case of inhomogeneous spatial distribution of $\rho_{sfc}(M, \lambda, \mu_0, \mu, \varphi)$. In this study we assume the surface to have a homogeneous $\rho_{sfc}(\lambda, \mu_0, \mu, \varphi)$, therefore the dependence on the target M can be waived and the Eq. (3.11) can be written in a simplified form as:

$$\begin{aligned} \rho_{TOA}(M, \lambda) &= \rho_{atm}(\lambda, \mu_0, \mu, \varphi) + \rho_{sfc}(M, \lambda, \mu_0, \mu, \varphi) \exp(-\tau / \mu_0) \exp(-\tau / \mu) + \bar{\rho}_{sfc}(M, \lambda, \mu_0, \mu, \varphi) \\ &\times \left\{ \exp(-\tau / \mu) E(\mu_0) + T_1(\lambda, \mu_0) E(\mu) + s(\lambda) \frac{\bar{\rho}_{sfc}(M, \lambda, \mu_0, \mu, \varphi) T_1(\lambda, \mu_0) T_2(\lambda, \mu)}{1 - \bar{\rho}_{sfc}(M, \lambda, \mu_0, \mu, \varphi) \cdot s(\lambda)} \right\} \end{aligned} \quad (3.12)$$

with all the terms defined as above.

Various measurements and models show (Leroux et al., 1998b; Winther et al., 1999; Aoki et al., 2000; Li and Zhou, 2004; Peltoniemi et al., 2005; Kokhanovsky et al., 2005a; Hudson et al., 2006; Peltoniemi, 2007; Negi et al., 2010;), that for most observation-illumination geometries snow is rather far from a Lambertian reflector (except for fresh snow (Winther, 1994)), and has significant directional reflectance properties, especially in the region of forward scattering for large illumination angles. For our particular application large sun zenith angles are of frequent occurrence, therefore the effect of forward scattering can be significant and has to be taken into account in most cases. Therefore the accuracy of Eq. 3.8 and Eq. 3.12 will be checked for the case of a highly reflective non-Lambertian surface, which is a parameterization of field snow BRDF measurements (Degünther and Meerkötter, 2000).

To perform the accuracy study of Eq. 3.8 and 3.12, we used a forward radiative transfer (RT) model SCIATRAN (Rozanov et al., 2005). For this $\rho_{TOA}(\lambda, \mu_0, \mu, \varphi)$ was calculated in three different ways: first, by setting the atmosphere and surface parameters in the RT model and solving the RT equations for different aerosol loads and geometries, therefore achieving the „reference” $\rho_{TOA}^{true}(\lambda, \mu_0, \mu, \varphi)$; then, by calculating each of the terms separately and putting into Eq. 2, therefore achieving $\rho_{TOA}^{Kaufman}(\lambda, \mu_0, \mu, \varphi)$; and finally, $\rho_{TOA}^{Tanre}(\lambda, \mu_0, \mu, \varphi)$ has been put together from the separately calculated terms using the Eq. 3.12.

Total transmittances $T_1(\lambda, \mu_0)$, $T_2(\lambda, \mu)$ and atmospheric hemispherical albedo $s(\lambda)$ were calculated using an approximation from (Kokhanovsky et al., 2005b).

The relative difference $\frac{\rho_{TOA}^{true}(\lambda, \mu_0, \mu, \varphi) - \rho_{TOA}^{Kaufman}(\lambda, \mu_0, \mu, \varphi)}{\rho_{TOA}^{true}(\lambda, \mu_0, \mu, \varphi)}$ of Eq. 3.8 and the relative difference $\frac{\rho_{TOA}^{true}(\lambda, \mu_0, \mu, \varphi) - \rho_{TOA}^{Tanre}(\lambda, \mu_0, \mu, \varphi)}{\rho_{TOA}^{true}(\lambda, \mu_0, \mu, \varphi)}$ of Eq. 3.12 are plotted for aerosol optical thickness (AOT) equal to unity in Fig. 3.16 and Fig. 3.17 respectively.

It is visible that $\rho_{TOA}^{Kaufman}(\lambda, \mu_0, \mu, \varphi)$ is overestimated by around 20% for most of the viewing geometries, with the accuracy getting worse for lower sun elevations.

For relatively high sun elevation ($\theta = 45^\circ$) and observation angles close to nadir, the accuracy of Eq. 3.12 is around 5%, which is much better than that of Eq. 3.8. However, for lower sun elevations $\rho_{TOA}^{Tanre}(\lambda, \mu_0, \mu, \varphi)$ is underestimated by around 30 %. For larger observation angles and $\theta = 65^\circ, 85^\circ$ the error is decreasing and in some cases gets close to zero, however for $\theta = 45^\circ$ the error of Eq. 3.12 is increasing to 20% for viewing angles of 50° . In general, Eq. 3.12 does not show much accuracy gain in comparison to Eq. 3.8. However, Eq. 3.12 contains one more unknown – average angular reflectance $\bar{\rho}_{sfc}(M, \lambda, \mu_0, \mu, \varphi)$, which is not present in Eq. 3.8. Also, Eq. 3.12 shows different accuracy for nadir and forward observation angles, which will cause stray assymetry between forward and nadir views during the retrieval. This effect is less pronounced in Eq. 3.8. Therefore for further AOT retrieval in this study we will use Eq. 3.8, which contains two unknowns: atmospheric reflectance $\rho_{atm}(\lambda, \mu_0, \mu, \varphi)$ and surface reflectance $\rho_{sfc}(\lambda)$.

It is important to note that the study has been performed for AOT = 1.0. Such high values are never the case in Arctic region. AERONET data for Arctic stations (e.g. PEARL, OPAL,

Resolute Bay, Barrow, Ny Ålesund, etc.) show background AOT of 0.03-0.05 and increased AOT during pollution events of AOT=0.1-0.3 with very rare exceptions. Therefore, it is acceptable to use Eq. 3.8 for the AOT retrieval in Arctic region. However, in case of very strong pollution the quality of the retrieval will drop and lead to under- or overestimation of AOT, depending on input data.

Single view surface model versus forward to nadir reflectance ratio

It is important to understand that Eq. 3.9 is the main equation of the AOT retrieval at 550nm; the reason why we have to introduce the weighting by the measured TOA reflectance and derive Eq. 3.10 is our insufficient knowledge about the underlying surface. In this subsection we will study how inaccurate it would be to use the measured TOA reflectance in the Eq. 3.8 instead of the real surface BRDF.

Introduced weighting by the TOA reflectances (Eq. 3.10), though inaccurate due to atmospheric effects, has its advantages when compared to a modeled snow BRDF:

1. **The relief contamination.** While assumed snow model would fail to represent the BRDF of real snow over tilted surfaces because the illumination-observation geometry of the satellite should be recalculated with respect to the surface tilt, the TOA reflectances weighted by the modeled BRDF will not expose this artifact to such an extent. Therefore, the relief contamination will be reduced within this approach.
2. **The snow type problem.** Even for the case of an ideal relief, over smooth horizontal surface the modeled snow BRDF is only valid for one peculiar kind of snow and is not able to adjust to the varying properties of real surfaces. Weighting by the measured TOA reflectances solves this problem and allows the retrieval to adjust to practically any encountered snow type.
3. **The scale problem.** Most models of snow directional properties and spectra are derived and validated using field measurements with the size of the sample at the scale of centimeters to meters. For remote sensing applications, completely different scales should be utilized, in most cases of around several kilometers. It is apparent that the optical properties of the surface will be different on different scales, caused e.g. by scale-dependent structure (sastrugi) or by surface impurities (e.g. ash and soot at the centimeter scale, but mountains and vegetation at the kilometer scale)

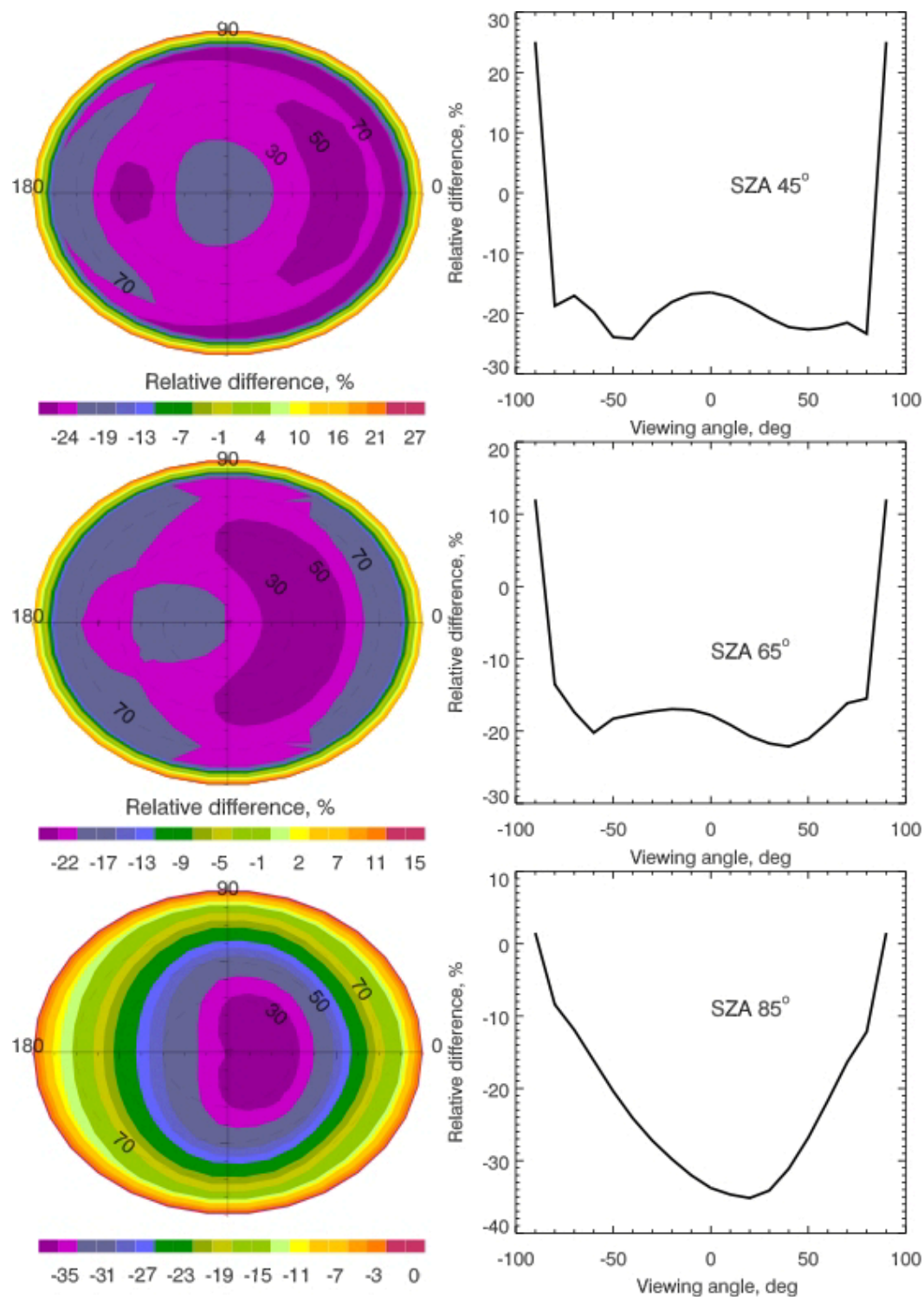


Fig.3.16 The relative error of Eq. 3.8 for the surface shown in Fig. 3.13 and aerosol phase function shown in Fig. 3.14, AOT=1. It is visible that $\rho_{TOA}^{Kaufman}(\lambda, \mu_0, \mu, \varphi)$ is overestimated by around 20% for most of the viewing geometries.

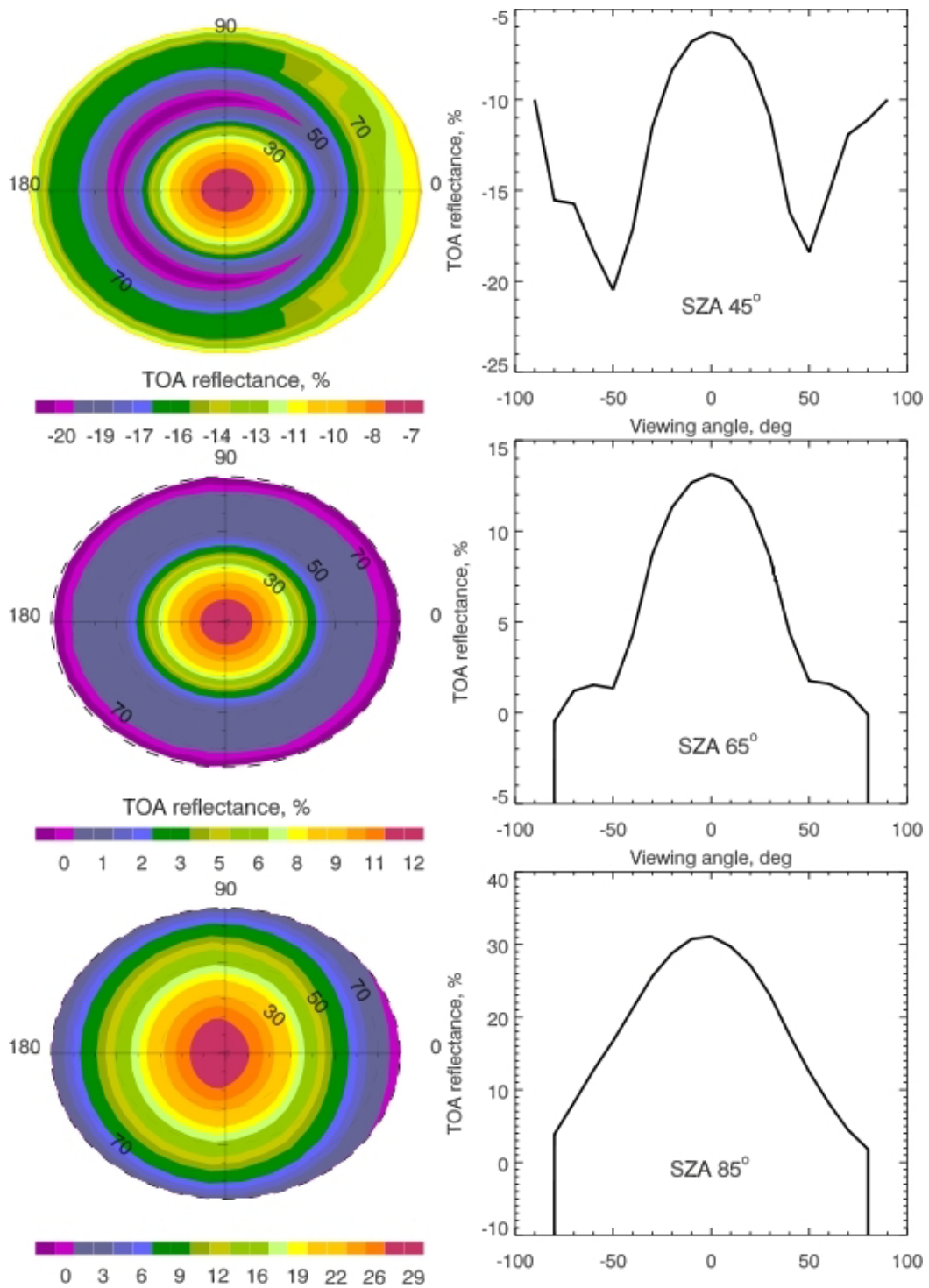


Fig.3.17 The relative error of Eq. 3.12 for the surface shown in Fig. 3.13 and aerosol phase function shown in Fig. 3.14, AOT=1. It is visible that $\rho_{TOA}^{Tanre}(\lambda, \mu_0, \mu, \varphi)$ is overestimated by around 5% for $\theta = 45^\circ$ and underestimated by around 30 % for lower illumination angles and observation angles close to nadir. For larger observation angles and $\theta = 65^\circ, 85^\circ$ the error is decreasing and in some cases is close to zero, however for $\theta = 45^\circ$ the error of Eq. 4 is increasing to 20% for viewing angles of 50° .

3 Developing the satellite aerosol retrieval

The perfect solution would be an up-to-date surface reflectance database, applicable to remote sensing tasks, e.g. derived with the airborne or spaceborne instruments. In the absence of such data, we use the measured TOA reflectances to fill the gap in the information about the surface.

So, the question is how large is the error due to atmospheric contamination in forward-nadir ratio of AATSR forward and nadir brightnesses in comparison to the clean snow BRDF ratio. To check the behavior of this error the radiative-transfer simulation with SCIATRAN was performed, where we calculated the reflectance of clean snow (no atmosphere) in two observation directions – 0° and 50° , with fixed sun illumination angle – 65° , and made the forward-nadir ratio of this clean snow for 3 observation directions 0° and 50° , with fixed sun illumination angle – 65° , and made the forward-nadir ratio of this clean snow for 3 azimuths – 0° , 96° , 180° . We did the same modeling and calculated the same ratio for system „snow+aerosol+ozone+Rayleigh scattering“ for different AOTs. The result is shown in Fig. 3.18.

Upper panel shows the dependence of the relative error on the AOT for the relative azimuth angles from 0° to 180° with the step of 12° . Lower panel illustrates the dependence of the relative error on the relative azimuth angle for AOT from 0 to 1.0.

It is clear, that for middle azimuths like 90° the error is about 2% and doesn't depend on AOT. This is caused by the shape of aerosol phase function – when both forward and nadir geometry are located at the same amplitude of aerosol phase function, means both nadir and forward aerosol reflectances *change equally with AOT and are not seen in the ratio*. The 2% error is caused by atmospheric (but not aerosol!) contamination and can be corrected.

At the extreme relative azimuth angles the error of such approach is higher, due to the details of aerosol phase function at these scattering angles, but it is unlikely to get such extreme azimuths in AATSR observations.

For an unlikely in the Arctic case of very high AOT (around 1.0) and for backscattering geometry (of rare occurrence on the AATSR observation geometries) the relative error of using measured TOA reflectances instead of the true snow BRDF is around 10% in the forward-nadir ratio. Less extreme geometries and AOTs exhibit lower errors in the surface reflectance ratio, of about 4% and 2% in the best case. This is of course better than a fixed snow BRDF model can provide on a global scale.

In order to correct for the residual 2% of the error, we introduce the simulated atmospheric correction appearing in Eq. 3.10 (compare to Eq. 3.9). To illustrate the advantage of this approach, we present the two AOT maps (See Fig. 3.19) of the same scene at Alaska, retrieved with the Eq. 3.9 using an assumed snow model for the surface BRDF (left panel) and Eq. 3.10 using the atmospheric correction and TOA reflectances instead of the true surface BRDF (right panel). The red dot shows the location of Barrow ground based station. The scene is cloud screened and features snow covered sea ice (upper part of the AOT map) and snow covered land and mountains (lower part of the AOT map). It is visible that the modeled snow BRDF (left panel) in this case was not able to represent the real surface properties, which resulted in high noise and general poor performance of the algorithm. The AOT map at the right panel was calculated with the Eq. 3.10; it is visible that this approach provides a much more smooth result, with no algorithm malfunctioning. It is important to

note, however, that in some cases the modeled snow BRDF can give good results (e.g. as shown by Istomina et al., 2009). However, the performance of the corrected Eq. 3.10 is better on the global scale (Istomina et al., 2010a). The phase function problem illustrated by Istomina et al. (2009), when the retrieved AOT changes drastically with the varying phase function, remains for the both modifications of the algorithm.

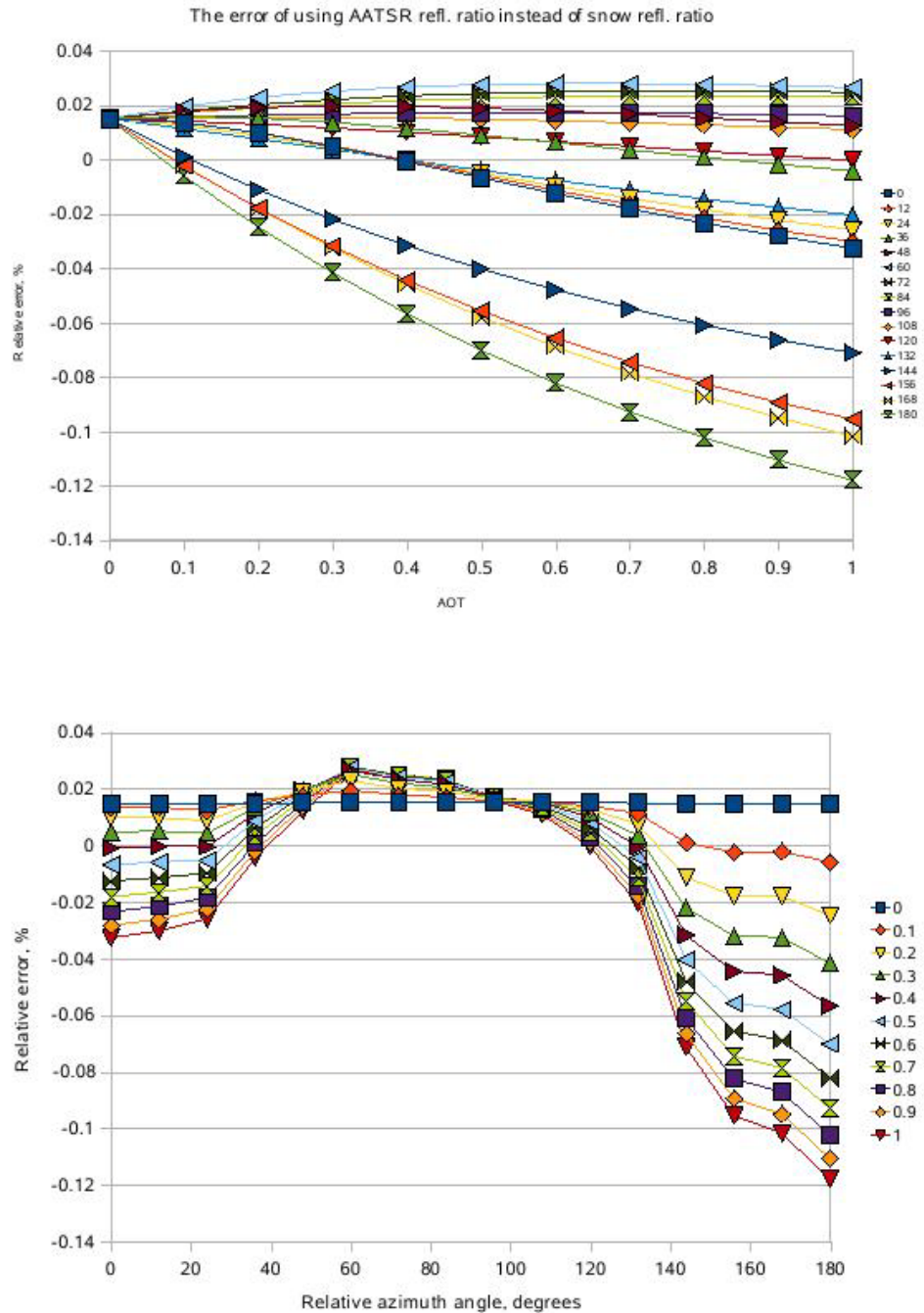


Figure 3.18. The relative error of using TOA reflectance values instead of the surface reflectance depending on AOT (upper panel) and relative azimuth angle (lower panel). See text for details.

3 Developing the satellite aerosol retrieval

In order to study the sensitivity of the retrieval based on the Eq. 3.10, we performed the RT simulations in the following way: the measured TOA reflectances for forward and nadir were simulated with SCIATRAN, and then artificially disturbed up and down by 5%. This means, the AOT retrieval was performed 3 times for each input AOT – for undisturbed simulated TOA reflectances, for the TOA reflectances both increased by 5%, and for the TOA reflectances both decreased by 5%. The input AOT range is from 0 to 1.0 with the step 0.1. Solar zenith angle was equal to 65° . Fig. 3.20 shows the relation of the resulting retrieved AOT to the input AOT with the blue solid line for the undisturbed case, and with the color ranges for the reflectances disturbed by 5%. Increased reflectances produce increased AOT, and vice versa. It is visible that the constant disturbance of reflectances by 5% produces not offset-like retrieval error, but an error, which increases with the AOT. This means that the assumption of the low atmospheric influence on the TOA reflectance is failing for larger AOTs as expected. However, for the AOTs below 0.3, the retrieval error can be assumed constant and gives the value of approximately ± 0.1 for the absolute AOT error. It is important to note that in general case of an AATSR scene we have no possibility to estimate how the underlying surface differs from the simulated surface; this implies the inability to estimate the accuracy of the retrieved AOT in general case.

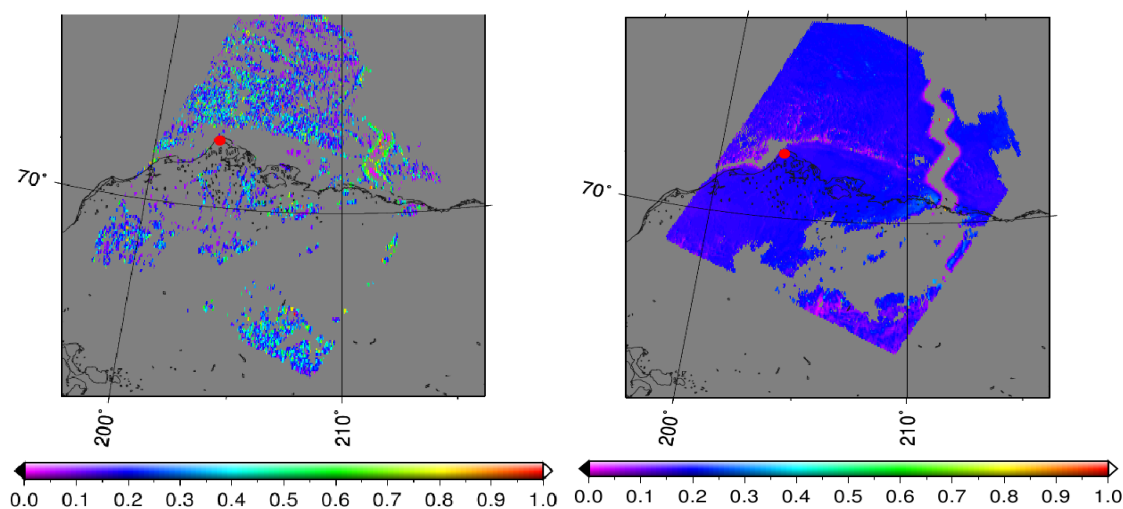


Figure 3.19. The advantage of using the measured TOA reflectances instead of assumed snow model to account for the surface reflective properties in the AOT retrieval: left panel shows the AOT retrieved using an assumed snow model; right panel shows the AOT retrieved using the measured TOA reflectances as the first approximation of the surface directional reflective properties in both forward and nadir directions.

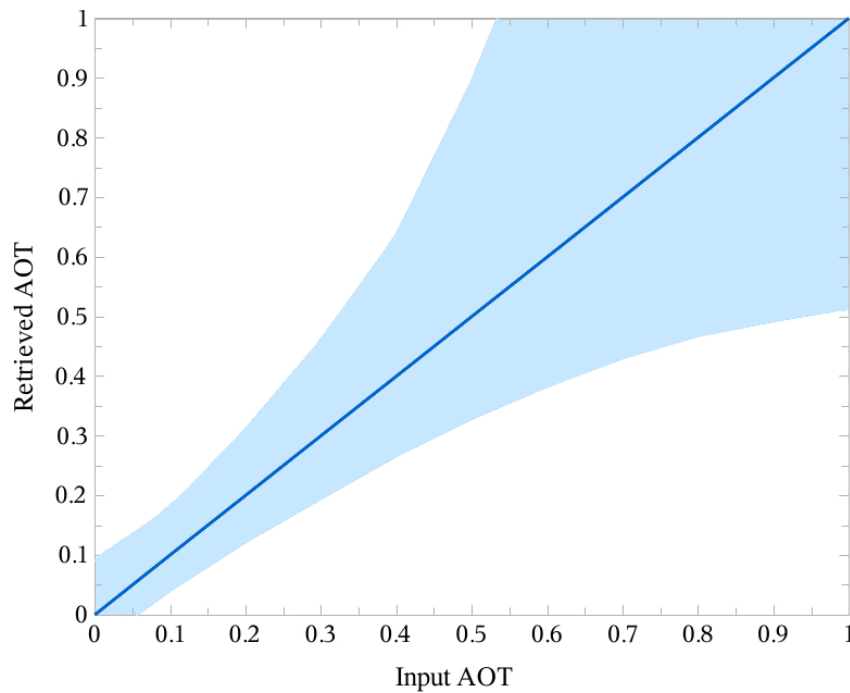


Figure 3.20. The dependence of the retrieved AOT on the input AOT for the RT simulated TOA reflectances a) undisturbed (blue solid line) b) increased by 5% (upper border of the color filled area) c) decreased by 5% (lower border of the color filled area).

3.3.4 Choosing the aerosol type and LUT calculations

The LUT describes the dependence of atmospheric reflectance $\rho_{atm}(\lambda, \mu_0, \mu, \varphi)$, surface reflectance $\rho_{sfc}(M, \lambda, \mu_0, \mu, \varphi)$ or top-of-atmosphere reflectance $\rho_{TOA}(\lambda, \mu_0, \mu, \varphi)$ on AOT for two AATSR channels, 550nm and 3.7 μ m.

$\rho_{atm}(\lambda, \mu_0, \mu, \varphi)$ includes the reflectance from aerosol load, Rayleigh path reflectance, ozone reflectance. Unlike Rayleigh scattering, the phase function of which is well known, aerosol reflectance $\rho_{aer}(\lambda, \mu_0, \mu, \varphi)$ is variable due to different particle size distribution, particle shape and chemical composition, which affects single scattering albedo and extinction of aerosol layer. All this makes aerosol reflectance highly dependent on illumination-observation geometry and variable from one aerosol type to another. This makes it impossible to create one atmospheric LUT which would represent aerosol properties well on global scale. Therefore, aerosol retrievals often utilize several atmospheric LUTs choosing between them by e.g. optimal estimation means. In this study, we would like to focus on the successful reduction of highly disturbing snow surface rather than retrieval of aerosol type and properties. Therefore we have calculated one atmospheric LUT for aerosol phase function shown in Fig. 3.14, for AOT from 0 to 1. As this phase function was measured during one of regular Arctic haze events, we consider it to be the best choice comparing to the variety of calculated phase functions. Rayleigh scattering was taken into account according to (Bucholtz, 1995) at sea level. However, for retrievals over elevated surfaces

3 Developing the satellite aerosol retrieval

such as e.g. Greenland, the dependence of Rayleigh optical thickness on temperature and pressure has to be considered:

$$\tau_{Ray}(\lambda, z) = \frac{P(z)}{P_0} \cdot \frac{T_0}{T(z)} \cdot \tau_{Ray}(\lambda, 0) \quad (3.13)$$

We use gtopo30 database to calculate the elevation of each pixel in order to find the pressure at the surface, and the brightness temperature of 12 μ m channel as the temperature at the surface.

The pressure at the elevation z $P(z)$ is calculated by the barometric elevation equation:

$$P(z) = P_0 \cdot e^{-\frac{M \cdot g_0 \cdot z}{R \cdot T(z)}} \quad (3.14)$$

where M is the molar mass of Earth's air, g_0 is the gravitational constant, R is the universal gas constant, and $T(z)$ is the temperature at the surface.

To avoid using approximations, we calculate the Rayleigh reflectance at sea level $\rho_{Ray}(\lambda, 0)$ with RT model for a given wavelength, and then scale it to the temperature and pressure according to Eq. 11 and 12, so that

$$\rho_{Ray}(\lambda, z) = \rho_{Ray}(\lambda, 0) \cdot \frac{T_0}{T(z)} \cdot e^{-\frac{M \cdot g_0 \cdot z}{R \cdot T(z)}} \quad (3.15)$$

Our particular case of high solar zenith angles requires careful accounting for airmasses, different from that usual to plane-parallel atmosphere model. For RT calculations of LUTs, we use pseudospherical model of the atmosphere. To correct AATSR measured quantities, we use approximation described in Kasten, Young (1989).

3.3.5 Application limits and sources of errors

1. Geometries

Frequently occurring in the Arctic cases of low solar elevations present a significant problem for the AOT retrievals over snow for two reasons:

- the insufficient amount of solar radiation reflected from the surface decreases signal to noise ratio and makes the task of surface discrimination immensely difficult;
- surface and aerosol directional reflectance properties at extreme scattering angles tend to vary with the surface or aerosol type more than at moderate scattering angles (especially in the forward scattering direction); in the situation of unknown surface or aerosol type the assumed directional properties will most likely be incorrect at these scattering angles.

In order to avoid both situations described above, we limit the solar zenith angles to 75° and allow all relative azimuth angles.

2. Surface properties

The surface TOA reflectance needs to be high enough for the assumption of the minor atmospheric role to hold (Eq. 3.10). For darker surfaces, such as for strongly polluted snow or melting sea ice (as can be seen in the further sections, the reflectance of this surface type might be as low as 0.2, see Fig. 3.21) and for some certain forward scattering illumination-observation geometries, the atmospheric role can be as high as 50% for AOT of about 0.2-0.3. In such conditions, Eq. 3.9 would be no longer valid. Therefore the case of decreased snow albedo (snow, contaminated by dust or other impurities, or sea ice covered with thin layer of snow) stays a separate and difficult problem, as this surface type is still too bright for the conventional AOT retrievals over land, but already too dark for the presented AOT retrieval over snow.

The Eq. 3.9 is also built on the assumption that the BRDF shape of the observed underlying surface is close enough to the simulated one. For the cases of relative azimuths being around 90° this assumption will be correct due to smooth snow BRDF shape at these angles for most snow types. The presented approach will even work in the case of varying snow albedo due to the TOA reflectance ratio used instead of the absolute TOA reflectance values.

3. Aerosol type

As was shown by Istomina et al. (2009), the amplitude of the retrieved AOT may vary drastically for the same scene depending on the chosen aerosol phase function, even in the case of fixed surface assumptions. In the absence of the spectrally sensitive AOT retrieval, it is important to choose an aerosol type which occurs frequently in nature, in order to keep the amplitude of the retrieved AOT maps close to reality. In our case, the chosen Arctic haze phase function corresponds well to the spring haze events used for the validation studies; the applicability of this phase function at a more general scale is only possible for qualitative studies of aerosol dynamics and distribution over snow.

4. Aerosol amount

The described approach is based on the assumption that the ratio of measured TOA reflectances is mainly constructed by the surface reflectances, with only small effect of the atmosphere. In case of clean snow and low AOT (< 0.3), the reflectance of the surface is so high that atmospheric effect in the ratio can be easily corrected as suggested in Eq. 3.10. For greater aerosol amounts, the assumption on a small effect of the atmosphere on the measured TOA reflectances is not valid, as can be seen from Fig. 3.18 and Fig. 3.20.

Lacking information on e.g. variety of aerosol types in the Arctic or the variety of snow surface albedos makes it impossible to estimate the total AOT retrieval error. These sources of errors created limitations on the retrieval applications (see Table 3.3 for summary). Considering the performed sensitivity study, the absolute AOT error retrieved with the VIS retrieval $\delta_{AOT,VIS}$ for AOT<0.3 and the case of 5% between the surface assumptions in the retrieval and the real surface is:

$$\delta_{AOT,VIS} = \pm 0.1$$

It is apparent that the variety of snow types creates the variability of nadir and forward TOA reflectances greater than 5%. This would cause greater AOT error and therefore limits the

application of the described AOT retrieval to the cases of fresh clean snow. This limitation is realized at the cloud screening and snow flagging step of the retrieval.

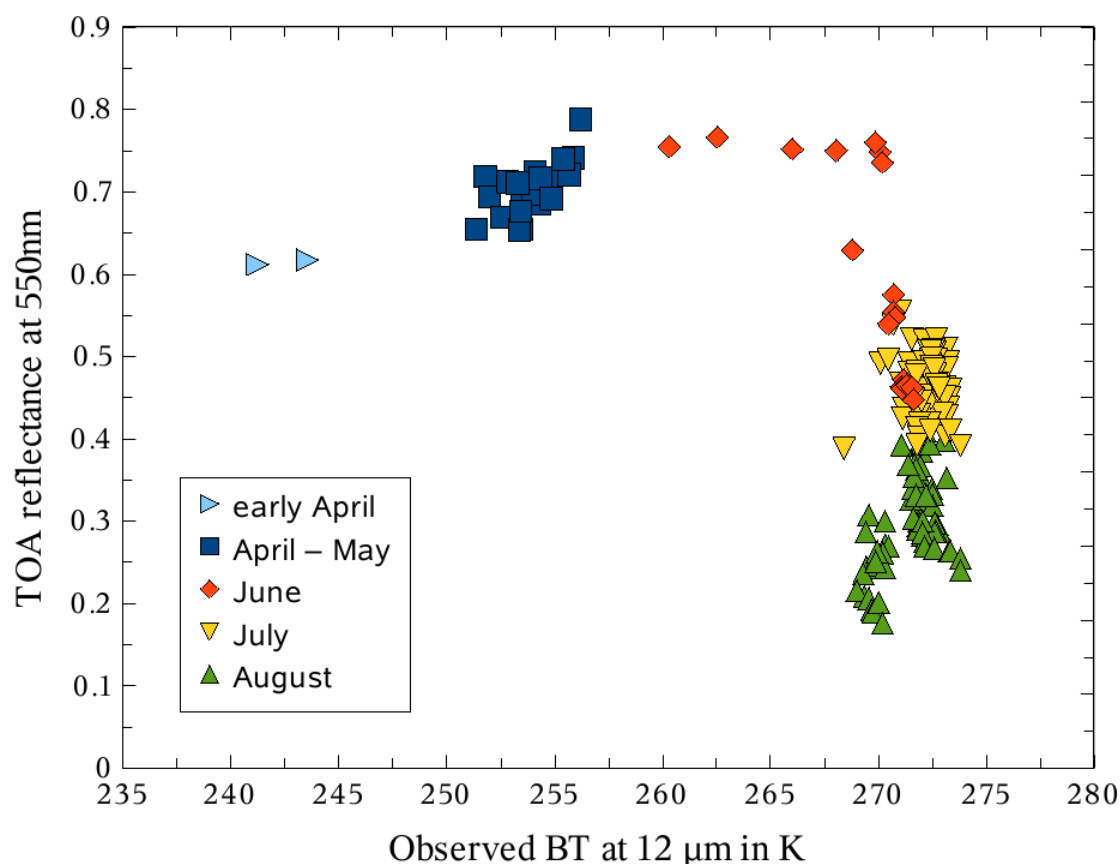


Figure 3.21. The evolution of surface type for ground based station OPAL with the time of the year. Most of the data points represent melting sea ice surface type (summer months), whereas data from April and May represent ice covered with snow. Only cloud free snow flagged data were taken into account. The dataset represents spring and summer months 2007-2009.

3.4 AOT retrieval in the infrared range of spectrum

As was indicated by Spangenberg et al. (2001) while evaluating snow directional reflectance at 3.7 μm from satellite, Arctic haze present in the scene may drastically influence the directional TOA reflectance at 3.7 μm. This contradicts to the common opinion that aerosol reflectance at longer wavelengths is too low to be used for AOT retrievals in this spectral region. Closer analysis of this problem showed the possibility to retrieve AOT over snow also in the IR (Istomina et al., 2011).

The forward RT simulations were performed for coarse and accumulation modes of the four main aerosol components to study the behavior of the directional TOA reflectance of an aerosol layer. The main result was the strong angular dependence of aerosol TOA IR reflectance at low sun elevations. This gives the opportunity to retrieve AOT at certain non-nadir observation angles due to the detectable values of aerosol IR reflectance. The

multiangle spaceborne observations can be used to observe the TOA reflectances at the necessary angles in order to estimate the aerosol load also at longer wavelengths. Due to snow and ice being almost perfect black bodies, the task of the AOT retrieval in the IR is close to the conventional task of the AOT retrieval over ocean in the VIS.

In current work, a method to retrieve AOT over snow with the use of AATSR channel at 3.7 μm has been developed. The algorithm utilizes its dual-viewing observation technique. For this, the extraction of the atmospheric reflectance out of measured brightness temperature (BT) at 3.7 μm has to be performed. Spangenberg et al. (2001) discussed the influence of infrared atmospheric reflectance onto the AATSR brightness temperature (BT) at 3.7 μm with respect to the problem of cloud detection over snow. As mentioned above, this idea has been successfully applied for cloud screening over snow using AATSR channel at 3.7 μm in combination with other AATSR channels (Istomina et al., 2010b). Good infrared calibration of AATSR instrument (Smith et al., 2001) provides the possibility of applying the same approach also to aerosol layers. The extracted IR directional reflectance is then corrected for possible surface contamination and utilized in the LUT approach in order to retrieve the AOT. The resulting AOT at 500nm is recalculated from that at 3.7 μm using a fixed Angström parameter.

The retrieval developed in this work, while not free from disadvantages, is robust and can present an alternative to the VIS AOT retrievals in cases of complicated surface or observation-illumination conditions.

Further subsections of this work are dedicated to analysis of snow and aerosol infrared properties, theoretical basis of the algorithm, sensitivity study, LUT description and discussion on applicability limits. The validation and application studies will be presented in the next sections.

3.4.1 The main features of aerosol and snow in the infrared

As measurements of snow thermal properties (Hori et al., 2006; English et al., 1995) show, snow is an almost perfect black body which emits according to its physical temperature. This is probably the most important snow feature relevant to this study. All subsequent snow properties like e.g. its very low reflectance in the AATSR IR spectral range (Wald (1994), MODIS USCB Emissivity Library) and the stability of the snow emissivity throughout the thermal region of the spectrum with only slight dependence on the snow grain size and liquid water content (Hori et al. (2006), see also Section 2.2.1) made it possible to neglect possible temporal and spatial variability of snow emissivity in this work.

In order to study the behavior of aerosol scattering characteristics depending on size distribution and wavelength we have calculated aerosol phase functions and single scattering albedo for spherical polydisperse particles with the refractive indices corresponding to four main aerosol components (water soluble, oceanic, soot, dust) for two wavelengths – 550nm and 3.7 μm . We used the Lorenz-Mie theory (De Rooij and Van Der Stap, 1984; Mishchenko et al., 1999) and lognormal size distribution (3.16).

$$n(r) = \text{const} \cdot r^{-1} \exp\left[-\frac{(\ln r - \ln r_g)^2}{2 \ln^2 \sigma_g}\right] \quad (3.16)$$

where const is chosen in such a way that $\int_0^\infty n(r) dr = 1$.

To represent coarse and accumulation aerosol modes, we took the geometric standard deviation σ which has been measured during an Arctic smoke event (Treffeisen et al., 2007), $\ln^2 \sigma_g = 0.22$, and average size parameters of dust storm aerosols $r_g = 1.7 \mu\text{m}$ for the coarse mode, and $r_g = 0.5 \mu\text{m}$ for the accumulation mode, with the effective radius equal to $2.9 \mu\text{m}$ for the coarse mode and $0.64 \mu\text{m}$ for the accumulation mode. Smaller particles (nucleation and Aitken modes) were not taken into account in this study.

The result of the calculation is shown in Fig. 3.22 for the coarse mode and in Fig. 3.23 for the accumulation mode. The refractive indices (Kokhanovsky, 2004) and calculated single scattering albedo are shown in Table 3.1 for 550nm and in Table 3.2 for $3.7 \mu\text{m}$.

It is visible that phase functions of water soluble, oceanic and dust aerosol components of both sizes show significant back- and forward scattering details at 550nm, however the forward scattering peak of accumulation mode is weaker than that of coarse mode by approximately one order of magnitude. The magnitude of backscattering details is very similar for the both particle sizes. For the coarse mode, the overall asymmetry of the phase functions at $3.7 \mu\text{m}$ and 550nm is very similar, with the exception of soot component, which shows a slightly lower asymmetry at phase angles larger than 20 degrees in comparison to the other components. The forward scattering peaks are, however, similar.

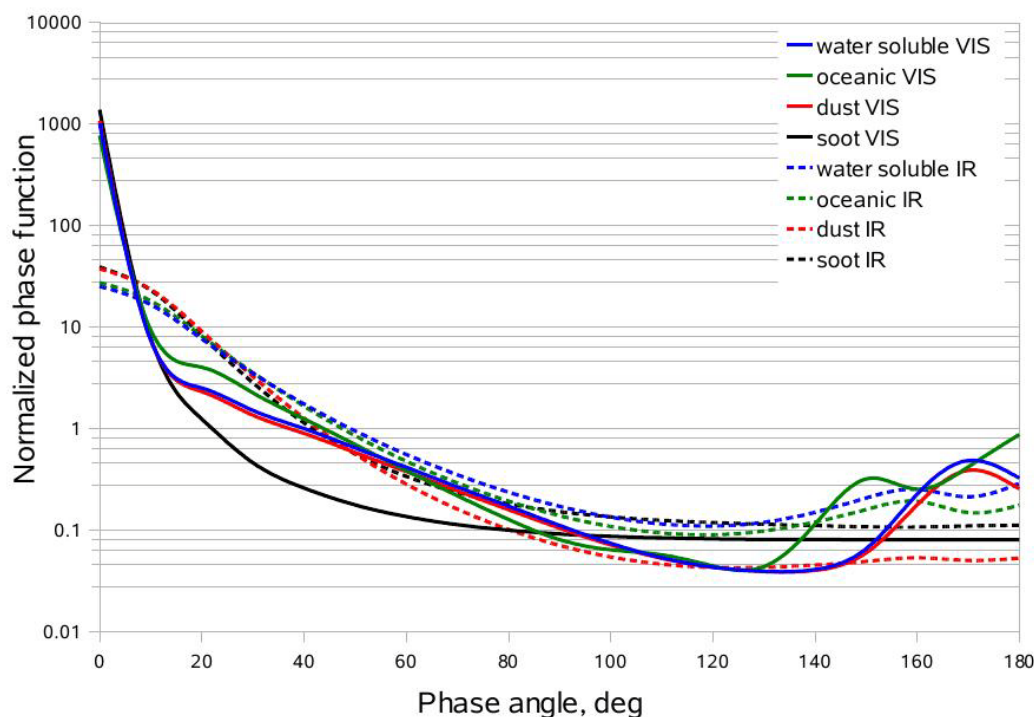


Figure 3.22. Phase functions for coarse mode of oceanic, water soluble, dust and soot aerosol components calculated for spherical polydisperse particle at 550nm (VIS, continuous line in the figure) and $3.7 \mu\text{m}$ (IR, dashed line in the figure). The phase functions are normalized to unity, see SSA in text.

For the accumulation mode, the asymmetry of all the phase functions at 550nm is clearly larger in comparison to the asymmetry at 3.7 μ m.

To study the influence of these phase function details on the angular reflectance with respect to wavelength change, we performed RT simulations. For this we used the forward RT model SCIATRAN developed at the University of Bremen (Rozanov et al., 2005) in order to calculate the TOA reflectance over black surface for accumulation and coarse modes of dust aerosol component at 550nm and 3.7 μ m for aerosol optical thickness 0.1. The result is shown in Fig. 3.24 for coarse mode and in Fig. 3.25 for accumulation mode.

It is visible that for the given AOT=0.1 the reflectance patterns are similar for both sizes and wavelengths, showing decreased reflectance around nadir and corresponding increase in the forward and backscattering directions at 550nm. The backscattering peak is absent at 3.7 μ m, which corresponds to the shape of phase functions discussed above. The expected extreme spectral decrease of reflectance is visible for accumulation mode, as opposed to relatively unchanged magnitudes of reflectance for the coarse mode. It is very important to notice that even for the accumulation mode the magnitude of IR reflectance in the upper forward quarter-sphere (azimuth angle less than 90 degrees) is of the same order as that at 550nm, nadir view. This makes it possible for the IR retrieval to deal with the values of same magnitude order as at 550nm, nadir, by simply using forward view within certain azimuth angles. For the coarse mode the situation is even better: no change of reflectance magnitude is observed at 3.7 μ m as compared to 550nm.

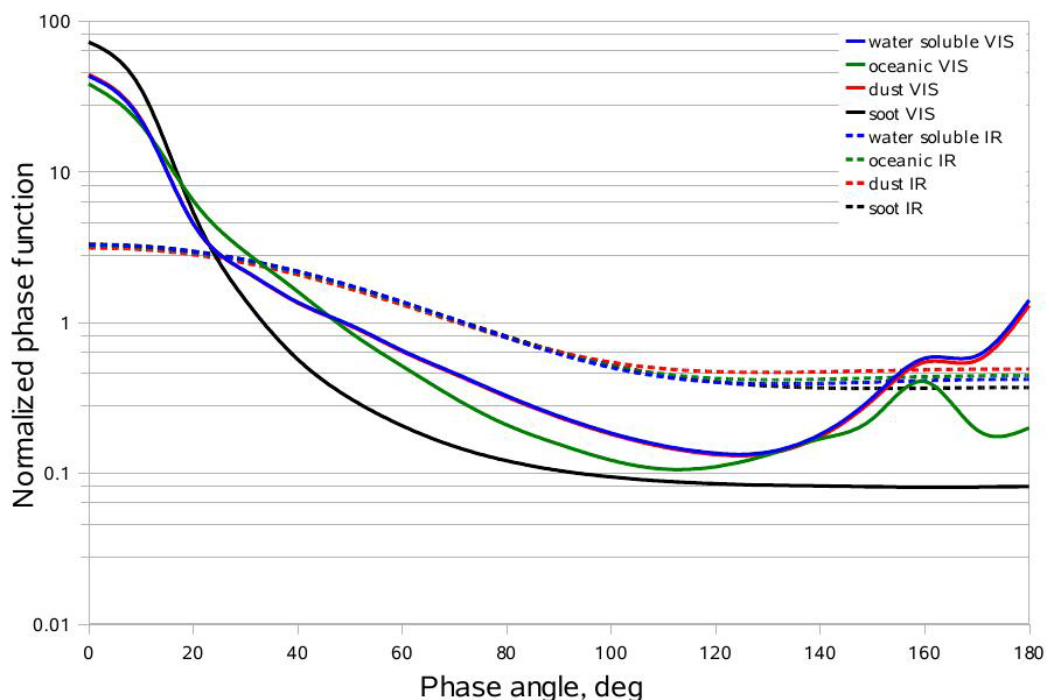


Figure 3.23. Phase functions for accumulation mode of oceanic, water soluble, dust and soot aerosol components calculated spherical polydisperse particles at 550nm (VIS, continuous line in the figure) and 3.7 μ m (IR, dashed line in the figure). The phase functions are normalized to unity, see SSA in text.

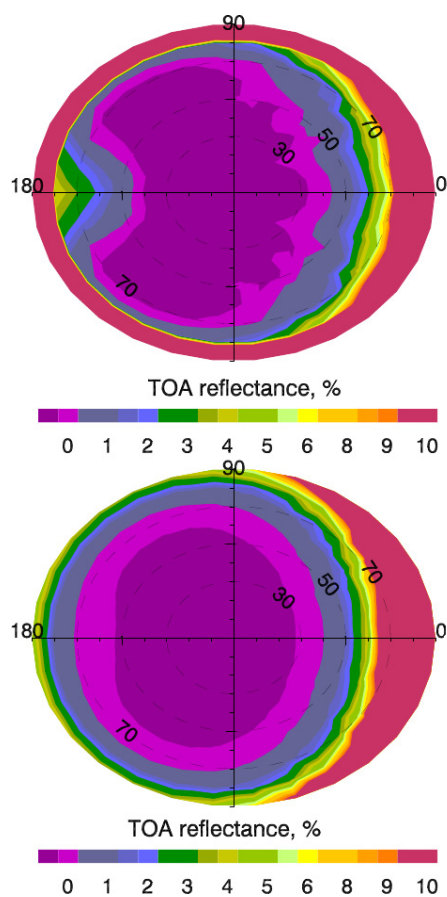


Figure 3.24. Angular behavior of aerosol reflectance for coarse mode of dust aerosol component 550nm (upper panel) and at 3.7µm (lower panel). Sun zenith angle is equal to 65 degrees, AOT=0.1.

Table 3.1. SSA, real n and imaginary χ part of the refractive index for coarse and accumulation mode of water soluble, oceanic, dust and soot aerosol components at 550nm.

Aerosol component	Refractive index		SSA	
	n	χ	Coarse mode	Accumulation mode
Water soluble	1.530	6.00E-03	0.75	0.92
Oceanic	1.381	4.26E-09	1.00	1.00
Dust	1.530	8.00E-03	0.71	0.89
Soot	1.750	4.40E-01	0.55	0.50

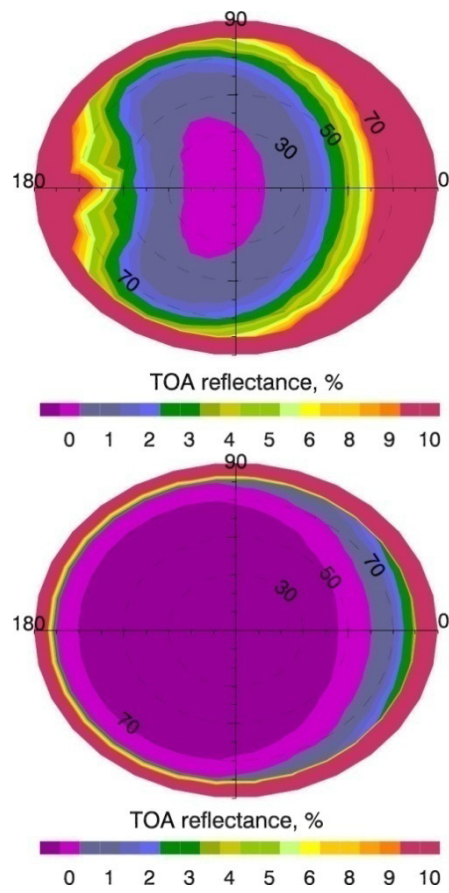


Figure 3.25. Angular behavior of aerosol reflectance for accumulation mode of dust aerosol component 550nm (upper panel) and at 3.7μm (lower panel). Sun zenith angle is equal to 65 degrees, AOT=0.1.

Table 3.2. SSA, real n and imaginary χ part of the refractive index for coarse and accumulation mode of water soluble, oceanic, dust and soot aerosol components at 3.7 μm.

Aerosol component	Refractive index		SSA	
	n	χ	Coarse mode	Accumulation mode
Water soluble	1.452	4.00E-03	0.97	0.96
Oceanic	1.398	2.90E-03	0.97	0.96
Dust	1.270	1.10E-02	0.91	0.74
Soot	1.900	5.7E-01	0.49	0.38

3.4.2 Theoretical basis

Unlike the AOT retrieval over snow in the VIS, the task of AOT retrieval over snow at 3.7 μm very much resembles the standard task of aerosol retrieval over dark surface (e.g. ocean) in the VIS. Some peculiarities, however, still exist. Some of them simplify the task, as e.g. negligible effect of Rayleigh scattering (and, correspondingly, surface elevation) at 3.7 μm , while the others are more challenging, like accurate extraction of atmospheric reflectance from the measured AATSR BT at 3.7 μm . The theoretical background and the details of LUT calculations are described in the further 3 subsections. Although current work is dedicated to aerosol retrieval, the discussed IR approach can also be used for the detection and retrieval of cloud properties over snow, providing an advantageous alternative to existing cloud retrieval methods over snow.

It is known that AATSR brightness temperature (BT) product measured at 3.7 μm is contaminated by atmospheric reflectance. Spangenberg et al. (2001) suggested a way to remove this contamination and extract reflectance $\rho_{atm}(3.7, \mu_0, \mu, \varphi)$ from the BT. This approach has been initially meant to be used for cloud/snow discrimination, as snow surface at a given wavelength is an almost perfect black body and does not reflect, whereas clouds (even thin cirrus) do have reflective properties. Like clouds, aerosol layers also cannot be considered to be black bodies, so their reflectance at 3.7 μm is not zero. The magnitude of this effect is much lower than that of clouds, however, good calibration of IR channels of AATSR (better than 0.1 Kelvin (Smith et al., 2001)) makes it possible to use this effect for AOT retrieval.

The already mentioned RTE solution for the system "surface + atmosphere" is the following:

$$\rho_{TOA}(\lambda, \mu_0, \mu, \varphi) = \rho_{atm}(\lambda, \mu_0, \mu, \varphi) + \frac{\rho_{sfc}(\lambda) \cdot T_1(\lambda, \mu_0) T_1(\lambda, \mu)}{1 - \rho_{sfc}(\lambda) \cdot s(\lambda)} \quad (3.17)$$

where $\theta = \arccos \mu$ is the observation zenith angle, φ is the relative azimuth angle, $\rho_{TOA}(\lambda, \mu_0, \mu, \varphi)$ is the total reflectance of the system "surface + atmosphere", $\rho_{atm}(\lambda, \mu_0, \mu, \varphi)$ is the atmospheric reflectance (the reflectance of the aerosol, Rayleigh scattering, ozone absorption), $s(\lambda)$ is the atmospheric hemispherical albedo, $T_1(\lambda, \mu_0) = E(\mu_0) + \exp(-\tau/\mu_0)$ is the atmospheric transmittance from TOA to the surface, $T_2(\lambda, \mu) = E(\mu) + \exp(-\tau/\mu)$ is the total atmospheric transmittance from the surface to a receiver (e.g., placed on a satellite), $E(\mu_0)$ and $E(\mu)$ are diffuse transmittances from TOA to the surface and from the surface to the receiver respectively, $\exp(-\tau/\mu_0)$ and $\exp(-\tau/\mu)$ are direct transmittances from top-of-atmosphere to the surface and from the surface to the receiver respectively, $\rho_{sfc}(\lambda)$ is the Lambertian reflectance of the surface.

Of course, Eq. 3.17 is still valid at 3.7 μm and can be written as:

$$\rho_{TOA}(3.7, \mu_0, \mu, \varphi) = \rho_{aer}(3.7, \mu_0, \mu, \varphi) + \rho_{sfc}(3.7) \quad (3.18)$$

where $\theta = \arccos \mu$ is the observation zenith angle, φ is the relative azimuth angle, $\rho_{TOA}(3.7, \mu_0, \mu, \varphi)$ is the calculated reflectance of the system "surface + atmosphere" at 3.7 μm , $\rho_{aer}(3.7, \mu_0, \mu, \varphi)$ is the aerosol reflectance at 3.7 μm (interpolated from LUT). Here

we neglect Rayleigh scattering and multiple scattering between the surface and the atmosphere, and assume that AOT is very small.

To estimate $\rho_{TOA}(3.7, \mu_0, \mu, \varphi)$ from $BT(3.7\mu m)$, we invert the Planck function in order to find the temperature corresponding to the radiance measurement at $3.7 \mu m$ and extract the reflectance part of it. This method used by Allen et al. (1990), Trepte et al. (1999), Spangenberg et al. (2001). The radiance measured at $3.7 \mu m$ can be expressed as following:

$$L_{3.7\mu m} = \varepsilon_{3.7\mu m} \cdot B_{3.7\mu m}(T_{surf}) + \rho_{TOA}(3.7, \mu_0, \mu, \varphi)L_0\mu_0 \quad (3.19)$$

where $\varepsilon_{3.7\mu m}$ is the surface emittance at $3.7 \mu m$, $B_{3.7\mu m}(T_{surf})$ is the Planck function at $3.7\mu m$ for the surface temperature, which is approximated by measured BT at $12 \mu m$. L_0 is the incident solar radiance at $3.7 \mu m$.

The first term of right hand side of Eq. 3.19 is the contribution to the measured radiance from the thermal emission of the surface assuming the transmittance of the atmosphere to be equal to 1. The second term on the right hand side is the contribution to the measured radiance due to the solar reflection. The amount of the reflected solar radiance reaching the satellite is determined by the incident solar radiance L_0 weighted by the cosine of the solar zenith angle μ_0 and the bidirectional reflectance of the surface and the atmosphere $\rho_{TOA}(3.7, \mu_0, \mu, \varphi)$.

Using Eq. 3.19, we can write:

$$\rho_{TOA}(3.7, \mu_0, \mu, \varphi) = \frac{B_{3.7\mu m}(T_{3.7\mu m}) - \varepsilon_{3.7\mu m} \cdot B_{3.7\mu m}(T_{12\mu m})}{\mu_0 \cdot S_{3.7\mu m}} \quad (3.20)$$

where $T_{3.7\mu m}$ is the measured $3.7\mu m$ brightness temperature, $T_{12\mu m}$ is the measured $12\mu m$ brightness temperature, μ_0 is the cosine of solar zenith angle, $S_{3.7\mu m}$ is the solar constant at $3.7\mu m$ ($3.47 \text{ Wm}^{-2}\mu\text{m}^{-1}$), $\varepsilon_{3.7\mu m}$ is the clear snow emittance, $B_{3.7\mu m}(BT)$ is the Planck function at $3.7\mu m$ for some temperature BT.

It is important to note that in case of surface being a perfect black body, the term $\rho_{sfc}(3.7)$ $\rho_{sfc}(3.7)$ in Eq. 3.18 is equal to zero. However, snow emissivity $\varepsilon_{3.7\mu m}$ may be not constant throughout the scene; therefore surface contamination can be still possible and is included in Eq. 3.18. As can be seen from Fig. 3.22 and 3.23, aerosol reflectance in the nadir direction is negligibly small. Within this assumption, relatively high nadir values of calculated $\rho_{TOA}(3.7, \mu_0, 0, \varphi)$ would mean that emissivity $\varepsilon_{3.7\mu m}$ used in the calculation is different from the real emissivity of the scene, and $\rho_{TOA}(3.7, \mu_0, 0, \varphi)$ is nothing but the surface contamination which needs to be subtracted from the forward TOA reflectance $\rho_{TOA}(3.7, \mu_0, 55, \varphi)$ in order to get the forward aerosol reflectance $\rho_{aer}(3.7, \mu_0, 55, \varphi)$.

Within the assumption of no angular variability of snow emissivity, we can get the surface-free aerosol reflectance:

$$\rho_{aer}(3.7, \mu_0, 55, \varphi) = \rho_{TOA}(3.7, \mu_0, 55, \varphi) - \rho_{TOA}(3.7, \mu_0, 0, \varphi) \quad (3.21)$$

This $\rho_{aer}(3.7, \mu_0, 55, \varphi)$ is used for the LUT interpolation.

Our particular case of low sun angles requires careful accounting for airmasses, different from that usual to plane-parallel atmosphere model. For RT calculations of LUTs, we use pseudospherical model of the atmosphere. To correct AATSR measured quantities, we use

approximation described in Kasten, Young (1989). To perform the comparison of the retrieved AOTs to the ground based measurements, we bring all the AOTs at 3.7 μm to 500nm using a fixed Angström parameter equal to 1.0.

3.4.3 Sensitivity study

In order to check the performance of Eq. 3.19 and Eq. 3.20, we performed RT simulations with the forward model SCIATRAN. For this we simulated 3.7 μm and 11 μm brightness temperatures for both nadir and forward views for a surface with the temperature 263 K and atmosphere with the AOT from 0 to 1 at 550nm. The illumination angle is equal to 65°, observation angles are 0° and 55° respectively, the relative azimuth angle is equal to 0°. We also calculated the TOA reflectance at 3.7 μm for the same conditions. The difference between the simulated TOA reflectance at 3.7 μm and the one reconstructed from the BT using Eq. 3.19 is shown in Fig. 3.26 for the both viewing geometries. The color filled areas represent the error in the reconstructed TOA reflectance at 3.7 μm , which occurs due to calibration error of AATSR BT product of $\pm 0.1\text{K}$. The relative error of such a reconstruction is around 1% for the forward view and around 12% for the nadir view, which appears to be reasonable as the nadir view reflectance has much smaller order of magnitude in comparison to the forward view reflectance.

Then, these reconstructed TOA reflectances at 3.7 μm were used for the AOT retrieval according to Eq. 3.19. The relative error of the retrieved AOT depending on the input AOTs is shown in Fig. 3.27. Again, the color filled areas represent the error in the retrieved AOT which occurs due to the calibration error in AATSR BT product of $\pm 0.1\text{K}$. As our simulations did not include any surface, the simulated retrieval was performed without the surface correction introduced in Eq. 3.21. The simulation shows that the sensitivity of retrieved AOT to the AATSR BT calibration error of $\pm 0.1\text{K}$ is around several percent.

3.4.4 Choosing the aerosol type and LUT calculation

Unlike e.g. Rayleigh scattering, the phase function of which is well known, aerosol reflectance $\rho_{aer}(\lambda, \mu_0, \mu, \varphi)$ is variable due to different particle size distribution, particle shape and chemical composition, which affects single scattering albedo and extinction of aerosol layer. Aerosol reflectance is therefore highly dependent on illumination-observation geometry; it also varies between the aerosol types. Similar to the case of LUT for the AOT retrieval in the VIS, it is impossible to create one atmospheric LUT which would represent aerosol properties well on global scale, and we do not pursue this task. For our case of the Arctic aerosol, we took the advantage of ground based aerosol measurements and created a LUT using phase function and single scattering albedo values measured in situ during one of the regular pollution events in Arctic (Treffeisen et al., 2007; Stohl et al., 2007).

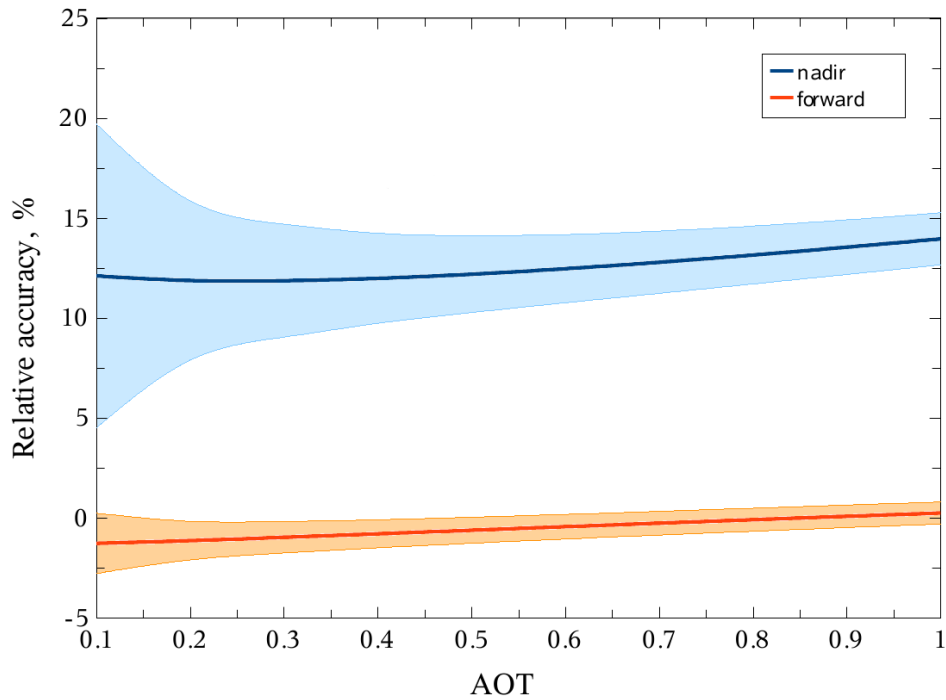


Figure 3.26. Relative error of TOA reflectance reconstructed from the BT at $12\mu\text{m}$ and $3.7\mu\text{m}$ for the forward (red curve) and nadir (blue curve) views. Filled areas show the sensitivity of the TOA reflectance at $3.7\mu\text{m}$ to the AATSR calibration error of $\pm 0.1\text{K}$.

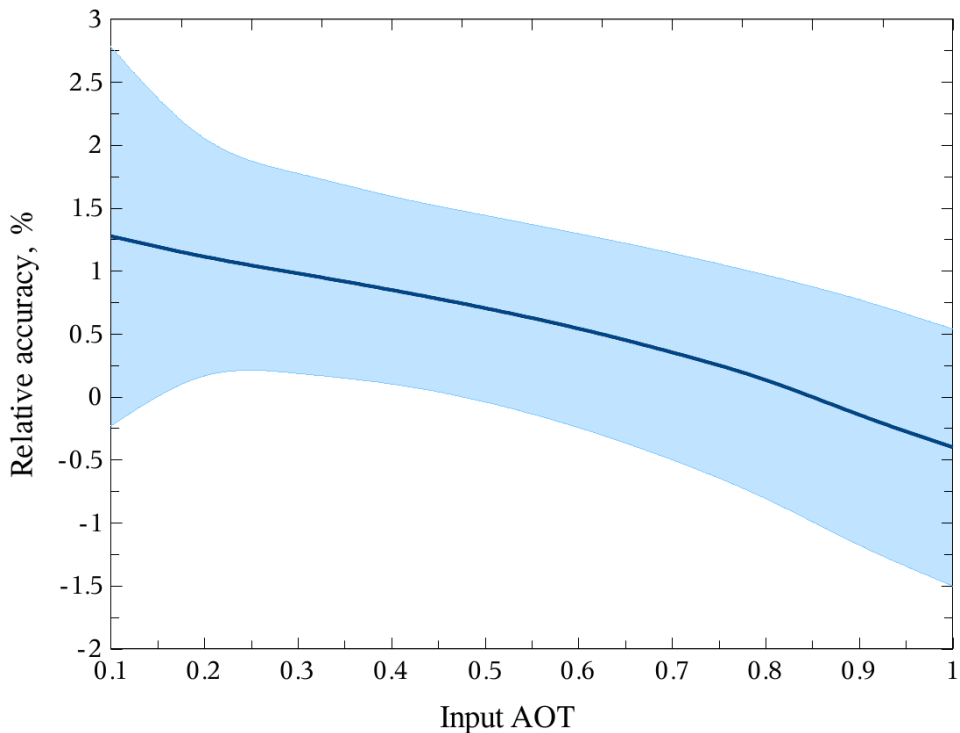


Figure 3.27. The relative error of the retrieved AOT for a given input AOT (blue line). The color filled area shows the sensitivity of the retrieved AOT to the AATSR BT calibration error of $\pm 0.1\text{K}$.

3 Developing the satellite aerosol retrieval

It has been measured on 23.03.2000 at Spitsbergen, Ny Ålesund, Svalbard, 78.923° N 11.923° E, by the Alfred Wegener Institute for Polar and Marine Research at 867 nm. The AOT at 550nm was around 0.15, single scattering albedo 0.74 with the average Angström alpha equal to 1.46. This phase function is shown in Fig. 3.28. One can see the clear resemblance of this phase function to the IR phase functions in Fig. 3.22, despite of the much shorter wavelength. The LUT has been calculated for a variety of illumination geometries (solar zenith angle from 35° to 85° with the step of 10°), observation geometries (viewing zenith angle from 0° to 90° with the step of 10°) and relative azimuth angles (from 0° to 180° with the step of 12°). The AOT range was from 0 to 1 (at 500nm). The LUT has been calculated with the single scattering albedo equal to 0.90 at 550nm and 0.71 at 3.7μm, which corresponds to the accumulation mode of the dust-like aerosol (see Table 3.1 and 3.2). It is important to note that the current phase function corresponds to a certain particle size distribution (Angström alpha value of 1.46). While this spectral slope of aerosol is quite common (as seen from AERONET data for Arctic stations), larger or smaller particles can cause large scatter of the reflectance data, which would cause similar scatter in the retrieved AOTs. This scatter can be reduced only with aerosol-type sensitive retrieval, which requires multispectral observations. Over snow this task is quite challenging and will be solved in the next versions of the retrieval.

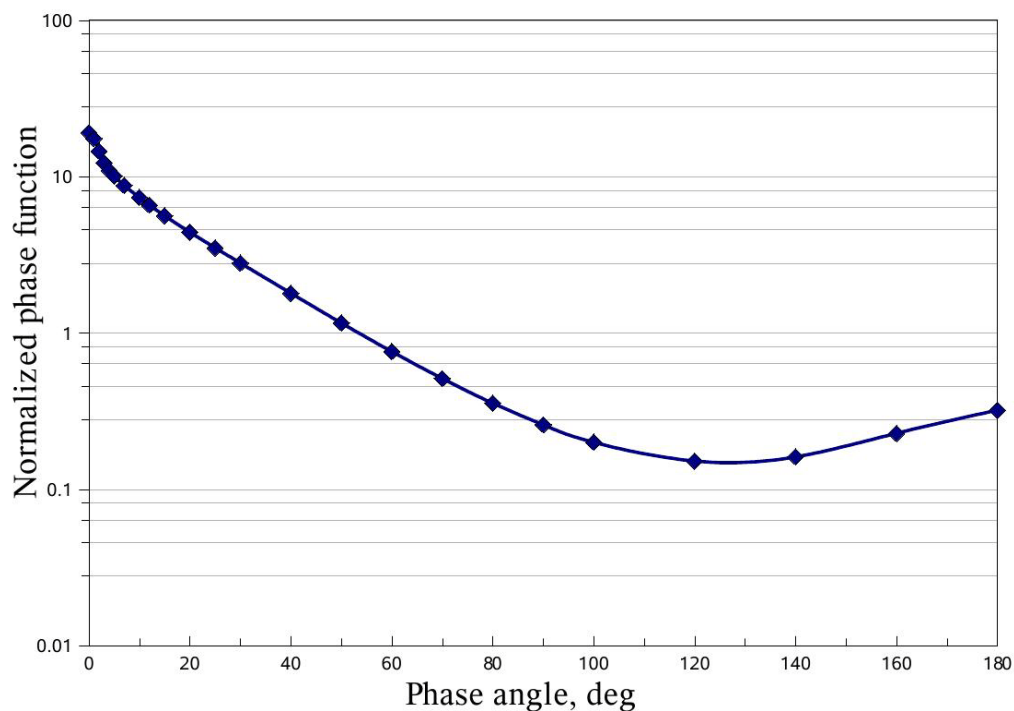


Figure 3.28. The phase function of Arctic haze measured on 23.03.2000 during one of the regular haze events at Spitsbergen, Ny Ålesund, Svalbard, 78.923° N 11.923° E, by the Alfred Wegener Institute for Polar and Marine Research at 867 nm.

3.4.5 Application limits and sources of errors

As in case of the AOT over snow retrieval in the visible spectral region, there are 4 main problematic points to consider:

1. Illumination geometry

At $3.7 \mu\text{m}$ the amount of solar radiation reflected from the atmosphere is much less than that in the visible spectral region; this makes the forward scattering directions preferable for the IR retrieval in comparison with the moderate scattering angles due to greater values of measured TOA reflectances. As the forward RT modeling shows, the nadir and backscattering directions do not contain sufficient atmospheric signal at the given wavelength. Therefore the IR AOT retrieval only operates within the $0^\circ - 90^\circ$ interval of the relative azimuth angles.

Opposite to the AOT retrieval in the visible spectral range, the similarity of the IR phase functions of different aerosol components ensure the IR AOT retrieval to “guess” the aerosol phase function even at the extreme scattering angles. In the case of negligible surface reflectance, this allows us to utilize the full range of the solar zenith angles – 40° to 90° .

2. Surface properties

Unlike the AOT retrieval in the visible spectral region, where the surface reflectance needs to be high enough for the assumption of low atmospheric effect to hold, in the IR the surface reflectance needs to be low enough to let the atmospheric signal be detectable.

As was already shown in the subsection 3.3.5, the surface directional reflectance properties vary with time of the year as the surface type evolves; at $3.7 \mu\text{m}$ this evolution of the surface type only has negative consequences if the surface becomes a less perfect black body. In case of snow covered sea ice evolving to melting sea ice and eventually open water, the surface stays a black body and therefore the IR AOT retrieval can be applied over any of these surfaces. The case of snow covered terrain, vegetation or mountains is more complicated as none of these surfaces can be considered to be black bodies at this wavelength in the snow free state. We leave it to our snow flagging algorithm to only pick out surfaces or mixtures of surface types exhibiting mainly snow-like behavior.

When such pixels are picked out, the problem of snow reflectance at $3.7 \mu\text{m}$ is solved under an assumption that the nadir TOA reflectance only contains the signal from the surface and that eventual surface reflectance does not depend on the direction. While the first assumption will be discussed later, the assumption about snow being a Lambertian reflector at $3.7 \mu\text{m}$ has been discussed by Spangenberg et al. (2001). It has been shown that the directional TOA reflectance of snow covered scenes increases with the increase of the observational zenith angle from 0° to 60° by approximately 0.006. This difference in TOA reflectance corresponds to the layer of Arctic haze with the AOT of about 0.05-0.1, depending on geometry, which is quite close to the background aerosol layer in the Arctic and might have been overlooked by Spangenberg et al. In that case, the directional dependence of snow TOA reflectance is negligible and our assumption about snow being a Lambertian reflector is correct; in the opposite case, the error in the retrieved AOT might be around 0.05-0.1.

3. Aerosol type

Due to the similarity of the phase functions of the aerosol components in the IR the varying aerosol chemical composition should not present a problem for the algorithm applications; however, particle size distribution presents limitations. Though regularly occurring Arctic haze appears to be rather similar from year to year, for more general applications of the algorithm the aerosol types and sources other than the Arctic haze should be considered. The IR TOA reflectance of the aerosol fine mode ($<0.5 \mu\text{m}$) is under the detection limits of the AATSR sensor. The AOT of these particles cannot be retrieved with the presented IR retrieval. Therefore, the performance of the retrieval will only refer to the amount of the coarse and accumulation mode particles present in the scene. For larger particles, the limitation on the relative azimuth angles becomes less strict; for smaller particles, the performance of the retrieval is best for the principal plane and forward scattering region.

Another point to be considered is the recalculation of the AOT retrieved at $3.7 \mu\text{m}$ to the visible wavelength, e.g. 500 nm . Unfortunately, such a recalculation has to be done for validation and comparison studies. It is obvious that the accuracy of such a recalculation will depend on aerosol particle size distribution, and we can expect underestimation of AOT(500nm) for aerosol consisting of mainly small particles both due to low scattering efficiency of these particles in the IR spectral region and due to insufficient spectral slope while recalculating into the VIS spectral region. The opposite is valid for larger particles, AOT of which might be overestimated. Overall, the fixed Angström exponent while recalculating the IR AOT into VIS might cause AOT dependent scatter in the AOT(500nm) of up to $0.5 \cdot \text{AOT}$ for $\text{AOT} < 0.3$, depending on the difference in aerosol types.

4. Aerosol amount

Aerosol amount affects the performance of the IR AOT retrieval algorithm for three following reasons:

1. Possible surface contamination and its incorrect correction due to directional properties of snow IR reflectance is relatively less for larger aerosol amounts.
2. The accuracy of AOT recalculation into the visible wavelength, or the accuracy of the aerosol spectral slope “guess”, is of immense importance for significant aerosol loads as the amplitude of scatter in case of the wrong guessed Angström parameter increases with the AOT.
3. As increasing the aerosol amount increases the TOA aerosol reflectance in both nadir and forward directions, the assumption about the measured nadir TOA reflectance only containing surface signal is no longer valid in case of an increased aerosol load. In this case, the true TOA forward aerosol reflectance will be reduced (see Eq. 12) by the value of the nadir TOA aerosol reflectance of that aerosol layer. It is important to note that for low solar elevations the TOA aerosol reflectance at nadir is of 10^{-2} order of magnitude even for $\text{AOT}=1.0$, which is our uncertainty level for the surface directional variability and produces the AOT error of ± 0.1 . Due to very rare occurrence of large AOT (>0.3) in the Arctic, this problem is not considered in the current version of the algorithm, but will be solved in its future versions.

In total, the possible error of the AOT retrieved with the IR retrieval is induced by the surface uncertainty δ_{surf} , AATSR calibration error δ_{calibr} , unknown aerosol type $\delta_{Angström}$ and can be expressed as

$$\delta_{AOT,IR} = \delta_{surf} + \delta_{calibr} + \delta_{Angström} = \pm 0.1 \pm 0.53 \cdot AOT$$

For the summary of the IR AOT retrieval algorithm specifications, see Table 3.3.

3.5 Summary

The developed AOT retrieval algorithm contains of the three parts. They are:

1. snow/cloud discrimination;
2. AOT retrieval over snow and ice in the VIS spectral region;
3. AOT retrieval over snow and ice in the IR spectral region.

These parts of the algorithm will be briefly summarized here.

Snow/cloud discrimination

The cloud/snow discrimination was performed as introduced in Istomina et al. (2010).

It uses a combination of relative thresholds in seven AATSR channels in order to discriminate the spectral behavior of clear snow scene from that of cloud, land, ocean, etc. These criteria connect nadir top of atmosphere reflectances in visible (Eq. 3.5, 3.6), near-infrared (Eq. 3.1) and brightness temperatures in thermal infrared (Eq. 3.2, 3.3) regions of spectrum.

$$\left| \frac{BT(3.7 \mu m) - BT(10.8 \mu m)}{BT(3.7 \mu m)} \right| < 3\% \quad (3.5)$$

$$\left| \frac{BT(3.7 \mu m) - BT(12 \mu m)}{BT(3.7 \mu m)} \right| < 3\% \quad (3.6)$$

$$\frac{R_{TOA}(0.87 \mu m) - R_{TOA}(1.6 \mu m)}{R_{TOA}(0.87 \mu m)} > 80\% \quad (3.1)$$

$$\frac{R_{TOA}(0.87 \mu m) - R_{TOA}(0.66 \mu m)}{R_{TOA}(0.87 \mu m)} < 10\% \quad (3.2)$$

$$\left| \frac{R_{TOA}(0.66 \mu m) - R_{TOA}(0.55 \mu m)}{R_{TOA}(0.66 \mu m)} \right| < 40\% \quad (3.3)$$

While the visible (VIS) and near-infrared (NIR) criteria (Eq. 3.1, 3.5, 3.6) select scenes with the spectral behavior similar to snow spectrum, the thermal infrared (TIR) thresholds (Eq. 3.2, 3.3) distinguish cloud free areas over surfaces with emissivity close to unity (snow, open ocean). The combination of both VIS/NIR and TIR criteria makes it possible to distinguish various states of the system „surface+atmosphere“. For example, cloud free case would correspond to conditions (Eq. 3.2) and (Eq. 3.3) being true, due to the absence of „stray“ cloud reflectance at 3.7 μm . On the contrary, if the TIR criteria (Eq. 3.2) and (Eq. 3.3) are false, there is a non black body present in the scene – either a cloud, or e. g. bare soil area. True VIS (Eq. 3.5, 3.6) and NIR criteria (Eq. 3.1) mean that the observed spectrum is close to

3 Developing the satellite aerosol retrieval

a snow spectrum, which could mean snow, ice cloud, or thin water cloud over snow as well. If at least one of VIS/NIR criteria is false, there is a possibility of either a thick water cloud with the NIR (Eq. 3.1) criterion failing, or surface which a spectrum different from that of snow (e.g. ocean, bare soil, vegetation, etc).

AOT retrieval over snow in the visible and infrared parts of spectrum

After the cloud free snow covered scenes have been picked out, the AOT retrieval takes place. It can be done in two different ways, at 550nm or at 3.7 μ m. Both AOT retrieval algorithms utilize the AATSR dual-view observational scheme and LUT approach.

In the **visible AOT retrieval**, the forward and nadir views are used in the ratio in order to remove the influence of the surface albedo and reduce the role of the unknown surface directional reflectance properties. Therefore, only the asymmetry of directional reflectance of the scene between forward and nadir views is used for the AOT retrieval:

$$\frac{\rho_{sfc}^f(\lambda, \mu_0, \mu, \varphi)}{\rho_{sfc}^n(\lambda, \mu_0, \mu, \varphi)} = \frac{\rho_{TOA}^f(\lambda, \mu_0, \mu, \varphi) - \rho_{atm}^f(\lambda, \mu_0, \mu, \varphi)}{\rho_{TOA}^n(\lambda, \mu_0, \mu, \varphi) - \rho_{atm}^n(\lambda, \mu_0, \mu, \varphi)} \cdot \frac{T_2^n(\lambda, \mu)}{T_2^f(\lambda, \mu)} \quad (3.9)$$

It is also used to approximate the forward to nadir ratio of the surface BRDF, along with the simulated atmospheric correction.

$$\frac{\rho_{sfc}^f(550, \mu_0, \mu, \varphi)}{\rho_{sfc}^n(550, \mu_0, \mu, \varphi)} = \frac{\rho_{sfc,sim}^f(550, \mu_0, \mu, \varphi)}{\rho_{sfc,sim}^n(550, \mu_0, \mu, \varphi)} \cdot \frac{\rho_{TOA,sim}^n(550, \mu_0, \mu, \varphi, \tau)}{\rho_{TOA,sim}^f(550, \mu_0, \mu, \varphi, \tau)} \cdot \frac{\rho_{TOA}^n(550, \mu_0, \mu, \varphi)}{\rho_{TOA}^f(550, \mu_0, \mu, \varphi)} \quad (3.10)$$

where all terms are defined as in Sect. 3.3.2.

The AOT is then found in iterations as a root of the Eq. 3.9.

The **infrared AOT retrieval** is based on the assumption of snow being an almost perfect black body. The AATSR BT at 3.7 μ m is extracted in order to get the TOA reflectance at 3.7 μ m according to Spangenberg et al. (2001):

$$\rho_{TOA}(3.7, \mu_0, \mu, \varphi) = \frac{B_{3.7\mu m}(T_{3.7\mu m}) - \varepsilon_{3.7\mu m} \cdot B_{3.7\mu m}(T_{12\mu m})}{\mu_0 \cdot S_{3.7\mu m}} \quad (3.20)$$

The resulting IR TOA reflectance for the nadir view is assumed to only consist of the surface signal, whereas the forward IR TOA reflectance contains atmospheric signal together with the surface contamination. Under the assumption of no angular variability of snow emissivity, one can get the surface-free aerosol reflectance

$$\rho_{aer}(3.7, \mu_0, 55, \varphi) = \rho_{TOA}(3.7, \mu_0, 55, \varphi) - \rho_{TOA}(3.7, \mu_0, 0, \varphi) \quad (3.21)$$

which is then used for the LUT-based AOT retrieval. All the terms are defined as in Sect. 3.4.2.

The applicability limits of both IR and VIS AOT retrieval algorithms are presented in Table 3.3.

Table 3.3. Comparison of features of the IR and VIS AOT retrieval algorithms

	VIS (550nm)	IR (3.7μm)
Solar zenith angle	40° – 75°	40° – 90°
Relative azimuth	0° – 180°	0° – 90°
Viewing angle	Dual view	Forward
Aerosol	Total AOT (Arctic Haze)	Coarse mode, > 0.5 μ m (Arctic Haze)
Surface	Clean, bright snow (bright surface is needed for the ratio assumptions to be held)	Black body-like surfaces (ocean, sea ice and snow – also melting)
Accuracy	Surface induced absolute AOT error ± 0.1 for AOT(550nm) < 0.3 and coinciding aerosol type.	Surface and aerosol type induced absolute AOT error = $\pm 0.1 \pm 0.5 \text{AOT}$ for AOT(550nm) < 0.3. Relative AOT error induced by AATSR BT calibration for coinciding aerosol type $\pm 3\%$.

4 Validation

All the parts of the AOT over snow retrieval algorithm developed within this work have been validated against independent ground based and spaceborne measurements. Current section describes the following validation studies:

- validation of the developed cloud clearing/snow flagging routine against MODIS and micro-pulse lidar data;
- validation of the VIS and IR AOT against ground based AERONET data;
- comparison of the resulting AOT over snow with the corresponding AOT over ocean retrieved with the independent BAER algorithm using MERIS data.

The validation studies described in this section are performed over the widest available range of AOT values, from background to pollution events, on a very local spatial scale (corresponding to the ground based stations). The AOT retrievals on larger spatial scale up to the whole North Polar region have also been performed for selected pollution events. These case studies are described in Section 5.

4.1 Comparison to MPL and MODIS data

A reliable cloud screening method is very important for aerosol retrievals, as clouds that contaminate the retrieved AOT are able to drastically distort the quality of the aerosol product. On the other hand, quality validation of cloud screening methods against other space borne instruments is a difficult task, mainly due to the fast evolution and relocation of clouds and following difficulties with the collocation of the two cloud products of interest.

The cloud clearing method described before has undergone a rather extensive validation on a sequence of AATSR data for spring 2006, at Spitsbergen (approximately 100 scenes) against the Micro-Pulse Lidar network data (Welton et al., 2001; Campbell et al., 2002). The frequency of correct detections is 95% of cases, with resulting 5% of wrong detections being connected to thin clouds (Fig. 4.1), or to a particular case of surface (Fig. 4.2).

Both figures show the scene over Spitsbergen, with the Micro Pulse Lidar located in Ny Ålesund (78°.91667N, 11°.93300E), in the western part of the island. For the Fig. 4.1 (11.05.2006) the MPL indicates the presence of a very thin cloud at 1 km altitude. The discussed cloud screening technique is not able to see it. The MODIS cloud mask shown for comparison is also not able to detect cloud for this point. At the same time, good

4 Validation

correspondence of the two cloud masks throughout the rest of the image is reassuring. The reason of the wrong detection for this case might be the size of the cloud: subpixel cloud detection with a radiometer is a separate task which is out of scope of the current research.

Fig. 4.2 shows the same scene, but on 08.05.2006. According to the MPL, the Ny Ålesund area is cloud free, but our cloud clearing method does not detect clear snow at this point. The MODIS cloud product indicates this area as “probably clear”, which is inconclusive. Studying the AATSR reflectances shows slightly darker surface. This might be shadowing by mountains or extremely contaminated snow surface. Such surfaces are screened out as they are not clear snow.

It is obvious that thin and subpixel clouds would present a challenge for our cloud screening method; they are simply not thick enough to disturb the spectral shape of the pixel

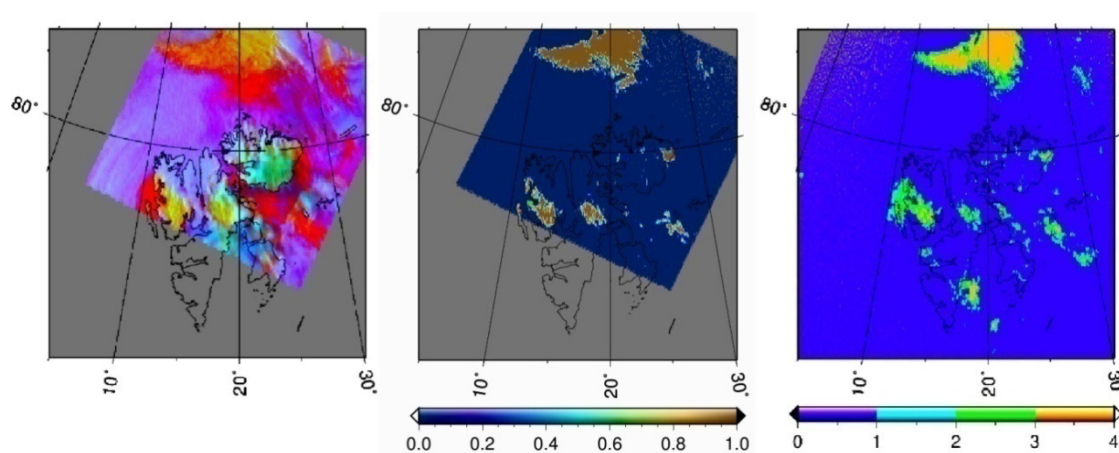


Figure 4.1. Left panel shows the false color composite (red is $11\mu\text{m}$ BT, green is 550nm reflectance, blue is $1.6\mu\text{m}$ reflectance) of the initial AATSR scene, 11 May 2006, 16h26'26", orbit number 21938; middle panel is the screened AATSR scene, probability of clean snow; right panel is MODIS cloud mask: 1 – cloudy, 2 – probably cloudy, 3 – probably clear, 4 - clear. MODIS scene is for 11.05.2006, 16h40'.

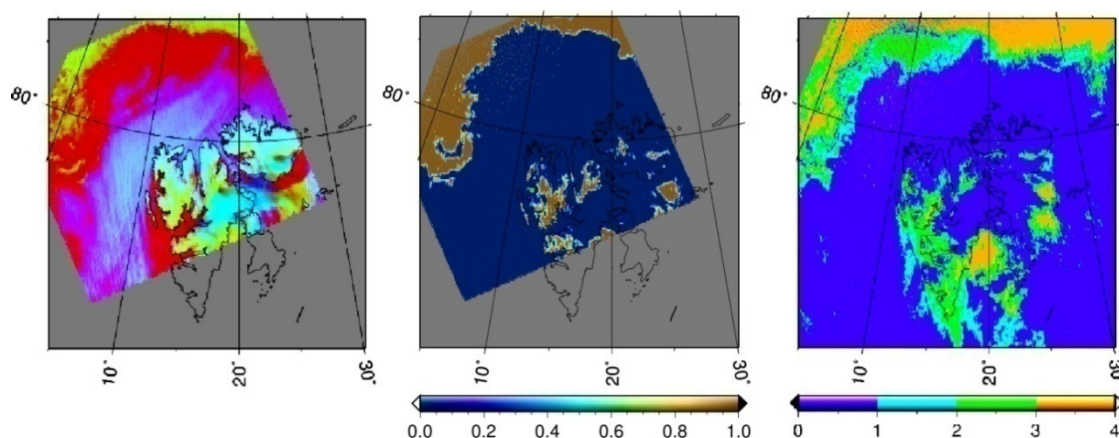


Figure 4.2. Left panel shows the false color composite (red is $11\mu\text{m}$ BT, green is 550nm reflectance, blue is $1.6\mu\text{m}$ reflectance) of the AATSR scene, 08 May 2006, 13h02'12", orbit number 21893; middle panel is the screened AATSR scene, probability of clean snow; right panel is MODIS cloud mask: 1 – cloudy, 2 – probably cloudy, 3 – probably clear, 4 - clear. MODIS scene is for 08.05.2006, 12h55'.

significantly. Restricting the spectral shape criteria would solve this problem, also reducing the fraction of contaminated snow scenes in the output data and leaving only fresh clean snow. This cloud clearing regime might be very useful for snow surface studies such as snow grain size or snow albedo, because it screens out all the cases with more or less pronounced atmospheric component, also with the aerosol load present. However, such a regime is not applicable to aerosol retrievals, where various aerosol loads are needed. In other words, the spectral shape criterion can be adjusted to fit the certain task. For the AOT retrieval, we allow a rather wide scatter in the spectral shape criteria in order to keep the natural atmospheric variety of the data. This also ensures that various (perhaps challenging) snow types will be present in the data serving as an input to further AOT retrievals.

The comparison to MODIS and operational AATSR cloud masks for different kinds of snow surface

A set of AATSR scenes from both Northern and Southern hemispheres has been processed in order to check the performance of the presented cloud screening method over different kinds of snow surface. The results were compared to the operational AATSR cloud mask from level 1b AATSR product, and to the MODIS cloud product. As the exact temporal collocation of AATSR and MODIS is impossible, the closest available observation was chosen. This issue does not allow pixel-to-pixel collocation of the two sensors, therefore the comparison is presented for visual analysis. It is important to understand the difference between the conventional cloud mask product (MODIS, operational AATSR) and our clear snow flag: cloud masks detect cloudy or clear conditions over any kind of surface, which is not necessarily clear snow. This invokes differences between the presented snow flag product and the conventional cloud masks; these, however, tend to be rather small over the snow-covered Arctic scenes.

The results of the presented snow flagging method are shown together with MODIS and AATSR operational cloud mask for eight different cases of clouds over different snow surfaces (Figs. 3.7, 3.8, 4.3-4.8). They include scenes over Alaska, Greenland, the Scandinavian Peninsula, Northern part of Russia, Himalayan mountains, Antarctica and feature snow, snow covered sea ice and land ice, snow covered mountains and peaks, snow covered forest.

Figs. 3.7, 3.8, 4.3-4.6 indicate the good correspondence of the presented snow flag to MODIS derived clear areas. Clouds are not mistaken for snow (Fig. 4.3). Flat snow, either on ice or on land, is a convenient surface for cloud screening (Figs. 3.7, 3.8, ice part of Fig. 4.5). Snow covered mountain peaks are well recognized (Figs. 4.3, 4.4, 4.7). Snow covered forest (Fig. 4.4) is recognized not continuously; only single brightest snow pixels are detected. The presented method appears to be a stricter than the MODIS cloud mask. E.g., the case of smooth snow surface (as seen in the MODIS cloud mask) is not recognized very well (Fig. 4.8, Antarctica). The reason is most probably the illumination-observation geometry or some type of snow here overlooked, which is located outside the suggested spectral shape criterion. Extensive research is needed to understand if this is the feature of all the Antarctic snow or just the feature of one special day or location.

AATSR operational cloud mask corresponds to MODIS and developed here snow flag rather well in some cases (Fig. 4.3, 4.4, lower part of Fig. 4.5). In other cases it shows poor

4 Validation

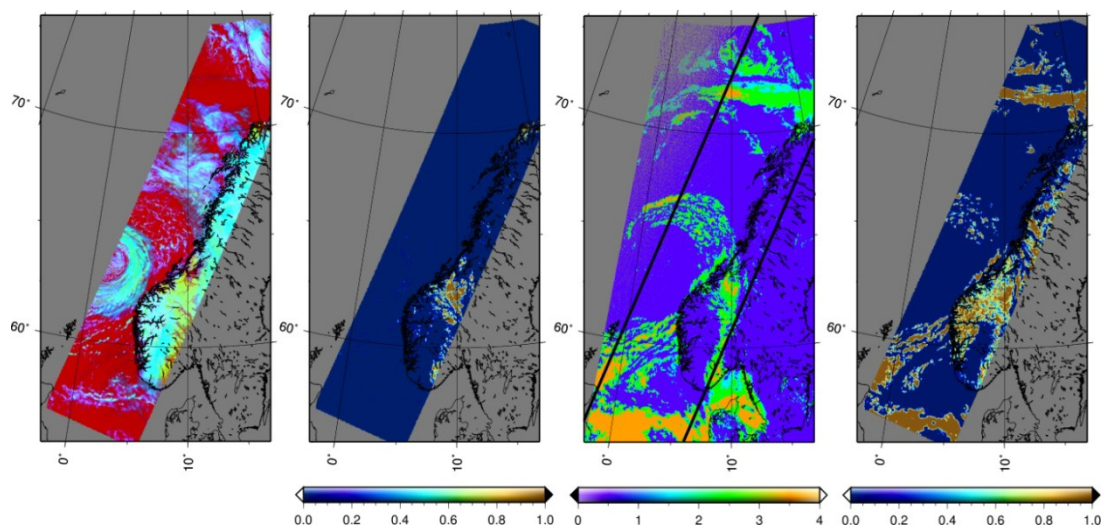


Figure 4.3. Scandinavian Peninsula, AATSR: 14 April 2006, 10h38'17", orbit number 21547. MODIS: 14 April 2006, 10h35'. Left panel is the false color composite (red is 11 μ m BT, green is 550nm reflectance, blue is 1.6 μ m reflectance) of initial AATSR scene; second left panel is the clear snow mask of AATSR scene (0 – not snow, 1 – clear snow) achieved with presented method; third left panel is MODIS cloud mask: 1 – cloudy, 2 – probably cloudy, 3 – probably clear, 4 – clear; right panel is operational AATSR cloud mask from level-1b product: 0 – cloudy, 1- clear.

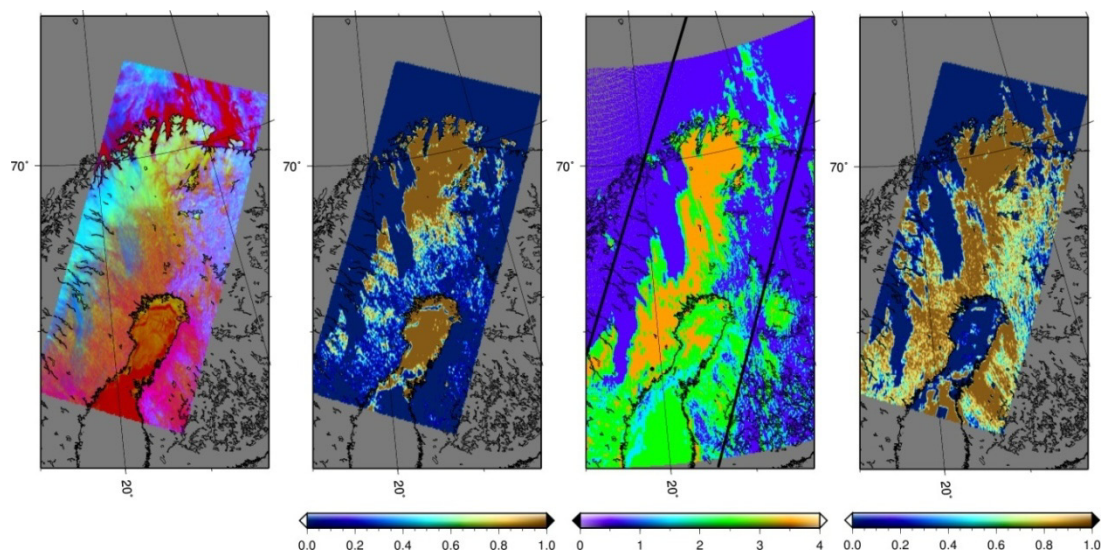


Figure 4.4. Scandinavian Peninsula, AATSR: 22 April 2006, 09h47'27", orbit number 21661. MODIS: 22 April 2006, 09h40'. Left panel is the false color composite (red is 11 μ m BT, green is 550nm reflectance, blue is 1.6 μ m reflectance) of initial AATSR scene; second left panel is the clear snow mask of AATSR scene (0 – not snow, 1 – clear snow) achieved with presented method; third left panel is MODIS cloud mask: 1 – cloudy, 2 – probably cloudy, 3 – probably clear, 4 – clear; right panel is operational AATSR cloud mask from level-1b product: 0 – cloudy, 1- clear.

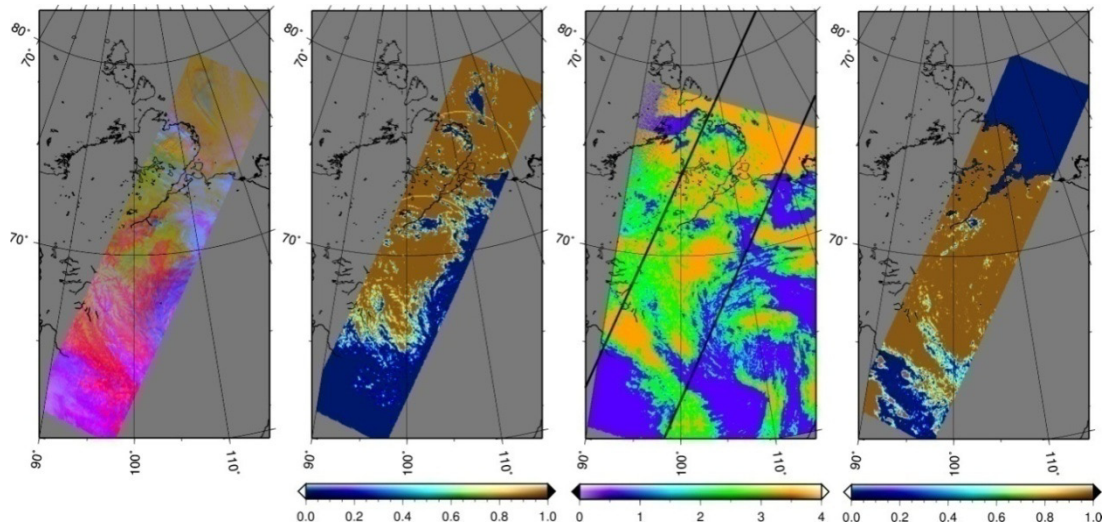


Figure 4.5. Northern part of Russia. AATSR: 22 April 2006, 04h43'20", orbit number 21658. MODIS: 22 April 2006, 04h45'. Left panel is the false color composite (red is $11\mu\text{m}$ BT, green is 550nm reflectance, blue is $1.6\mu\text{m}$ reflectance) of initial AATSR scene; second left panel is the clear snow mask of AATSR scene (0 – not snow, 1 – clear snow) achieved with presented method; third left panel is MODIS cloud mask: 1 – cloudy, 2 – probably cloudy, 3 – probably clear, 4 – clear; right panel is operational AATSR cloud mask from level-1b product: 0 – cloudy, 1- clear.

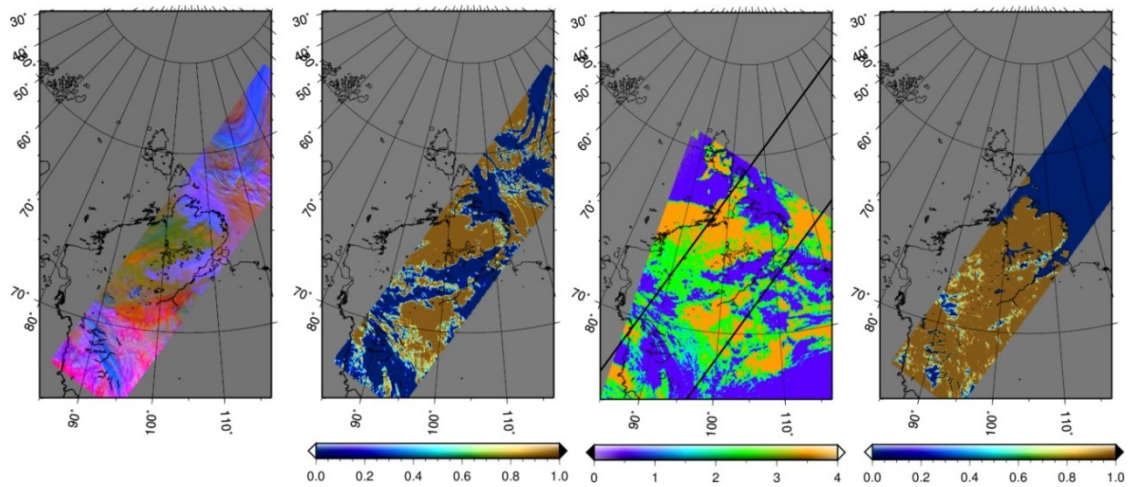


Figure 4.6. Northern part of Russia. AATSR: 21 April 2006, 05h13'21", orbit number 21644. MODIS: 21 April 2006, 05h40'. Left panel is the false color composite (red is $11\mu\text{m}$ BT, green is 550nm reflectance, blue is $1.6\mu\text{m}$ reflectance) of initial AATSR scene; second left panel is the clear snow mask of AATSR scene (0 – not snow, 1 – clear snow) achieved with presented method; third left panel is MODIS cloud mask: 1 – cloudy, 2 – probably cloudy, 3 – probably clear, 4 – clear; right panel is operational AATSR cloud mask from level-1b product: 0 – cloudy, 1- clear.

4 Validation

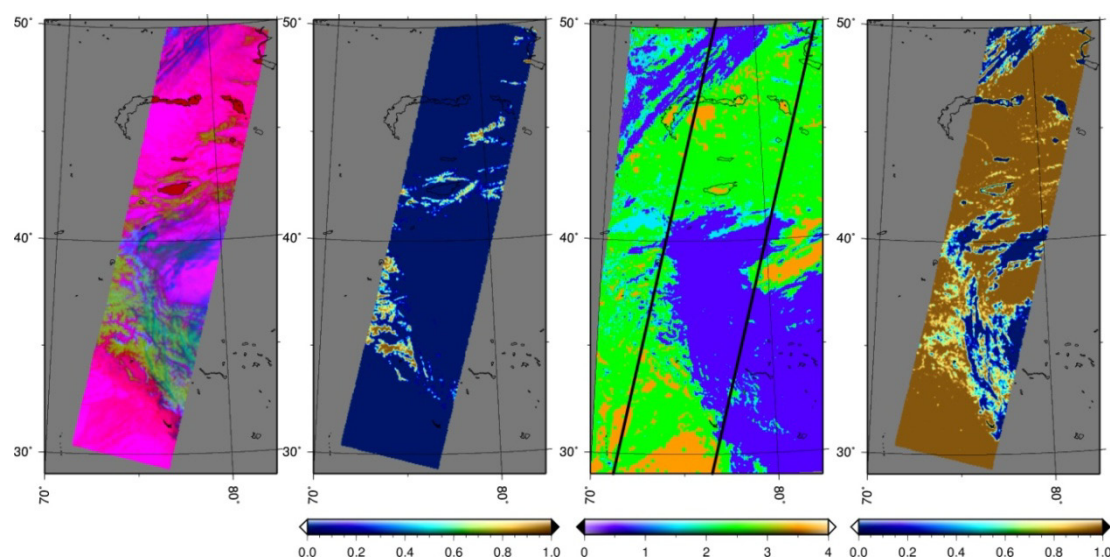


Figure 4.7. Himalayan mountains. AATSR: 18 April 2006, 05h17'59", orbit number 21601. MODIS: 18 April 2006, 05h20'. Left panel is the false color composite (red is 11µm BT, green is 550nm reflectance, blue is 1.6 µm reflectance) of initial AATSR scene; second left panel is the clear snow mask of AATSR scene (0 – not snow, 1 – clear snow) achieved with presented method; third left panel is MODIS cloud mask: 1 – cloudy, 2 – probably cloudy, 3 – probably clear, 4 – clear; right panel is operational AATSR cloud mask from level-1b product: 0 – cloudy, 1- clear.

performance, while presented snow flag and MODIS cloud mask still correspond well (Fig. 3.7, 3.8 4.5, 4.6). The AATSR operational cloud mask (initially developed for use over ocean) is not always reliable over snow surfaces and therefore was not used for our AOT retrieval. In general, according to the comparison to MODIS cloud mask, the quality of the presented cloud/snow discrimination appears to be reasonably good.

4.2 Comparison with AERONET

The VIS AOT retrieval algorithm

The VIS AOT retrieval algorithm has been validated against ground based AERONET data from the four high Arctic stations. They are:

- Barrow (N71°18'43", W156°39'54"), altitude 0 m.
- Resolute Bay (N74°43'58", W94°54'00"), 40 m.
- Hornsund (N77°00'00", E15°33'00"), 10 m.
- Longyearbyen (N78°13'22", E15°38'56"), 30 m.

The first two AERONET stations are located in the Western Hemisphere; Barrow is located at the Arctic Plains, Alaska, US, on the shore of Beaufort Sea. The climate at Barrow can be characterised as the polar desert. Resolute Bay is located at the Queen Elizabeth Islands,

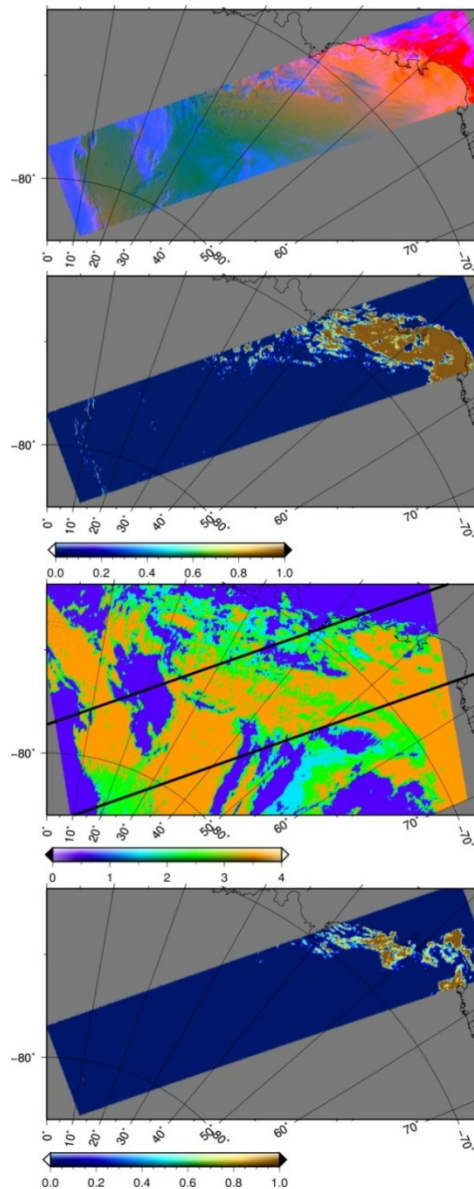


Figure 4.8. Antarctica, AATSR: 20 January 2006, 05h16'00", orbit number 20341. MODIS: 20 January 2006, 05h00'. Top panel is the false color composite (red is $11\mu\text{m}$ BT, green is 550nm reflectance, blue is $1.6\mu\text{m}$ reflectance) of initial AATSR scene; second from top panel is the clear snow mask of AATSR scene (0 – not snow, 1 – clear snow) achieved with presented method; third from top panel is MODIS cloud mask: 1 – cloudy, 2 – probably cloudy, 3 – probably clear, 4 – clear; lowest panel is operational AATSR cloud mask from level-1b product: 0 – cloudy, 1 – clear.

Nunavut, Canada, on the shore of the Arctic Waterway. Hornsund and Longyearbyen AERONET stations are both located at the Svalbard archipelago, Norway. Longyearbyen is the administrative centre of Svalbard and is located on the western coast of Spitsbergen, the largest island of the Svalbard archipelago. Longyearbyen has an Arctic tundra climate. Station Hornsund is located on the northern shore of the Hornsund fjord at the southern part of Spitsbergen. None of these stations is located at the permanent snow cover; the available

4 Validation

data points were thoroughly analyzed manually and with the snow flagging routine before the validation. Most of the data points were screened out due to cloudiness or insufficient snow cover. All AERONET data with extreme values of Angström coefficient for 440-870 nm (less than 0.5 and more than 2.0) were not taken into account. The maximum allowed time difference between the AATSR overflight and the AERONET measurement was equal to 15 minutes. The AERONET AOT value has been compared to the mean AOT, retrieved from the satellite around given station within the 5 km radius. allowed The result is shown in Fig. 4.9.

Unfortunately, AERONET data for these Arctic stations overlapping with the AATSR overflights are sparse, therefore it was impossible to pick a sufficient set of points of one haze event at one station. Therefore we picked available AERONET measurements, taken from April to June during years 2003-2008. As we only use one aerosol type – “Arctic haze”, we only took the spring measurements. However, spatial and temporal heterogeneity of the measurements of course plays its role. The solid brown line in Fig. 4.9 is the linear regression for all the stations, the correlation coefficient equals to 0.32. Detailed look onto each AERONET station can give an impression on the spatial dependence of the correlation quality. E.g. for Barrow station AERONET AOTs and retrieved values correspond rather well, whereas for, e.g. Resolute Bay we can observe significant overestimation of retrieved AOT. This can indicate the wrong aerosol type, which makes the implementation of aerosol type detection necessary. Most of the points in Fig. 4.9 are located within the 0.05 corridor along 1 to 1 line.

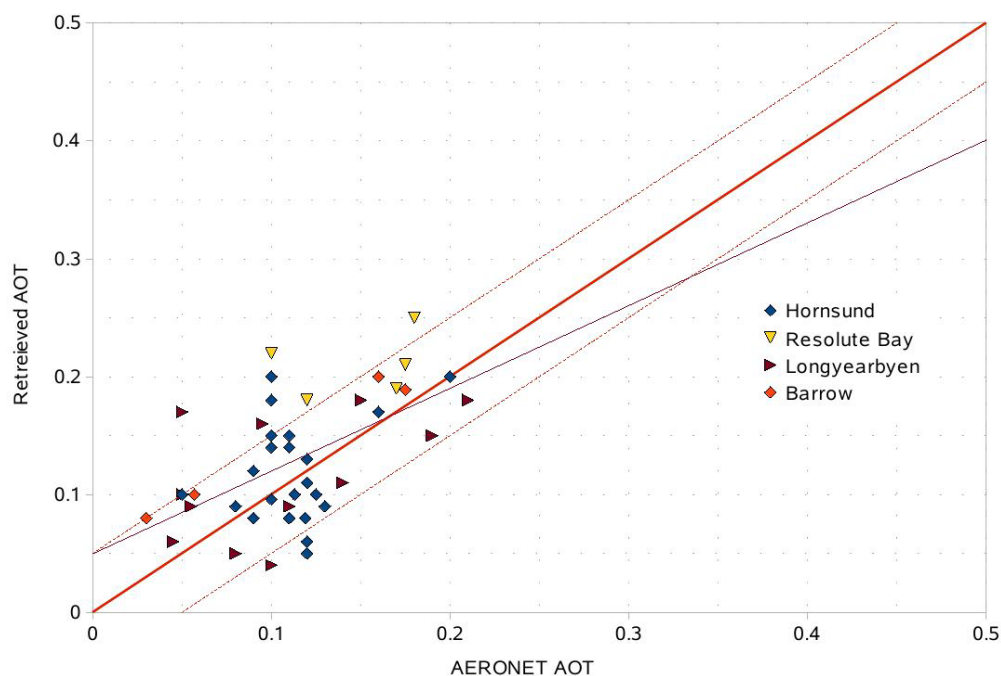


Figure 4.9. Correlation between AERONET data for the four high Arctic stations and retrieved AOT at 550nm. The correlation is station dependent; most of the point are within the 0.1 scatter from the 1 to 1 line. RMSD = 0.0482, $R^2 = 0.32$.

The IR AOT retrieval algorithm

The IR AOT retrieval algorithm has been validated against AERONET measurements for the four high Arctic stations. The chosen stations feature frequent AATSR overflights and provide statistically significant amount of data in long datasets. These stations are OPAL (N 79°59'24'', W 85°56'20'', altitude 0 m), PEARL (N 80°03'14'', W 86°25'01'', altitude 615 m), Thule (N 76°30'57'', W 68°46'08'', altitude 225 m), Kangerlussuaq (N 66°59'45'', W 50°37'15'', altitude 320 m). The first three stations are located on the fjords of Queen Elisabeth Islands and Knud Rasmussen Land; and the latter is located at the south-western shore of Greenland. It is visible that none of the stations is located on a permanent snow cover and feature clear snow in spring and bare soil and rocks in summer and autumn. This would lead to losing the vast majority of the validation data. To avoid this, we have chosen a point within 1 ° of longitude and 0.5 ° of latitude away from each station, possibly located on the permanent snow cover (for Greenland) or on the sea ice (for Queen Elisabeth Islands). Thus we shift from snow/bare soil/rocks mixture to melting sea ice, which is generally darker than snow but still keeps most of snow properties and is not screened out. An analysis of the cloud screened validation dataset for e.g. station OPAL is shown in Fig. 3.21. It is visible that most of the points are from summer months and feature quite low TOA reflectance at 550nm together with high surface temperatures (yet below 0 °C). This corresponds to the surface type “melting sea ice without snow cover”. Low temperatures and high TOA reflectances at 550nm are the features of the springtime points which are “snow covered sea ice”. AOT retrieval is possible over both of these surface types.

The validation dataset for PEARL contains approximately 200 points and 130 points for OPAL. These points are from spring and summer of years 2007, 2008, 2009. Stations Thule and Kangerlussuaq provided with less cloud free observations; in addition, the location of these stations is such that overlapping with AATSR was poor. This gave around 40 points from years 2007 and 2008 for Thule, and 20 points from years 2008 and 2009 for Kangerlussuaq.

All the data has been cloud screened and snow flagged as described above. The extreme values of Angström coefficient for 440-870 nm (less than 0.5 and more than 2.0) in AERONET data were considered to be out of applicability ranges of our aerosol type assumptions. These were not taken into account. To ensure good temporal collocation between the AATSR overflight and the AERONET data, the the maximum allowed time difference between the two was set to not more than 15 minutes. We applied spatial averaging of the AATSR data within 0.1 ° of latitude and 1 ° of longitude around the earlier chosen point near the station. The range of sun zenith angles of the entire validation dataset is from approximately 55° to 75°, with the vast majority of the values around 60°. Average relative azimuth angle is approximately 30°.

The comparison has to be performed at 500nm as AERONET gives the best temporal coverage at this wavelength. To estimate the AOT at 500nm with the retrieval 3.7 μm, we use a fixed Angström parameter equal to 1.0. The correlation plot for each station is shown in Fig. 4.10 (OPAL), Fig. 4.11 (PEARL), Fig. 4.12 (Thule), Fig. 4.13 (Kangerlussuaq). The dashed line represents the linear regression of the data.

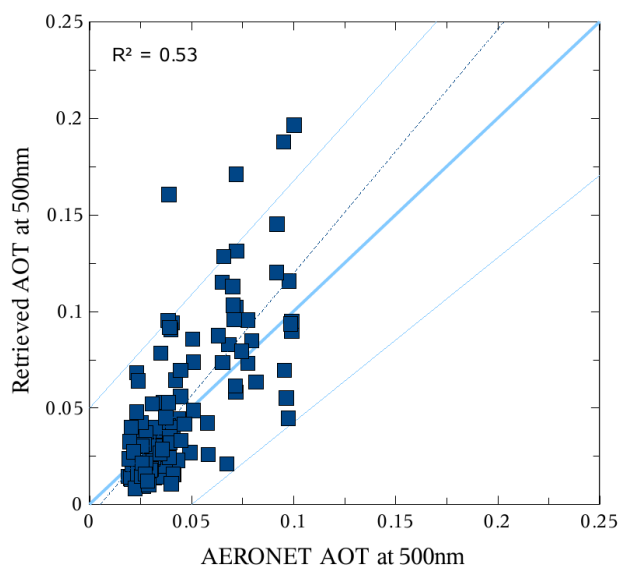


Figure 4.10. Comparison of the retrieved AOTs derived from AATSR product as $3.7\mu\text{m}$ and AERONET AOTs for station OPAL. The dashed line represents the linear regression of the data. $\text{RMSD} = 0.0283$, $R^2=0.53$.

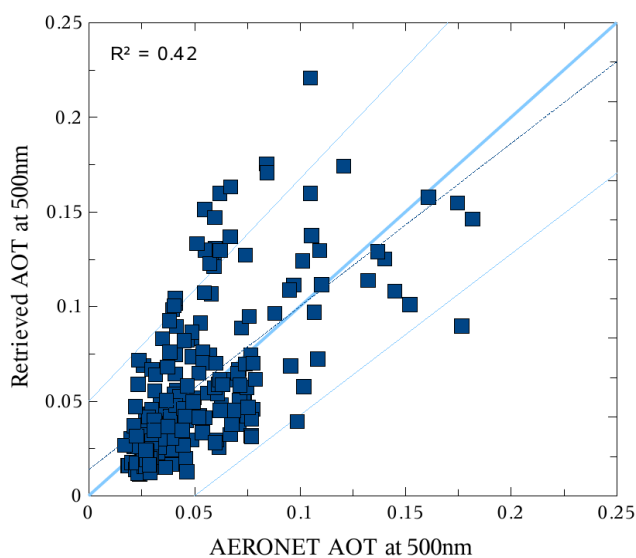


Figure 4.11. Comparison of the retrieved AOTs derived from AATSR product as $3.7\mu\text{m}$ and AERONET AOTs for station PEARL. The dashed line represents the linear regression of the data. $\text{RMSD} = 0.0329$, $R^2=0.42$.

Each of the correlation plots shows growth of the retrieved AOT scatter with the growth of ground based AOT. This can be explained by the greater relative influence of the aerosol type and the corresponding spectral slope for the larger AOT values. As we use the fixed Angström coefficient for all the AERONET range from 0.5 to 2.0 for 440-870 nm, this scatter is to be expected and can be corrected with the spectral AOT retrieval which is supposed to be the next version of the retrievals developed within this work.

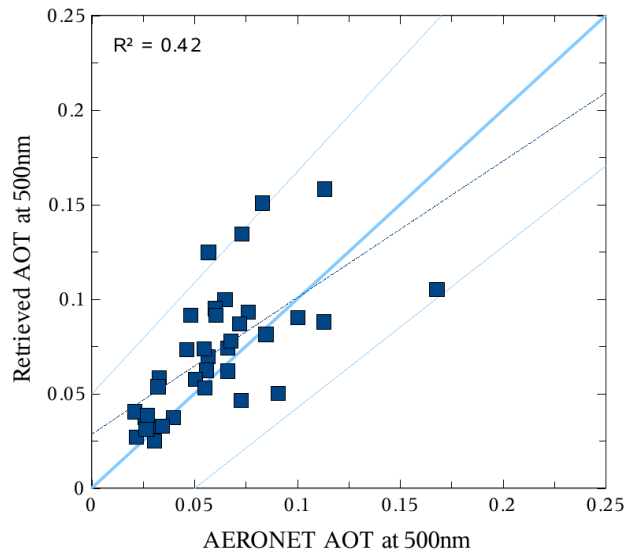


Figure 4.12. Comparison of the retrieved AOTs derived from AATSR product as $3.7\mu\text{m}$ and AERONET AOTs for station Thule. The dashed line represents the linear regression of the data. $\text{RMSD} = 0.0293$, $R^2=0.42$.

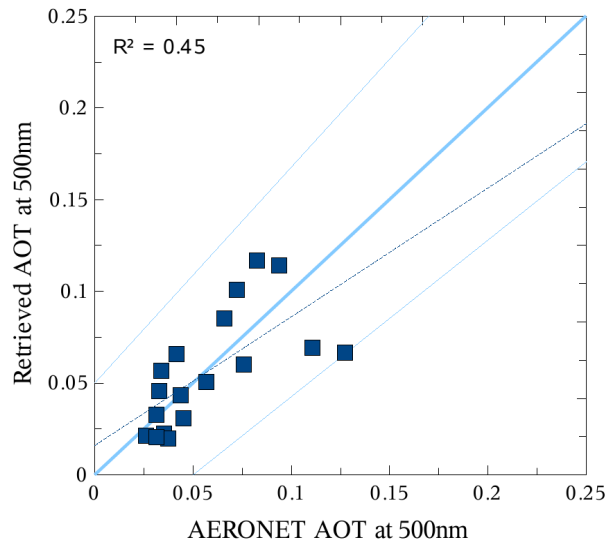


Figure 4.13. Comparison of the retrieved AOTs derived from AATSR product as $3.7\mu\text{m}$ and AERONET AOTs for station Kangerlussuaq. The solid line represents the linear regression of the data. $\text{RMSD} = 0.0289$, $R^2=0.45$.

At AOTs less than 0.1 the retrieval works satisfactory with no significant over- or underestimation. As the vast majority of AOT values in the Arctic are below 0.1, the retrieved AOT maps can give a good estimate of the AOT distribution over snow.

4.3 Comparison with MERIS

In the absence of other satellite AOT products over snow, it is possible to perform validation of the AOT retrieval algorithm over snow using the AOT products retrieved over other surfaces types. For this one can use matching areas of e.g. snow and open water and evaluate the quality of the match. Unlike ground based observations, such an approach has the advantage of similarity of the illumination-observation geometries and spatial resolution of the two products in question. For this purpose in the current work we use the Bremen Aerosol Retrieval (BAER) - an independent AOT retrieval over various surfaces (for our application, we use the AOT retrieved over open water), developed at the University of Bremen (Dinter et al., 2009). This retrieval utilizes single view (nadir) MERIS (MEdium Resolution Imaging Spectrometer) data and is able to retrieve AOT over various surfaces, from open water to bright reflecting desert. The advantage of this instrument is that it is located on the same satellite platform as the AATSR sensor (ENVISAT); therefore good temporal collocation of both instruments is possible. In addition, wide swath of MERIS (1150km against 512km of AATSR) creates spatial coverage which overlaps with and exceeds the AATSR coverage. This enables good spatial collocation. In order to perform the comparison between the two AOT products, over open water (MERIS data, BAER) and over snow (AATSR data, presented AOT retrieval), we need to find a cloud free location where snow-covered sea ice or land is surrounded by open water. The Svalbard archipelago meets this criterion. While the climate of Svalbard is dominated by its high latitude, with the average summer temperature at 4 C to 6 C and January averages at 12°C to -16 , the North Atlantic Current moderates Svalbard's temperatures causing an increase of up to 20 C higher than winter temperatures at similar latitudes in Russia and Canada. This keeps the surrounding waters open and navigable most of the year, which enables the BAER AOT retrieval algorithm over water to perform. The interior fjord areas and valleys, sheltered by the mountains, have larger temperature differences than the coast, causing colder winter temperatures and sufficient snow cover for the VIS AOT retrieval over snow. The complicated relief of Svalbard (see Svalbard elevation map in Fig. 4.14) presents a challenge for both snow flagging algorithm and AOT retrieval algorithm, due to the presence of various snow types, mountain shadows, and differently tilted surface in the scene.

A confirmed Arctic smoke event which happened in the beginning of May, 2006 at Spitsbergen has been chosen for the comparison of AOT products over snow covered land and over water. This event has been described by Treffeisen et al. (2007), Stohl et al. (2007), Eckardt et al. (2007). Agricultural fires in the Eastern Europe were the source of biomass burning aerosol, which was transported rapidly due to an atypically warm weather pattern in the European Arctic. The smoke was constrained to the lowest 2km in the troposphere during the transport. The deposition of the atmospheric aerosol caused a rapid decrease of the snow albedo during the episode; the samples of the polluted snow show elevated amounts of sulphate, nitrate, potassium and ammonium ions, confirming the relation of the snow discoloration to the biomass burning aerosols (Stohl et al., 2007).

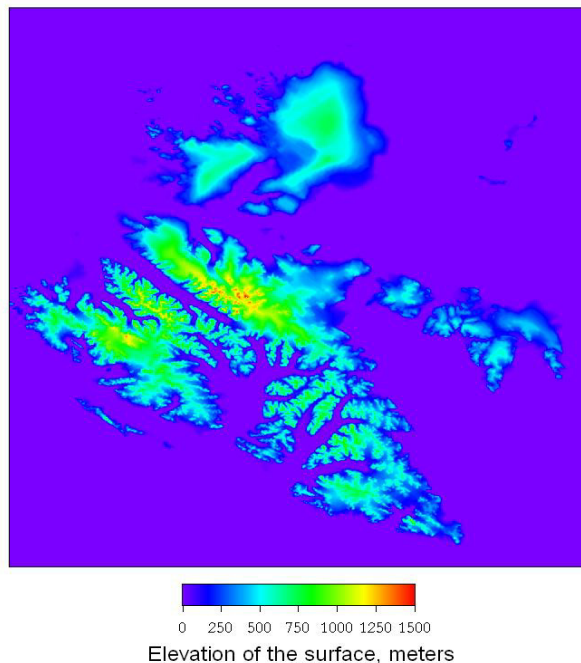


Figure 4.14. Elevation map of Svalbard archipelago; complicated relief of the mountainous areas creates a challenge for the snow flagging routine and the VIS AOT retrieval, due to the mixture of rocks, snow, mountain shadows in the mountain regions and bare soil with snow on the shores.

The global situation of the biomass burning aerosol being transported into the Arctic can be seen in the map of the AOT over open water retrieved with the BAER algorithm using MERIS data (Fig. 4.15). The arrow shows the direction of the aerosol transport into the Arctic.

The AATSR scene of Svalbard during the Arctic smoke event (3rd of May, 2006, 12:19.25, orbit number 21820), which features cloud free snow covered areas together with the open water, has been chosen for the comparison. The AATSR nadir view does not show any evidence of pollution at 550nm (Fig. 4.16).

As was discussed above, snow is not a Lambertian reflector. Therefore, the pixel where the surface has a tilt will show other directional reflectance properties (as opposed to a level surface). To the retrieval, this tilted pixel would appear to be a totally different type of surface with another BRDF. In the current version of the algorithm, such an anomaly of the surface BRDF for a given (satellite) observation-illumination geometry is treated within the forward to nadir ratio approach (Eq. 3.9, 3.10). This reduces the relief induced noise and the resulting AOT appears to be smoother and less surface dependent. The previous version of the retrieval (Istomina et al., 2009) was not able to interpret the brighter pixels caused by specular reflection off the snow surface correctly; such brighter pixels were interpreted as the AOT increase, and darker shadow pixels – as AOT decrease (not shown here). The current version of the algorithm does not show this artifact to such an extent. The comparison of the BAER product (AOT over water) and AOT over snow is shown in Fig. 4.17. The values over Svalbard were retrieved using the presented VIS AOT retrieval over snow and the AATSR data; all the other AOT values over open water were retrieved by BAER using the MERIS

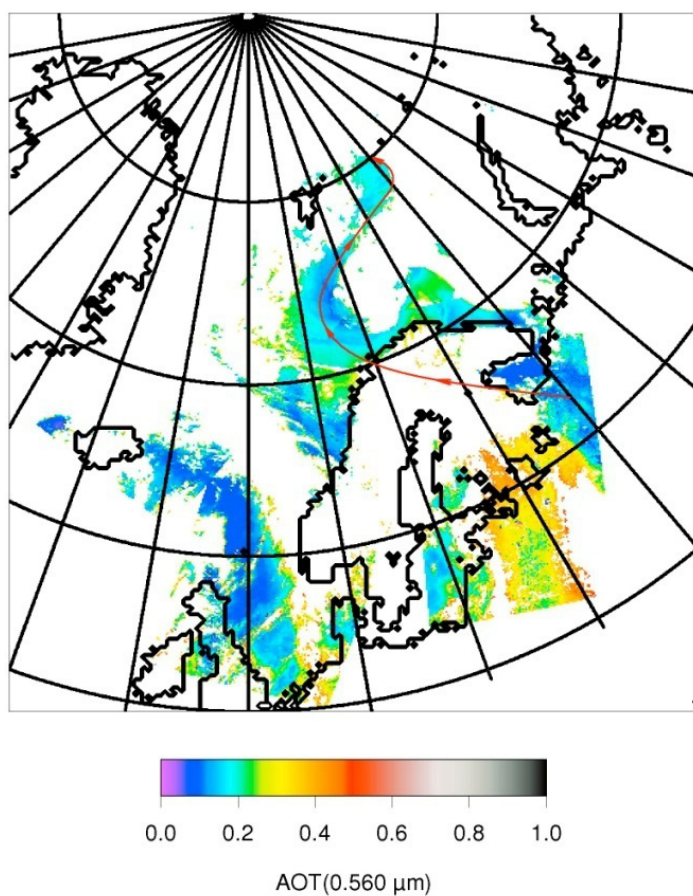


Figure 4.15. Agricultural fires caused a significant biomass burning pollution which was transported rapidly from the Eastern Europe into the Arctic. The arrow shows the direction of the aerosol transport to Svalbard archipelago, where the aerosol event has been observed at Ny Ålesund and Zeppelin stations. The AOT at 560nm was retrieved over open water with BAER algorithm using the data from MERIS sensor onboard ENVISAT.

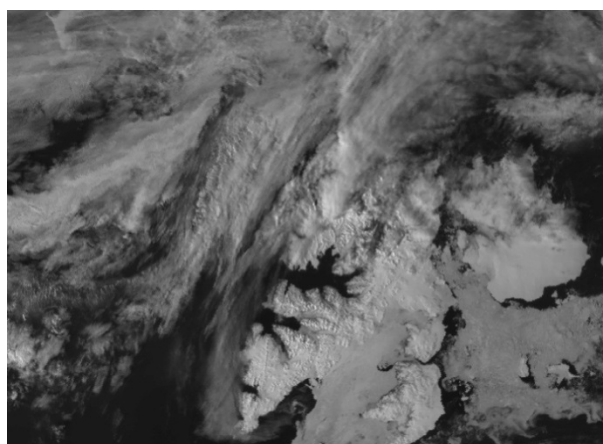


Figure 4.16. AATSR image for Spitsbergen, the 3rd of May, 2006, 12:19.25, orbit number 21820, 550nm channel, nadir view. The image does not show any evidence of the smoke aerosol present in the scene.

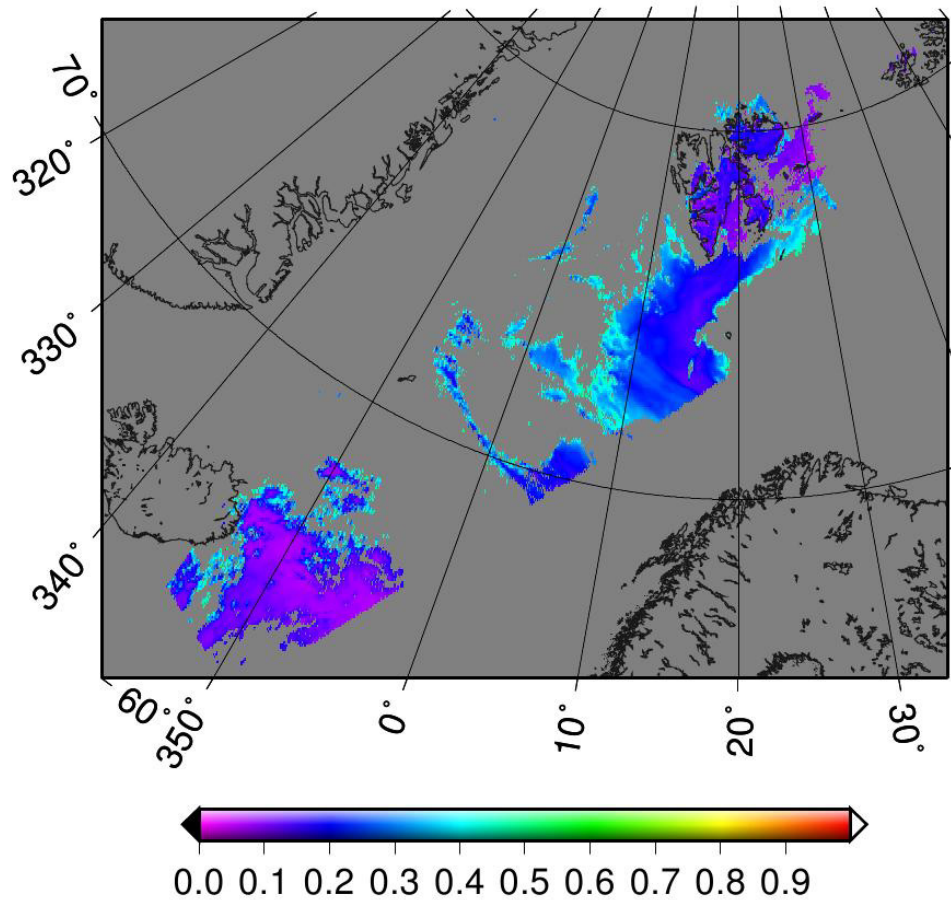


Figure 4.17. Comparison of BAER AOT over ocean (MERIS data) to AOT over snow (AATSR data), the 3rd of May 2006, 12:19.25, AOT retrieved at 550 nm. All the AOT values over Spitsbergen are over snow; all the other values are over open water. The higher AOT values at the edges of the BAER derived scene are probably due to partial cloud contamination.

data. The comparison shows no obvious difference between the AOT over snow and AOT over water and overall quite a good correspondence of the two independent retrievals to each other, with the AOT over snow following the biomass aerosol flow pattern indicated by the BAER product; the increased AOT at the edges of the cloudy areas are the residual cloud pixels and the transition between the cloudy and cloud free atmosphere; these increased values should not be taken into account during the analysis.

An attempt to evaluate the performance of the VIS AOT retrieval over snow has been made also using the AATSR data over water; for this we performed a simple single view retrieval over manually selected areas of open water, and interpolated the “Arctic Haze” LUT in order to retrieve the AOT for the each pixel; the surface was assumed to be absolutely black, i.e. all the TOA signal over open water was assumed to come from the atmosphere. This AOT retrieval over snow and open water has been made for the same AATSR scene of Spitsbergen, during the Arctic smoke event on the 3rd of May 2006, 12:19.25, orbit number 2180. Fig. 4.18 shows the result of this retrieval. The AOT values, marked with the red circles, are over open water. All the other values are over snow and ice.

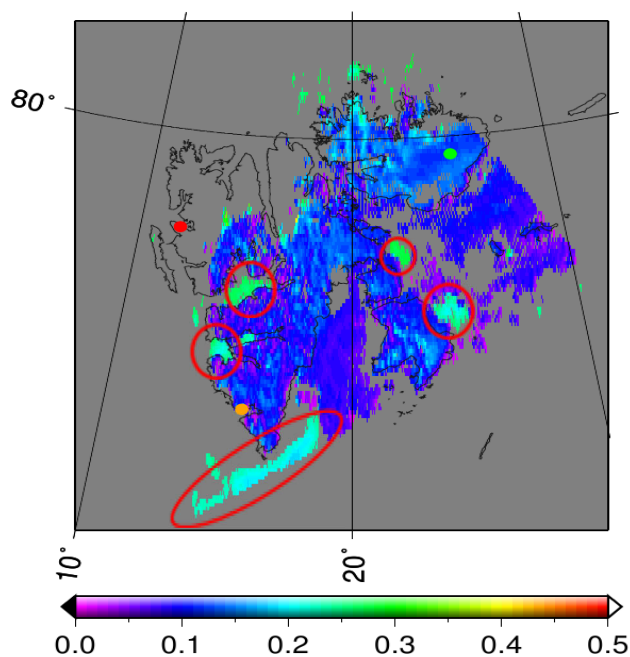


Figure 4.18. AOT (550 nm) over snow and open water for the AATSR scene of Spitsbergen, the 3rd of May 2006, type of aerosol “Arctic haze”. Red circles mark the AOT retrieved over ocean, all the other AOT values are over snow and ice.

The difference between these two types of retrieval is around 0.1, which can be caused by unscreened subpixel ice sheets in the ocean, subpixel clouds or unscreened thin clouds. The most probable reason for the discrepancy is the incorrect accounting for ocean surface reflectance. In this study we assumed the ocean surface to be absolutely black; the accuracy of this assumption depends on many factors and is out of scope of this study; the presented AOT retrieval over the ocean is only to illustrate the absence of a drastical AOT difference between the AOT over snow and the AOT over ocean.

5 Case studies

Several noticeable pollution events which occurred in the Arctic region in the recent years have been chosen to illustrate the performance of the developed AOT retrievals, and to further validate the retrieval. This means that the chosen pollution events should possibly overlap with independent space borne and ground based measurements, and be of possibly different nature in order to cover wide range of the surface and aerosol properties. The events which satisfy these conditions and which were selected for the AOT retrieval application studied are listed below:

- Mineral dust formation and transport on Greenland during July 04/05, 2008, with the complementary report and photographs from witnesses at the ground;
- Biomass burning pollution transport to Ny Ålesund in spring 2006, with the complementary data retrieved with BAER (AOT over ocean, using MERIS data) and the ground based sunphotometer AOT measurements at NyÅlesund;
- Boreal forest burning in Canada which originated pollution transport into Alaska during summer 2004, with the complementary data from MODIS (AOT over land and ocean).
- Kizimen volcano eruption at Kamchatka, 29-30 March 2011 with the complementary data from GOME-2 (BrO and SO₂ products) and photographs from the ground.

For these events extensive AOT retrievals have been performed. The results have been compared to the independent observations. A test of the algorithm performance over Antarctica has also been performed. The next subsections are dedicated to the detailed description of the performed retrievals and comparisons.

5.1 Case study: dust formation and transport on Greenland during July 04/05, 2008

On the 4th of July, 2008, in the vicinity of Kangerlussuaq, West Greenland, north-easterly winds mobilized mineral dust from open soils along the Søndre Strømfjord (see Fig. 5.1). The dust pollution developed during the morning of a cloud free day and reached its maximum in the early afternoon. The dust layer has been observed about 15 km west of Kangerlussuaq and was associated with the horizontal visibility of about 10km. The maximal thickness of the dust layer was estimated to be 500 m above the ground at early afternoon.

On the following day, July 5, no dust mobilization was observed, however, a katabatic wind of a limited range was present when approaching the ice sheet. This wind did not reach highly erodible landforms of the fjord.



Figure 5.1. A dust event has been observed at Greenland on 04.07.2008 near Kangerlussuaq, where strong winds mobilized mineral particles from areas of open land. The horizontal visibility as estimated by witnesses was around 10km. Image courtesy E. Schultz

A circulation system in the Søndre Strømfjord consists of a downstream flow at ground level and a katabatic upstream flow at higher elevations. The lower downstream wind is mobilizing mineral dust and transporting it away from the ice sheet. During the transport the dust is being elevated in the turbulent flow and then caught by the katabatic winds, which transport the finer fraction (2-3 μm) of the pollution backwards onto the ice sheet. Near Kangerlussuaq the existence of such a backflow was confirmed by balloon measurements of Oerlemans and Vugts (1993) and by investigation flights of Heinemann (1999). The range of the backflow is still unknown; it was assumed to be around 150 meters (Oerlemans and Vugts,1993) and around 1000 meters (Heinemann, 1999).

In order to estimate the AOT using the reported values of visibility and the pollution layer thickness, a variation of the Koschmieder equation suggested by Bäumer et al. (2008). The equation can be written in the following way:

$$V=3.912 z \tau^{-1} \quad (5.1)$$

where V is the horizontal visibility, z is the height of the pollution layer, τ is the AOT at 550nm. Given the above mentioned parameters of the pollution event, we get the AOT of approximately 0.4.

The closest to the pollution event AATSR overflight was on 05.07.2008, 14h 46min 02s, orbit number 33187. The retrieved AOT map is shown in Fig. 5.3, left panel. The increased AOT to the east of Kangerlussuaq (left bottom corner) is shown with the arrow, as well as the similar event at the opposite side of Greenland (right upper corner). The same mechanism of dust mobilization is supposed to be valid there, and the probable source of the mineral dust is visible to the north-east of the pollution itself. AATSR reflectances at visible wavelengths do not show any evidence of the increased aerosol load or different surface type at these points (see Fig.5.2, left panel for location near Kangerlussuaq and right panel for the opposite shore of Greenland).

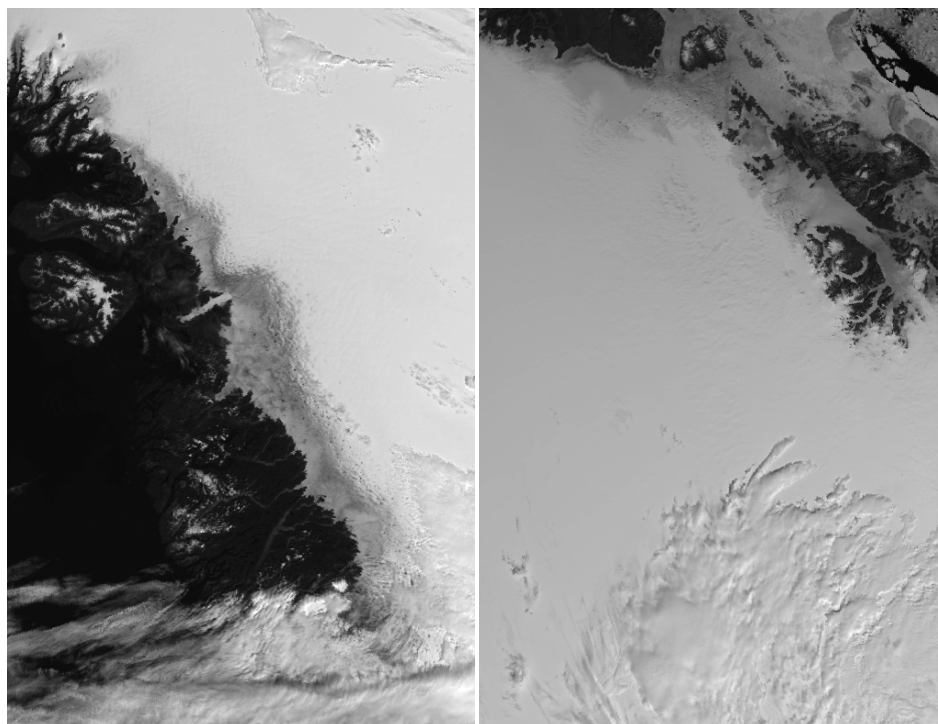


Figure 5.2. AATSR nadir view reflectances at 550nm for the area near Kangerlussuaq (left panel) and for the NE-Greenland (right panel). Neither of them shows signs of aerosol pollution.

It is apparent that the IR AOTs (Fig. 5.3, left panel) resemble the same pattern as TOA reflectances at 3.7 μ m (Fig. 5.3, right panel).

In order to exclude the possibility of surface features being mistaken for the aerosol pollution on the 5th of July, the AOT retrieval has been performed for another AATSR overflight on 15.07.2008, 14h 32min 18s, orbit number 33330. Fig. 5.4 (left panel) shows the AOT map retrieved with the IR algorithm over Greenland for this date. No evidence of pollution is visible in the Kangerlussuaq area, which proves that the increase of AOT near Kangerlussuaq on July, 5 2008 visible in the retrieved AOT map is not a surface feature, but an atmospheric pollution.

Fig. 5.4 (right panel) shows the AOT retrieved with the VIS retrieval for the day of the dust event. It is visible that the AOT pattern resembles that of the IR AOT (Fig. 5.3, left panel), but the amplitude of the AOT is much higher. While we certainly expect the AOT retrieved with the VIS algorithm to be higher than that of the IR algorithm due to the fact that smaller

particles are better scatterers in the VIS spectral region, such a large discrepancy over a presumably clear area might indicate a problem with the surface type or aerosol type. In particular, the surface type on Greenland in the middle of summer is, as observers report, “melting glacier, firn”. Such a surface type would for sure present a challenge for the aerosol retrieval. Independent space borne MODIS retrieval of surface reflective properties also experiences difficulties over Greenland at solar zenith angles greater than 55° (Wang, Zender, 2010). This problem of possible surface contamination should be studied in future.

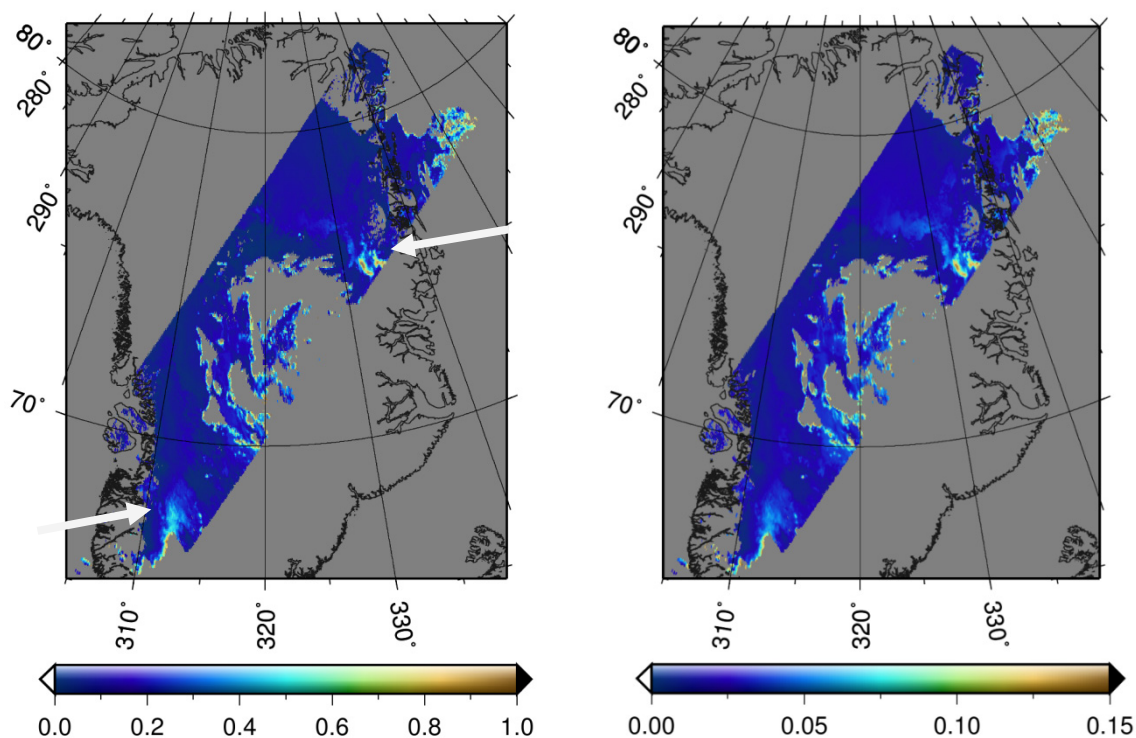


Figure 5.3. The map of retrieved AOT over Greenland on 05.07.2008, 14h 46min 02s, orbit number 33187 (left panel). Arrows indicate increased AOT near Kangerlussuaq (left bottom corner), where a dust event has been observed on 04.07.2008 (see Fig. 13), and on the NE-Greenland (right upper corner), where the same mechanism of dust mobilization is expected. The $3.7\mu\text{m}$ reflectance map of the same scene (right panel) shows the same pattern as the AOT.

AERONET station Kangerlussuaq (N $66^\circ 59'45''$, W $50^\circ 37'15''$) shows no evidence of a dust event neither on July 4 nor on July 5. Fig. 5.1 and the observers' reports, however, objectively indicate the presence of mineral dust pollution. Station Kangerlussuaq provides an AOT(500nm) of 0.028 and an Angström exponent (440-870) around 0.8 for the 4th of July. The probable reason for this discrepancy is highly non-uniform aerosol layer of mobilized mineral dust.

5.2 Case study: biomass burning pollution transport to Ny Ålesund, spring 2006

As was discussed by Stohl et al., 2007, Treffeisen et al., 2007 in spring 2006 the European Arctic experienced one of the most significant air pollution episodes ever recorded there. Abnormally warm temperatures in the Arctic and cold spring in the Europe formed a continuous surface of constant potential temperature, which enabled a rapid transport of smoke from Eastern Europe. Agricultural fires were the source of the biomass burning pollution in the European Arctic. The first pulse of smoke arrived at Spitsbergen already on 27 April, and was then followed by the

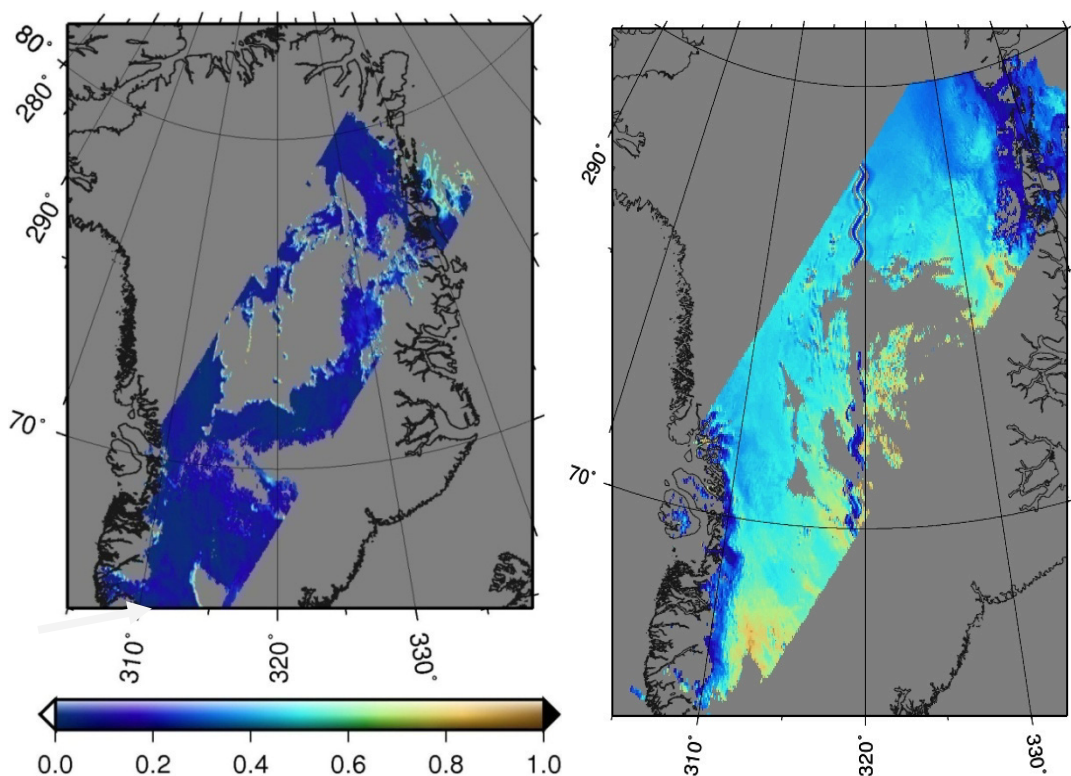


Figure 5.4. Left panel: The map of retrieved AOT over Greenland after the discussed dust event, on 15.07.2008, 14h 32min 18s, orbit number 33330. No evidence of pollution is visible in the Kangerlussuaq area (shown with the arrow). Right panel: the map of retrieved AOT over Greenland for the discussed dust event, 05.07.2008, 14h 46min 02s, orbit number 33187, with the VIS AOT retrieval. The AOT pattern is the same as in the IR retrieval product. Different AOT magnitude might indicate surface contamination due to a problematic surface type “melting glacial snow and ice, firn” present in the scene.

peak of pollution on 2nd and 3rd of May 2006. The view of Svalbard during the biomass burning pollution events as seen with the AATSR is shown in Fig. 4.16. The global situation of the AOT transport is shown in Fig. 4.15.

5 Case studies

The ground based observations of the AOT performed at Ny Ålesund, Svalbard, 78.923° N, 11.923° E by the Alfred Wegener Institute for Polar and Marine Research are shown in the Fig. 5.5. The biomass burning pollution event is clearly visible at the beginning of May; the AOT reached 0.6 at 500nm, which is a significant pollution as compared to the background AOT value of 0.05 – 0.1.

The time sequence of the AOT maps retrieved with the VIS AOT retrieval for this event is shown in Fig. 5.6. The low background values of the VIS AOT are observed for 20.04, 26.04,

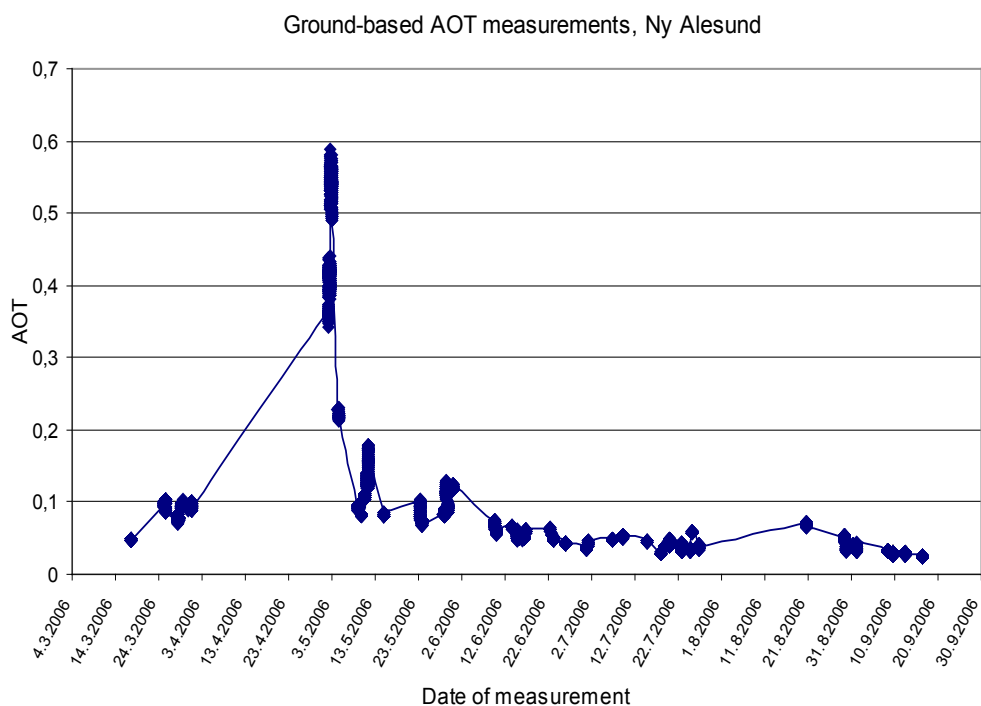


Figure 5.5. The ground based measurements of the AOT(500nm) performed at Ny Ålesund, Svalbard, 78.923° N, 11.923° E by the Alfred Wegener Institute for Polar and Marine Research in spring 2006. The biomass burning pollution event with the AOT reaching 0.5-0.6 was observed on the 2nd and 3rd of May, 2006. The usual for the Arctic background AOT of 0.05 resumed in June.

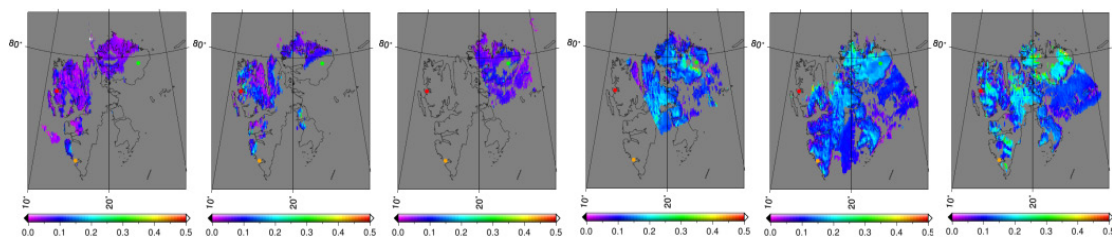


Fig. 5.6. The time sequence of the VIS AOT maps for (from left to right): 20.04, 26.04, 28.04, 02.05, 03.05, 04.05. 2006. The biomass burning pollution is visible for the 02.05, 03.05, 04.05. 2006. The maximum AOT observed by AATSR is around 0.3. Very low background values are observed on 20.04, 26.04, 28.04.2006, which corresponds to the ground based data.

28.04.2006 (three left panels of the image). An increase of the AOT associated with the biomass burning event is visible on 02.05, 03.05, 04.05.2006. The maximum VIS AOT was observed by the AATSR is around 0.3. The region of the ground based observations (Ny Ålesund at the west coast of Spitsbergen) is screened out as cloudy by our snow flagging algorithm for the days of the most aerosol pollution (the 2nd and the 3rd of May, 2006), therefore the direct comparison of the ground based AOT and the satellite AOT is not possible. The AOT dynamics of the time-sequence in Fig. 5.6 is similar to that of the ground based AOT data. This proves that our VIS AOT retrieval over snow is capable of showing the dynamic of aerosol amount on the qualitative level.

In order to study the fraction of larger particles during the biomass burning event, the IR AOT retrieval has been performed for the date of the most aerosol load on 3.05.2006 (Fig. 5.7). The various types of surface are present in the scene (see also Fig. 4.16 for the original AATSR image at 550nm), which affects the resulting AOT product. In the eastern part of the scene over the sea ice one can observe low coarse mode AOT and no significant aerosol pollution. No surface contamination is present in this part of the scene. Unfortunately, the complicated mountainous relief of Svalbard introduces a problem for the simple surface correction of the IR AOT retrieval algorithm. Strong surface contamination is visible in the western part of the scene. The reason for this is most probably the mixture of snow and rocks present in the scene. The types of surfaces present at Spitsbergen are illustrated in Fig. 5.8. It is visible that the surface features also bare rock areas along with the snowy areas. This type of surface presents a challenge for both VIS and IR retrieval over snow and also the VIS AOT retrieval over water (Fig. 4.18).

To illustrate the amount of the coarse mode particles during the discussed event at a more global scale, the IR AOT retrieval for 3.05.2006 and the whole Arctic region has been performed and shown in Fig. 5.9. This IR AOT is only retrieved over snow and sea ice with the original snow flagging routine as was described above. Due to the narrow AATSR swath the coverage is not complete. It is visible that the larger particles are absent in the Arctic for that day; the AOT ranges around 0.05-0.1 with some fluctuations over Greenland, Queen Elisabeth Islands and Siberia.

The VIS AOT map in Fig. 5.10 shows the total AOT for the 3rd of May, 2006. Unfortunately, the narrow swath of AATSR and rather cloudy conditions do not let us see the details of aerosol transport to Arctic. However, we can see the details of global distribution of aerosol at high latitudes. We can see the highly polluted belt at around 70° latitudes, whereas northern areas are less contaminated. The AOT overall is greater than the AOT of only coarse particles; a polluted belt with the AOT reaching 0.3 is visible at 70° latitudes. In some areas (marked with the arrows on both Fig. 5.10 and 5.9) both total and coarse mode AOTs are increased, indicating the presence of the coarse particles; in the other locations of the polluted belt, only the total AOT is increased, which indicates the presence of the fine particles. The area closer to the Pole is free from both fine and coarse aerosol particles. As can be seen in Fig. 4.15, the biomass burning pollution was also transported to Iceland. Though there is no continuous AOT product over Island due to cloudiness and broken snow cover at Iceland, both Fig. 5.9 and 5.10 show single pixels of increased AOT of around 0.2-0.3 over Iceland. The high AOT values over Greenland seen in the VIS and to some extent in the IR AOT product are not confirmed for this particular biomass burning event due to the absence of

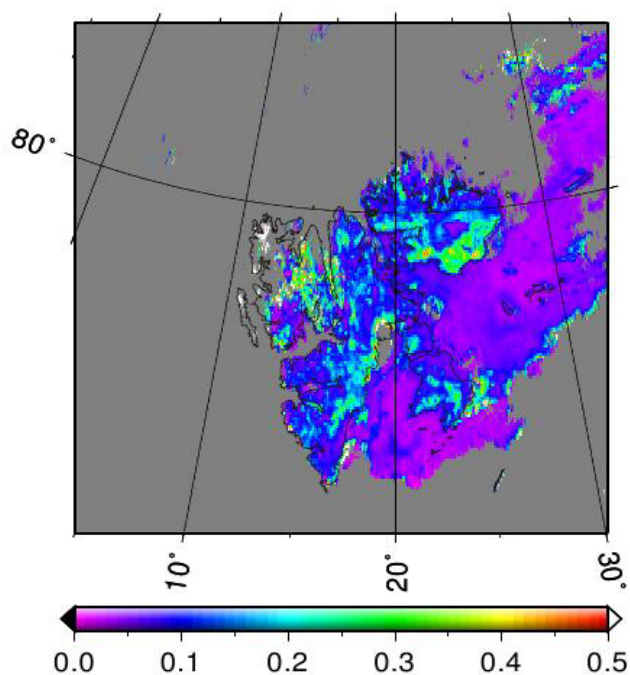


Fig. 5.7 The AOT map over Spitsbergen for the 3.05.2006. Retrieved at $3.7\mu\text{m}$ and recalculated into 550nm as described above. The coarse mode AOT pattern shows low AOT and turbulent aerosol flows in the eastern part of the scene over the sea ice. The surface contamination over some parts of the complicated mountainous terrain is observed.



Figure 5.8. The types of surfaces at Northern Spitsbergen after the biomass burning pollution event, on 19 June 2006. The surface features large rock areas along with the snow covered terrain. Coastal waters are contaminated with floating ice sheets. Image courtesy Rolf Stange (www.spitzbergen.de).

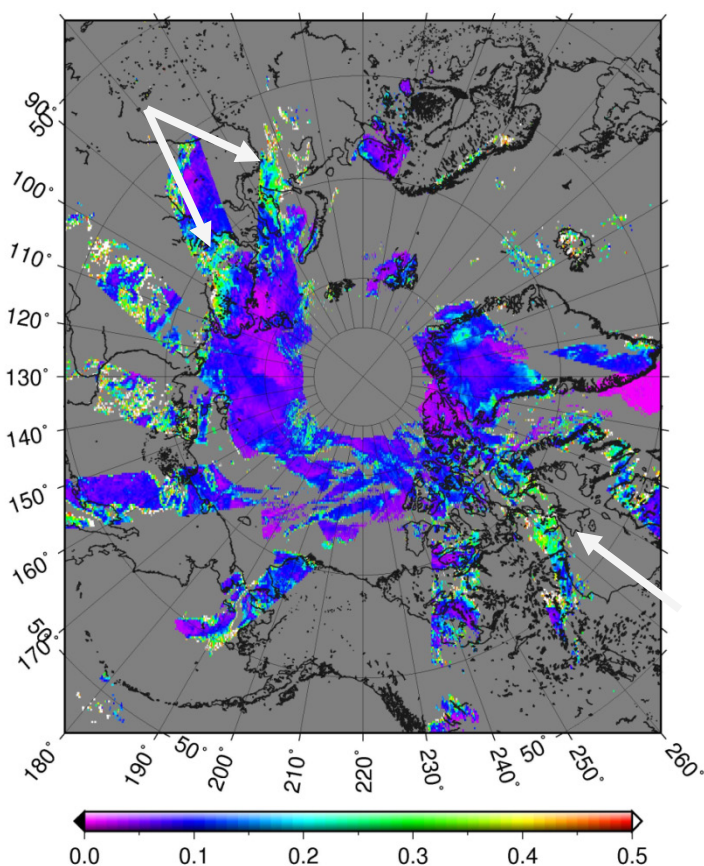


Figure. 5.9. Global IR AOT map retrieved at $3.7\mu\text{m}$ and recalculated into 550nm to illustrate the presence of larger particles on the 3rd of May, 2006, aerosol type “Arctic haze”. Background AOT of 0.05-0.1 is dominating with some fluctuations over Greenland, Queen Elisabeth Islands and Siberia. Residual cloud pixels are present at the edges of screened out cloudy areas.

ground based data from stations Summit, Kangerlussuaq, Thule, Resolute Bay, OPAL and PEARL for the particular day; however, as reported by Stohl et al., 2006, high AOT values of around 0.4-0.5 units were recorded over Greenland (at Summit station) and associated with another biomass burning event in 2004 over Alaska.

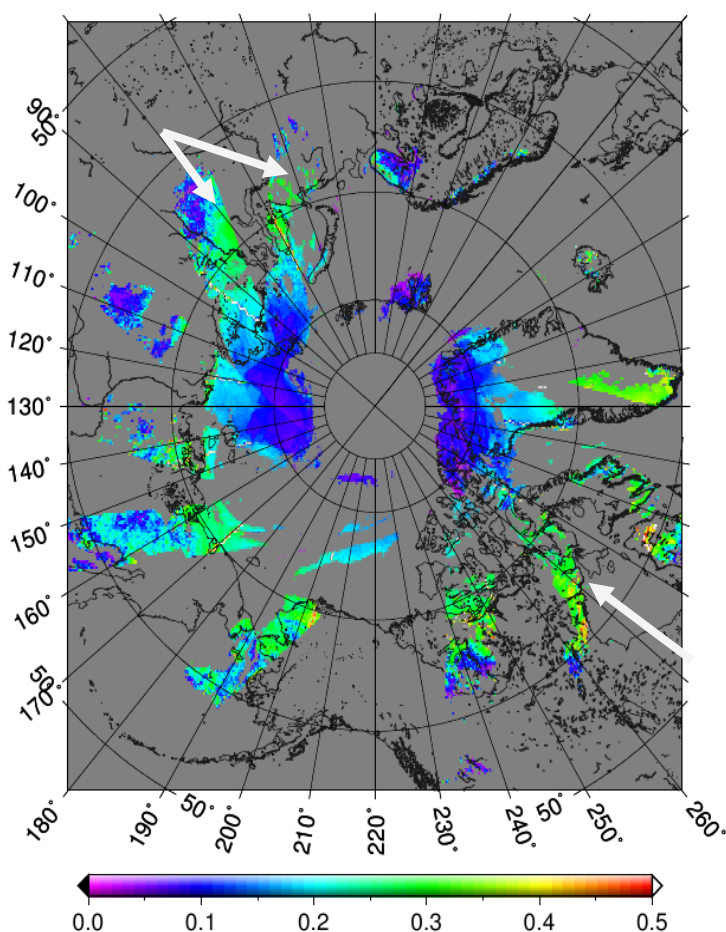


Figure 5.10. Global VIS AOT map retrieved 550nm to illustrate the total AOT on the 3rd of May, 2006, in the whole Arctic region. A polluted area with the total AOT reaching 0.3 is recognizable at the 70° latitude; the area closer to the Pole is aerosol free. Arrows show the areas of the increased coarse mode particles (see Fig.5.9), which overlap with the increased total AOT. This indicates the greater percentage of large particles in those areas.

5.3 Case study: boreal forest burning in Canada and transport to Alaska, summer 2004

During summer of 2004, a major boreal forest burning events has been recorded in Alaska and Canada. Over 2.7 million hectare of boreal forest burned in Alaska and 3.1 million hectare in Canada. Intense aerosol plumes from these fires were observed by research aircraft (de Gouw et al., 2006) and satellite instruments (e.g. MODIS AOT over land and ocean, see Fig. 5.11) over large parts of North America. The event has been described by Stohl et al. (2006). As can be seen in Fig. 5.11, a spectacular pollution with the AOT of 0.4-1.0 is occurring at the Beaufort Sea coast and at the Banks Island on the 4th of July, 2004. The island itself is not snow covered, as can be seen in Fig. 5.12, left panel (TOA reflectance at 550nm). The surrounding area is covered with the sea ice; MODIS AOT product has a gap in this area. The right panel of Fig. 5.11 shows the BT at 3.7 μ m; one can see the BT difference

between the sea ice, open water and land (the Banks Island). Thin cirrus clouds can be seen at the top of the image, as well as in the left bottom corner of the image. These clouds are not visible in the 550nm TOA reflectance plot; a layer of coarse mode particles indicated by an increased forward BT is shown with the arrow in the right panel of Fig. 5.12. As opposed to the nearby clouds, it is associated with the increased forward BT only in the forward view, without the corresponding increase in the nadir view. This area also appears polluted in the visible image at the left panel of Fig. 5.12. The scene shown in Fig. 5.12 presents a challenge for all three parts of the developed algorithm: cloud screening, VIS AOT retrieval and IR AOT retrieval. The scene features thin cirrus over snow (top of the image), thin cirrus mixed with a heavy pollution (left bottom corner) and aerosol load consisting of both fine and coarse mode. The performance of the presented AOT retrieval is visible in Fig. 5.13 for the VIS AOT retrieval (left panel) and the IR AOT retrieval (right panel). It is visible that all thin cirrus clouds have been successfully screened out, including the one mixed with the pollution. The aerosol pollution over the sea ice has not been screened out, though this area appears significantly darker than clear sea ice in the original TOA reflectance at 550nm image. The total AOT retrieved with the VIS AOT retrieval algorithm reaches 0.4 throughout the image and is higher at the coastal region (the bottom of the image); this corresponds well to the MODIS AOT presented in Fig. 5.11. The coarse mode particles which appears in the IR brightness

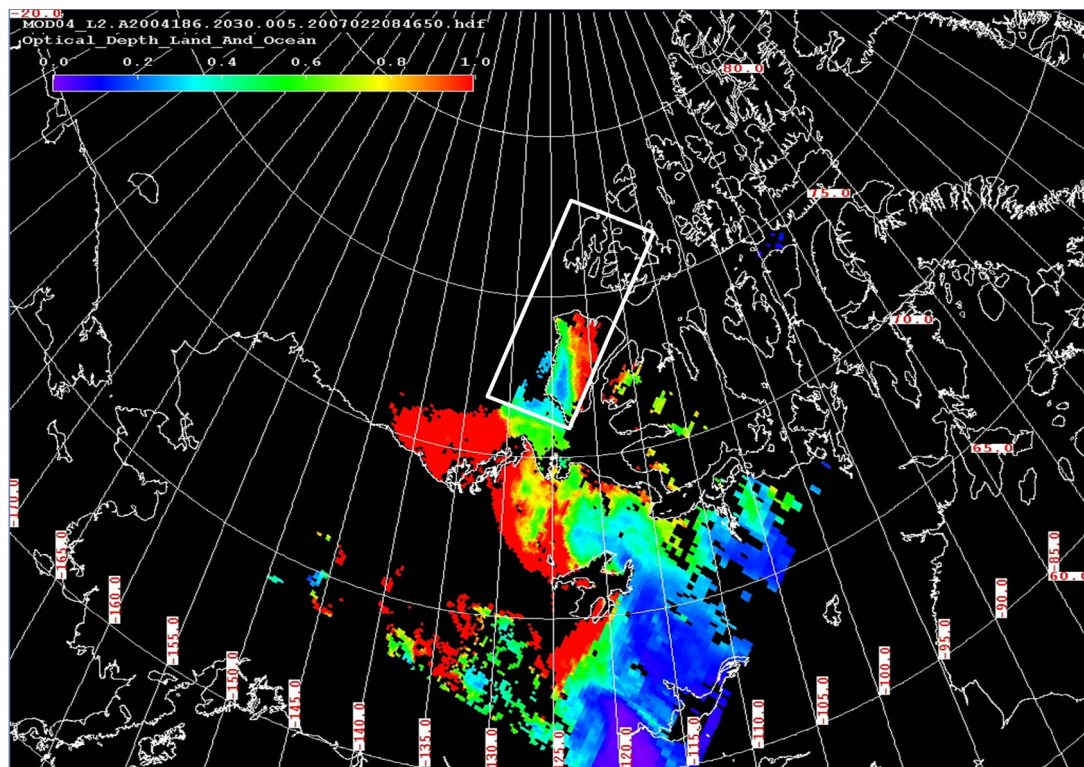


Fig. 5.11 The global situation of the boreal forest fires aerosol transport into the Alaskan Arctic from Canada on the 4th of July, 2004. MODIS AOT over land and ocean is shown. The section of the AATSR overflight for which the AOT over snow has been retrieved is shown with the rectangle.

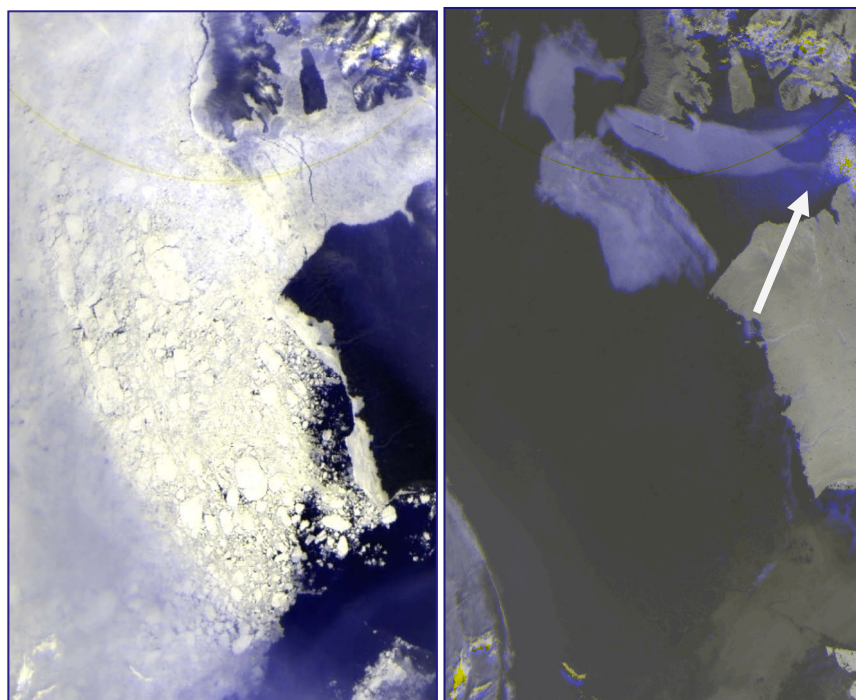


Figure 5.12. The AATSR imagery for the 4th of July, 2004, 20h36m22s, for the subset of the AATSR orbit 12263: left panel shows the TOA reflectance at 550nm, right panel shows the BT at 3.7µm. Both panels show the overlay of the nadir (yellow) and forward (blue) views.

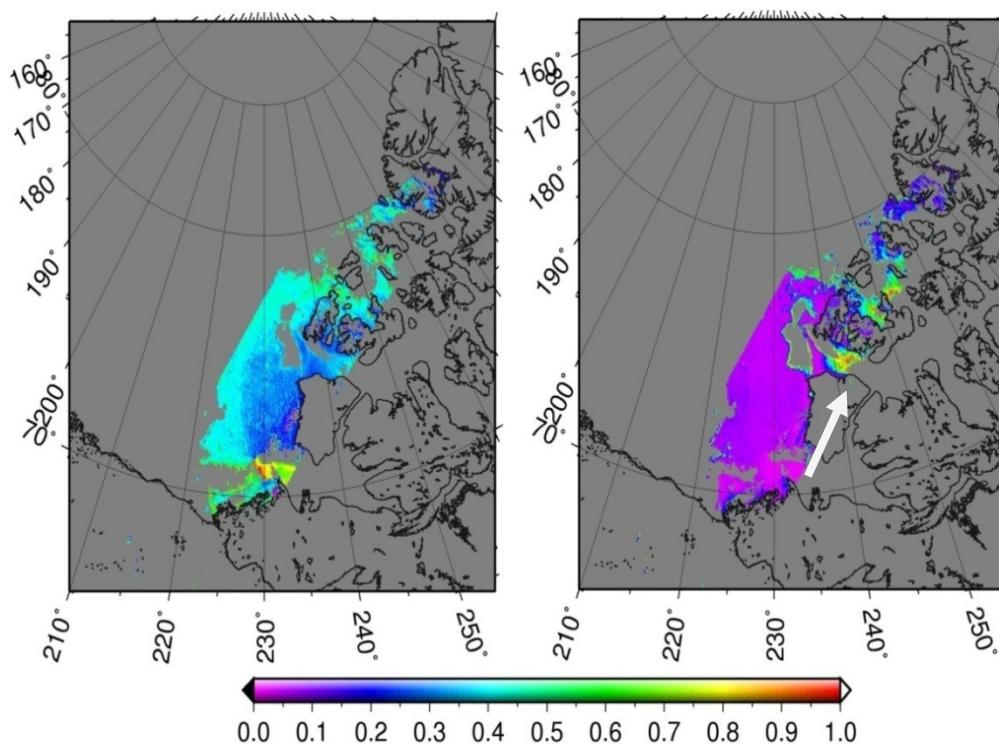


Figure. 5.13. The VIS AOT (left panel) and the IR AOT (right panel) of the AATSR overflight shown in Fig. 5.12.

temperatures in Fig. 5.12 (right panel) is also present in the retrieved coarse mode AOT in Fig. 5.13 (right panel). It appears to be the only area where the large particles are present, which corresponds to the IR brightness temperature plot in Fig. 5.12, which is reasonable for the biomass burning pollution which consists of fine particles mainly.

Both IR and VIS AOT retrievals fill the gap of the AOT product over snow which is seen in the MODIS data and also give an impression on the particle size distribution and the spatial aerosol distribution of the scene.

5.4 Case study: Kizimen volcano eruption at Kamchatka, spring 2011

A series of the Kizimen volcano eruptions occurred at Kamchatka peninsula in winter and spring 2010-2011. The Kizimen volcano is located 265 kilometers away from Petropavlovsk Kamchatsky city. Kizimen's last eruption occurred in the end of 1920-s, but in 2010 the volcano started to exhibit activity again. In June 2010 first signs of activity were reported, with the eruptions continuing episodically throughout the winter and spring 2011. One particular event on 29-30 March 2011 was associated with a spontaneous BrO emission, along with the SO₂ emission. To find out whether these emissions were also associated with the ash plume and whether the plume is visible with a satellite sensor, we performed the AOT retrieval for the location of interest at the time of eruption, 30.03.2011.



Figure 5.14 Kizimen volcano eruption, Kamchatka, 29.03.2011. Image courtesy I.Shpilenok.

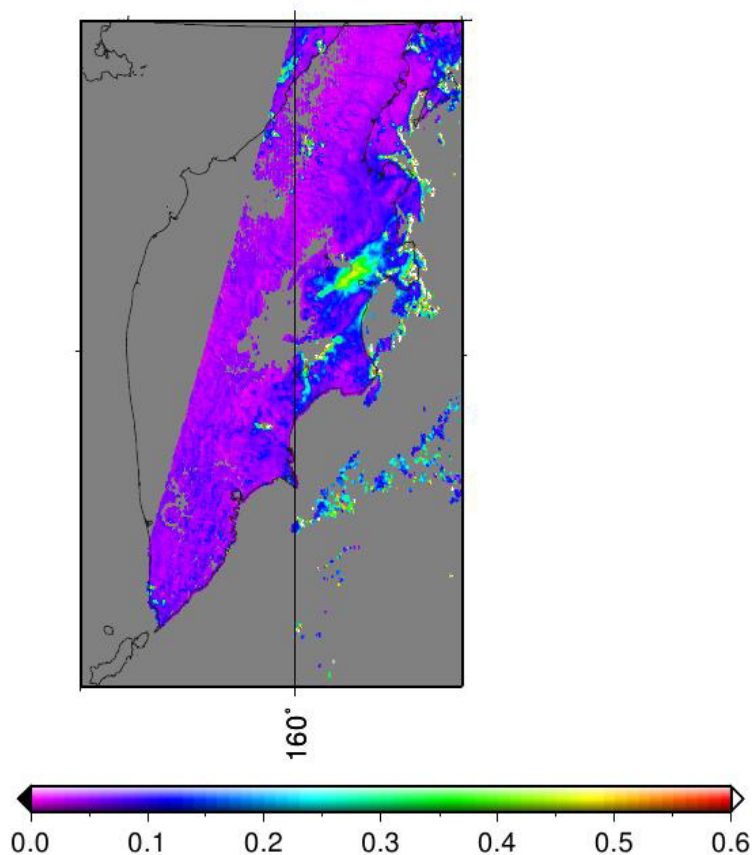


Figure 5.15 The IR AOT map of the Kizimen volcano eruption at Kamchatka peninsula. 30.03.2011, 00h00m21s, orbit number 47472. Clear ash plume with the AOT of coarse particles reaching 0.4-0.5 is visible among the areas with low background AOT of around 0.05.

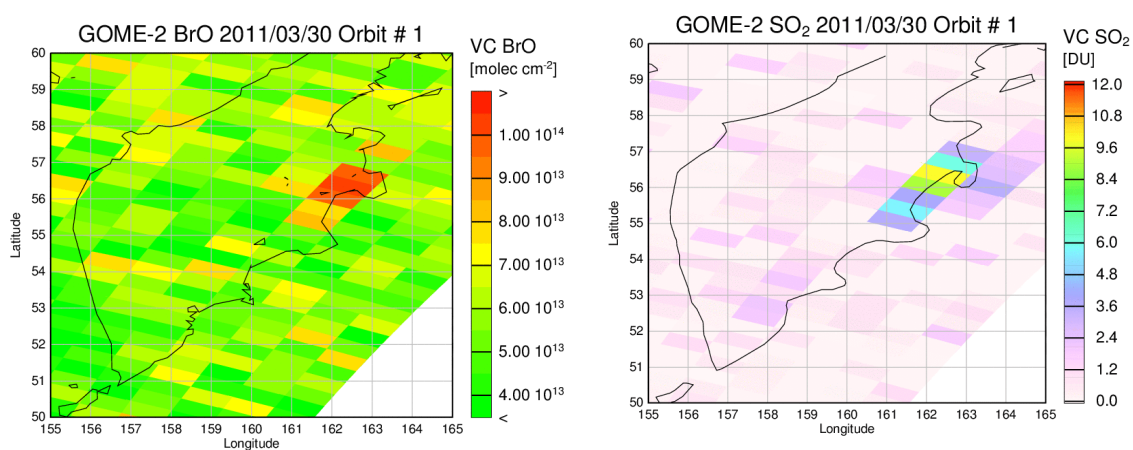


Figure 5.16 GOME-2 BrO and SO₂ products for 30.03.2011, Kamchatka peninsula. A clear SO₂ and BrO increase associated with the volcano eruption is visible in the scene, confirming the location of the ash plume in Fig. 5.15. Data courtesy Andreas Richter, IUP.

The ground based photograph of the Kizimen volcano, where the eruption occurred, is shown in Fig. 5.14. The picture also shows the strongly polluted snow even near the top of the volcano. As seen in the figure and also reported observers, falling ash caused strong snow discoloration throughout spring, 2011. For this reason the VIS AOT retrieval has not been performed for this case.

As seen in Fig. 5.15, the AOT of the coarse mode particles reaches 0.5 in the center of the ash plume, which appears to be an underestimation when comparing to the photograph in Fig. 5.14. Unfortunately, no AATSR overflight is available for 29.03.2011, for which the ground based photograph was taken, so there is no way to confirm the retrieved AOT in a quantitative way. However, the IR AOT retrieval obviously is able to give the impression on the spatial aerosol distribution on the qualitative level.

5.5 Case study: Antarctic background aerosol, 6th January 2011

Though this work is dedicated to AOT retrieval over snow in the Arctic region, it is interesting to test the ability of the algorithm to perform over other snow covered surfaces, e.g. Antarctica. Antarctica is the cleanest, least polluted regions on Earth due to the absence of internal pollution sources and large distance to any other anthropogenic sources. Fig. 5.17 shows one of the typical for Antarctica plots of AOT dynamics and amplitude – AOT time sequence for January and February 2010 for station “South Pole observatory NOAA”, (S 89°59'45”, E 70°17'60”, altitude 2850m). To avoid possible cloud contamination in the AOT product, AERONET data of Level 2.0 were taken (cloud screened and quality assured AOT).

As we expect very low AOT and rather fine particles in Antarctica, the VIS AOT retrieval has been chosen for this case study. The retrieval has been performed for the 6th of January 2011, the false color composite (blue is $\rho_{550\text{nm}}$, red is $\text{BT}_{3.7\mu\text{m}}$) of the initial AATSR scene is shown in Fig. 5.18, so that colder objects (clear snow and ice clouds) appear to be blue, whereas warmer objects (water clouds) appear reddish. The scene features some water and ice clouds in the middle and the northern parts of the image; the area of cloud free snow is in the southern (lower left) part of the image. The right panel of Fig. 5.18 presents the resulting AOT(550nm) map. It is visible that the retrieved AOTs over the cloud free snow area correspond to the expected background value of 0.03. The cloudy part of the scene, however, presents a problem as not all clouds are screened out. It is visible that warm water clouds have been successfully removed, but the cloud screening routine tends to omit colder ice clouds. Similar problem was already mentioned in Sect. 4.1, where (see Fig. 4.8) the cloud screening algorithm was not able to discriminate snow and cloud correctly. The reason for this discrepancy might be very thin ice clouds at low solar zenith angles, which (depending on observation-illumination geometry) might not disturb the spectral shape of the scene enough to be screened out, or thicker, not transparent ice clouds, which have exactly the same spectral signature as snow. These factors have to be studied in future to allow the developed methods to be used also in Antarctica.

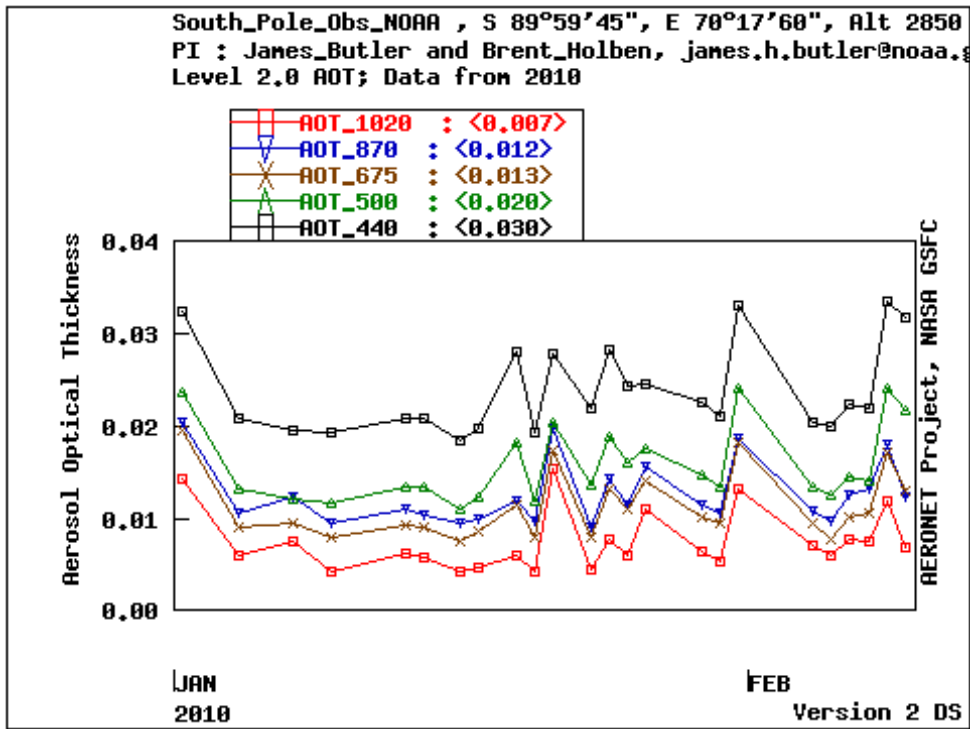


Figure 5.17. A typical background AOT at the AERONET station “South Pole” is around 0.03 at 440nm. Source: <http://aeronet.gsfc.nasa.gov>.

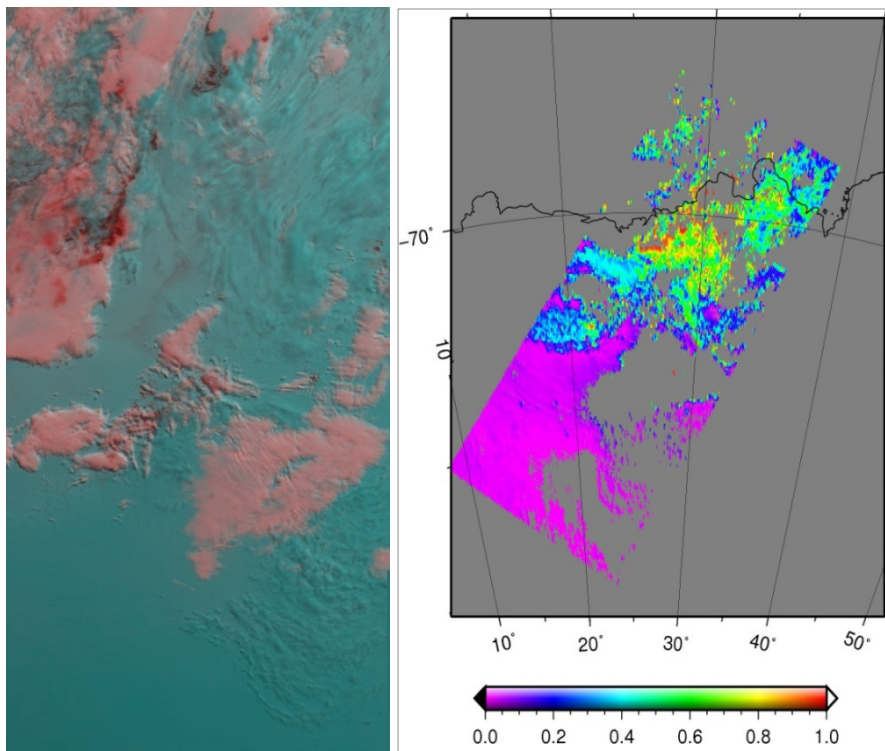


Fig. 5.18. Left panel shows the false color composite (blue is $\rho(550\text{nm})$, red is BT ($3.7\mu\text{m}$)) of the original AATSR scene for 06.01.2011, 6h23'10", orbit number 46283. Right panel shows the AOT(550nm) retrieval for this scene.

6 Summary and outlook

This thesis is dedicated to the AOT retrieval over snow and ice on the basis of AATSR dual view radiometric multispectral data using unique algorithms and methods developed within this work. The outcome of the research described within this thesis is the AOT over snow product, which enables the analysis of spatial distribution and transport of atmospheric aerosol in the Arctic region on local to global scales, which has not been possible before this work. This product is of immense importance for assessing the climatic state of the Arctic region.

This task was achieved in several steps by developing a new cloud clearing and snow flagging, an AOT retrieval algorithm in the visible spectral region and coarse mode AOT retrieval in the infrared spectral region.

Cloud clearing and snow flagging

In the absence of reliable cloud clearing methods over snow for the AATSR sensor, distinguishing cloud free snow covered areas became a complementary task connected to the AOT retrieval as residual clouds may drastically distort the aerosol product. This task has been solved within this work to ensure that the quality of the snow mask is sufficient for aerosol retrieval.

A simple and robust cloud screening method was developed for AOT retrieval over snow using AATSR observations. The method uses a spectrum-shape control in seven VIS, NIR and TIR AATSR channels and does not require time-sequences of data, morphological analysis of the scene or manual tuning to set absolute thresholds. The method was compared to MODIS cloud mask for various dates and locations and showed good correspondence with it over flat snow, snow-covered mountain peaks, snow-covered forest and snow-covered ice. Both MODIS cloud mask and the developed snow mask were compared to AATSR operational cloud mask for nadir view, and showed that for some cases of snow surface the quality of AATSR operational cloud mask provided in the Level 1-b AATSR product is questionable. The AATSR operational cloud mask (initially developed for the use over ocean) needs an update for the use over other surfaces.

The cloud screening developed within this work was validated against MPL data. The reliability of the method is 95% (on approximately 100 scenes). The presented cloud screening over snow and the spectral signature recognition method have a lot of potential and can be extended to work over other types of surface (including the complicated mixtures of snow with the other surface types). It can also be tuned to exclude aerosol pollution from the output clear snow mask (for example, for snow grain size retrievals or other applications

connected to the retrievals of the surface optical properties). Such retrieval provides an alternative to conventional usage of manually derived absolute thresholds and could be a candidate for the upcoming ESA Sentinel 3 mission.

AOT retrieval algorithm in the visible spectral region

A dual-view algorithm for AOT retrieval over snow in the visible spectral regions has been established and validated within this work. The developed AOT retrieval algorithm is based in the ratio of the two AATSR observation direction – forward and nadir – in order to reduce the role of high snow surface spectral albedo and only work with the directional properties of the surface at the two mentioned directions. The directional properties of the surface are approximated with the observed TOA reflectances as the first approximation, and then iteratively corrected for the atmospheric effect within the AOT retrieval procedure. This approach ensures the use of the optimal surface properties unique for each scene and provides an advantageous alternative to the modeled surface directional properties.

A comprehensive feasibility analysis involving RT simulations has been performed for this approach and showed a gain of performance quality as compared to conventional approach of modeled surface reflectances. This approach may potentially be applied also to the other surface types.

The AOT retrieval over snow was validated against AERONET data from the four High Arctic stations (Barrow, Resolute Bay, Hornsund, Longyearbyen). The correlation plot shows reasonable correlation within the uncertainties, caused by differences between AERONET instruments, unknown aerosol type and snow properties. Temporal analysis of the data can help to investigate the reasons of scatter (if it was, e.g., aerosol type change).

The performance of the algorithm was demonstrated for the 550nm wavelength, but it can be also used for the other AATSR channels where snow has relatively high spectral reflectance, e.g. 660nm or 870nm. This algorithm can also be adapted to other multiview satellite sensors, like MISR or SLST of the future Sentinel 3 mission.

Coarse mode AOT retrieval in the infrared spectral region

In order to get the impression on the role of the coarse particles in the retrieved AOT, an infrared 3.7 μm AATSR channel was used. Due to the low aerosol reflectance at this wavelength, a comprehensive analysis of aerosol scattering characteristics at 3.7 μm using RT calculations was performed. This involved simulating TOA reflectance and phase functions for coarse and accumulation modes of four main aerosol components. It was discovered that strong angular dependence of aerosol IR reflectance makes it possible to retrieve AOT at 3.7 μm at non-nadir angles. At the same time, aerosol reflectance is low for the nadir observation geometry, which allows us to use AATSR nadir observations at this wavelength for surface correction. A performed sensitivity study showed that AATSR IR calibration error would affect the resulting AOT within the range of several percent. Therefore the formerly known method of inverting the Planck function in order to extract the reflectance part from the BT product was used for the coarse mode AOT retrieval over snow. Further, a LUT-based algorithm was established to retrieve AOT over snow.

The developed method has been validated against 4 high Arctic AERONET stations and shows reasonable agreement with no obvious over- or underestimation for AOT values below

0.1. The uncertainty of the retrieval grows with the AOT due to larger effect of aerosol type at larger AOTs. The presented method tends to be sensitive to large particles and could also be implemented for IR retrievals of clouds.

Results from the case studies and comparisons to independent satellite retrievals

Both VIS and IR AOT retrievals have been compared to the independent satellite retrievals to validate the AOT product. A number of case studies for pollution events in the Arctic have been performed to test the performance of the retrieval. These pollution events and the results of the satellite AOT retrieval are shortly described below.

Mineral dust formation and transport on Greenland during July 04/05, 2008 possibly occurred due to the special circulation system at Søndre Strømfjord including a downstream flow at ground level and an upstream flow at higher elevations, with the latter transporting aerosols onto the ice sheet. AATSR AOT retrieval performed for the 5th July 2008 showed a coarse AOT increase in the direction of the ice sheet, thus confirming the existence of the katabatic winds in the area. To confirm that the observed AOT increase has the atmospheric nature (and not the surface feature), the AATSR AOT retrieval has been performed for the next cloud free AATSR overflight on 15th July 2008 and did not show any surface features in the area of interest. The VIS and IR AOT patterns generally correspond to each other, with the total VIS AOT being greater than the coarse IR AOT. Such an AOT offset might be caused by surface contamination of the VIS AOT retrieval.

Biomass burning pollution transport to NyÅlesund occurred due to abnormally warm **spring 2006**, and the ground based sunphotometer observations show the increase of the AOT up to 0.6 at 500nm, which is a significant event for the Arctic region. In order to study the dynamics of the event, the VIS AATSR AOT retrieval has been applied to the time sequence of satellite scenes over Spitsbergen. The AOT increase is visible at the beginning of May 2006, which corresponds to the ground based observations. The IR AOT retrieval performed for the 3rd of May 2006 showed rather low fraction of coarse particles, which is often the case for biomass burning pollution events. The VIS and IR AOT retrievals were performed for the 3rd of May, 2006 to show the global AOT distribution in the whole Arctic region. The AOT pattern shows a polluted belt at 70° latitude, with cleaner areas closer to the pole.

Boreal forest burning in Canada originated pollution transport into Alaska during summer 2004. The destination and pathways of this transport were partly lying over the snow and sea ice surfaces, and the MODIS AOT product being used to monitor this event had gaps over these bright reflecting regions. The AATSR AOT retrieval over snow and ice performed for the 4th of July, 2004, filled the gap in the AOT product and enabled detailed analysis of the fine and coarse particles distribution within the studied scene. The AATSR AOT product corresponds well to that of MODIS; a good accuracy of the developed cloud screening algorithm is confirmed with correctly screening out cirrus clouds over snow, but leaving coarse mode aerosol pollution unscreened.

Kizimen volcano eruption at Kamchatka, 29-30 March 2011 was associated with the BrO and SO₂ emissions according to the GOME-2 data. Ground observers confirmed the existence of the volcano ash plume on these dates. Satellite IR AOT retrieval has been performed to find out whether this pollution event is visible from space. The resulting AOT product

6 Summary and Outlook

showed an increase of the AOT at the location of the BrO and SO₂ plumes, thus corresponding to GOME-2 data and the ground observations.

All the retrieved AOT maps show reasonable AOT patterns and correspond well to the AOT retrievals using MERIS and MODIS data, and to SO₂ and BrO products retrieved with GOME2 data.

The test of the algorithm over Antarctica showed the ability of the method to correctly estimate the background AOT also over Antarctic snow surfaces.

The case study performed for the dust storm event observed at Greenland may prove the existence of the backward katabatic wind circulation which has been modeled but not confirmed by observations so far.

Open questions and future work

The developed algorithms are the first promising steps towards a retrieval of AOT over snow. However, on the long term there are still possibilities to improve these algorithms.

In some cases, the existing surface correction is not sufficient and produces an AOT offset for both VIS and IR AOT retrievals; this is most probably connected to insufficiently considered snow surface directional properties and need further investigation.

Also, the usage of a fixed aerosol type on extended temporal and global scale is a very rough approximation; it introduces an offset in the resulting AOT product depending on how far the assumed aerosol type is from the real aerosol load within the scene. This also produces a fairly large scatter in the coarse mode AOT product of the IR AOT retrieval algorithm. This disadvantage can be corrected with the multispectral AOT retrieval, and the first step towards such retrieval has been made within this work via establishing two AOT retrievals in the VIS and IR spectral regions. The fully operational spectral AOT retrieval over snow is the subject of the future research.

Including these improvements could strengthen the capabilities of retrieving AOT over snow and lead to more accurate observations of AOT in the Arctic region. As was already mentioned, the presented algorithm is not limited to the AATSR satellite sensor, but is adaptable to future missions with similar specifications. Setting up such retrievals for global scale long term processing will help to clarify many uncertainties about aerosol influence on regional and global climate.

Bibliography

Ackerman, A.S., et al., 2000b: Effects of aerosols on cloud albedo: evaluation of Twomey's parameterization of cloud susceptibility using measurements of ship tracks. *J. Atmos. Sci.*, 57, 2684–2695.

Ackerman, S.A., Strabala, K.I., Menzel, W.P., Frey, R.A., Moeller, C.C. and Gumley, L.E., 1998: Discriminating clear sky from clouds with MODIS, *J. Geophys. Res.*, 103, 32.141-32.157.

Aitken, J., 1920: *Collected Scientific Papers*, edited by G. G. Knott, College University Press, London, pp. 591.

Albrecht, B., 1989: Aerosols, cloud microphysics and fractional cloudiness. *Science*, 245, 1227–1230.

Allen, R.C., P.A. Durkee, and C.H. Wash, 1990: Snow/Cloud Discrimination with Multispectral Satellite Measurements. *J. Appl. Meteor.*, 29, 994–1004.

Ångström, A., 1961: Techniques of determining the turbidity of the atmosphere. *Tellus*, 13:214–223.

Aoki, Te., Aoki, Ta., Fukabori, M., Hachikubo, A., Tachibana, Y., Nishio, F., 2000: Effects of snow physical parameters on spectral albedo and bidirectional reflectance of snow surface, *J. Geophys. Res.*, 105, D8, 10,219-10,236, 1999JD901122.

Barrie, L. A., 1986: Arctic air pollution: An overview of current knowledge, *Atmos. Environ.*, 20, 643– 663.

Barrie, L.A., 1996: Occurrence and trends of pollution in the Arctic troposphere. In: Wolff and Bales (eds.). *Chemical exchange between the atmosphere and polar snow*, pp. 93-130. Springer-Verlag, Heidelberg, NATO ASI Series 1: Global Environmental Change 43.

Barrie, L. A., Bottenheim, J. W., Schnell, R.C., Crutzen, R.C. and Rasmussen, R.A., 1988: Ozone destruction and photochemical reactions at polar sunrise in the lower Arctic atmosphere. *Nature* 334, 138-141.

Barrie, L.A., R.M. Hoff, and S.M. Daggupaty, 1981: The influence of mid-latitudinal pollution sources on haze in the Canadian Arctic. *Atmos. Environ.* 15, 1407-1419.

Barry, R.G., 1996: The parameterization of surface albedo for sea ice and its snow cover. *Prog. Phys. Geogr.* 20, 63-79.

Bäumer, D., Vogel, B., Versick, S., Rinke, R., Mohler, O., Schnaiter, M., 2008: Relationship of visibility, aerosol optical thickness and aerosol size distribution in an ageing air mass over South-West Germany, *Atmos. Environment*, 42, 5, 989-998, doi: 10.1016/j.atmosenv.2007.10.017.

Bigg, E.K., 1980: Comparison of aerosol at four baseline atmospheric monitoring stations. *J. appl. Met.* 19, pp. 521–533.

Birks A.R., 2007: AATSR Technical Note. Improvements to the AATSR IPF relating to Land Surface Temperature Retrieval and Cloud Clearing over Land (pp. 12). Available at: http://earth.esa.int/pub/ESA_DOC/ENVISAT/AATSR/LSTNote_IPFv6.0.pdf

Blanchet, J-P. and Girard, E., 1995: Water vapour-temperature feedback in the formation of continental Arctic air: Implication for climate. *Sci. Total. Environ.* 160/161, 793-802.

Bibliography

Blanchet, J.-P. and R. List, 1987: On radiative effects of anthropogenic aerosol components in Arctic haze and snow, *Tellus* 39B, pp. 293–317.

Bokoye, A. I., Royer, A., O’Neil, N. T. and McArthur, L. J. B., 2002: A North American Arctic Aerosol Climatology using ground-based sunphotometry. *Arctic (Journal of the Institute of North America)* 55, 215–228.

Bory, A. J. M., Biscaye, P. E., & Grousset, F. E. D. A. F., 2003: Two distinct seasonal Asian source regions for mineral dust deposited in Greenland (NorthGRIP). *Geophysical Research Letters*, 30(4), 1–4.

Borys, R., 1989: Studies of ice nucleation by arctic aerosol on AGASP-II. *J. Atmos. Chem.*, 9, 169–186.

Bowling, S. A., and G. E. Shaw, 1992: The thermodynamics of pollutant removal as an indicator of possible source areas of Arctic Haze. *Atmos. Environ.*, 26A, 2953–2961.

Brasseur, G. P., Orlando, J., Tyndall, G., 1999: *Atmospheric Chemistry and Global Change*. Oxford University Press, 654p.

Bréon, F.-M., and Colzy, S., 1999: Cloud detection from the spaceborne POLDER instrument and validation against surface synoptic observations, *J. Appl. Meteor.*, 38, pp. 777–785.

Bridgman, H. A., Schnell, R. C., Kahl, J. D., Herbert, G. A., and Joranger, E., 1989: A major haze event near Point Barrow, Alaska: Analysis of probable source regions and transport pathways. *Atmos. Environ.* 23, 2537–2549.

Brock, C.A., L.F. Radke, J.H. Lyons, and P.V. Hobbs, 1989: Arctic hazes in summer over Greenland and the North American Arctic, I, Incidence and origins, *J. Atmos. Chem.* 9, 129 – 148.

Bucholtz, A., 1995: Rayleigh-scattering calculations for the terrestrial atmosphere. *Appl. Opt.*, Vol.34, pp.2765–2773.

Campbell, J.R., Hlavka, D.L., Welton, E.J., Flynn, C.J., Turner, D.D., Spinhirne, J.D., Scott, V.S., and Hwang, I.H., 2002: Full-Time, Eye-Safe Cloud and Aerosol Lidar Observation at Atmospheric Radiation Measurement Program Sites: Instruments and Data Processing, *J. Atmos. Oceanic Technol.*, 19, 431–442.

Cess, C.R., 1983: Arctic aerosol: model estimates of the interactive influences upon the surface-troposphere radiation budget, *Atmospheric Environment* 17, pp. 2555–2564.

Chandrasekhar, S., 1950: *Radiative Transfer*. (International Series of Monographs on Physics) Oxford: Clarendon Press; London: Oxford University Press. XIV, 394 pp.

Choudhury, B.J. and A.T.C. Chang, 1981: The albedo of snow for partially cloudy skies, *Boundary-Layer Meteorol.* 20, pp. 371–389.

Chylek, P. and J.A. Coakley, 1973: Man-made aerosol and the heating at atmosphere over polar regions. *Climate of the Arctic*. In: G. Weller and S.A. Bowling, Editors, *Proceedings of Twenty-fourth Alaska Science Conference Fairbanks, Alaska*, pp. 159–160.

Chylek, P., and J. Wong, 1995: Effect of absorbing aerosols on global radiation budget. *Geophys. Res. Lett.*, 22(8), 929–931.

Clarke, A.D. and K.J. Noone, 1985: Soot in the Arctic snowpack: A cause for perturbations in radiative transfer, *Atmospheric Environment* 19, pp. 2045–2053.

- Clarke, A.D., 1989: In-situ measurements of the aerosol size distributions, physicochemistry, and light absorption properties of Arctic haze, *J. Atmos. Chem.*, 9, 255-267.
- Colbeck, S. C., 1979: Grain clusters in wet snow. *Journal of Colloid and Interface Science*, 72(3), 371–384.
- Coulier, P. J., 1875: Note sur une nouvelle propriété de l'air, *J. de Pharmacie et de Chimie*, Paris, Ser. 4, 22:165-173, 22:254-255.
- Curier, L., G. de Leeuw, P. Kolmonen, A. –M. Sundström, L. Sogacheva, Y. Bennouna, 2009: Aerosol retrieval over land using the ATSR dual-view algorithm. In: A. A. Kokhanovsky and G. de Leeuw (Eds.), *Satellite Aerosol Remote Sensing Over Land*, Springer-Praxis (Berlin).
- Curry, J. A., 1983: On the formation of continental polar air. *J. Atmos. Sci.*, 40, 2279-2292.
- Curry J. A., 1987: The contribution of radiative cooling to the formation of cold-core anticyclones. *J. Atmos. Sci.*, 44, 2575-2592.
- Curry, J.A., 1995: Interactions Among Aerosols, Clouds and Climate of the Arctic Ocean. *The Science of the Total Environment*, 160/161, 777-791.
- Curry, J.A. and G. F. Herman, 1985: Infrared radiative properties of Arctic stratus clouds. *J. Clim. Appl. Met.*, 24, 525-538.
- Curry, J. A., F. G. Meyer, L. F. Radke, C. A. Brock, and E. E. Ebert, 1990: Occurrence and characteristics of lower tropospheric ice crystals in the Arctic. *Int. J. Climatol.*, 10, 749-764.
- Curry, J. A., and L. F. Radke, 1993: Possible role of ice crystals in ozone destruction of the lower Arctic atmosphere. *Atmos. Environ.*, 27A, 2873-2880.
- Curry, J. A., Rossow, W.B., Randall, D. and Schramm, J. L., 1996: Overview of Arctic cloud and radiative characteristics. *J. Climate* 9, 1731-1764.
- Curry, J.A., J.L. Schramm, M.C. Serreze, and E.E. Ebert, 1995: Water vapor feedback over the Arctic Ocean. *J. Geophys. Res.*, 100, 14,223-14,229.
- Degünther, M., Meerkötter, R., 2000: Influence of inhomogeneous surface albedo on UV irradiance: Effect of a stratus cloud, *Journ. Geophys. Res.*, 105, D18, 22,755-22,761.
- Delene, D. J. and Ogren, J. A., 2002: Variability of aerosol optical properties at four North American surface monitoring sites, *J. Atmos. Sci.* 59, 1135–1150.
- DeRooy W. A., C. C. A. H. Van Der Stap, 1984: Expansion of Mie scattering matrices in generalized spherical functions, *Astronomy and Astrophysics*. 131, pp. 237-248.
- Deuze, J. L., F. M. Breon, C. Devaux, et al., 2001: Remote sensing of aerosols over land surfaces from POLDER-ADEOS-1 polarized measurements *J. Geophys. Res.*, 106, 4913– 4926.
- Diner, D. J., J. Martonchik, R. A. Kahn et al., 2005: Using angular and spectral shape similarity constrains to improve MISR aerosol and surface retrievals over land, *Remote Sens. of Env.*, 94, 155-171.
- Diner, D., Clothiaux, E., Di Girolamo, L., 1999: MISR Multi-angle imaging spectro-radiometer algorithm theoretical basis. Level 1 Cloud detection, Jet Propulsion Laboratory, JPL D-13397.

Bibliography

- Dinter, T., von Hoyningen-Huene, W., Burrows, J. P., Kokhanovsky, A., Bierwirth, E., Wendisch, M., Müller, D., Kahn, R., Diouri, M., 2009: Retrieval of aerosol optical thickness for desert conditions using MERIS observations during the SAMUM campaign. *Tellus B*, 61, 229-238.
- Domine F., Albert, M., Huthwelker, T., Jacobi, H.-W., Kokhanovsky, A. A., Lehning, M., Picard, G., Simpson, W. R., 2008: Snow physics as relevant to snow photochemistry, *Atmos. Chem. Physics*, 8, 171-208.
- Domine, F., Salvatori, R., Legagneux, L., Salzano, R., Fily, M., Casacchia, R., 2006: Correlation between the specific surface area and the short wave infrared (SWIR) reflectance of snow, *Cold Reg. Sci. Technol.*, 46, 60–68.
- Dörnbrack, A., Stachlewska, S., Ritter, C., Neuber, R., 2010: Aerosol distribution around Svalbard during intense easterly winds. *Atmos. Chem. and Phys.*, 10, 1473-1490. DOI: 10.5194/acp-10-1473-2010.
- Dozier J, Painter T.H., 2004: Multispectral and hyperspectral remote sensing of alpine snow properties. *Annual Review of Earth and Planetary Sciences* 32: 465–494. DOI: 10.1146/annurev.earth.32.101802.120404.
- Dozier, J., and Warren, S. G., 1982: Effect of viewing angle on the infrared brightness temperature of snow: *Water resources Research*, v. 18, p. 1424-1434.
- Durkee, P. A., Pfeil, F., Frost, E., and Shema, R., 1991: Global analysis of aerosol particle characteristics. *Atmos. Environ.*, 24A:2457–2471.
- Emery, C.A., R.M. Haberle and T.P. Aekerman, 1992: A one-dimensional modelling study of carbonaceous haze effects on the springtime arctic environment, *J. Geophys. Res.* 97, pp. 20599–20613.
- English, S.J., Jones, D.C., Hewison, T.J., Saunders, R.W., Hallikainen, M., 1995: Observations of the emissivity of snow and ice surfaces from the SAAMEX and MACSI airborne campaigns, *Geoscience and Remote Sensing Symposium, 1995. IGARSS '95, "Quantitative Remote sensing for Science and Applications"*, International, vol. 2, pp. 1493-1495.
- Forster, P., V. Ramaswamy, P. Artaxo, T. Berntsen, R. Betts, D.W. Fahey, J. Haywood, J. Lean, D.C. Lowe, G. Myhre, J. Nganga, R. Prinn, G. Raga, M. Schulz and R. Van Dorland, 2007: Changes in Atmospheric Constituents and in Radiative Forcing. In: *Climate Change 2007: The Physical Science Basis. Contribution of Working Group I to the Fourth Assessment Report of the Intergovernmental Panel on Climate Change* [Solomon, S., D. Qin, M. Manning, Z. Chen, M. Marquis, K.B. Averyt, M. Tignor and H.L. Miller (eds.)]. Cambridge University Press, Cambridge, United Kingdom and New York, NY, USA.
- Foster, J. L., J.W. Winchester, and E.G. Dutton, 1992: The date of snow disappearance on the Arctic tundra as determined from satellite, meteorological station and radiometric in situ observations, *IEEE Transactions on Geoscience and Remote Sensing*, 30(4), 793-798.
- Fraser, R. S., 1976: Satellite measurements of mass of saharan dust in the atmosphere. *Appl. Opt.*, 15:2471–2479.
- Gafurov, A., and Bárdossy, A., 2009: Cloud removal methodology from MODIS snow cover product, *Hydrol. Earth Syst. Sci.*, 13, pp. 1361-1373.
- Garrett, T. J., Radke, L. F. and Hobbs, P. V., 2002: Aerosol effects on the cloud emissivity and surface longwave heating in the Arctic, *J. Atmos.Sci.*, 59, 769–778.

- Garrett, T. J., and C. Zhao, 2006: Increased Arctic cloud longwave emissivity associated with pollution from mid-latitudes, *Nature*, 440, 787–789, doi:10.1038/nature04636.
- Garrett, T. J., Zhao, C., Dong, X., Mace, G. G. and Hobbs, P. V., 2004: Effects of varying aerosol regimes on low-level Arctic stratus. *Geophys. Res. Lett.*, 31, doi:10.1029/2004GL019928.
- Gerland, S., Winther, J.-G., Ørbæk, J.B., Liston, G. E., Øritsland, N. A., Blanco, A., Ivanov, B., 1999: Physical and optical properties of snow covering Arctic tundra on Svalbard, *Hydrological Processes* 13, 2331-2343.
- Goody, R.M., and Yung, Y.L., 1989: *Atmospheric Radiation: Theoretical Basis*. ISBN:0195102916. Univ. Press. Oxford.
- Grey, W.M.F., North, P.R.J. and Los, S.O., 2006a: Computationally efficient method for retrieving aerosol optical depth from ATSR-2 and AATSR data, *Applied Optics*, 45, 2786 - 2795.
- Grey, W.M.F., North, P.R.J., North, S. O., Los, S. O., Mitchell, R. M., 2006b: Aerosol optical depth and land surface reflectance from multi-angle AATSR measurements: Global validation and inter-sensor comparisons. *IEEE Transactions on Geoscience and Remote Sensing*, 44, 2184 - 2197.
- Griggs, M., 1975: Measurements of atmospheric aerosol optical thickness over water using erts-1 data. *Journal of the Air Pollution Control Association*, 25:622–626.
- Han, W., 1996: Remote sensing of surface albedo and cloud properties in the Arctic from AVHRR measurements, 29 pp., D.S. thesis, Univ. of Alaska, Fairbanks.
- Hansen, A.D.A. and H Rosen, 1984: Vertical distribution of particulate carbon, sulphur and bromine in the Arctic haze and comparison with ground-level measurements at Barrow, Alaska. *Geophys. Res. Lett.* 11, 381 – 384.
- Hansen, J., and L. Nazarenko, 2004: Soot climate forcing via snow and ice albedos. *Proc. Natl. Acad. Sci.*, 101, 423-428, doi:10.1073/pnas.2237157100.
- Hansen, J., M. Sato, and R. Ruedy, 1997: Radiative forcing and climate response. *J. Geophys. Res.*, 102(D6), 6831–6864.
- Hansen, J.E., and J.W. Hovenier, 1974: Interpretation of the polarization of Venus. *J. Atmos. Sci.*, 31, 1137-1160.
- Harris, J. and J. Kahl, 1994: Analysis of 10 days isentropic flow patterns for Barrow, Alaska: 1985–1992, *Journal of Geophysical Research* 99, pp. 25845–25855.
- Haywood, J.M., and K.P. Shine, 1995: The effect of anthropogenic sulfate and soot aerosol on the clear sky planetary radiation budget. *Geophys. Res. Lett.*, 22(5), 603–606.
- Heintzenberg, J. and S. Larssen, 1983: SO₂ and SO₄ in the Arctic. Interpretation of observations at three Norwegian Arctic-Subarctic stations, *Tellus*, 35B, 255 – 265.
- Heintzenberg, J. et al., 2003: Arctic Haze over Central Europe, *Tellus*, 55B, 796-807.
- Heintzenberg, J., 1980: Particle size distribution and optical properties of Arctic haze. *Tellus*, 32B, 251 – 260.
- Herber, A., L.W. Thomason, H. Gernandt, U. Leiterer, D. Nagel, K.H. Schulz, J. Kaptur, T. Albrecht and J. Notholt, 2002: Continuous day and night aerosol optical depth observations in the arctic between 1991 and 1999, *Journal of Geophysical Research* 107 (D10) 6-1–6-14.

Bibliography

- Herman J. R., P. K. Bhartia, O. Torres, C. Hsu, C. Seftor, and E. Celarier, 1997: Global distribution of UV-absorbing aerosols from Nimbus 7/TOMS data. *J. Geophys. Res.*, 102, 16911-16922.
- Hillamo, R.E., V.-M. Kerminen, W. Maenhaut, J.-L. Jaffrezo, S. Balachandran and C.I. Davidson, 1993: Size distributions of atmospheric trace elements at Dye 3, Greenland – 1. Distribution characteristics and dry deposition velocities. *Atmos. Environ.* 27A(17-18): 2787-2803.
- Hobbs, P. V., and A. L. Rangno (1998), Microstructures of low and middlelevel clouds over the Beaufort Sea, *Q. J. R. Meteorol. Soc.*, 124, 2035–2071.
- Hobbs, P., 1993: *Aerosol-Climate-Cloud Interactions*, Academic Press Inc, 240p.
- Hoff, R.M., 1988: Vertical structure of Arctic haze observed by Lidar. *J. Appl. Met.* 27,125 – 139.
- Hoff, R.M., W.R. Leitch, P. Fellin, and L.A. Barrie, 1983: Mass-size distributions of chemical constituents of the winter Arctic aerosol. *J. Geophys. Res.* 88: 10947 – 10956.
- Hopper, J.E., D.E.J. Worthy, L.A. Barrie, and N.B.A. Trivett, 1994: Atmospheric observations of aerosol black carbon, carbon dioxide and methane in the High Arctic. *Atmos. Environ.* 28: 3047 – 3054.
- Hori, M., Te. Aoki, T. Tanikawa, H. Motoyoshi, A. Hachikubo, K. Sugiura, T.J. Yasunari, H. Eide, R. Storvold, Y. Nakajima, F. Takahashi, 2006: In-situ measured spectral directional emissivity of snow and ice in the 8-14 um atmospheric window, *Remote Sensing of Environment*, 100, 486-502.
- Hoyningen-Huene, W. von, M. Freitag, J.P. Burrows, 2003: Retrieval of aerosol optical thickness over land surfaces from top-of-atmosphere radiance, *Journal of Geophysical Research*. 108, No D9, 4260, 1-20.
- Hudson, S. R., S. G. Warren, R. E. Brandt, T. C. Grenfell, D. Six, 2006: Spectral bidirectional reflectance of Antarctic snow: Measurements and parametrization, *Journal of Geophysical Research*. 111, D18106.
- Hudson, S.R., and S.G. Warren, 2007: An explanation for the effect of clouds over snow on the top-of-atmosphere bidirectional reflectance. *J. Geophys. Res.*, 112, D19202.
- Husar, R. B., Prospero, J. M., and Stowe, L. L., 1997: Characterization of tropospheric aerosols over the oceans with the NOAA advanced very high resolution radiometer optical thickness operational product. *J. Geophys. Res.*, 102:16,889–16909.
- ICSU, 2004. International Council for Science, 2004. A Framework for the International Polar Year 2007-2008 produced by the ICSU IPY 2007-2008 Planning Group.
- IPCC, 2007: *Climate Change 2007: The Physical Science Basis*. Contribution of Working Group I to the Fourth Assessment Report of the Intergovernmental Panel on Climate Change (IPCC). Editors: S. Solomon, D. Qin, M. Manning, Z. Chen, M. Marquis, K.B. Averyt, M. Tignor and H.L. Miller. Cambridge University Press, Cambridge, UK.
- Istomina, L.G., von Hoyningen-Huene, W., Kokhanovsky, A. A., Burrows, J. P., 2010a: Retrieval of aerosol optical thickness in Arctic region using dual-view AATSR observations. *Proceedings of ESA Atmospheric Science Conference, Barcelona, Spain, 07-11 Sept. 2009, ESA SP-676*.
- Istomina L., W. von Hoyningen-Huene, A. A. Kokhanovsky, and J. P. Burrows, 2010b: The detection of cloud free snow covered areas using AATSR measurements, *Atmos. Meas. Tech.*, 3, 1-13.
- Istomina, L.G., von Hoyningen-Huene, W., Kokhanovsky, A.A., Rozanov, V.V., Schreier, M., Dethloff, K., Stock, M., Treffeisen, R., Herber, A., Burrows, J. P., 2009: Sensitivity study of the dual-

view algorithm for aerosol optical thickness retrieval over snow and ice, Proceedings of the 2nd MERIS/(A)ATSR user workshop, ESRIN, Frascati, Italy, 22-26 Sept. 2008, ESA SP-666.

Istomina, L. G., von Hoyningen-Huene, W., Kokhanovsky, A. A., Schultz, E., and Burrows, J. P., 2011: Remote sensing of aerosols over snow using infrared AATSR observations, *Atmos. Meas. Tech.*, 4, 1133-1145, doi:10.5194/amt-4-1133-2011.

Iversen, T. and E. Joranger, 1985: Arctic air pollution and large scale atmospheric flows, *Atmos. Environ.*, 19, 2099 – 2108.

Jacobson, M.Z., 2002: Control of fossil-fuel particulate black carbon and organic matter, possibly the most effective method of slowing global warming. *J. Geophys. Res.*, 107(D19), 4410, doi:10.1029/2001JD001376.

Jin, Z.H. and Simpson, J.J., 2000: Bidirectional anisotropic reflectance of snow and sea ice in AVHRR channel 1 and channel 2 spectral regions - Part II: Correction applied to imagery of snow on sea ice *IEEE Trans. on geoscience and remote sensing*, 38 (2): 999-1015.

Kahl, J.D. and A.D.A. Hansen, 1989: Determination of regional sources of aerosol black carbon in the Arctic. *Geophys. Res. Lett.* 16(4): 327 – 330.

Kasten, F., Young, A.T., 1989: Revised optical air mass tables and approximation formula, *Appl. Optics*, 28, 22, 4735-4738.

Kaufman, Y. J., D. Tanré, H. R. Gordon, T. Nakajima, J. Lenoble, R. Frouin, H. Grassl, B. M. Herman, M. D. King, and P. M. Teillet, 1997: Passive remote sensing of tropospheric aerosol and atmospheric correction for the aerosol effect, *J. Geophys. Res.*, 102(D14), 16,815–16,830.

Kaufman, Y.J., Tanre, D., Remer, L.A., Vermote, E.F., Chu, A. Holben, B.N., 1997: Operational remote sensing of tropospheric aerosol over land from EOS moderate resolution imaging spectroradiometer. *J. Geophys. Res.* 102(D14), 17051-17067.

Key, J., and Barry, R.G., 1989: Cloud cover analysis with Arctic AVHRR data. 1. Cloud detection, *J. Geophys. Res.*, 94, D15, pp. 18.521-18.535.

Key, J. R., T. Uttal, R. Stone, X. Wang, S. Frisch, and M. Shupe, 2006: SEARCH Atmospheric element I: Retrospective analysis of Arctic clouds and radiation from surface and satellite measurements, final report to the NOAA for funding under the SEARCH program, 27 pp., *Natl. Environ. Satell., Data and Inf. Serv.*, NOAA, Madison, Wis.

Kokhanovsky, A. A., 2004: *Light Scattering Media Optics: Problems and Solutions*, Chichester: Springer-Praxis Books in Environmental Sciences, 3rd Edition.

Kokhanovsky, A.A., 2006: *Cloud Optics*, Eds.: Mysak, L.A., Hamilton, K., Publ.: Springer.

Kokhanovsky A. A., T. Aoki, A. Hachikubo, M. Hori, E. Zege, 2005a: Reflective properties of natural snow: approximate asymptotic theory versus in situ measurements, *IEEE Transactions on Geoscience and Remote Sensing*. 43, 1529-1535.

Kokhanovsky, A.A., F.-M. Breon, A. Cacciari, E. Carboni, D. Diner, W. Di Nicolantonio, R.G. Grainger, W.M.F. Grey, R. Höller, K.-H. Lee, Z. Li, P.R.J. North, A. Sayer, G. Thomas, W. von Hoyningen-Huene, 2007: Aerosol remote sensing over land: a comparison of satellite retrievals using different algorithms and instruments, *Atmos. Res.*, doi:10.1016/j.atmosres.2007.02.008.

Kokhanovsky, A. A., B. Mayer, V. V. Rozanov, 2005b: A parameterization of the diffuse transmittance and reflectance for aerosol remote sensing problems, *Atmospheric Research*. 73, 37-43.

Bibliography

- Kokhanovsky, A.A., Rozanov, V. V., Aoki, T., Odermatt, D., Brockmann, B., Krüger, O., Bouvet, M., Drusch, M., Hori, M., 2010: Sizing of snow grains using backscattered solar light, submitted to International Journal of Remote Sensing.
- Krijger, J. M., Aben, I., and Schrijver, H., 2005: Distinction between clouds and ice/snow covered surfaces in the identification of cloud-free observations using SCIAMACHY PMDs, *Atmos. Chem. Phys.*, 5, 2729-2738, doi:10.5194/acp-5-2729-2005.
- Kuittinen, R., 1997: Optical and thermal sensors in snow cover monitoring. In: S. Wunderle (ed.), *Proceedings of the EARSeL Workshop: 'Remote Sensing of Land Ice and Snow'*, Freiburg, S. 7–20.
- Lacis A.A., J. Chowdhary, M.I.Mishchenko, B. Cairns, 1998: Modeling errors in diffuse-sky radiation: Vector vs. scalar treatment, *Geophysical research letters*. 25, 135-138.
- Leaitch, W.R., R.M. Hoff, and J.L. MacPherson, 1989: Airborne and Lidar measurements of aerosol and cloud particles in the troposphere over Alert Canada in April 1986. *J. Atmos. Chem.* 9(1-3): 187 – 212.
- Leaitch, W.R., R.M. Hoff, S. Melnichuk and A. Hogan, 1984: Some physical and chemical properties of the Arctic winter aerosol in northeastern Canada. *J. Clim. Appl. Met.* 23:916 – 928.
- Leck, C., Norman, M., Bigg, E. K. and Hillamo, R., 2002: Chemical composition and sources of the high Arctic aerosol relevant for fog and cloud formation. *J. Geophys. Res.* 10, doi:DOI: 10.1029/2001JD001463.
- Leighton, H., 1983: Influence of the Arctic haze on the solar radiation budget, *Atmospheric Environment* 17, pp. 2065–2068.
- Lenoble, J., 1985: *Radiative Transfer in Scattering and Absorbing Atmospheres: Standard Computational Procedures*. A. Deepak Publishing. p.583.
- Leroux, C., and M. Fily, 1998a: Modeling the effect of sastrugi on snow reflectance, *J. Geophys. Res.*, 103(E11), 25,779– 25,788.
- Leroux, C., J.-L. Deuze, P. Goloub, C. Sergent, M. Fily, 1998b: Ground measurements of the polarized bidirectional reflectance of snow in the near-infrared spectral domain: comparisons with model results, *Journal of Geophysical Research*. 103, No D16, 19.721-19.731.
- Leroy, M., J. Deuzé, F. Bréon, O. Hautecoeur, M. Herman, J. Buriez, D. Tanré, S. Bouffiès, P. Chazette, and J. Roujean, 1997: Retrieval of atmospheric properties and surface bidirectional reflectances over land from POLDER/ADEOS, *J. Geophys. Res.*, 102(D14), 17023-17037.
- Levy, R. C., Remer, L. A., Kleidman, R. G., Mattoo, S., Ichoku, C., Kahn, R., Eck, T. F., 2010: Global evaluation of the Collection 5 MODIS dark-target aerosol products over land. *Atm. Chem. and Phys.*, 10(21), 10399-10420.
- Levy, R. C., Remer, L. A., Tanre, D., Kaufman, Y. J., Ichoku, C., Holben, B. N., Livingston, J. M., Russell, P. B., Maring, H., 2003: Evaluation of the Moderate-Resolution Imaging Spectroradiometer (MODIS) retrievals of dust aerosol over the ocean during PRIDE. *J. Geophys. Res. –Atm.*, 108(D19), 8594.
- Li, S., 1982: A model for the anisotropic reflectance of pure snow, M.S. thesis, 60 pp., Univ. of Calif., Santa Barbara.
- Li, S. M. and Barrie, L. A., 1993: Biogenic sulphur aerosols in the Arctic troposphere. 1. Contributions to sulphate. *J. Geophys. Res.* 98D, 20 613–20 622.

- Li, S., X. Zhou, 2004: Modelling and measuring the spectral bidirectional reflectance factor of snow-covered sea ice: an intercomparison study, *Hydrol. Process.* 18, 3559-3581.
- Lindsay, R. W. and J. Zhang, 2005: the thinning of arctic sea ice, 1988-2003: have we passed a tipping point?, *J. Climate*, 18, 4879-4894.
- Liou, K., 1992: *Radiation and Cloud Processes in the Atmosphere*, vol. 20, Oxford Monograph on Geology and Geophysics.
- Liou, K.N., 2002: *An Introduction to Atmospheric Radiation*. second edn. ISBN:0-12-451451-0. Academic Press.
- Liu, Y., Key, J.R., Frey, R.A., Ackerman, S.A. and Menzel, W.P., 2004: Nighttime polar cloud detection with MODIS, *Remote Sens. of Environment*, 92, 181-194.
- Lohmann, U., and J. Feichter, 2005: Global indirect aerosol effects: A review. *Atmos. Chem. Phys.*, 5, 715-737.
- Lotz, W.A., Vountas, M., Dinter, T., Burrows, J.P. , 2009: Cloud and surface classification using SCIAMACHY polarization measurement devices, *Atmos. Chem. Phys.*, 9, pp. 1279-1288.
- Lyapustin, A., Tedesco, M., Wang, Y., Aoki, T., Hori, M., Kokhanovsky, A., 2009: Retrieval of snow grain size over Greenland from MODIS, *Remote Sens. of Environment*, 113, 1976-1987.
- Lyapustin, A., Wang, Y., Frey, R., 2008: An automated cloud mask algorithm based on time series of MODIS measurements, *J. Geophys. Res.*, 113, D16207, doi: 10.1029/2007JD009641.
- Lyapustin, A., Wang, Y., 2009: The time series technique for aerosol retrievals over land from MODIS. In: *Satellite Aerosol Remote Sensing over Land*. Eds: Kokhanovsky A. A., de Leeuw, G. - Springer Praxis Publ. Chichester, p. 69-99.
- Lyapustin, A.; Wang, Y.; Laszlo, I.; Kahn, R.; Korokin, S.; Remer, L.; Levy, R.; Reid, J. S., 2011: Multiangle implementation of atmospheric correction (MAIAC): 2. Aerosol algorithm. *J. Geophys. Res -Atm*, 116, D03211.
- Martins, J. V., Tanré, D., Remer, L., Kaufman, Y., Mattoo, S. and Levy, R., 2002: MODIS Cloud screening for remote sensing of aerosols over oceans using spatial variability, *Geophys. Res. Lett.*, 29(12), 8009, doi:10.1029/2001GL013252.
- Martonchik, J.V., D.J. Diner, K.A. Crean. and M.A. Bull, 2002: Regional aerosol retrieval results from MISR. *IEEE Trans. Geosci. Remote Sens.* 40, 1520-1531.
- Martonchik, J.V., D.J. Diner, R. Kahn, B. Gaitley, and B.N. Holben, 2004: Comparison of MISR and AERONET aerosol optical depths over desert sites. *Geophys. Res. Lett.* 31, L16102, doi:10.1029/2004GL019807.
- Maykut, G.A., 1986: The surface heat and mass balance. In N. Untersteiner (ed.), *The Geophysics of Sea Ice*. NATO ASI Ser., Ser. B Phys., Vol. 146. New York: Plenum, pp. 395-464.
- McCracken, M.C., R.D. Cess and G.L. Potter, 1986: Climatic effects of anthropogenic arctic aerosols: an illustration of climatic feedback mechanisms with one- and two-dimensional climate models, *J. Geophys. Res.* 91, pp. 14450-14455.
- Meijer, S.N., W.A. Ockenden, A. Sweetman, K. Breivik, J.O. Grimalt, and K.C. Jones, 2003. Global distribution and budget of PCBs and HCB in background surface soils: Implications for sources and environmental processes, *Environ. Sci. Technol.*, 37, 667 - 672.

Bibliography

- Mendonca, B.G., DeLuisi, J.J., and Schroeder, J.A., 1981: Arctic Haze and perturbation in the solar radiation fluxes at Barrow, Alaska, Proceedings from the 4th Conference on Atmospheric Radiation. *Atm. Met. Sco.*, Toronto, Ontario, Canada, pp. 95-96.
- Meyer, F. G., J. A. Curry, C. A. Brock, and L. F. Radke, 1991: Springtime visibility in the Arctic. *J. Appl. Meteor.*, 30, 342-357.
- Min, Q.-L., and M. Duan, 2004: A successive order of scattering model for solving vector radiative transfer in the atmosphere, *J. Quant. Spectrosc. Radiat. Transfer*, 87, 243– 259.
- Minnis, P., Chakrapani, V., Doelling, D.R., Nguyen, L., Palikonda, R., Spangenberg, D.A., Uttal, T., Arduini, R.F., Shupe, M., 2001: Cloud coverage and height during FIRE ACE derived from AVHRR data, *J. Geophys. Res.*, 106, D14, pp. 15.215-15.232.
- Mishchenko, M. I., 1993: Light scattering by size-shape distributions of randomly oriented axially symmetric particles of size comparable to a wavelength. *Appl. Opt.*, 32:4652–4666.
- Mishchenko M. I., A. A. Lacis, L. D. Travis, 1994: Errors induced by the neglect of polarization in radiance calculations for Rayleigh-scattering atmospheres, *J. Quant. Spectrosc. Radiat. Transfer*. 51, 491-510.
- Mishchenko M. I., J. M. Dlugach, E. G. Yanovitskiy, N. T. Zakharova, 1999: Bidirectional reflectance of flat, optically thick particulate layers : an efficient radiative solution and applications to snow and soil surfaces, *J. Quant. Spectrosc. Radiat. Transfer*. 63, 409-432.
- Mitchell, J.M., 1957: Visual range in the polar regions with particular reference to the Alaskan Arctic, *J. Atmos. Terr. Phys. Spec. Suppl.*, 195-211.
- Negi, H.S., Singh, S.K., Kulkarni, A.V., Semwal, B.S., 2010: Field-based spectral reflectance measurements of seasonal snow cover in the Indian Himalaya. *International Journal of Remote Sensing*, 31, 9, 2393-2417.
- Nicodemus, F. E., Richmond, J. C., Hsia, J. J., Ginsberg, I. W., and Limperis, T., 1977: Geometrical considerations and nomenclature for reflectance. *Science And Technology* 160, 1-52.
- Nolin, A. W. and Liang, S., 2000: Progress in bidirectional reflectance modeling and applications for surface particulate media: snow and soils. *Remote Sensing Review* 18, 307-342.
- Noone, K.J. and A.D. Clarke, 1988: Soot scavenging measurements in Arctic snowfall. *Atmos. Environ.* 22(12): 2773 – 2779.
- North, P.R.J., 2002: Estimation of aerosol opacity and land surface bidirectional reflectance from ATSR-2 dual-angle imagery: operational method and validation. *Journal of Geophysical Research* 107 (D12), DOI: 10.1029/2000JD000207: 1-11.
- O'Brien, H. W., and R. H. Munis, 1975: Red and near-infrared spectral reflectance of snow, RREL Res.Rep. 32, 18 pp., U.S. Army Cold Reg. Res. Eng. Lab., Hanover, N.H.
- Ohtake, T., 1993: Freezing points of H₂SO₄ aqueous solutions and formation of stratospheric ice clouds. *Tellus B - Chem. Phys. Meteor.*, 45, 138-144
- Ohtake, T., Jayaweera, K. L. F. and Sakurai, K.-I. 1982: Observation of ice crystal formation in lower Arctic atmosphere. *J. Atmos. Sci.*, 30, 2898-2904.
- Oltmans, S. J., Schnell, R.C., Sheridan, P.J. et al., 1989: Seasonal surface ozone and filterable bromine relationship in the high Arctic. *Atmos. Environ.* 23, 2431-2441.

- O'Neill, N.T., M. Campanelli, A. Lupu, S. Thulasiraman, J.S. Reid, M. Aube, L. Neary, J.W. Kaminski, J.C. McConnell, 2006: Evaluation of the GEM-AQ air quality model during the Quebec smoke event of 2002: Analysis of extensive and intensive optical disparities, *Atmos. Envir.*, 40, 20, 3737-3749, DOI: 10.1016/j.atmosenv.2006.03.006.
- Overpeck, J. T., Sturm, Francis, J. A., Perovich, D. K., Serreze, M. C., Benner, R., Carmack, E. C., Chapin III, F. S., Gerlach, S. C., Hamilton, L. C., Hinzman, L. D., Holland, M., Huntington, H. P., Key, J. R., Lloyd, A. H., Macdonald, G. M., McFadden, J., Noone, D., Prowse, T. D., Schlusver, P. and Vörösmarty, 2005: Arctic system on trajectory to new state. *Eos Trans.*, 86, pp. 309, 312–313
- Overpeck, J., Hughen, K., Hardy, D., Bradley, R., Case, R., Douglas, M., Finney, B., Gajewski, K., Jacoby, G., Jennings, A., Lamourex, S., Lasca, A., MacDonald, G., Moore, J., Retelle, M., Smith, S., Wolfe, A. and Zielinski, G., 1997: Arctic environmental change of the last four centuries. *Science*, 278, pp. 1251–1256.
- Pacyna, J.M. and B. Ottar, 1988: Vertical distribution of aerosols in the Norwegian Arctic. *Atmos. Environ.* 22(10): 2213-2223.
- Pacyna, J.M., V. Vitolis and J.E. Hanssen, 1984: Size differentiated composition of the Arctic aerosol at Ny Alesund Zeppelin. *Atmos. Environ.* 18: 2447 – 2459.
- Peltoniemi, J. I., 2007: Spectropolarised ray-tracing simulations in densely packed particulate medium *J. Quant. Spectrosc. Radiat. Transfer.* 108, 180-196.
- Peltoniemi, J. I., S. Kaasalainen, J. Näränen, L. Matikainen, J. Piironen, 2005: Measurement of directional and spectral signatures of light reflectance by snow, *IEEE Transactions on Geoscience and Remote Sensing.* 43, 2294-2304.
- Penkett, S.A., N.J. Blake, P. Lightman, A.R.W. Marsh, P. Anwyl, and G. Butcher, 1993: The seasonal variation of nonmethane hydrocarbons in the free troposphere over the North Atlantic Ocean: Possible evidence for extensive reaction of hydrocarbons with the nitrate radical, *J. Geophys. Res.*, 98, 2865-2885.
- Penner, J.E., et al., 2001: Aerosols, their direct and indirect effects. In: *Climate Change 2001: The Scientific Basis. Contribution of Working Group I to the Third Assessment Report of the Intergovernmental Panel on Climate Change* [Houghton, J.T., et al. (eds.)]. Cambridge University Press, Cambridge, United Kingdom and New York, NY, USA, pp. 289–348.
- Petzold, D. E., 1977: An estimation technique for snow surface albedo. *Climat. Bull.*, 21, 1-11.
- Polissar, A. V., P.K. Hopke, P. Paatero, W.C. Malm and J.F. Sisler, 1998: Atmospheric aerosol over Alaska, 2. Elemental composition and sources, *Journal of Geophysical Research* 103, pp. 19,045–19,057.
- Polissar, A.V., P.K. Hopke and R.L. Poirot, 2001: Atmospheric aerosol over Vermont: chemical composition and sources, *Environmental Science and Technology* 35, pp. 4604–4621.
- Porch, W.M., and M.C. McCracken, 1982: Parametric study of the effects of arctic soot on solar radiation, *Atmos. Environ.* 16, pp. 1365–1371.
- Quinn, P.K., et al., 2007: Arctic Haze: current trends and knowledge gaps, *Tellus*, 59B, 99-114.
- Quinn, P.K., Miller, T.L., Bates, T.S., Ogren, J.A., Andrews, E. and co-authors, 2002: A three-year record of simultaneously measured aerosol chemical and optical properties at Barrow, Alaska, *J. Geophys. Res.*, 107, D11, doi: 10.1029/2001JD001248.

Bibliography

- Qunzhu, Z., Meisheng, C., Xuezhi, F., Fengxian, L., Xianzhang, C., Wenkun, S., 1985: A study of spectral reflection characteristics for snow, ice and water in the north of China, in: *Hydrological Applications of Remote Sensing and Remote Data Transmission*, edited by: Goodison, B. E., Proceedings of the Hamburg Symposium, August 1983, IAHS Publ No. 145, 451–462.
- Radke, F.S., J.H. Lyons, D.A. Hegg, P.V. Hobbs, and I.H. Bailey, 1984: Airborne observations of arctic aerosols, I, Characteristics of arctic haze. *Geophys. Res. Lett.* 11, 393-396.
- Rahn, K.A., R.D. Borys and G.E. Shaw, 1977: The Asian source of Arctic haze bands, *Nature* 268, pp. 713–715.
- Ramaswamy, V., et al., 2001: Radiative forcing of climate change. In: *Climate Change 2001: The Scientific Basis. Contribution of Working Group I to the Third Assessment Report of the Intergovernmental Panel on Climate Change* [Houghton, J.T., et al. (eds.)]. Cambridge University Press, Cambridge, United Kingdom and New York, NY, USA, pp. 349–416.
- Randles, C.A., L.M. Russel, and V. Ramaswamy, 2004: Hygroscopic and optical properties of organic sea salt aerosol and consequences for climate forcing, *Geophys. Res. Lett.*, 31, L16108, doi: 10.1029/2004GL020628.
- Rees, W. Gareth, 2006: *Remote Sensing of Snow and Ice*. Taylor & Francis, 312 p.
- Remer, L. A., Kaufman, Y. J., Tanre, D., Mattoo, S., Chu, D. A., Martins, J. V., Li, R. R., Ichoku, C., Levy, R. C., Kleidman, R. G., Eck, T. F., Vermote, E., Holben, B. N., 2005: The MODIS aerosol algorithm, products, and validation. *J. Atm. Sci.*, 62(4), 947-973.
- Rosen, H., T. Novakov and B.A. Bodhaine, 1981: Soot in the Arctic, *Atmospheric Environment* 15, pp. 1371–1374.
- Rothrock, D. A., Zhang, J. and Yu, Y., 2003: The Arctic ice thickness anomaly of the 1990s: A consistent view from observations and models. *J. Geophys. Res.*, 108(C3), 3083, doi: 10.1029/2001JC001208.
- Rozanov, A. A., V. V. Rozanov, M. Buchwitz, A. A. Kokhanovsky, J. P. Burrows, 2005: SCIATRAN 2.0-a new radiative transfer model for geophysical applications in the 175-2400 nm spectral range, *Adv. Space Res.* 36, 1015-1019.
- Rozanov, V. V., Diebel, D., Spurr, R. J. D., and Burrows, J. P., 1997: Gometran: A radiative transfer model for the satellite project GOME, the plane-parallel version, *J. Geophys. Res.*, 102, 16 683–16 695.
- Salisbury, J. W., D'Aria, D. M., and Wald, A. E., 1994: Measurements of thermal infrared spectral reflectance of frost, snow, and ice: *Jour. of Geophysical Research*, v. 99, p. 24,235-24,240.
- Samarskij, A.A., 2002: *The theory of difference schemes*, Dekker, New York.
- Sayer, A. M., G. E. Thomas, R. G. Grainger, 2010: A sea surface reflectance model for (A)ATSR, and application to aerosol retrievals, *Atmos. Meas. Tech.* 3, 813-838, 2010. doi:10.5194/amt-3-813-2010.
- Serreze, M. C. and Barry, R.G., 2005: *The Arctic Climate System*. Cambridge University Press, Cambridge Atmospheric and Space Science Series, 385p.
- Serreze, M. C. and J. A. Francis, 2006: The Arctic on the fast track of change. *Weather* 61: 65-69.
- Shaw, G.E., 1981: Eddy diffusion transport of Arctic pollution from the mid-latitudes: a preliminary model, *Atmos. Environ.*, 15, 1483 – 1490.

- Shaw, G.E., 1982: Atmospheric turbidity in the polar regions. *J. Appl. Meteor.* 21, 1080–1088.
- Shaw, G.E., 1983: On the aerosol particle size distribution spectrum in Alaskan air mass systems: Arctic haze and non- haze episodes, *J. Atmos. Sci.* 40, pp. 1313–1320
- Shaw, G.E., 1984: Microparticle size spectrum of Arctic haze. *Geophys. Res. Lett.* 11: 409 – 412.
- Shaw G. E., 1986: Aerosols in Alaskan air masses. *J. Atmos. Chem.*, 4, 157-171.
- Shaw, G. E., 1987: Aerosols as climate regulators: A climate biosphere linkage? *Atmos. Env.*, 21, 985-1086.
- Shaw, G. E., 1995: The Arctic Haze phenomenon, *Bull. Am. Met. Soc.*, 76, 2403-2413.
- Shaw, G.E. and K. Stamnes, 1980: Arctic haze: perturbation of the Polar radiation budget, *Am. N.Y. Acad. Sci.* 338, 533 – 539.
- Shaw, G. E., K. Stamnes, and Y. X. Hu, 1993: Arctic haze: Perturbation to the radiation field, *Meteorol. Atmos. Phys.*, 51, 227– 235.
- Shaw, G.E. and Wendler, G., 1972: Atmospheric turbidity measurements at McCall Glacier in northern Alaska. In: *Proc. Atmospheric Radiation Conference.*
- Shindell, D., and G. Faluvegi, 2009: Climate response to regional radiative forcing during the twentieth century. *Nature Geosci.*, 2, 294-300, doi:10.1038/ngeo473.
- Siewert, C.E., 2000: A concise and accurate solution to Chandrasekhar's basic problem in radiative transfer, *J. Quant. Spectrosc. Radiat. Transfer* 64, pp. 109–130.
- Simpson, J.J., Tsou, Y.L., Schmidt, A. Harris, A., 2005: Analysis of Along Track Scanning Radiometer-2 (ATSR-2) data for clouds, glint and sea ice surface temperature using neural networks. *Remote Sensing of Environment*, 98, 152-181.
- Smith, D.L., Delderfield, J., Drummond, D., Edwards, T., Mutlow, C.T., Read, P.D., and Toplis, G.M., 2001: Calibration of the AATSR instrument, *Adv. Space Res.*, 28, 1, 31-39.
- Sobolev, V. V., 1956: *Radiative Transfer in Stellar and Planetary Atmospheres.* Gostekhteorizdat, Moscow.
- Sobolev, V. V., 1975: *Light scattering in planetary atmospheres.* Oxford and New York, Pergamon Press (International Series of Monographs in Natural).
- Sogacheva, L., P. Kolmonen, A.-M. Sundström, L. Curier, V. Aaltonen and G. de Leeuw, 2009: Aerosol retrieval over Finland using the dual-view AATSR retrieval algorithm, *Proceedings of the 2nd MERIS/(A)ATSR user workshop, ESRIN, Frascati, Italy, 22-26 Sept. 2008, ESA SP-666.*
- Spangenberg, D. A., V. Chakrapani, D.R. Doelling, P. Minnis, and R.F. Arduini, 2001: Development of an automated Arctic cloud mask using clear-sky satellite observations taken over the SHEBA and ARM NSA sites. *Proc. 6th Conf. on Polar Meteor. and Oceanography, San Diego, CA, May 14-18, 2001, 246-249.*
- Stamnes, K., S. Tsay, W. Wiscombe and K. Jayaweera, 1988: Numerically stable algorithm for discrete-ordinate-method radiative transfer in multiple scattering and emitting layered media. *Appl. Opt.*, 27, 2502-2509.

Bibliography

Stankevich D., Istomina L., Shkuratov Yu., Videen G., 2007: The coherent backscattering effects in a random medium as calculated using a ray tracing technique for large non-transparent spheres, *Journal of Quantitative Spectroscopy and Radiative Transfer*, 106, 1-3, 509-519.

Stohl, A., Andrews, E., Burkhardt, J., Forster, C., Herber, A., Hoch, S., et al., 2006: Pan-arctic enhancements of light absorbing aerosol concentrations due to North American boreal forest fires during summer 2004, *J. Geophys. Res.*, 111, D22214, doi:10.1029/2006JD007216.

Stohl, A., C. Forster, A. Frank, P. Seibert, and G. Wotawa, 2005: Technical Note : The Lagrangian particle dispersion model FLEXPART version 6.2. *Atmos. Chem. Phys.* 5, 2461-2474.

Stohl, A., T. Berg, J. F. Burkhardt, et al., 2007: Arctic smoke – record high air pollution levels in the European Arctic due to agricultural fires in Eastern Europe in spring 2006, *Atmospheric Chemistry and Physics*. 7, 511-534.

Stone, R., G. Anderson, E. Andrews, E. Dutton, J. Harris, E. Shettle, and A. Berk, 2005: Asian dust signatures at Barrow: observed and simulated, *IEEE Workshop on Remote Sensing of Atmospheric Aerosol, An Honorary Workshop for Prof. John A. Reagan*, 5-6 April 2005a, University of Arizona, Tucson Arizona, USA, 74-79.

Stone, R. S., E. G. Dutton, J. M. Harris, and D. Longenecker, 2002: Earlier spring snowmelt in northern Alaska as an indicator of climate change, *J. Geophys. Res.*, 107(D10), 4089, doi:10.1029/2000JD000286.

Stonehouse, B., 1986: *Arctic Air Pollution*. In: B. Stonehouse, Editor, Cambridge University Press, Cambridge.

Stroeve, J. C., Serreze, M. C., Fetterer, F., Arbetter, T., Meier, M., Maslanik, J., and Knowles, K., 2005: Tracking the Arctic's shrinking ice cover: Another extreme September minimum in 2004. *Geophys. Res. Lett.*, 32, doi: 10.1029/2004GL021810

Tanré, D., Herman, M., Deschamps, P.Y., de Leffe, A., 1979: Atmospheric modeling for space measurements of ground reflectances, including bidirectional properties, *Appl. Optics*, 18, 21, 3587-3594.

Tanré, D., Y. J. Kaufman, M. Herman, and S. Mattoo, 1997: Remote sensing of aerosol properties over oceans using the MODIS/EOS spectral radiances, *J. Geophys. Res.*, 102(D14), 16,971–16,988, doi:10.1029/96JD03437.

Tedesco, M., and Kokhanovsky, A. A., 2007: The semi-analytical snow retrieval algorithm and its application to MODIS data, *Rem. Sens. Env.*, 110, 317-331.

Thomas G. E., Dean S. M., Carboni E, Grainger R.G., Poulsen C.A., Siddans R. and Kerridge B. J., 2005: *ATSR-2/AATSR algorithm theoretical base document*, ESA Globaerosol ATBD.

Tomasi, C., Vitale, V., Lupi, A., Di Carmine, C., Campanelli, M., Herber, A., Treffeisen, R., Stone, R.S., Andrews, E., Sharma, S., Radionov, V., von Hoyningen-Huene, W., Stebel, K., Hansen, G.H., Myhre, C.L., Wehrli, C., Aaltonen, V., Lihavainen, H., Virkkula, A., Hillamo, R., Ström, J., Toledano, C., Cachorro, V.E., Ortiz, P., de Frutos, A.M., Blindheim, S., Frioud, M., Gausa, M., Zielinski, T., Petelski, T., Yamanouchi, T., 2007: Aerosols in polar regions: A historical overview based on optical depth and in situ observations, *J. Geophys. Res.*, 112, D16205, doi: 10.1029/2007JD008432.

Treffeisen R., P. Tunved, J. Ström, A. Herber, J. Bareiss, A. Helbig, R. S. Stone, W. Hoyningen-Huene, R. Krejci, A. Stohl, and R. Neuber, 2007: Arctic smoke – aerosol characteristics during a record smoke event in the European Arctic and its radiative impact, *Atmospheric Chemistry and Physics*. 7, 3035-3053.

- Trenberth, K. E., J. T. Fasullo, and J. Kiehl, 2009: Earth's global energy budget. *Bull. Amer. Meteor. Soc.*, 90, No. 3, 311-324, doi: 10.1175/2008BAMS2634.1.
- Trepte, Q., Arduini, R.F., Chen, Y., Sun-Mack, S., Minnis, P., Spangenberg, D.A., Doelling, D.R., 2001: Development of a daytime polar cloud mask using theoretical models of near-infrared bidirectional reflectance for ARM and CERES, Proc. AMS 6th Conf. Polar Meteorology and Oceanography, San Diego, CA; May 4-18, pp. 242-245.
- Trivett, N.B.A., L.A. Barrie, J.P. Blanchet, R.M. Bottenheim, R.M. Hoff and R.E. Mickle, 1989: An experimental investigation of Arctic haze at Alert, N.W.T., March 1985. *Atmos. Ocean.* 26: 341 – 376.
- Twomey, S., 1977: *Atmospheric Aerosols*. Elsevier.
- Twomey, S., 1977: The influence of pollution on the shortwave albedo of clouds, *J. Atmos. Sci.*, 34, 1149-1152.
- Twomey, S., 1991: Aerosols, clouds, and radiation. *Atmos. Environ.*, 25, 2435–2442.
- Valero, F.J.P., T.P. Ackerman and W.J.Y. Gore, 1989: The effects of the arctic haze as determined from airborne radiometric measurements during AGASP 2. *J. Atmos. Chem.* 9, pp. 225–244.
- van de Hulst, H.C. 1981: *Light Scattering by Small Particles* (Wiley, NY, 1957; Dover, NY, 1981).
- VanCuren, R. A., and T. A. Cahill, 2002: Asian aerosols in North America: Frequency and concentration of fine dust, *J. Geophys. Res.*, 107(D24), 4804, doi:10.1029/2002JD002204.
- Veefkind, J.P., G. de Leeuw, and P.A. Durkee, 1998: Retrieval of aerosol optical depth over land using two-angle view satellite radiometry during TARFOX, *Geophysical Research Letters*, 25, 3135-3138.
- Vermote, E.F., N. El Saleous, C.O. Justice, Y.J. Kaufman, J.L. Privette, L. Remer, J.C. Roger, and D. Tanré, 1997: Atmospheric correction of visible to middle-infrared EOS-MODIS data over land surfaces : Background, operational algorithm and validation, *J. Geophys. Res.*, 102 (D14): 17131-17141.
- von Hoyningen-Huene, W. A. A. Kokhanovsky, J. P. Burrows, V. Bruniquel-Pinel, P. Regner, F. Baret, 2006: Simultaneous determination of aerosol- and surface characteristics from top-of-atmosphere reflectance using MERIS on board of ENVISAT, *Adv. in Space Res.*, 37, 12, 2172-2177, doi: 10.1016/j.asr.2006.03.017.
- von Hoyningen-Huene, W., J.M. Yoon, M. Vountas, L.G. Istomina, G. Rohen, T. Dinter, A.A. Kokhanovsky, and J.P. Burrows, 2010: Retrieval of spectral aerosol optical thickness over land using ocean color sensors MERIS and SeaWiFS, *Atmos. Meas. Tech. Discuss.*, 3, 2107–2164
- Waggoner, A.P. and R.E. Weiss, 1980: Comparison of the fine particle mass concentration and light scattering extinction in ambient aerosol. *Atmos. Environ.* 14: 623 – 626.
- Wald, A.E., 1994: Modeling thermal infrared (2-14 μ m) reflectance spectra of frost and snow, *J. Geophys. Res.*, 99, B12, 24,241-24,250, 94JB01560.
- Wang, X., and Zender, C. S., 2010: MODIS snow albedo bias at high solar zenith angles relative to theory and to in situ observations in Greenland, *Remote Sensing of Environment*, 114, 563–575.
- Wania, F., 2003: Assessing the potential of persistent organic chemicals for long-range transport and accumulation in polar regions, *Environ. Sci. Technol.*, 37, 1344 – 1351.
- Warren, S. G., 1982: Optical Properties of Snow, *Rev. Geophys.*, 20(1), 67–89.
- Warren, S.G., and Wiscombe, W.J., 1980: A model for the spectral albedo of snow. II: Snow containing atmospheric aerosols, *J. Atmos. Sci.* 37, 2734-2733,

Bibliography

Warren, S.G., R.E. Brandt, and P. O'Rawe Hinton, 1998: Effect of surface roughness on bidirectional reflectance of Antarctic snow. *J. Geophys. Res. (Planets)*, Vol. 103, No. 25, pp. 789-807.

Welton, E. J., Campbell, J.R., Spinhirne, J.D., Scott, V.S., 2001: Global monitoring of clouds and aerosols using a network of micro-pulse lidar systems. *Proc. Int. Opt. Eng.* 4153, 151-158.

Whitby, K. T. and B. Cantrell, 1976: Fine particles, *Proc. Internat'l Conf. on Environ. Sensing and Assessment*, Institute of Electrical and Electronic Engineers.

Winther, J., G., 1994: Spectral bi-directional reflectance of snow and glacier ice measured in Dronning Maud Land, Antarctica, *Ann. Glaciol.* 20, 1-5.

Winther, J.-G., S. Gerland, J.B. Ørbæk, B. Ivanov, A. Blanco, J. Boike, 1999: Spectral reflectance of melting snow in a high Arctic watershed on Svalbard: some implications for optical satellite remote sensing studies, *Hydrological Processes*. 13, 2033-2049.

Wiscombe, W. J., Warren, S. G., 1980: A model for the spectral albedo of snow, I. Pure snow. *Journal of the Atmospheric Sciences* 37(12): 2712-2733.

Xie, Y., Yang, P., Gao, B.-C., Kattawar, S. G. W., and Mishchenko, M. I., 2006: Effect of ice crystal shape and effective size on snow bidirectional reflectance, *J. Quant. Spectrosc. Radiat. Transfer*, 100, 457-469, doi:10.1016/j.jqsrt.2005.11.056.

Yong Xue, Jianping Guo, and Xiaoye Zhang, 2009: Aerosol Optical Thickness Retrieval over non-Lambertian Land Surface with Synergistic Use of AATSR Radiance Measurements and MODIS Derived Albedo Model Parameters. *Atmospheric Research*, Vol. 93, pp736-746.

Závody, A.M., Mutlow, C.T., Llewellyn-Jones, D.T., 2000: Cloud clearing over the ocean in the processing of data from the Along-Track Scanning Radiometer (ATSR). *Journal of Atmospheric and Oceanic Technology*, 17, 595-615.

Zhang, T., K. Stamnes, and S.A. Bowling, 1996: Impact of clouds on surface radiative fluxes and snowmelt in the Arctic and subarctic, *J. Clim.* 9, 2110-2123.

Zhang, Y., 1999: MODIS UCSB Emissivity Library. Available from <http://www.icess.ucsb.edu/modis/EMIS/html/em.html>

List of abbreviations

AATSR	Advanced Along-Track Scanning Radiometer
AERONET	Aerosol Robotic NETwork
AOD	aerosol optical depth
AOT	aerosol optical thickness
ATSR	Along-Track Scanning Radiometer
AVHRR	Advanced Very High Resolution Radiometer
BAER	Bremen Aerosol Retrieval
BRDF	bidirectional reflectance-distribution function
BRF	bidirectional reflectance factor
BT	brightness temperature
CCN	cloud condensation nuclei
CMDL	Climate Monitoring & Diagnostics Laboratory
DN	digital number
ENVISAT	Environmental Satellite
GBTR	Gridded Brightness Temperature/ Reflectance
GLI	Global Imager
IN	ice nuclei
IPCC	International Panel on Climate Change
IR	infrared spectral region
LOSU	level of scientific understanding
LUT	look-up table
LWC	liquid water content
MERIS	Medium Resolution Imaging Spectrometer
MISR	Multi-angle Imaging SpectroRadiometer
MODIS	Moderate Resolution Imaging Spectroradiometer
NDVI	normalized differenced vegetation index
NIR	near infrared spectral region
NOAA	The National Oceanic and Atmospheric Administration
OPAL	the Zero altitude PEARL Auxiliary Laboratory
OT	optical thickness
PEARL	Polar Environment Atmospheric Research Laboratory
POLDER	POLarization and Directionality of the Earth Reflectance
RF	radiative forcing
RMSD	root mean square deviation
RT	radiative transfer
RTE	radiative transfer equation
SeaWiFS	Sea-viewing Wide Field-of-view Sensor
SEVIRI	Spinning Enhanced Visible Infra-Red Imager
SGLI	Second Global Imager
SLST	Sea and Land Surface Temperature Instrument
SSA	single scattering albedo

List of abbreviations

SZA	solar zenith angle
TIR	thermal infrared spectral region
TOA	top of atmosphere
UCSB	University of California, Santa Barbara
UMBC	University of Maryland, Baltimore County
USGS	U.S. Geological Survey
VIS	visible spectral region

List of used symbols

Latin:

a	surface albedo
$a_n (b_n)$	complex-valued Mie coefficients
A	planetary albedo
$B_\lambda(\text{BT})$	Planck function at some λ for temperature BT
d	particle size
ds	infinitesimal length (path)
E	diffuse transmittance
f	bidirectional reflectance-distribution function (BRDF)
F	solar irradiance at the top of atmosphere (TOA)
g	asymmetry parameter
I	radiance (radiation intensity). See subscripts and superscripts for local meaning
I	Stokes vector
J	radiance source term
m	complex refractive index
M	target observation point
$M(z)$	air mass
n	real part of the complex refractive index
$n(r)$	number size distribution
p	scattering phase function (indicatrix)
Q	horizontal (vertical) linear polarization component of the Stokes vector
Q_s	scattering efficiency
Q_e	extinction efficiency
Q_a	absorption efficiency
r	distance
r_e	effective radius
$r(\lambda)$	atmospheric hemispherical albedo
R	radius of the Earth; particle radius
S	solar constant (1367 W m ⁻²)
$T_1(\lambda, \mu_0)$	total (direct + diffuse) atmospheric transmittance from the TOA to the surface
$T_2(\lambda, \mu)$	the total (direct + diffuse) atmospheric transmittance from the surface to a receiver
T_e	effective radiation emission temperature of the Earth
U	tilted linear polarization component of the Stokes vector
V	circular polarization component of the Stokes vector
z	altitude

List of used symbols

Greek:

α	Ångström wavelength exponent; particle size parameter
$\beta_a(\beta_w, \beta_t)$	first-order loss rate constant for dry deposition (wet deposition, transport to the stratosphere)
δ_{AOT}	AOT retrieval error
ε	emittance
θ	viewing zenith angle
θ_0	solar zenith angle
ϑ	scattering angle
λ	wavelength
μ	cosine of the viewing angle, $\cos \theta$
μ_0	cosine of the illumination angle, $\cos \theta_0$
$\rho_{TOA}(\lambda, \mu_0, \mu, \varphi)$	total directional reflectance at the TOA
$\rho_{atm}(\lambda, \mu_0, \mu, \varphi)$	atmospheric directional reflectance at the TOA
$\rho_{sfc}(\lambda)$	surface Lambertian reflectance at the TOA
$\rho_{sfc}(\lambda, \mu_0, \mu, \varphi)$	surface directional reflectance at the TOA
$\bar{\rho}_{sfc}(M, \lambda, \mu_0, \mu, \varphi)$	average angular reflectance of the target illuminated with the diffuse light only
$\langle \rho_{sfc}(M, \lambda, \mu_0, \mu, \varphi) \rangle$	component of the $\rho_{sfc}(\lambda, \mu_0, \mu, \varphi)$ accounting for multiple light scattering from the environment of the target M in the direction of the observation
σ	the Stefan-Boltzmann constant
σ_a	volume absorption coefficient
σ_e	volume extinction coefficient
σ_s	volume scattering coefficient
Σ_{res}	residence time
τ	optical thickness (depth)
τ_A	aerosol optical thickness (AOT)
τ_R	Rayleigh optical thickness
τ_G	gaseous optical thickness
φ	azimuthal angle of the detector
φ_0	azimuthal angle of the sun
φ'	relative azimuth angle, equals $\varphi_0 - \varphi$
χ	imaginary part of the complex refractive index
ω_0	single scattering albedo
$\bar{\omega}_0$	bulk single scattering albedo
Ω	the unit solid angle

Acknowledgements

I would like to thank all people who supported me throughout all these years and made this work possible.

Many thanks to Prof. Dr. J. P. Burrows and PD Dr. W. von Hoyningen-Huene for providing me with the opportunity to work in the “Aerosol/Cloud” group as a doctoral student. You gave me enormous amount of scientific support and encouragement and at the same time a great degree of freedom in the research. This allowed me to learn a lot during these years and is greatly appreciated.

A special gratitude I would like to express toward Dr. A. Kokhanovsky, who always expressed much interest in my work, provided with lots of energetic and fruitful discussions and a lot of advice and support.

I would like to thank Dr. V. Rozanov and Dr. A. Rozanov for their constant willingness to help. Thank you also for developing and maintaining SCIATRAN, which is a unique scientific tool and is immensely useful for the scientific community.

Many thanks to the “Aerosol/Cloud” group (past and present) and the whole IUP, where I felt comfortable and at home. Thank you Conny, Luca, Jongmin, Tilman, Guenther, Marco, Anja, Andreas Hilboll, Ali, Anna Serdyuchenko and Victor Gorshelev. Your cheerful presence in my life influenced this work greatly!

I would like to acknowledge Heiko Schellhorn and Heiko Schroeter for their fast and efficient IT help, and smooth running of IUP network and computational resources.

I am grateful

to ESA for providing AATSR data;

to NASA for providing MODIS data;

to R. Treffeisen and M. Stock for providing their aerosol phase function measurements;

to M. Mishchenko for providing the Lorenz-Mie code;

to Norm O’Neill, Brent Holben, Piotr Sobolevsky, Rick Wagener, James Butler for their effort in establishing and maintaining AERONET sites PEARL, OPAL, Thule, Kangerlussuaq, Hornsund, Barrow, Longyearbyen, Ny Ålesund, South Pole observatory NOAA;

to Andreas Richter for providing GOME-2 products;

to Tilman Dinter and W. von Hoyningen-Huene for providing BAER product;

to Masataka Shiobara and Andrea Gross for running the MPL site Ny Ålesund;

to Rolf Stange for providing photographs of Spitsbergen;

to Igor Shpilenok for providing photographs of the Kizimen volcano eruption;

to Deutsche Forschungsgemeinschaft for supporting this work within the project “Arctic Aerosol”.

Acknowledgements

I would like to express gratitude to A. Pochanin, Y. Isaev and D. Stankevich, for their never ceasing support.

A great deal of my interest and inspiration in clouds and cloud detection over snow comes from discussions with Mathias Schreier, who was always ready to help in many ways. This is very much appreciated!

As a separate line, I would like to thank my mother, Tatyana Istomina, and my sister, Svetlana Isaeva, for their interest in my work, and for faith in me. Thank you very much!